Bio-inspired Zinc Chlorin Dye Assemblies for Supramolecular Electronics

Dissertation zur Erlangung des
naturwissenschaftlichen Doktorgrades
der Julius-Maximilians-Universität Würzburg

vorgelegt von
Sanchita Sengupta
aus Kalkutta, Indien

Würzburg 2011

Eingereicht am:
bei der Fakultät für Chemie und Pharmazie

1. Gutachter: Prof. Dr. Frank Würthner
2. Gutachter:
der Dissertation

1. Prüfer: Prof. Dr. Frank Würthner
2. Prüfer:
3. Prüfer:

des Öffentlichen Promotionskolloquiums:

Tag des öffentlichen Promotionskolloquiums:
_____

Doktorurkunde ausgehändigt am:
_____

für meine Eltern

Abbreviations

Abs	absorption
AFM	atomic force microscopy
BChl	bacteriochlorophyll
CD	circular dichroism
Chl	chlorophyll
Cryo-TEM	cryo-transmission electron microscopy
DCC	dicyclohexylcarbodiimide
DCM	dichloromethane
DFT	density functional theory
DLS	dynamic light scattering
DMAP	4-dimethylaminopyridine
DMF	*N*, *N*-dimethylformamide
DPTS	4-dimethylaminopyridinium-*p*-toluolsulfonate
DSC	differential scanning calorimetry
EM	electron microscopy
ESI	electron spray ionisation
HOMO	highest occupied molecular orbital
HOPG	highly oriented pyrolytic graphite
HPLC	high performance liquid chromatography
HRMS	high resolution mass spectrometry
HR-TEM	high resolution transmission electron microscopy
LC	liquid crystal/liquid crystalline
LH	light-harvesting
LUMO	lowest unoccupied molecular orbital
MALDI TOF	matrix-assisted laser desorption injection time-of-flight
MAS	magic angle spinning
Me	methyl
MeOH	methanol
M.p.	melting point
nm	nanometer
NMR	nuclear magnetic resonance
OH	hydroxy
OFET	organic field effect transistor

OLED	organic light emitting diode
OMe	methoxy
POM	polarized optical microscope/microscopy
ppm	parts per million
PR-TRMC	pulse radiolysis-time resolved microwave conductivity
RC	reaction center
RP	reversed phase
RT	room temperature
SEM	scanning electron microscopy
SPM	scanning probe microscopy
STEM	scanning transmission electron microscopy
STM	scanning tunneling microscopy
TEM	transmission electron microscopy
TFT	thin film transistor
THF	tetrahydrofuran
TOF	time of flight
UV/Vis	ultraviolet/visible
XRD	x-ray diffraction
ZnChl	zinc chlorin

Table of Contents

Acknowledgement

First of all, I like to express my sincere gratitude to my supervisor Prof. Dr. Frank Würthner for providing me the chance to pursue my PhD study in his research group. I am extremely obliged to him for providing me the oppurtunity to work on a fascinating topic in his group and for his numerous valuable education, guidance, and suggestions at every step. The experience that I have gained in his research group over the last years have been very helpful for my professional as well as personal growth.

I am grateful to Dr. Chantu Saha-Möller not only for his careful correction of my manuscripts, annual reports, posters, valuable suggestions, but also for his encouragement and support in all matters throughout this time. Thanks to Ms. Christiana Toussaint for her kind help on all the administrative work.

I like to enormously thank Dr. Xin Zhang for his great patience and involvement with TEM measurements of my samples and for his valuable guidance, in particular, with regard to sample preparation for electron microscopic studies. It has been a pleasure to learn so much from him. Thanks to Dr. Shinobu Uemura for her help with AFM and STM measurements of my samples and fruitful scientific discussions and Dr. Vladimir Stepanenko for his kind help with AFM, STEM and SEM measurements of my samples. Thanks to Ana-Maria Krause for her help with DSC measurements and helpful discussion on liquid crystals. I like to thank Dr. Gustavo Fernández for valuable discussions, in particular, on Chapters 1, 3 and 5, Dr. Matthias Stolte for useful suggestions and particular help with the German translation of Chapter 6 and Dr. Karl Thorley for his suggestions in improving Chapter 2 of this thesis. Many thanks to Ms. Ana Reviejo for designing the graphical illustrations with Strata 3D program used in this thesis. Thanks to Felix Schlosser for his kind help with handling of the recycling GPC machines. I like to thank Dr. Matthias Grüne, Ms. Elfriede Ruckdecshel for their kind help with NMR measurements and Dr. Michael Büchner for mass spectra measurements.

I like to sincerely thank all the collaborating groups for different measurements and for successful collaborations: Prof. Dr. Huub J. M. de Groot and Dr. Swapna Ganapathy (Universiteit Leiden, Netherlands) for solid-state NMR measurements of samples, Prof. Dr. Laurens D. A. Siebbeles, Dr. Ferdinand C. Grozema and Dr. Sameer Patwardhan (Technical University of Delft, Netherlands) for charge carrier mobility measurements of the samples and for fruitful scientific discussions. Thanks to Dr. Ute Baumeister (Universität Halle) for powder X-Ray diffraction measurements and for her kind help in preparation of two of the

publications. Thanks to Prof. Dr. Lifeng Chi and Dr. Daniel Ebeling (Universität Münster) for conductive AFM measurement of one of the samples.

I particularly acknowledge Dr. Valerie Huber for introducing me to the research topic and for her kind help and guidance in initial days of my PhD. I am thankful to all our present and past group members for their help and for the pleasant time that I spent with all of them. Thanks to Xin, Vladimir, Shinobu, Matthias, Gustavo, Kingsuk, Suhrit, Florian, Felix, Martin, Benjamin, Marina, Ralf, Marcel, Ana-maria, Charlotte, Daniel, Ulrich, Hannah, Maria, Ana, Christina, Shao, Lilli, Sabin, Karl, Peter, Mei-jin, Zengqi, Linlin, Hebing, Joachim and all others. I like to thank my friends, in particular, Poulomi, Tuli, Sameer, Kingsuk and Soma for their support and the nice time that I spent with all of them. Finally, I am thankful to my family back home for their concern, support and for providing me the strength to face the challenges in life.

Chapter 1

Introduction and Aim of the Thesis

Organic electronics is an important research area in academia and industry that has witnessed significant breakthroughs during the last decade.[1,2] The quest for technological innovations is never-ending, which ensures the design of a wide variety of advanced materials with new or improved (opto)electronic properties for optimum device performance. The chemistry of functional organic dyes/pigments has made significant contributions in this regard. In recent years, there has also been great interest in the use of self-assembling organic materials as the active component in (opto)electronic devices[3,4,5] such as organic field-effect transistors (OFETs),[1,6,7] organic light-emitting diodes (OLEDs) and organic solar cells.[8] This has led to the development of a new scientific research area termed as "supramolecular electronics."[3,4,5,9]

Self-assembling materials are of specific interest, since they provide facile mechanism for assembling large number of molecules into structures that can bridge length scales from nanometers to macroscopic dimensions. This leads to synergistic and emergent properties, not intrinsic to the building blocks themselves, such as charge transport. (Opto)electronic device performance is to a large extent determined by the mobility of charge carriers, which strongly depends on the material morphology.[6-9] The relation between the supramolecular organization of the active organic material and charge carrier transport is thus pivotal for improving device performance. Biosupramolecular electronics is also a fascinating research area that has emerged in recent years.[10] Strongly interacting π-stacked molecules are found in many important biological systems such as the primary electron donor within photosynthetic reaction center (RC) proteins,[11,12] the base pairs within duplex DNA biopolymers and bacteriochlorophylls (BChls) in photosynthetic light-harvesting complexes (LHCs).[13] DNA is an excellent natural archetype for unidirectional charge transport for which electrical transport measurements through single polymers, bundles have indeed been reported.[14]

The natural LHCs of plants and photosynthetic bacteria are one of the most fascinating functional molecular assemblies. Chlorophylls play pivotal role in photosynthesis, a multistep

process that transduce solar energy into chemical energy.[15,16] The two major steps that can be distinguished in the primary processes of photosynthetic energy conversion are harvesting of light and migration of light energy to the RC and charge separation and subsequent electron transfer to the RC. The effectiveness of these processes relies on two fundamental physicochemical principles. Firstly, organization of BChls mediated by proteins, into precisely ordered structures to obtain extraordinarily high cross-sections for light absorption. Secondly, extremely fast energy migration within the LHC to ensure that the excitation energy is available for photo-induced energy or electron transfer processes. In higher plants, green algae, heliobacteria and purple bacteria,[14-16] the antenna system is embedded within the photosynthetic membrane. In some photosynthetic organisms, such as green sulphur bacteria (*Chlorobiaceae*) and green filamentous bacteria (*Chloroflexaceae*), the major LH apparatus is formed by chlorosomes, which are oblong bodies attached to the side of the cell membrane.[17] Chlorosomes are nearly protein-free and their structure and function rely solely on the self-aggregation of antenna pigments. Chlorosomes contain the highest density of chromophores for any antenna system known in nature. BChl assemblies show very high exciton mobilities[18] which make these aggregates interesting for applications in supramolecular photonics.

To contribute to the structural elucidation of these biologically important assemblies, semisynthetic zinc chlorins (ZnChls) have been designed and their aggregation properties have been investigated in detail previously[19,20,21,22] in two PhD theses in our group.[19a,21] Zinc chlorin assemblies are the ideal structural and functional mimics of the natural chlorosomal antennae. Structural mimics of chlorosomes have been reported by other groups as well,[23,24,25,26] some of which have provided insights into the structure[27,28] and energy transport processes of natural chlorosomal assemblies. The optical and redox properties associated with chlorin dyes suggest that these dye assemblies might also be well-suited for charge transport although such studies are rather scarce.[29] Owing to its outstanding excitonic, optical and redox properties, the chlorosomal superstructure is extremely appealing for the design of self-assembling, biomimetic functional material for charge transport.

The main aim of this thesis is to design zinc chlorin derivatives functionalized with a wide variety of peripheral substitutions and investigation of their self-assembly behavior in solution, in the solid state and on surfaces. Furthermore, charge transport properties of different zinc chlorin assemblies have been investigated and correlated with their bulk packing modes. By virtue of their ability to self-assemble into well-ordered excitonically coupled π-stacks in solution, on surfaces and in solid state and their excellent charge transport

and conductive properties, zinc chlorin assemblies accordingly hold great promise for their utilization in (bio)supramolecular electronics.

Chapter 2 titled "State of Knowledge" provides an overview on structural features of natural LH complexes in purple bacteria and green sulphur bacteria (chlorosomes) and provides a brief description of different models known to describe the chlorosomal architecture till date. Chlorosomes occur in a broad heterogeneity owing to wide biodiversity in nature hence they are the only class of antennae systems for which no precise structural information is currently available. Hence, their exact superstructure is controversially discussed in literature. Structural characterization of chlorosomes have relied mostly on combination of complementary spectroscopic and microscopic techniques such as absorption and circular dichroism (CD) spectroscopy, solid-state NMR, electron microscopy and powder X-ray diffraction. Hence, this chapter provides an overview on the structural models proposed for chlorosomal superstructures based on such interdisciplinary studies. In the last section, artificial chlorosomal assemblies, namely, rod-like and stack assemblies, based on semisynthetic zinc chlorins are discussed in detail (schematic models of such assemblies are shown in Figure 1).

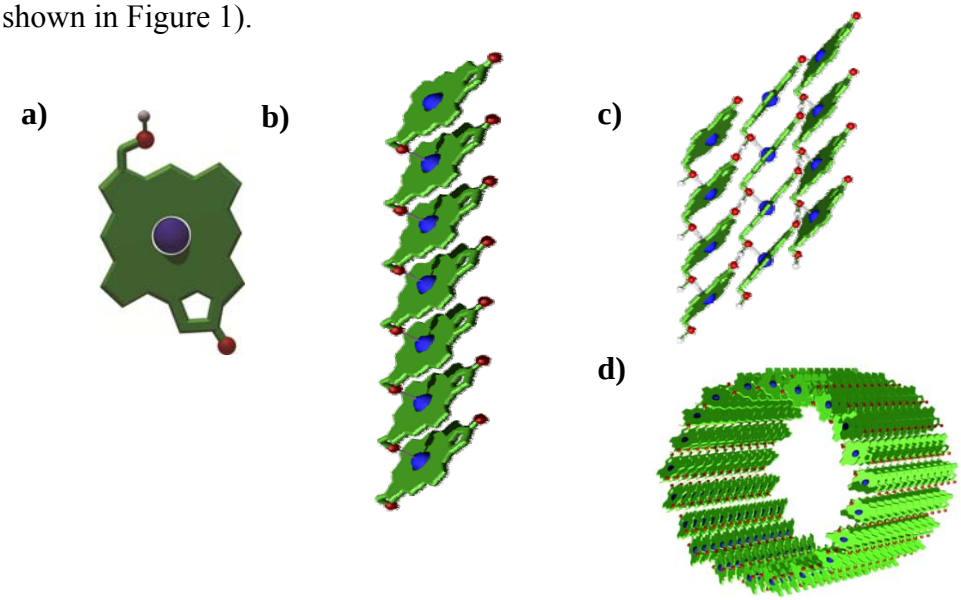

Figure 1. a) Zinc chlorin monomer, green unit indicates the chlorin macrocycle, zinc ion and oxygen atoms are represented by blue and red spheres, respectively; b) representation of intermolecular interactions i.e., π-π stacking and zinc-oxygen coordination (indicated by grey rods) leading to formation of one-dimensional parallel stacks; c) interstack hydrogen bonding connecting the zinc chlorin parallel π stacks formed by π-π stacking and zinc-oxygen coordination; d) tubular superstructures formed by zinc 3^1-hydroxy chlorins.

Chapter 3 describes the synthesis and structural characterizations of 3^1-hydroxy zinc chlorins **1a**, **2a**, **3** and 3^1-methoxy zinc chlorins **1b**, **2b** (Chart 1) that form rod-like/tubular and one-(and two-) dimensional stack aggregates, respectively (see models in Figure 1).

These supramolecular polymers in solution have been studied in detail by UV/Vis and CD spectroscopy, dynamic light scattering (DLS) method providing insights into self-assembly process and aggregate sizes in solution. Detailed electron microscopic studies such as transmission electron microscopy (TEM) and scanning transmission electron microscopy (STEM) provided unequivocal evidence for well-defined hollow tubular assemblies of 3^1-hydroxy zinc chlorins for the first time. Lyophilization of these two types of aggregates of **1a** and **1b** from solution led to microcrystalline solid state materials. Subsequently, the microstructures of these two types of aggregated π-stacks of zinc chlorins in the solid state, i.e. rod and stack aggregates, have been assessed by a combination of solid-state magic angle spinning (MAS) NMR, molecular modelling and powder X-ray diffraction (XRD). The combination of these techniques unambiguously provided a unique three-dimensional packing of these dyes in solid state. Finally, charge transport in these two types of aggregates in solid state were probed by electrodeless pulse radiolysis-time resolved microwave conductivity (PR-TRMC) technique,[30,31] and both tubular and stack aggregates exhibited high charge carrier mobilities. The charge transport properties were found to strongly depend on the supramolecular structures, revealing a profound structure-property relationship. Notably, direct electrical transport was successfully measured in the tubular assemblies of ZnChl **3** for the first time by conductive AFM technique and these single supramolecular wires were found to possess high conductivity. These combined results justify the suitability of these highly ordered assemblies for (bio)supramolecular electronics.

Chapter 4 describes the design of zinc chlorins **4-6** functionalized with "Percec type" second generation dendron wedge substituents[32] at the 17^2-position possessing 3^1-methoxy groups (Chart 1) and their self-assembly on surface and in the solid state mediated by the dendron substitutions. These dyes exhibited well-defined surface adlayers depending upon the shapes of the attached second generation dendron wedges. Based on the two-dimensional spatial demands and steric effects induced by these dendritic segments, these dyes spontaneously self-assembled into linear or cyclic assemblies on atomically flat and conductive highly oriented pyrolytic graphite (HOPG) surface, as revealed by detailed scanning probe microscopy (SPM) i.e., atomic force microscopy (AFM) and scanning tunneling microscopy (STM) studies. Furthermore, the appended dendron wedge of intermediate size (with six alkyl chains) in ZnChl **5** imparted novel liquid crystalline (LC) properties to it. The LC properties have been investigated in detail by variety of techniques such as polarisation optical microscopy (POM), differential scanning calorimetry (DSC),

AFM and powder XRD. These studies indicated that **5** self-assemble hierarchically; first forming hexameric rosettes which subsequently self-assemble into nano-segregated columns aided by π-π stacking of ZnChls. The charge transport behavior of the columnar LC phases of zinc chlorin **5** were investigated by PR-TRMC technique and were found to exhibit appreciable charge carrier mobilities.

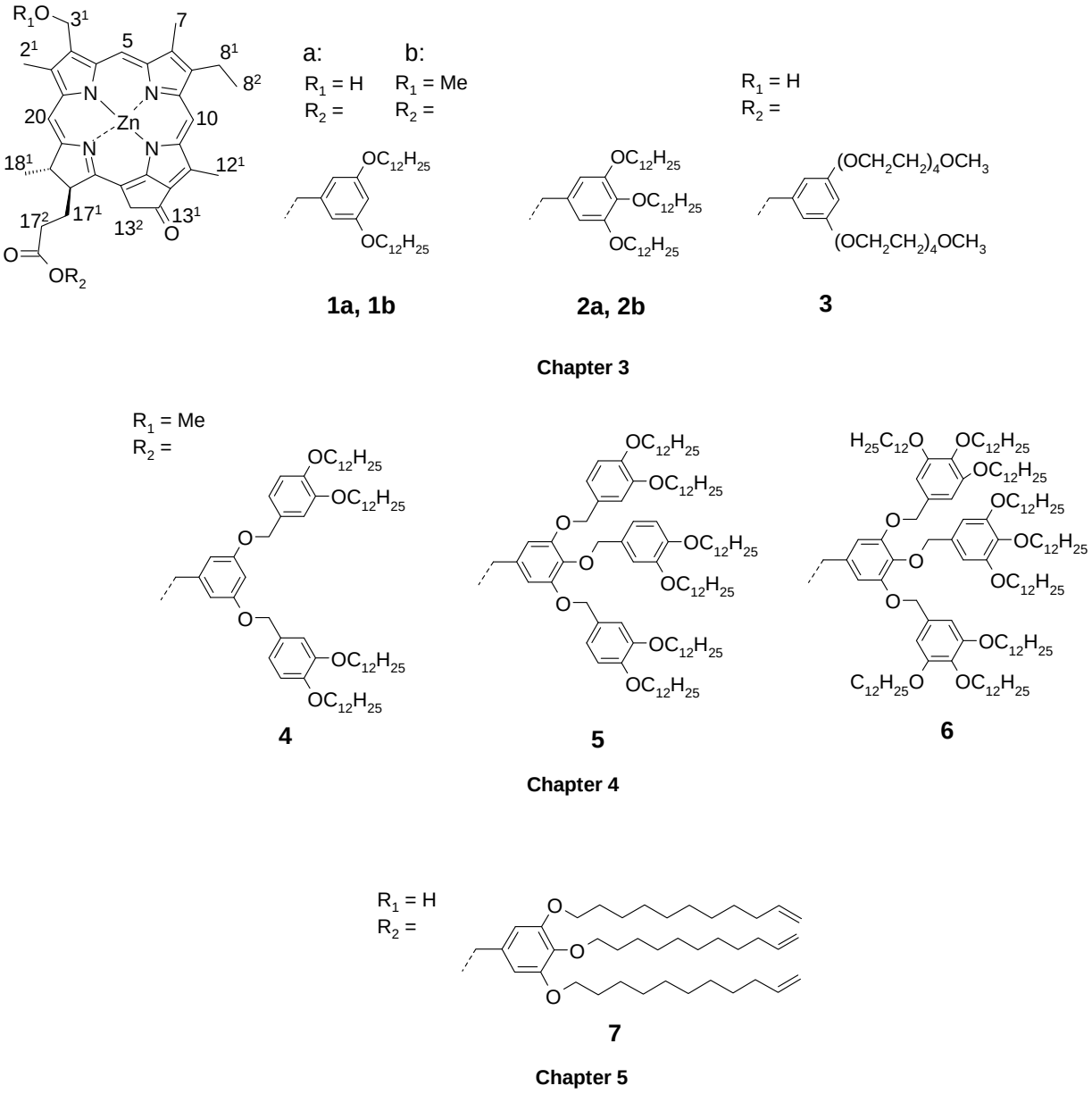

Chart 1. Chemical structures of zinc chlorin compounds synthesized and studied in this work.

Chapter 5 describes the synthesis of zinc chlorin derivative **7** (Chart 1) functionalized with undecyl functional groups bearing terminal olefinic groups and 3^1-hydroxy functionality. The compound self-assembles into nanorod/tubular aggregates in non-polar solvents similar to 3^1-hydroxy zinc chlorins described in Chapter 3, with functionalizable surface. The self-

assembly behavior has been investigated by UV/Vis absorption, CD spectroscopy, DLS studies and AFM. Appreciable charge carrier mobilities were obtained for these aggregates in solid state by the PR-TRMC technique. Importantly, the electron-rich terminal olefinic groups provided some contrast in electron microscopic techniques such as TEM, STEM and scanning electron microscopy (SEM). As a result, tube-like aggregates could be visualized by electron microscopy for the first time for such assemblies under different sample preparation conditions. Furthermore, the chemically accessible olefinic groups of the rod/tube-like assemblies could be cross linked by in-situ metathesis polymerization reaction. The intratubular cross-linked aggregates could be characterized by AFM, UV/Vis, CD and fourier transform infrared (FTIR) spectroscopy.

The thesis concludes with summaries in English and German in **Chapter 6**.

References and notes

(1) Forrest, S. R.; Thompson, M. E. *Chem. Rev.* **2007**, *107*, 923–925 and articles published in this thematic issue of *Chem. Rev*.

(2) *Electronic Materials: the Oligomer Approach* Wiley-VCH, Weinheim, 1998.

(3) Hoeben, F. J. M.; Jonkheijm, P.; Meijer, E. W.; Schenning, A. *Chem. Rev.* **2005**, *105*, 1491–1546.

(4) Schenning, A.; Meijer, E. W. *Chem. Commun.* **2005**, 3245–3258.

(5) Grozema, F. C.; Siebbeles, L. D. A. *Int. Rev. Phys. Chem.* **2008**, *27*, 87–138.

(6) Yamamoto, Y.; Zhang, G.; Jin, W.; Fukushima, T.; Ishii, N.; Saeki, A.; Seki, S.; Tagawa, S.; Minari, T.; Tsukagoshi, K.; Aida, T. *Proc. Natl. Acad. Sci. U. S. A.* **2009**, *106*, 21051–21056.

(7) Guo, X. F.; Xiao, S. X.; Myers, M.; Miao, Q.; Steigerwald, M. L.; Nuckolls, C. *Proc. Natl. Acad. Sci. U. S. A.* **2009**, *106*, 691–696.

(8) Schmidt-Mende, L.; Fechtenkotter, A.; Müllen, K.; Moons, E.; Friend, R. H.; MacKenzie, J. D. *Science* **2001**, *293*, 1119–1122.

(9) a) Meijer, E. W.; Schenning, A. *Nature* **2002**, *419*, 353–354; b) Yamamoto, Y.; Fukushima, T.; Suna, Y.; Ishii, N.; Saeki, A.; Seki, S.; Tagawa, S.; Taniguchi, M.; Kawai, T.; Aida, T. *Science* **2006**, *314*, 1761–1764; c) Hill, J. P.; Jin, W.; Kosaka, A.; Fukushima, T.; Ichihara, H.; Shimomura, T.; Ito, K.; Hashizume, T.; Ishii, N.; Aida, T. *Science* **2004**, *304*, 1481–1483; d) Würthner, F.; Chen, Z.; Hoeben, F. J. M.; Osswald,

P.; You, C.-C.; Jonkheijm, P.; van Herrikhuyzen, J.; Schenning, A. P. H. J.; van der Schoot, P. P. A. M.; Meijer, E. W.; Beckers, E. H. A.; Meskers, S. C. J.; Janssen, R. A. J. *J. Am. Chem. Soc.* **2004**, *126*, 10611–10618.

(10) a) Shinwari, M. W.; Deen, M. J.; Starikov, E. B.; Cuniberti, G. *Adv. Funct. Mater.* **2010**, *20*, 1865–1883; b) Kumar, A.; Sevilla, M. D. *Chem. Rev.* **2010**, *110*, 7002–7023; c) Matile, S.; Jentzsch, A. V.; Montenegro, J.; Fin, A. *Chem. Soc. Rev.* **2011**, *40*, 2453–2474; d) Bhosale, R.; Misek, J.; Sakai, N.; Matile, S., *Chem. Soc. Rev.* **2010**, *39*, 138–149; e) Uhlenheuer, D. A.; Petkau, K.; Brunsveld, L. *Chem. Soc. Rev.* **2010**, *39*, 2817–2826; f) Stupp, S. I. *Nano Letters* **2010**, *10*, 4783-4786; g) Tovar, J. D.; Rabatic, B. M.; Stupp, S. I. *Small* **2007**, *3*, 2024–2028.

(11) Scheuring, S.; Sturgis, J. N.; Prima, V.; Bernadac, A.; Levy, D.; Rigaud, J. L. *Proc. Natl. Acad. Sci. U. S. A.* **2004**, *101*, 11293–11297.

(12) Beljonne, D.; Curutchet, C.; Scholes, G. D.; Silbey, R. J. *J. Phys. Chem. B* **2009**, *113*, 6583–6599.

(13) Doust, A. B.; Wilk, K. E.; Curmi, P. M. G.; Scholes, G. D. *J. Photochem. Photobiol. a-Chemistry* **2006**, *184*, 1–17.

(14) a) Genereux, J. C.; Wuerth, S. M.; Barton J. K. *J. Am. Chem. Soc.* **2011**, *133*, 3863–3868; b) Genereux, J. C.; Barton, J. K. *Chem. Rev.* **2010**, *110*, 1642–1662; c) Grozema, F. C.; Tonzani, S.; Berlin, Y. A.; Schatz, G. C.; Siebbeles, L. D. A.; Ratner, M. A. *J. Am. Chem. Soc.* **2009**, *131*, 14204–14205; d) Guo X.; Gorodetsky A.; Hone J.; Barton, J. K.; Nuckolls C. *Nat. Nanotech.* **2008**, *3*, 163–167; e) Porath, D.; Bezryadin, A.; de Vries, S.; Dekker, C. *Nature* **2000**, *403*, 635–638.

(15) Bahatyrova, S.; Frese, R. N.; Siebert, C. A.; Olsen, J. D.; van der Werf, K. O.; van Grondelle, R.; Niederman, R. A.; Bullough, P. A.; Otto, C.; Hunter, C. N. *Nature* **2004**, *430*, 1058–1062.

(16) a) McDermott, G.; Prince, S. M.; Freer, A. A.; Hawthornthwaitelawless, A. M.; Papiz, M. Z.; Cogdell, R. J.; Isaacs, N. W. *Nature* **1995**, *374*, 517–521; b) Pullerits, T.; Sundstrom, V. *Acc. Chem. Res.* **1996**, *29*, 381–389.

(17) Balaban, T. S.; Tamiaki, H.; Holzwarth, A. R. (Ed. Würthner F.) *Supramolecular Dye Chemistry* **2005**, *258*, 1–38.

(18) a) Prokhorenko, V. I.; Steensgard, D. B.; Holzwarth, A. R. *Biophys. J.* **2000**, *79*, 2105–2120; b) Pšenčík, J.; Ma, Y.-Z.; Arellano, J. B.; Hála, J.; Gillbro, T. *Biophys. J.* **2003**, *84*, 1161–1179; c) Scholes, G. D.; Rumbles, G. *Nat. Mater.* **2006**, *5*, 683–696.

(19) a) Huber V. Dissertation, Universität Würzburg 2007; b) Huber, V.; Katterle, M.; Lysetska, M.; Würthner, F. *Angew. Chem., Int. Ed.* **2005**, *44*, 3147–3151; c) Huber, V.; Sengupta, S.; Würthner, F. *Chem.–Eur. J.* **2008**, *14*, 7791–7807.

(20) Huber, V.; Lysetska, M.; Würthner, F. *Small* **2007**, *3*, 1007–1014.

(21) Röger C. Dissertation, Universität Würzburg 2007.

(22) a) Röger, C.; Miloslavina, Y.; Brunner, D.; Holzwarth, A. R.; Würthner, F. *J. Am. Chem. Soc.* **2008**, *130*, 5929–5939; b) Röger, C.; Müller, M. G.; Lysetska, M.; Miloslavina, Y.; Holzwarth, A. R.; Würthner, F. *J. Am. Chem. Soc.* **2006**, *128*, 6542–6543.

(23) Balaban, T. S.; Linke-Schaetzel, M.; Bhise, A. D.; Vanthuyne, N.; Roussel, C.; Anson, C. E.; Buth, G.; Eichhofer, A.; Foster, K.; Garab, G.; Gliemann, H.; Goddard, R.; Javorfi, T.; Powell, A. K.; Rosner, H.; Schimmel, T. *Chem.–Eur. J.* **2005**, *11*, 2268–2275.

(24) Tamiaki, H. *Coord. Chem. Rev.* **1996**, *148*, 183–197.

(25) Prokhorenko, V. I.; Holzwarth, A. R.; Müller, M. G.; Schaffner, K.; Miyatake, T.; Tamiaki, H. *J. Phys. Chem. B* **2002**, *106*, 5761–5768.

(26) Tamiaki, H.; Amakawa, M.; Shimono, Y.; Tanikaga, R.; Holzwarth, A. R.; Schaffner, K. *Photochem. Photobiol.* **1996**, *63*, 92–99.

(27) Tamiaki, H.; Takeuchi, S.; Tsudzuki, S.; Miyatake, T.; Tanikaga, R. *Tetrahedron* **1998**, *54*, 6699–6718.

(28) Balaban, T. S. *Acc. Chem. Res.* **2005**, *38*, 612–623.

(29) Kassi, H.; Leblanc, R. M.; Hotchandani, S. *Physica Status Solidi B-Basic Research* **2000**, *220*, 931–939.

(30) Warman, J. M.; de Haas, M. P.; Dicker, G.; Grozema, F. C.; Piris, J.; Debije, M. G. *Chem. Mater.* **2004**, *16*, 4600–4609.

(31) Warman, J. M.; Van de Craats, A. M. *Mol. Cryst. Liq. Cryst.* **2003**, *396*, 41–72.

(32) Rosen, B. M.; Wilson, C. J.; Wilson, D. A.; Peterca, M.; Imam, M. R.; Percec, V. *Chem. Rev.* **2009**, *109*, 6275–6540.

Chapter 2

State of Knowledge

In this introductory chapter, the first part provides a brief overview on "supramolecular electronics" based on self-assembled nanostructures. The design of self-assembled architectures conducive to charge transport and hence electronic applications is often inspired from nature. Therefore, in the next section, structural features of natural light harvesting (LH) complexes in purple bacteria and green sulphur bacteria (chlorosomes), which serve as models for the rational design of architectures suitable for supramolecular electronics, are presented. The structural and functional features of chlorosomes have been intensively investigated by a combination of complimentary spectroscopic, crystallographic and microscopic techniques such as UV/Vis, circular dichroism spectroscopy, solution and solid-state magic angle spinning (MAS) NMR, powder X-ray diffraction (XRD), electron microscopy (EM) and many other techniques in the literature. A very brief overview on such studies is thus briefly presented. Finally, J-type aggregates designed from semisynthetic zinc chlorin derivatives are discussed in detail that are appropriate structural as well as functional mimics of natural chlorosomes, and are potentially well-suited systems for supramolecular electronic applications.

2.1. Supramolecular Electronics

The last decade has witnessed tremendous progress in the field of organic electronics.[1-4] The search for new semiconducting materials with high charge carrier mobilities and hence improved device performances in OFETs, OLEDs and organic photovoltaics still continues. Currently there is also great interest in the utilization of self-assembled organic materials as the active component in (opto)electronic device fabrication.[5-9] One of the major focuses of modern supramolecular chemistry is the organization of functional molecular building blocks by non-covalent interactions such as hydrogen bonding, π-π-interactions, donor-acceptor and ionic interactions, host-guest interactions, dipolar and solvophobic interactions, and metal-ligand coordination.[10] *Supramolecular electronics*, a term introduced by Meijer and co-workers, is a field of research dealing with electronic functions arising from self-assembled π-conjugated materials in the length regime of 5-100 nanometers (nm) that is intermediate to molecular electronics and plastic electronics.[11-15] Nanoscale performance is to a large extent determined by the mobility of charge carriers, which strongly depends on material morphology of such systems. Therefore, a fundamental understanding of the relationship between the supramolecular organization of the electronically active organic material and their charge transport properties is essential for development of self-assembled π system-based (opto)electronic devices and subsequent improvement of such device performances.

2.1.1. Representative Architectures for Supramolecular Electronics

Unidimensional channelled architectures formed from π-conjugated systems, particularly fibers and columns such as nanorods and nanotubes that facilitate hopping of charge carriers have been studied extensively.[11-14,16] Particularly, discotic columnar liquid crystals (DLCs) based on a large class of π-conjugated molecules such as triphenylenes,[17,18] hexabenzocoronenes (HBCs),[19-21] contorted HBCs[8,22] porphyrins and phthalocyanines[23] and perylene bisimides[24-27] have evolved as the new generation of organic semiconductors.[19-21,28-30] Other unconventional building blocks include those based on dendrimers and dendrons[31] that form a rich library of supramolecular architectures potentially attractive for supramolecular electronics.[14,32,33] The pioneering work of Aida and co-workers on the family of molecularly engineered graphenes with a self-assembled one-dimensional tubular shape and a chemically accessible surface constitutes an important step towards supramolecular electronics.[34-36] They designed amphiphilic hexa-peri-hexabenzocoronene (HBC) that self-assembled to form discrete nanotubes by π-π stacking,

characterized by an aspect ratio greater than 1000, having uniform widths consisting of helical arrays of the π-stacked graphene molecules and exterior and interior surfaces covered by hydrophilic triethylene glycol chains.[34] Those graphitic nanotubes were redox active, and a single piece of the nanotube showed an electrical conductivity of 2.5 megaohms upon doping with an oxidant.[34]

Controlled self-assembly of trinitrofluorenone-appended gemini-shaped amphiphilic HBCs selectively formed nanotubes or microfibers with different photochemical properties. In these several micrometer long nanotubes, a molecular layer of electron-accepting trinitrofluorenone laminates an electron-donating graphitic layer of π-stacked hexabenzocoronene. The coaxial nanotubular structure allowed photochemical generation of spatially separated charge carriers and a quick photoconductive response with a large on/off ratio greater than 10^4.[35]

Molecular graphenes with covalently linked C_{60} fullerene pendants (HBC-C_{60}) were designed that self-assembled into coaxial nanotubes with walls consisting of π-stacked HBC arrays, whereas the nanotube surface is fully covered by a molecular layer of clustering C_{60}. These coaxial nanotubes exhibited an ambipolar character in the field-effect transistor output (hole mobility (μ_h) = 9.7×10^{-7} cm^2/Vs; electron mobility (μ_e) = 1.1×10^{-5} cm^2/Vs) and displayed photovoltaic response upon light illumination.[36] As evaluated by an electrodeless flash-photolysis time-resolved microwave conductivity (FP-TRMC) technique, the intratubular hole mobility (2.0 cm^2/Vs) of a co-assembled nanotube containing 10 mol % of HBC-C_{60} is as large as the intersheet mobility in graphite.

Recent contribution of the Aida group involves the design of a chiral and enantiomerically pure amphiphilic porphyrin-fullerene dyad that self-assembled into nanofibers with a built-in D/A heterojunction,[37] while its racemic form, under identical conditions, self-assembled into submicrometer-sized spheres with a D/A arrangement essentially different from that in the nanofiber assembly. The former aggregate clearly displayed photoconduction with an ambipolar charge-transporting character, with electron and hole mobilities, estimated from time-of-flight (TOF) technique, of 0.14 and 0.10 cm^2/Vs respectively,[37] which are comparable to or even better than those reported for top-class organic D/A heterojunction materials.

In pioneering work, Percec and co-workers synthesized fluorine-carrying clusters of highly branched polymers called “dendritic wedges”. When electron donor and acceptor groups were attached, these wedges self-assembled into supramolecular columns by charge transfer interactions and the self-assembly of these wedges provided liquid crystallinity to the organic

components. The charge-carrier mobilities, as determined by the TOF method, were in the range of 10^{-4}–10^{-3} cm^2/Vs, well within the values needed for self-assembled system-based electronic devices.[14]

Nature often provides the inspiration for rational design of self-assembling material for charge transport and electronic applications. Owing to their importance in nature and technology, tetrapyrrole based macrocycles such as phthalocyanines and porphyrins are probably one of the most studied classes of dyes. Their intense absorption bands in the visible range and their favorable redox properties enabled varied applications in electronics.[23] Charge transport behavior of porphyrinoids (mainly porphyrins and phthalocyanines) have been extensively studied in solid state[23,38] in regard to applications in organic electronics and photovoltaics.[39-42] On the other hand, studies on the charge transport behavior of their natural counterparts, i.e., structurally related chlorophylls and their aggregates, could not be found in the literature. Few studies on hole transport in microcrystalline chlorophyll *a* (Chl *a*) are reported by TOF measurements performed on Al/Chl *a*/Au sandwich cells, where hole mobilities of 0.002 cm^2/Vs have been obtained for microcrystalline Chl *a* in the absence of disorder.[43,44] The charge transport capabilities of chlorophylls and their aggregates and impending applications in (opto)electronic devices such as OFETs based on this important class of chromophores is mostly unexplored.

2.1.2. Supramolecular Architectures Inspired from Nature

Many of the self-assembly motifs used in supramolecular chemistry find their inspiration from nature where molecular self-assembly underlies the basis for the formation of large functional structures in living organisms. Designing supramolecular architectures with functions mimicking natural systems gives rise to emerging oppurtunities in material science. Furthermore, it also contributes significantly to bridge the gap between natural and artificial systems in order to understand the guidelines used to assemble units in a hierarchical organization. Representative examples of naturally occurring self-assembled structures are the secondary and tertiary structure of proteins, the π-stacked structure of DNA held in place by hydrogen bonds between nucleobases in the opposite strands,[45] and the organization of bacteriochlorophylls (BChls) in light-harvesting (LH) complexes of green and purple bacteria.[46] The channelled structure of Tobacco Mosaic Virus (TMV) capsid proteins serves as a biological inspiration for self-assembling supramolecular dendrons and dendrimers.[47,48]

Photosynthetic organisms are ubiquitous on the surface of the earth and are responsible for the development and sustenance of all life on earth (Figure 1).[49,50] Photosynthesis is an integrated system in which light harvesting, photoinduced charge separation, and catalysis combine to carry out two of the most thermodynamically demanding processes, i.e., the oxidation of water and the reduction of carbon dioxide. Among the many different classes of photosynthetic organisms, many varied types of light-harvesting and electron transport systems are used. However, they all use the same basic strategy, whereby the light energy is initially collected and concentrated by an antenna system containing many chromophores, mainly chlorophylls, followed by energy transfer to a specialized reaction center (RC) protein, where this captured energy is converted into chemical energy through a cascade of electron-transfer reactions. An antenna, or light-harvesting molecule, is one which increases the cross section for absorption of solar energy without undergoing charge separation itself. Following photoexcitation of an antenna chromophore array, a series of one or more energy transfer steps occur, which funnels the excitation energy to a site at which charge separation occurs.

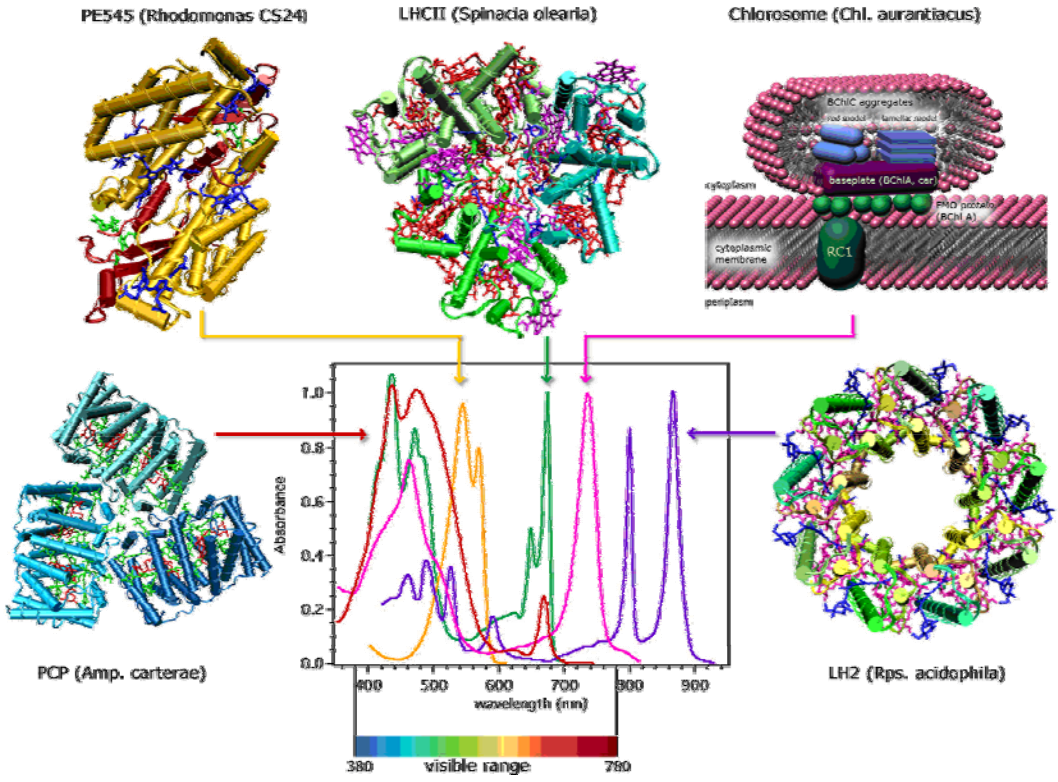

Figure 1. Representative light-harvesting systems occurring in nature and their respective absorption spectra.[49,50] Reprinted from ref. 49, 50, with permission from the American Chemical Society and personal communication with Prof. G. D. Scholes.

Photosynthesis is divided into two reactions namely, the light reaction and the dark reaction. Light reactions are the "photo" part of photosynthesis where light is absorbed by pigments and

energy storage molecules, ATP and NADPH, are generated. On the other hand, dark reactions are the light-independent "synthesis" part of photosynthesis where the ATP and NADPH molecules created during the light reactions power the production of glucose.

2.2. Natural Light Harvesting Antenna systems

Photosynthesis can be classified into oxygenic photosynthesis carried out by cyanobacteria and plants, and non-oxygenic photosynthesis carried out by purple bacteria, green sulphur and non-sulphur bacteria and heliobacteria.[49,50] In green plants, algae and cyanobacteria, photosystem I (PS I) functions to produce NADPH that is used to reduce carbon dioxide in the reactions of the Calvin cycle, while photosystem II (PS II) catalyzes the conversion of light energy into redox agents capable of splitting water (H_2O). Oxygenic organisms harness solar energy to extract the H^+ and e^- from H_2O, required for the fixation of CO_2. On the other hand, photosynthetic bacteria have much simpler photoconversion pathways, since they evolved at a time when earth had a reducing atmosphere. Non-oxygenic organisms cannot generate the necessary oxidizing potential, to oxidize H_2O and therefore extract H^+ and e^- from alternative compounds like H_2S. Under normal conditions both organisms use the derived H^+ and e^- for the synthesis of ATP, NAD(P)H and ultimately CO_2 fixation, to produce carbohydrates such as starch and glycogen. In most photosynthetic organisms like purple bacteria, cyanobacteria, dinoflagellates and green plants, the pigments in both antenna and reaction center complexes are non-covalently bound to specific sites on proteins, and the geometrical arrangements of the pigments are largely determined by pigment-protein interactions. The green photosynthetic bacteria, on the other hand, possess unique rod-like peripheral membrane antenna complexes known as chlorosomes,[51] which contain a relatively small amount of protein compared to very dense and high pigment content. The following section discusses structural features of dye organization in these two LH systems i.e., purple bacteria[52-55] and the chlorosomes in green sulphur bacteria.

2.2.1 LH apparatus of Purple Bacteria

The most studied photosynthetic apparatus till date is that of the purple non-sulphur bacteria.[52-55] The antenna system of purple bacteria consists of two types of protein-pigment complexes namely LH-I and LH-II complex and a single type of reaction center (RC). While LH-I is the integral membrane protein complex that is bound to the photosynthetic RC, LH-II is the

peripheral protein-pigment complex which gathers light energy and funnels the excitation energy to LH-I by fluorescence resonance energy transfer (FRET) processes. The LH-II complex, which surrounds LH-I, absorbs at 800 nm and 850 nm; and LH-I, which in turn surrounds the RC, absorbs at a lower energy i.e., 875 nm. The energy cascade serves to funnel electronic excitations from the LH-IIs through LH-I to the RC. Both of these pigment-protein complexes are membrane bound and utilize bacteriochlorins and carotenoids. In most natural photosynthetic LH complexes, sunlight is not only collected by chlorophyll or BChls, which are powerful absorbers in the violet, blue and red wavelength region of the sunlight, but they are supported by accessory LH dyes such as phycobiliproteins[56] and carotenoids that can utilize the intensive green region of the solar spectrum. Purple bacteria absorb light mainly at wavelengths of about 500 nm through carotenoids and above 800 nm through BChls, spectral region complementary to that of plants and algae. The exact architecture of LH-II of two species, namely *Rhodopseudomonas* (Rps.) *acidophila* (Figure 2) and *Rhodospirillum* (Rs.) *molischianum* was elucidated by a combination of high-resolution XRD and ab initio molecular modelling. The crystal structure and atomic force microscopy (AFM) images of the LH-II antenna protein from purple photosynthetic bacteria revealed that its constituent BChls are arrayed in a cyclic structures (Figure 3, Figure 4).

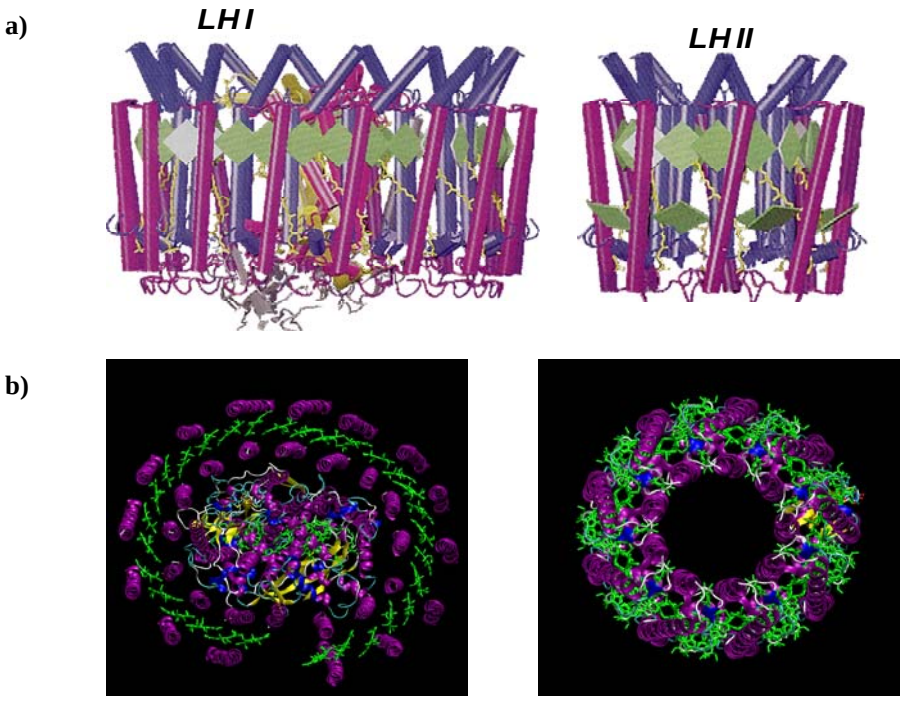

Figure 2. Schematic representation of light-harvesting complexes LH-I and LH-II from *Rhodpseudomonas acidophila*, a) side view and b) top view of membrane integrated complex. Adapted and reprinted with permission from ref. 55.

These studies led to the understanding of structure-function relationship in bacterial LH systems. Subsequently, considerable efforts have been invested in designing synthetic mimics for these cyclic chromophore arrays, some of which have provided useful insights into the photophysics of energy collection and excitation energy transfer in such cyclic systems.

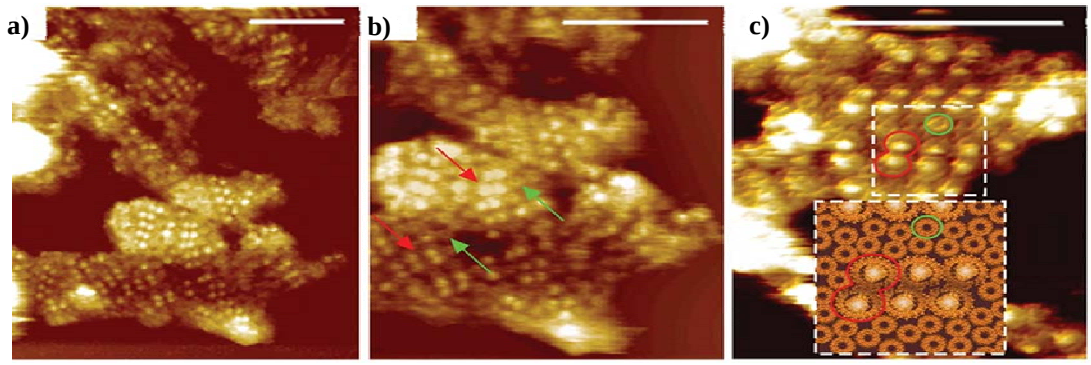

Figure 3. AFM images of native photosynthetic membranes from the wild-type purple bacterium *Rhodobacter sphaeroids* a) Large-scale view of several membrane fragments; b) higher-magnification view showing a region of dimeric RC–LH1–PufX core complex arrays (red arrows) and associated LH2 complexes (green arrows); c) Three-dimensional view of core complex arrays surrounded by LH2 complexes. The inset at the bottom is a representation of the region denoted by the dashed box in the centre, using model structures derived from atomic resolution data. Scale bar, 100 nm in all panels. Reprinted from ref. 54, with permission from Nature Publishing Group.

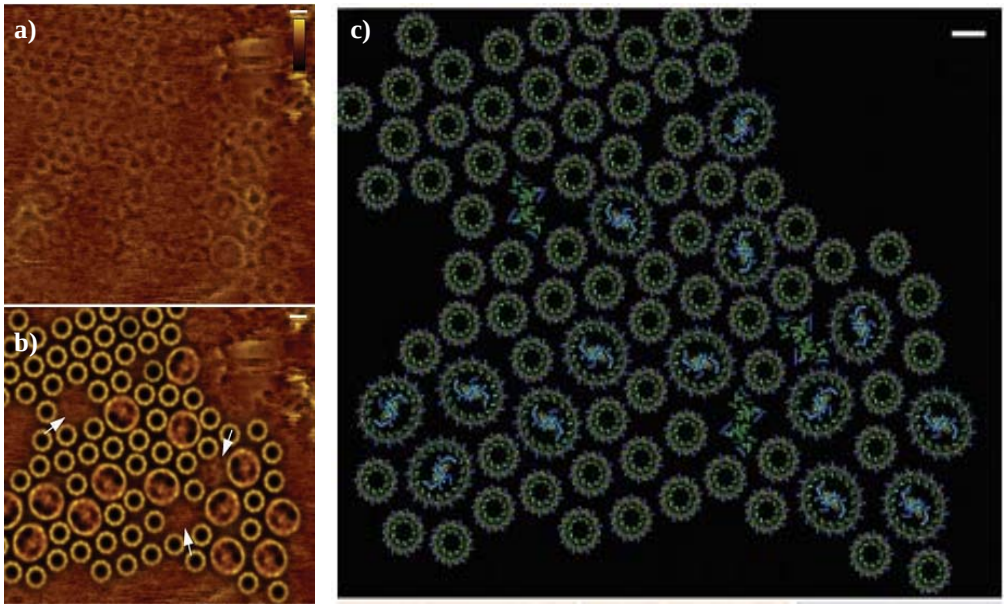

Figure 4. AFM images of the photosynthetic apparatus of a native chromatophore membrane a) Raw AFM data; b) Fitting of the LH2 and core-complex averages corresponding to the relative positions and orientations in the topograph; c) Model of the LH2 structures and the core-complexes based on the AFM topograph. Reprinted from ref. 53, with permission from National Academy of Sciences.

The features of light harvesting in purple bacteria can serve as a background to a comparison of the alternative antenna system discussed in next section that are formed only via inter-pigment interactions without the assistance of a protein scaffold.

2.2.2. LH Apparatus of Green Sulphur Bacteria: Chlorosomes

Green sulphur bacteria grow under anoxygenic environments where the light intensities are extremely low and the single photon absorption rate is less than 1 photon per hour. To survive under such low light conditions, they have evolved specialized extra-membranous antenna systems called chlorosomes.[51] Chlorosomes are light-harvesting organelles found in all green sulfur bacteria (phylum Chlorobi), some filamentous anoxygenic phototrophs of the phylum Chloroflexi,[51] a new type of green sulfur bacteria discovered in hydrothermal deep-water sources at depths of 2300 m[57] and the newly discovered aerobic phototroph, *Candidatus Chloracidobacterium thermophilum* of phylum *Acidobacteria*.[58] Chlorosomes are one of the most fascinating examples of functional dye assemblies created by about 250,000 BChls,[59] stabilized solely through pigment-pigment interactions between the BChls and are extremely efficient ultra-fast light harvesters. Chlorosomes are found attached to the cytoplasmic side of the cell membrane via the baseplate to a BChl *a* containing protein complex (Figure 5), called the Fenna-Mathews-Olson protein complex (FMO). The photonic excitations are funnelled into the membrane bound RC via the FMO protein complexes. The high pigment concentration leads to an exceptionally high optical cross-section of the chlorosomes. Moreover, self-organization of the chromophores into stable three-dimensional architectures achieved mainly by interpigment interactions is easier to control and mimic artificially than pigment-protein systems prevailing in other antenna complexes discussed in previous section.[60]

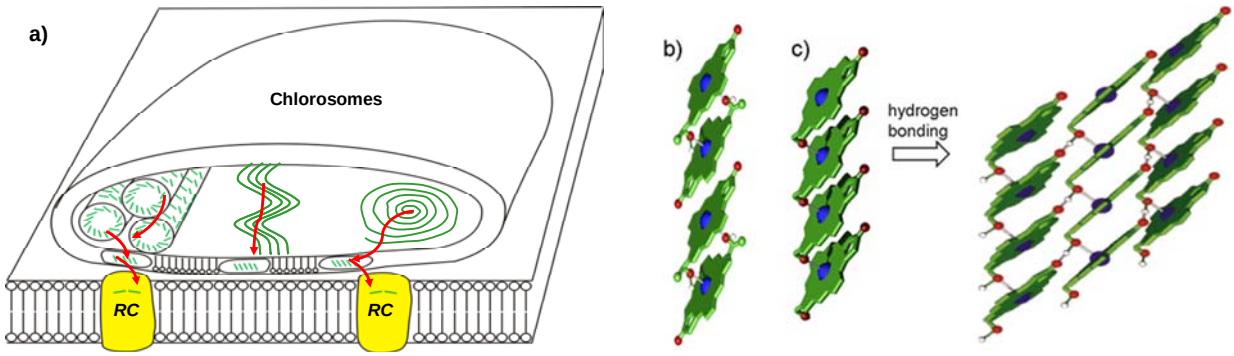

Figure 5. Schematic representation of the macroscopic organization of BChl *c-e* pigments in the ellipsoidal bodies of chlorosomes for which tubular rod (left), lamellar (middle), and spiral (right) arrangements have been suggested. The red arrows indicate the pathways for the energy transfer to the reaction centers (RC). The exact organization of BChls in the chlorosomal antennae systems is still a matter of much debate and has been discussed in detail later. In (b), two BChl molecules form an antiparallel dimeric unit held together by two magnesium-oxygen coordinate bonds and π-π stacking. Further assembly is governed by π-π stacking and hydrogen bonding (not shown), which may lead to a variety of structures of similar thermodynamic stability. In (c), slipped stacks are formed by magnesium-oxygen coordination and π-π stacking, and further self-assembly by hydrogen bonding affords the curvature that is a characteristic feature of the chromosomal BChl aggregates. Reprinted from ref. 60 with permission from Wiley-VCH Verlag GmbH & Co. KGaA.

Chlorophylls are macrocyclic tetrapyrroles characterized by a fifth, isocyclic ring and a central magnesium (Chart 1)[51] or, in rare cases, zinc ion.[61] They occur at porphyrins, chlorin or bacteriochlorin oxidation levels (Figure 6). The porphyrin has double bonds at carbon atoms 7 and 8, and 17 and 18. The latter is in the reduced state in chlorins, whereas both double bonds are in reduced state in bacteriochlorins. The most prevalent species is Chl *a*, which is present in all oxygenic photosynthetic organisms. Some chlorophyll derivatives are named bacteriochlorophylls (BChls) due to the fact that they are the predominant chromophores in some photosynthetic bacteria. Notably, only BChl *a* and *b* contain a bacteriochlorin cycle, while BChl *c*, *d*, and *e* are based on a chlorin skeleton structure (Chart 1).

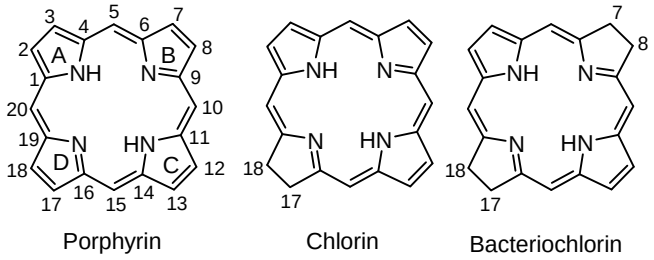

Figure 6. Structural formula of porphyrin, chlorin (saturated at C-17/C-18) and the bacteriochlorin (saturated at C-7/C-8 and C-17/C-18). The numbering in all the tetrapyrroles are indicated in porphyrin.

The absorption spectra of the cyclic tetrapyrrole dyes are influenced by the π-perimeter of these chromophores and by the nature of the central metal ion and substituents. The UV/Vis spectra of porphyrinoids are dominated by an intensive transition in the near UV region (~ 400 nm), which is referred to as B band or Soret band. Furthermore, the free porphyrin base exhibits two less intensive electronic transitions in the range of 500-660 nm, the so called Q_x and Q_y bands showing a defined vibronic fine structure.

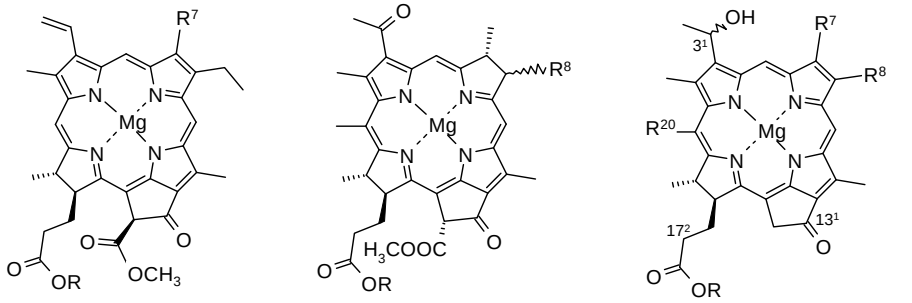

Chart 1. Chemical structures of the photosynthetic chromophores chlorophyll *a* and *b* and BChl *a*-*e*.

The chlorosomal superstructure is established by self-assembly, driven by non-covalent interactions without requiring proteins for structural control and BChl positioning. These interactions are: (i) coordination of the C-3^1-hydroxy to the magnesium ion, (ii) hydrogen bonding between the C-3^1-hydroxy to the C-13^1-ketogroup, (iii) π–π stacking of chlorin macrocycles, (iv) electrostatic interactions, in particular, the polarized keto group with negative charge on oxygen interacts electrostatically with Mg^{2+}, which is considered to be the most important electrostatic contribution to the aggregation[51] and (v) partitioning of aliphatic tails into the hydrophobic parts of the superstructures. These combined interactions result into well-defined dye aggregates with J-type excitonic coupling.[60-66]

2.3. Redox Properties of Chlorophylls

In order to assess the suitability of chlorins as organic semiconductors, insights into their redox properties are of prime importance. The redox processes taking place in chlorins and other cyclic tetrapyrroles have been described in detail previously.[67-69] For large organic molecules, the primary redox potential difference E_{ox}^1-E_{red}^1 = ΔE is generally close to singlet excitation energy ε_s of the molecule. The singlet excitation energy of porphyrins is about ε_s = 2.2 eV, and the experimentally determined redox potential difference for porphyrins is ΔE = 2.25 ± 0.15 V. The corresponding primary redox potential difference (singlet excitation energy), ΔE (ε_s) values for Chl *a*, *b* and BChl *a* were 1.73-1.80 V (1.85 eV), 1.83 V (1.91 eV) and 1.59 V (1.58 eV), respectively.[69] The redox processes in chlorophylls take place in the chlorin ring or at the central metal ion according to an electrochemical rule predicted for chlorins.[69] For metal substituted chlorins, spectroelectrochemical measurements provided clues for discriminating the redox sites i.e., discrimination between central metal and chlorin ring.[69] According to the empirical electrochemical rule formulated, if the redox processes take place exclusively in the chlorin ring without involving the central metal ions, then the first and second oxidation and reduction potential values should obey the following rule:

E_{ox}^2-E_{ox}^1 = 0.30 V

E_{red}^1-E_{red}^2 = 0.40 V

The reported values for chlorophyll *a*

E_{ox}^2-E_{ox}^1 = 0.20 V

E_{red}^1-E_{red}^2 = 0.40 V

and BChl *a*

E_{ox}^{2}-E_{ox}^{1} = 0.35 V

E_{red}^{1}-E_{red}^{2} = 0.35 V

are in agreement with the empirical electrochemical rule. The third and further reductions of Chl *a* are not observed by cyclic voltammetry down to a potential of -2.56 V vs NHE. The upper lowest unoccupied molecular orbital (LUMO) levels are substantially higher in case of chlorins than those of the metalloporphyrins. This results in strong resistance of chlorins to third or further reduction. On the other hand, metal-centred redox processes do not obey this empirical electrochemical rule. It was also proposed that chlorins containing central metal ions like Mg, Cu, Zn, Pd, Hg and metal free base chlorins show the oxidation and more importantly the reduction processes exclusively on the chlorin ring.[69] The reported oxidation potentials are + 0.80 V and + 1.10 V vs normal hydrogen electrode (NHE) and tetrabutylammonium perchlorate (TBAP) as supporting electrolyte or chlorophyll *a* in dichloromethane. The corresponding reduction potentials were not reported. Redox potentials vs NHE in a variety of solvents could be found in the literature.[69]

In early calculations of metalloporphyrin absorption spectra, these molecules were regarded as a 16-membered cyclic polyene system with 18 π-electrons with a D_{4h} symmetry (Figure 6).[70-72] However, simple linear combination of atomic orbital-molecular orbital (LCAO-MO) calculations showed that metalloporphyrins exhibit a pair of highest occupied molecular orbitals (HOMO) with symmetries a_{2u} and a_{1u} and four nodes, respectively, and a degenerate pair of LUMO levels with the symmetry e_g and five nodes.

Gouterman developed the four-orbital model on the basis of the free-electron model (Figure 7) and LCAO-MO calculations and proposed that the optical spectra of cyclic tetrapyrroles (porphyrins, chlorins and bacteriochlorins) result from linear combinations of one-electron promotions between the two HOMOs and two LUMOs.[71,72] The two HOMOs of cyclic tetrapyrroles are termed as b_1 and b_2, while the two LUMOs are termed as c_1 and c_2. Metalloporphyrins have D_{4h} symmetry and the molecular π*-orbitals c_1 and c_2 are degenerate, since the in-plane x- and y-axes are equivalent (Figure 7).[71,72] Two out of the four promotions are x-polarized ($b_1 \rightarrow c_2$; $b_2 \rightarrow c_1$) and two promotions are y-polarized ($b_1 \rightarrow c_1$; $b_2 \rightarrow c_2$). The transition dipole moments of the promotions interact in pairs to give four possible combinations, in which they either reinforce or oppose each other. The additive combination of the two x-polarized promotions causes the B_x band and the subtractive combination gives rise to the Q_x band. B_y and Q_y bands originate in a similar manner from the y-polarized transitions. For metalloporphyrins, x- and y-polarized electronic transitions are degenerate (Figure 7). The intensities of Q_x and Q_y

bands are proportional to λ_x^2 and λ_y^2, respectively, which can be calculated from the initial energy gap Δ between the allowed B and Q bands and from the energies ε of the HOMO and LUMO orbitals:

$$\lambda_x = \frac{(\varepsilon(c_2) - \varepsilon(b_1)) - (\varepsilon(c_1) - \varepsilon(b_2))}{2\Delta}$$

$$\lambda_y = \frac{(\varepsilon(c_1) - \varepsilon(b_1)) - (\varepsilon(c_2) - \varepsilon(b_2))}{2\Delta}$$

The Q band intensity becomes very weak for a high degree of degeneration of the respective x and y transitions, as is the case for metalloporphyrins (Figure 7). However, in the case of chlorins, the degeneracy in x and y direction is removed. Orbitals b_2 and c_1 have electron density at the reduced positions, thus, their energy is increased. This effect is even more pronounced for bacteriochlorins due to two reduced positions. However, LUMO c_2 is not influenced by the pyrrole ring saturation and homologous porphyrins, chlorins, and bacteriochlorins have very similar reduction potentials.

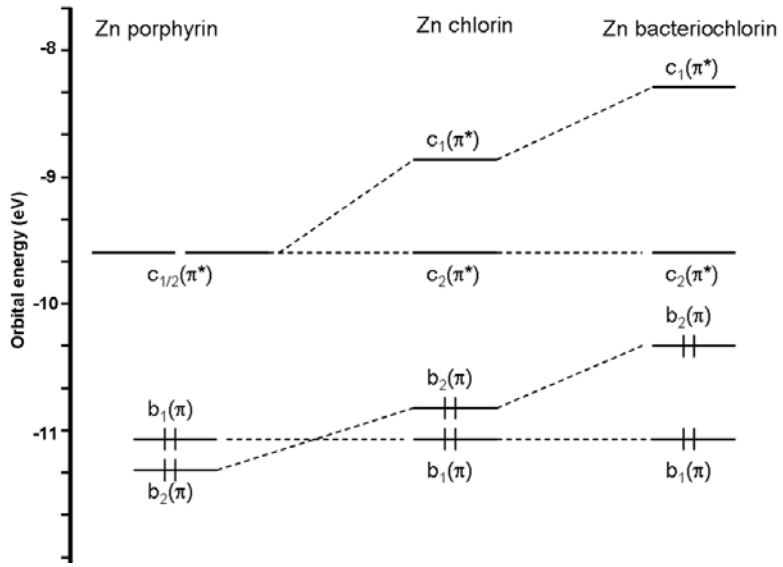

Figure 7. Energy level diagram of Zn-porphyrins, chlorins and bacteriochlorins (with energy values used from references 67 and 69.

The changes in orbital energies of porphyrins, chlorins, and bacteriochlorins have the following consequences for the four one-electron transition energies: $b_1 \rightarrow c_1$ (y-polarized) > $b_1 \rightarrow c_2$ (x-polarized) > $b_2 \rightarrow c_1$ (x-polarized) > $b_2 \rightarrow c_2$ (y-polarized). For all tetrapyrroles, the x-promotion energies ($b_1 \rightarrow c_2$ and $b_2 \rightarrow c_1$) are similar for porphyrins, chlorins, and bacteriochlorins. As a result, the Q_x bands are found at similar wavelengths. However, the two promotions that comprise the

Q_y transitions ($b_1 \rightarrow c_1$ and $b_2 \rightarrow c_2$) are very different in energy for chlorins and even more for bacteriochlorins. The intensity of Q_y bands increases with the degree of saturation. Furthermore, a bathochromic shift is observed for Q_y bands from porphyrins to chlorins and further to bacteriochlorins, since the energy of Q_y band becomes increasingly dominated by the promotion with lower energy, and hence the decreasing $b_2 \rightarrow c_2$ promotion.

2.4. Overview on Structural Elucidation of Chlorosomes

The structural elucidation of chlorosomal LH systems since its discovery in 1964 up until 2007 have been comprehensively reviewed in two recent PhD theses.[67,68] Hence, this topic is discussed only very briefly in this section focussing on new recent developments. Chlorosomal models have been controversially discussed in the literature mostly based on interdisplinary studies such as UV/Vis and CD spectroscopy,[73-76] electron microscopy,[77-80] powder XRD,[81-84] solid state NMR techniques,[85-94] and so on. Because they form very large and compositionally heterogeneous mixtures in these organelles, no crystals of aggregated BChls or chlorosomes and no atomistic level details are currently available despite great endeavors by researchers engaged in these studies.

Chlorosomes were first reported in 1964[77] and their structure was characterized primarily by electron microscopy.[81] Detailed models for the organization of the BChls in chlorosomes date back to the pioneering freeze-fracture electron microscopic studies of Staehelin and co-workers.[77-79] These studies suggested that the BChls are presumably arranged in tubular structures with a diameter of ~ 10 nm in *Chlorobium limicola* and ~ 5 nm in *Chloroflexus aurantiacus*.

Based on electron microscopy, solid-state NMR, molecular modelling and spectroscopic data, different models were proposed for the molecular arrangement of the BChls in chlorosomes.[51,74-76] These models can be classified into two principal groups based on the asymmetric repeating unit (Figure 8): a) parallel-chain model with BChl monomer as the building block (proposed by Holzwarth and Schaffner in 1994[73]; Balaban et al., in 1995[85]; van Rossum et al., in 2001[86]); and b), antiparallel model with so-called ‘‘piggy-back’’ or closed BChl dimer as a building block (Nozawa et al., 1994;[74] Wang et al., 1999[75,76]). The terms parallel and antiparallel refer to the mutual orientation of the Q_y transition dipoles. In all of these models, short-range order was deduced from the results of optical spectroscopy[73,89,90] and solid state NMR[85-88,91-94] (Holzwarth and Schaffner, in 1994[73]; Nozawa et al., in 1994[74]; Balaban et al., in 1995[85]; Wang et al., in

1999;[75,76] van Rossum et al., in 2001[86]). On the other hand, the long-range order was proposed constraining the models to resemble the rod-like elements proposed initially by Staehelin and co-workers based on electron microscopy.[78,79,95,96] The protein-free tubular structure of chlorosomes of BChl *d* derivative was first proposed by Holzwarth and Schaffner.[73] The predicted diameter of the rod elements was about 5.4 nm (Mg-Mg distance), i.e. very similar to that found for the rod elements in the chlorosomes of *Chloroflexus Aurantiacus*.[73] Recently, the above "tube-like" picture of chlorosome was questioned by Pšenčík and co-workers, who applied cryo-electron microscopy (cryo-EM) and low-angle X-ray diffraction to re-evaluate the structure of the BChls in chlorosomes.[81] They concluded that the BChls are arranged in undulating lamellae rather than tubular structures. From the results obtained from powder XRD experiments, cell dimensions of the aggregates were in better agreement with the models proposed by Nozawa and co-workers[74] i.e., anti-parallel chain model[74-76] than the parallel chain model[73] of Holzwarth and co-workers. Conflicting structural models for chlorosomes have been derived from many spectroscopic and electron microscopic assessments and from studies with chemical analogs. These studies led to the proposal of a variety of supramolecular structures, such as single- and double-walled rods, and multilayered cylindrical structures, fibril-like, lamellar, and rolled-up sheets. However, in spite of much research, rod-based models for BChl organization in chlorosomes is still the most widely accepted model.

Very recently, high-resolution cryo-EM studies for chlorosomes of *Cb. tepidum* suggested that multi-layered tubular or rolled sheet antennae with variable diameters and layer distances of ~ 2.1 nm with structurally less well-defined overall organization fill up the interior of chlorosomes.[97,98] The most recent model by Holzwarth, de Groot, Bryant and co-workers based on computational integration of two bioimaging techniques i.e., cryo-EM and solid-state MAS NMR studies, suggested that chlorosomal superstructures are built from pairs of alternating syn-anti-ligated BChl *d* stacked sheets that self-assemble into coaxial tubes and provide ultrafast helical exciton delocalization pathways along BChl stacks interconnected by hydrogen bonds.[97,98]

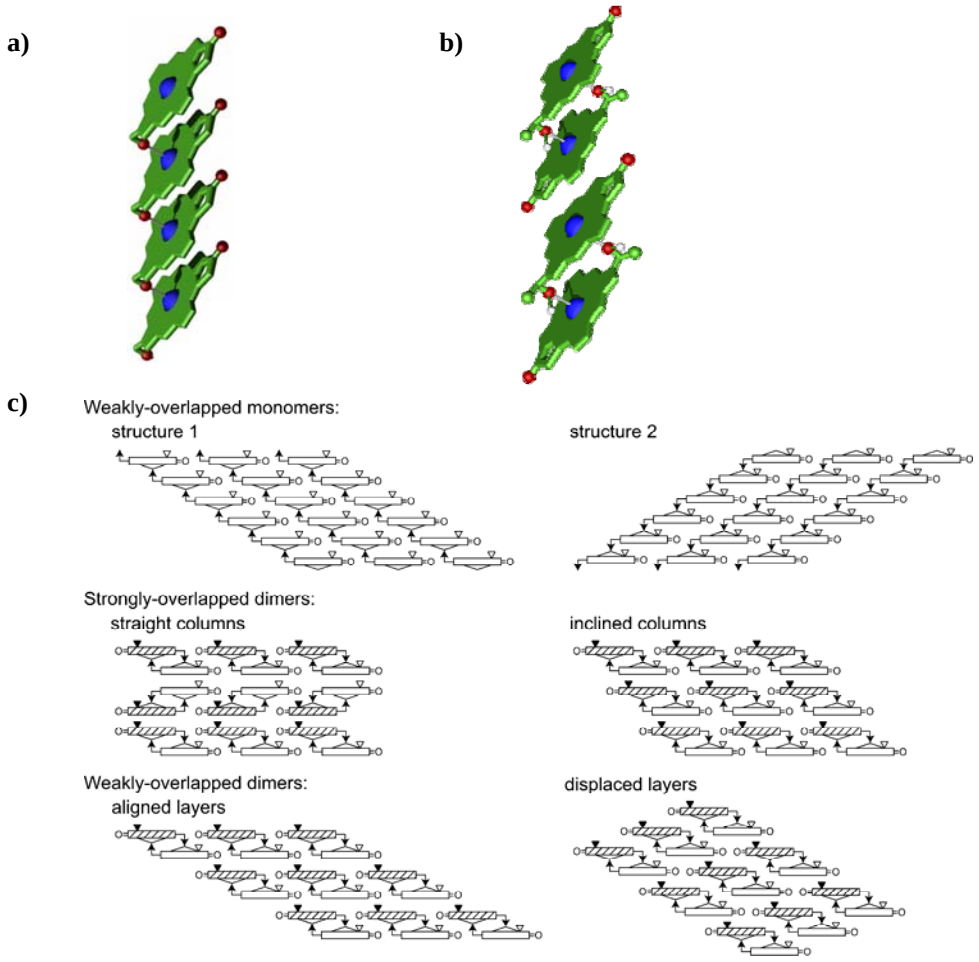

Figure 8. a) parallel chain model; b) antiparallel stacking built from closed dimers and c) various other stacking modes of macrocycles where each stacking exhibits a unique two-dimensional arrangement that is defined by the size and shape of the asymmetric chlorin unit. Reprinted from ref. 94, with permission from the American Chemical Society.

2.5. Other Recent Models based on Electron Microscopy

Electron microscopic studies of chlorosomes in literature have revealed strongly divergent structures that are believed to originate as results of functional morphology, different stages in the biogenesis of chlorosomes, or from differences in sample preparation.[78,95,96] In the last few years (2008-2010), important advancements have been made in the structural elucidations of chlorosomes. Oostergetel et al. have studied the long-range organization of BChl layers in intact chlorosomes of *Chlorobium tepidum* (*C. tepidum*) and its variant by cryo-EM.[97] End-on views revealed that chlorosomes are composed of several multi-layered tubules of variable diameter (20-30 nm) with some locally undulating non-tubular lamellae in between. The multi-layered tubular structures were more regular and larger in *C. tepidum* mutant than the [8-ethyl, 12-methyl]-BChl *d* variant. The data showed that wild-type *C. tepidum* chlorosomes did

not have a highly regular, long-range BChl *c* layer organization and contained several multilayered tubules (Figure 9a, top) rather than single-layer tubules or exclusively undulating lamellae as previously proposed.[97] However, on the side-on views, the chlorosomes appeared wedge-shaped or nearly rectangular (Figure 9, Figure 10). The multi-layered tubular structures were more regular and had a larger number of layers than in chlorosomes of wild-type *C. tepidum*. However fourier transformation of side-on views from the mutant indicated that the spacing between the layers was the same as those of the wild-type.[97] It was proposed that BChl layers are organized as coaxial cylinders or rolled-up sheets (Figure 9b), embedded in a matrix of structurally less well-defined BChl assemblies, and that the chlorosome did not have a highly regular supramolecular organization of their constituent BChl *c* molecules. Morever, the orientation of the tetrapyrrole rings or the contents of the unit cell could not be revealed by these studies.[97]

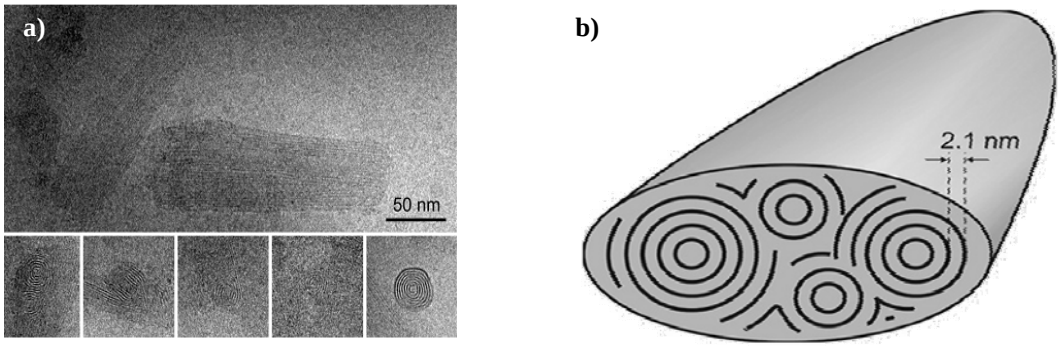

Figure 9. a) Cryo-EM images of isolated chlorosomes from a triple mutant of *Chlorobium tepidum* embedded in amorphous ice. In the upper frame chlorosomes are seen in side-on position; the lower row presents end-on views; b) Schematic model of the BChl aggregates in the chlorosomes of *C. tepidium* proposed based on cryo-EM studies. Multi-layered tubular or rolled up sheets of variable diameter are proposed to be embedded in a structurally less well-defined matrix. The spacing between BChl layers is 2.1 nm. Reprinted from ref. 97

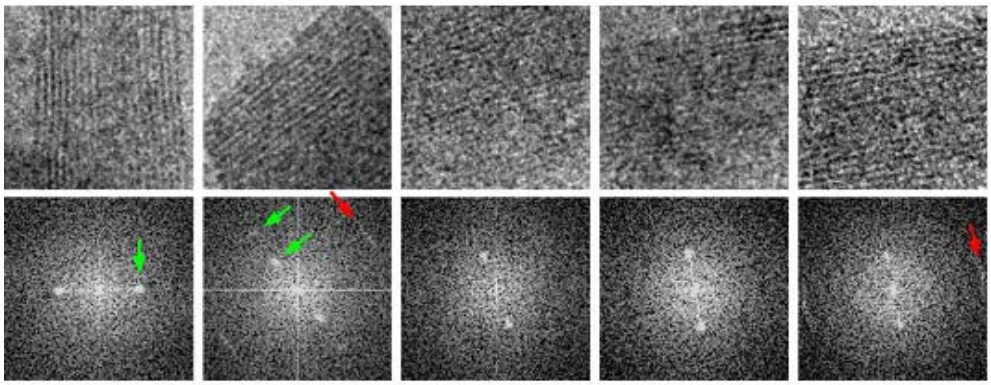

Figure 10. A gallery of selected side-on arrays with highest regularity in layer spacing and their corresponding Fourier transforms. The green arrows indicate 2.1-nm spacing between BChl layers, and 1.0-nm spacing in one particular array; the red arrows indicate a 0.8-nm spacing along the BChl layers.[97] Reprinted with permission from ref. 97.

This study was followed by high resolution solid-state MAS NMR investigation in order to obtain insights into the short range packing arrangements. The structure of a member of the chlorosome class was determined and compared with the wild type (WT) species. The chlorosomes of the green sulphur bacterium *Chlorobaculum tepidum* contained a complex mixture of BChl *c* molecules with variable degrees of methylation at carbons C-8^2 and C-12^1, variations in the esterifying alcohol side chain of C-17 carboxyl group, and both R-and S-chirality at the C-3^1 carbon. In this work, by constructing a triple mutant (i.e., performing variations at R_1, R_2 and R_3, see structure Figure 11), the heterogeneous BChl *c* pigment composition of chlorosomes of the green sulfur bacteria *Chlorobaculum tepidum* was simplified to nearly homogeneous BChl *d* (Figure 11). Computational integration of two different imaging techniques i.e., solid-state NMR and cryo EM (Figure 12-13) revealed a new syn-anti stacking mode and showed that ligated BChl *c* and *d* are self-assembled into coaxial cylinders to form tubular-shaped elements.[98] The data revealed the presence of alternating monomers that formed stacks, assembled into layers with the farnesyl tails alternately extending on both sides. The two possible intermolecular arrangements that could satisfy these constraints were the stacking model based on antiparallel monomer stacking or the alternating syn and anti monomer stacking (Figure 11a-d). In addition to the intrastack correlations, intermolecular correlations between carbons C-12^1/C-3^1, C-12^1/C-2^1, and C-12^1/C-3^2 were detected between rings I and III of adjacent BChl *d* molecules. The interstack correlations provided convincing evidence that syn-anti monomer stacking was the basic building block in the *bchQRU* chlorosome structure. Density functional theory (DFT) calculations were performed to estimate the ring currents for the syn-anti monomer model (Figure 11d), antiparallel monomer model (Figure 11b), and two earlier structural models that were proposed for BChl *c* in chlorosomes: the monomer-based, parallel-stack model[73] and the closed dimer model (Figure 11 a and b).[75,76] These calculations showed that only the parallel stack (11a) and syn-anti monomer stack (11d) could reproduce the experimentally observed ring current shifts. In these two arrangements, each BChl *d* molecule had significant overlap with two adjacent molecules, via rings I and III, at opposite sides of the aromatic cycle. The calculations for the closed dimer model (11b) gave anomalously large proton ring current shifts at C-5–H, C-3^1–H, and C-3^2–H3, whereas the antiparallel monomer stack (11c) gave a mismatch over the entire overlap region of C-1–C-5 and C-15–C-13^2. In these two arrangements, there was pronounced overlap with two neighbors at ring I and little overlap at ring III, and this produced strongly asymmetric ring current shift patterns which were not observed experimentally.

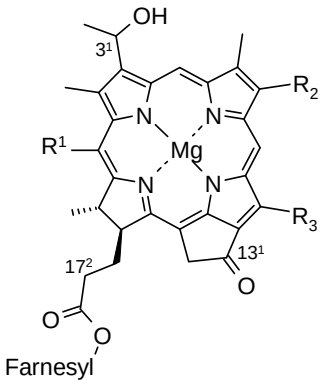

BChl homologues for C. *tepidum*.
In WT, R_1 = Me; R_2 = Et, *n*-Pr, or *i*-Bu; R_3 = Me, or Et.
In the *bchQRU* mutant R_1 = H; R_2 = Et; R_3 = Me.

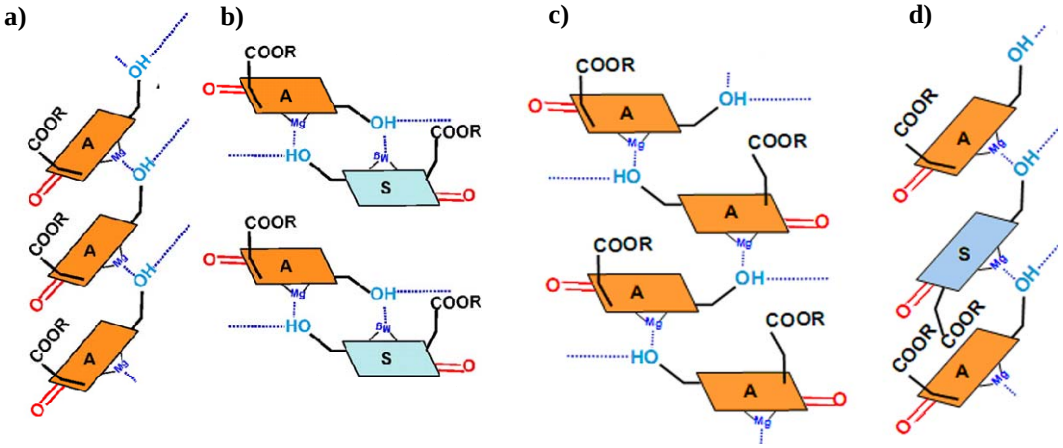

Figure 11. Top: Chemical structures of constituent BChl homologues for *C. tepidum*. In the WT, R_1 = Me; R_2 = Et, *n*-Pr, or *i*-Bu; R_3 = Me, or Et. In the *bchQRU* mutant R_1 = H; R_2 = Et; R_3 = Me; Bottom: Schematic representation of structural models used for the ring current shift calculations namely, a) parallel-stack model; b) closed dimer model; c) antiparallel monomer stack model; d) syn-anti monomer stack model. Reprinted from ref. 98 with permission from the National Academy of Sciences.

Electron microscopy micrographs of these samples revealed that the layers translated into a single pair of equatorial reflections at 2.1 nm whereas the stripes gave rise to strong layer lines that revealed a helical arrangement with an axial repeat distance of 0.83 nm (Figure 12). In addition to the reflections from the 2.1 nm layer spacing, this spacing could be reproduced in many images at high magnification (Figure 12).

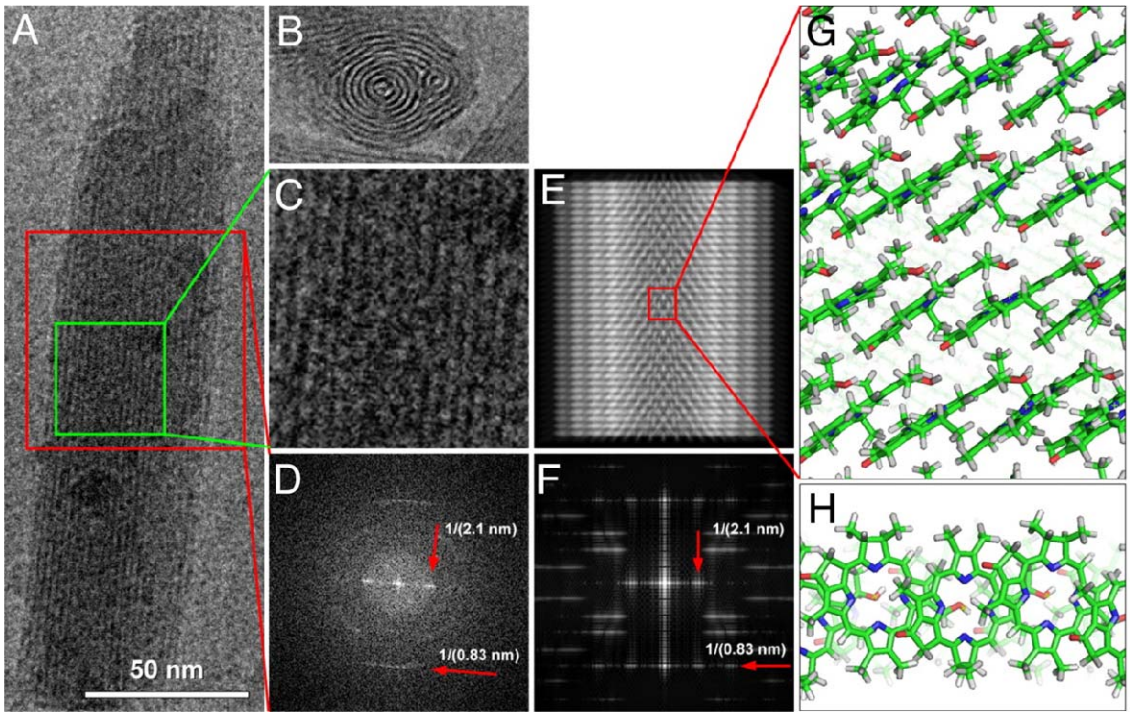

Figure 12. Integration of cryo-EM and NMR data to resolve the *bchQRU* mutant chlorosome structure. (A and B) cryo-EM image of isolated chlorosomes from the *bchQRU* mutant of *C. tepidum* embedded in amorphous ice. A chlorosome is seen in side-on view (A) and in end-on view, showing the layering of the BChls (B). (C) Enlarged region of the side-on view, indicated by the green box in A. (D) Fourier transform of the red-boxed region in A. The red arrows indicate reflections from a 2.1 nm spacing between BChl layers and a 0.83-nm spacing along the layers. (E and F) Simulated EM image and its Fourier transform, from a 17^2-farnesyl-R-[8-ethyl,12-methyl] BChl *d* helical rod model comprising of 4 tubes built from NMR-derived and geometry-optimized syn-anti monomer stacks that run along the circumference of the tubes, perpendicular to their long axis. The 1/0.83 nm periodicity corresponds to the spacing between adjacent BChl stacks running perpendicular to the tube axis. (G) Enlarged view of the boxed area in E. (H) Top view, i.e., along the tube axis. Reprinted from ref. 98 with permission from the National Academy of Sciences.

A helical exciton delocalization pathway that was realized with stacks running parallel or perpendicular to the tube axis in WT and mutant (Figure 13) respectively, and interconnected by hydrogen bonds was proposed to be the basis for the efficient and ultra fast light-harvesting. Based on these studies, chlorosomal superstructures were proposed to be built from syn-anti monomer stacks that were self-assembled into nanotubes.

In recent years, synthetic mimics of chlorosomes have been realized by several groups, which facilitated the further understanding of the structural and functional aspects of the natural chlorosomal LH antenna systems.[99-109]

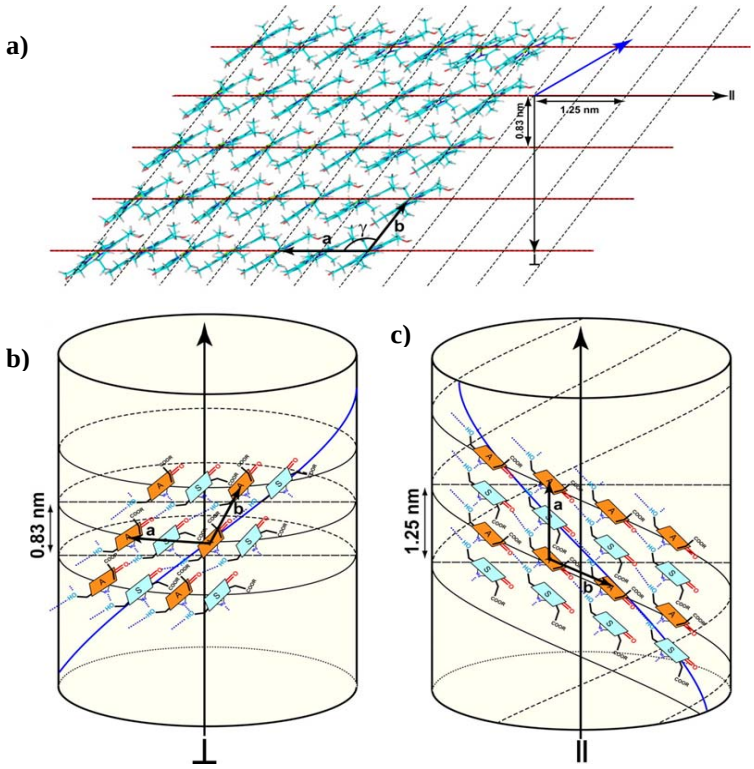

Figure 13. a) 7 × 5 section of the syn-anti array. The stacks are indicated by red lines. The separation perpendicular to the stacks is 0.83 nm. The unit cell dimensions are: a = 1.25, b = 0.98, γ =122°. The repeat in the direction parallel to the stack is 1.25 nm (b and c). Multistart helices with the long axis running perpendicular or parallel to the stacks with periodicities of 0.83 nm and 1.25 nm are indicated. The H-bond helices that connect BChl stacks via the carbonyls are shown in blue (right-handed in B and left-handed in c). Reprinted from ref. 98 with permission from the National Academy of Sciences.

2.6. Artificial Mimics of Chlorosomal LH Systems

The intriguing architectural principle for the supramolecular organization of BChls in chlorosomes can be mimicked using semisynthetic molecules which are pre-programmed for self-assembly. Thus, for the better understanding of chlorosomal LH systems, Tamiaki and co-workers developed a zinc chlorin model compound for the naturally occurring BChl *c* (see Figure 14).[100] Like BChls, the zinc chlorin model compound forms extended dye aggregates in non-polar solvents such as *n*-hexane or *n*-heptane. Intensive investigations of dye aggregates of BChl *c* and zinc chlorin model compound revealed nearly identical spectral and photophysical properties compared with those of the natural chlorosomal self-assemblies, confirming the suitability of zinc chlorin dyes for the imitation of chlorosomal antennae systems.[100,109] The major advantage of the zinc chlorin model compounds over the native bacteriochlorophylls lies in their easy semisynthetic accessibility from Chl *a* and their higher chemical stability compared to natural counterparts.

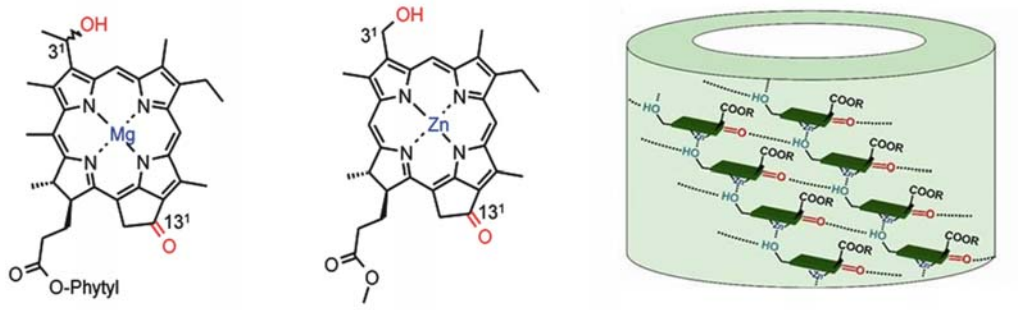

BChl *c* Zinc chlorin model compound

Figure 14. Structures of naturally occurring bacteriochlorophyll *c* and zinc chlorin model compound, and a schematic model showing the three non-covalent interactions involved in the formation of supramolecular tubular aggregates (right). Reprinted from ref. 105, with permission from Wiley-VCH Verlag GmbH & Co. KGaA.

Such semisynthetic zinc chlorin (ZnChl) compounds derived by synthetic modifications of Chl *a* form well-defined J-aggregates in solution and ordered π-stacks on surfaces.[104-106] They are the ideal mimics of the natural chlorosomal antennae systems possessing structural and functional features similar to those in natural counterparts.[107,108] The next section describes such previously studied systems in detail.

2.6.1. Semisynthetic Zinc Chlorins: Self-assembly in Solution and Organization on Surface

Three structural characteristics of semisynthetic metallochlorins are important for the formation of tubular J-aggregates (Figure 14): A central zinc ion for the coordination with the oxygen atom of the 3^1-hydroxy group, chlorin π-system for effective π–π interactions, and hydrogen-bond donor (3^1-hydroxy) and hydrogen-bond acceptor (13^1-keto) groups for interstack hydrogen bonding. Apart from these interactions, the side chains are considered to play significant role in the stabilization of these aggregates in solution as well as in the solid state. The first two interactions lead to a slipped π–π stacking as in the case of J-aggregates, whereas hydrogen bonding induces the curvature leading to a tubular structure, where the alkyl chains are presumably oriented towards the outside.[105,106]

Although the in vitro aggregates of the zinc chlorin model compound discussed in the previous section possess similar spectral properties to naturally occurring chlorosomal aggregates, they are prone to agglomeration owing to poor solubility in non-polar solvents. Consequently, only restricted information from spectroscopic investigations could be deduced. Balaban and co-workers addressed this problem by preparing related porphyrin assemblies and obtaining microcrystalline structures that were characterized by X-ray diffraction and electron

microscopy.[99] Würthner and co-workers have focused on zinc chlorin model compounds that afforded well-defined self-assembled aggregates with good solubility and lasting stability in solution to facilitate spectroscopic and microscopic investigations.[105]

Zinc chlorins **1**-**3** were functionalized with two or three dodecyl chains at the 17^2-position and ZnChls **4**, **5** contain hydrophilic polyethylene glycol chains at 17^2-position (see Chart 2), and their self-aggregation properties were investigated in non-polar solvents (for **1**-**3**) and in aqueous media (**4**, **5**), respectively. Zinc chlorins **1** and **3**-**5** possess a 3^1-hydroxy functionality whereas in **2**, the hydroxy functionality is replaced by a methoxy functional group. Furthermore, for a better understanding of the influence of an additional chirality center on 3^1-position on self-assembly, epimeric zinc chlorins (3^1S)-**6** and (3^1R)-**6** with two dodecyl chains analogous to **1** at the 17^2 position were synthesized to achieve enhanced solubility in non-polar solvents such as *n*-hexane or *n*-heptane.

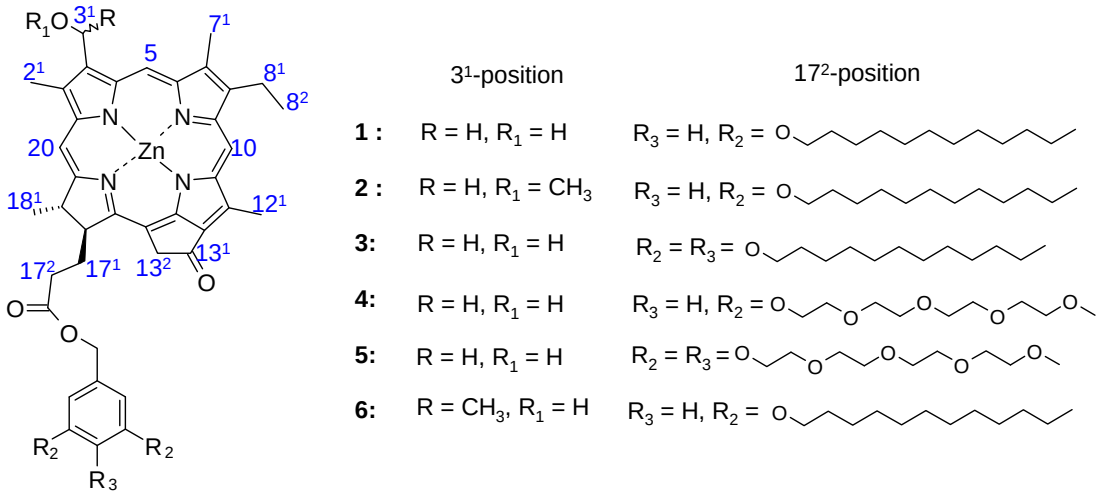

Chart 2. Chemical structures of 3^1-hydroxy and 3^1-methoxy zinc chlorin compounds **1**-**6** possessing various 17^2-substituents.

The formation of aggregates could be recognized by the instantaneous color change of turquoise blue monomer solutions to pale green aggregate solutions for all the compounds. Like BChl *c*, the ZnChl derivatives **1** and **3** showed these structural characteristics and their Q_y-band was bathochromically shifted from 648 nm in tetrahydrofuran (THF) to 741 nm in *n*-heptane or *n*-hexane containing 0.5 % v/v of THF as a result of J-aggregate formation (Figure 15).[105,106] Temperature-dependent UV/Vis and CD spectroscopic methods, as well as microscopic investigations, were performed to characterize the aggregation and explore the importance of particular functional groups and steric effects on the self-assembly behavior of these zinc chlorins. UV/Vis and CD spectroscopic studies have shown that the self-assembly of **1** and **3** is reversible.

Moreover, based on the congruent position of aggregate Q_y bands (λ_{max} =740-741 nm) in UV/Vis spectra and similar bisignate signals in the CD spectra of the aggregates of zinc chlorins **1** and **3**[105] and natural BChl *c* aggregates, it could be concluded that the short-range arrangement of these dyes in aggregate structures is quite similar to those given in their natural counterparts. Atomic force microscopy (AFM) studies on highly oriented pyrolytic graphite (HOPG) elucidated the structural properties of aggregates of ZnChl **1** and **3** which indicated rigid rods (Figure 15 a, c, d), with lengths of 300 ± 97 nm and heights of 5.8 ± 0.4 nm (vertical distance between the black and green triangle, Figure 15 b). The measured height of ~ 6 nm of these biomimetic zinc chlorin aggregates was in excellent agreement with electron microscopy data of BChl *c* rod aggregates in chlorosomes (*Chloroflexus aurantiacus*)[79] and thus complied with the tubular model postulated by Holzwarth and Schaffner.[73]

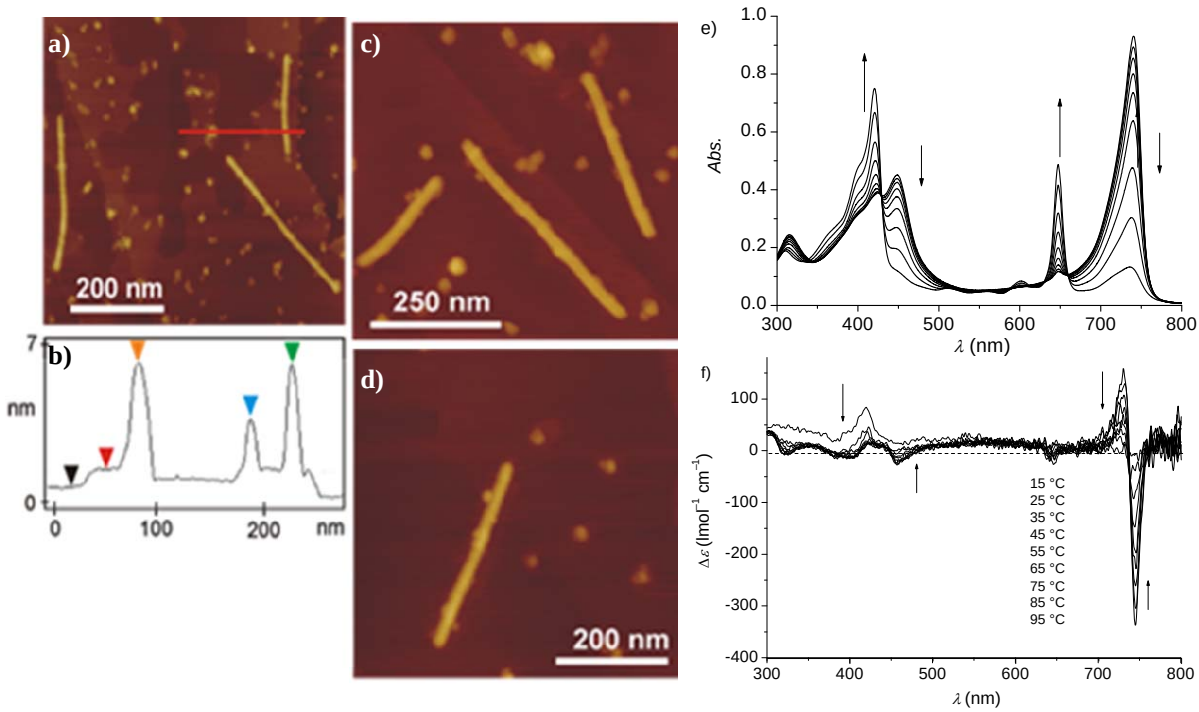

Figure 15. Tapping mode AFM images of aggregates of ZnChl **1** on HOPG. Different areas and enlargements of the sample are displayed in a), c) and d). b) shows the height profile along the red line in a). The sample was prepared by spin coating of aggregate solution of **1** in hexane/THF (100:1) on HOPG and measured in air. e) Temperature-dependent UV/Vis spectra and f) CD spectra of **1** in *n*-heptane/di-*n*-butyl ether (4:1) at $c = 1.1 \times 10^{-5}$ M. The initial temperature of 15 °C was increased successively in 10 °C steps up to 95 °C and at each temperature the solution was allowed to equilibrate prior to measurement; arrows indicate changes upon increasing temperature. Reprinted from ref. 105, with permission from Wiley-VCH Verlag GmbH & Co. KGaA.

Besides rod-aggregates, globular structures with average heights of 3.1±0.6 nm and 5.6±0.7 nm (vertical distance between the black and blue and black and orange triangles, respectively, in Figure 15B) could also be observed, which were either formed by degradation of rods during the spin-coating process or they co-existed in solution with the rod-aggregates.

The aggregation studies for ZnChls **4** and **5** were performed in aqueous media as these dyes possess 17^2-hydrophilic side chains. For this purpose, monomer stock solutions of **4** and **5** were prepared in THF and subsequently added to ultrapure Milli Q water to prepare aggregate solutions in water containing 1 vol % THF. The formation of aggregates of ZnChl **4** was evident by an immediate color change of turquoise blue monomer solutions to a pale green color of aggregate solutions and the red-shift of the Q_y aggregate band from 648 nm (in THF) to 733 nm (in water/THF 100:1) (Figure 16), indicating self-assembly of this dye. The Q_y aggregate band showed a further bathochromic shift to 747 nm within 24 hours, which was, however, accompanied with formation of some precipitate. Also in the case of **5**, which has three tetraethylene glycol side chains, no long-lasting solubility of the aggregates in water could be achieved. In fact, a slight shift of the Q_y aggregate band from 736 nm to 734 nm was observed after 24 hours (Figure 16), which could be attributed to the additional hydrophilic side chain in **5** having a higher spatial demand leading to destabilization of the aggregates. The solubility properties of ZnChls **4** and **5** in water/methanol were also examined, and similar spectral pattern to those in water/THF solvent combination were observed. However, attempts to visualize rod like aggregates with AFM after spin coating of the aggregates from water /THF (100:1) were not successful.

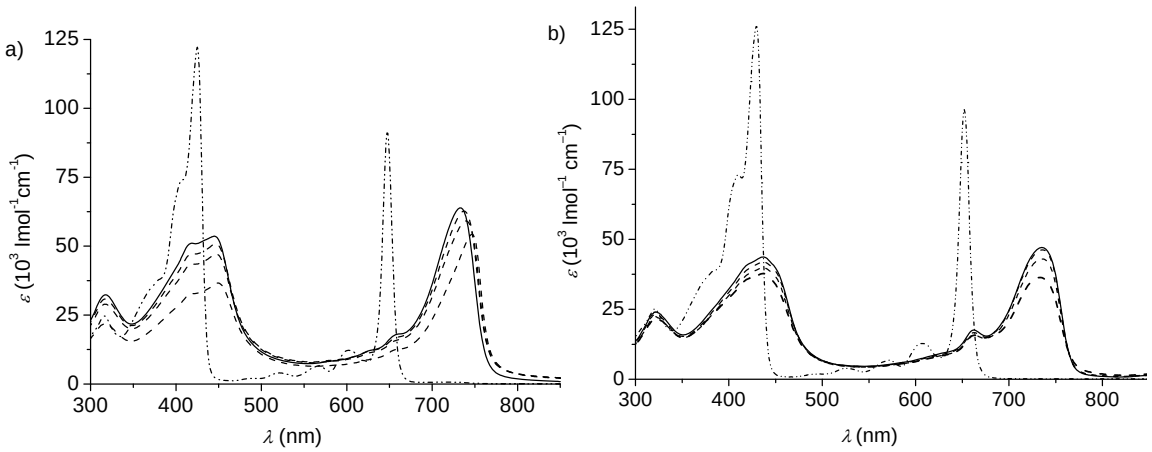

Figure 16. UV/Vis spectra of zinc chlorins a) **4** at $c = 5.8 \times 10^{-6}$ M and b) **5** at $c = 1.4 \times 10^{-5}$ M. Monomers (dash-dotted lines) in THF and aggregates (solid and dashed lines) in water with THF (100:1). Dashed lines refer to the aggregate spectra in a time course of 24 h. Reprinted from ref. 105, with permission from Wiley-VCH Verlag GmbH & Co. KGaA.

With ZnChl **5**, the formation of aggregates in water with a Q_y band maximum at 733-747 nm could be achieved (Figure 16), which lies in the same range as for chlorosomal aggregates. Further evidence for the formation of J-aggregates of **4** in water was provided by CD spectroscopy, as bisignate CD couplet, similar to that of **1** and **2** was observed. The positive and negative peak values appear in the higher wavelength region at λ = 742 nm ($\Delta\varepsilon$ = 362 M^{-1} cm^{-1})

and λ = 753 nm ($\Delta\varepsilon$ = -544 M^{-1} cm^{-1}), whereas at shorter wavelength positive and negative peak values occur at λ = 443 nm ($\Delta\varepsilon$ = 54 M^{-1} cm^{-1}) and λ = 466 nm ($\Delta\varepsilon$ = -29 M^{-1} cm^{-1}). In order to explore the impact of the 3^1 chirality center on self-assembly of zinc chlorins, the aggregation behavior of 3^1R/*S*-**6** was studied in detail by UV/Vis spectroscopy. Samples were prepared by dissolving (3^1R)-**6** and (3^1S)-**6** in THF to obtain monomer stock solutions, followed by the addition of non-polar solvent like *n*-heptane (*n*-heptane/THF 100:1) to initiate aggregate formation. In the case of aggregates of epimerically pure (3^1S)-**6** (Figure 17), a bathochromic shift of the absorption maxima of the Q_y band was observed from 648 nm (monomers) to 711 nm (aggregates), whereas the Q_y band for the aggregates of (3^1R)-**6** epimer shifted from 648 nm to 705 nm (Figure 17). In solutions of both epimers, a significant proportion of monomers prevailed even after 2-3 days. This is in contrast to ZnChls **1** and **3** for which monomers could hardly be observed under comparable experimental conditions. Additionally, the bathochromic shift of the Q_y band for (3^1R)-**6** and (3^1S)-**6** is less pronounced than the shift observed in the case of **1** and **3** (λ_{max} = 742 nm) without the 3^1-methyl group. These results indicate that (3^1R)-**6** and (3^1S)-**6** may form smaller oligomers rather than extended aggregates like rods as in the case of **1** and **3**. It is however noteworthy that the UV/Vis spectra of (3^1R)-**6** epimer shows a shoulder at about 747 nm (Figure 17), where the absorption maxima for the extended rod aggregates of **1** and **3** also appear. The stability of the aggregates of ZnChls (3^1R)-**6** and (3^1S)-**6** was explored by temperature-dependent UV/Vis measurements in the range 15 °C to 80 °C.

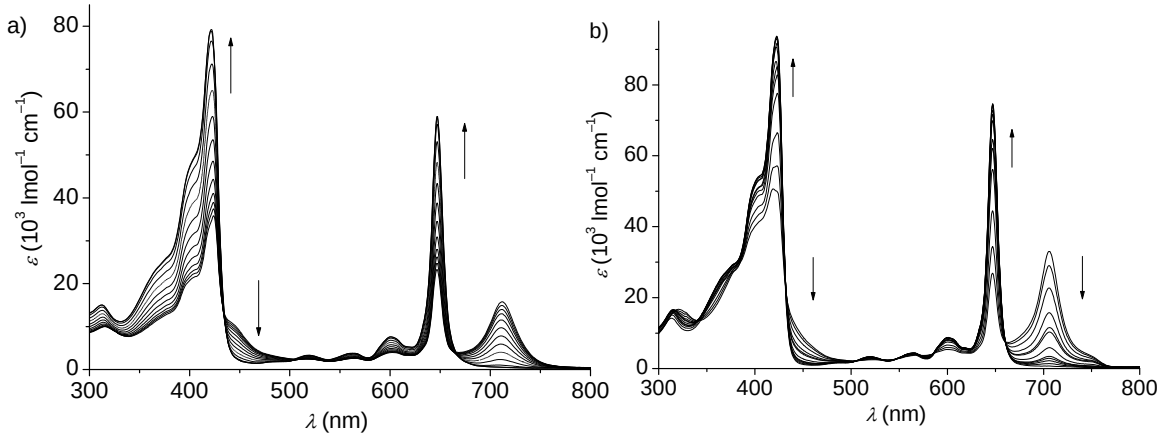

Figure 17. Spectroscopic investigation of zinc chlorin epimer (3^1S)-**6** in *n*-heptane/THF (100:1) at $c = 1.7 \times 10^{-5}$ M. a) UV/Vis spectra in the temperature range of 20-80 °C measured at 5 °C intervals by starting at 20 °C; the sample was allowed to equilibrate for 45 min prior to each measurement; arrows indicate changes upon increasing temperature; b) UV/Vis spectra in the temperature range of 20-80 °C measured at 5 °C intervals by starting at 20 °C, the sample was allowed to equilibrate for 45 min prior to each measurement; arrows indicate changes upon increasing temperature. Reprinted from ref. 105, with permission from Wiley-VCH Verlag GmbH & Co. KGaA.

With increasing temperature, the intensity of monomer bands of the zinc chlorins at 648 nm increased whilst the aggregate bands at 711 nm and 705 nm for (3^1S)-**6** and (3^1R)-**6**,

respectively, decreased which is indicative of the dissociation of aggregates at higher temperature. Upon cooling the aggregate solutions, the aggregate bands were completely recovered for both epimers, confirming that the aggregation is reversible. Distinct differences in CD spectra were also observed for these epimers. The amplitude of the CD signals for (3^1R)-**6** was not only higher in magnitude than that of (3^1S)-**17**, but also more intense and showed a well-defined bisignate shape similar to **1** and **3-5**. The negative CD signal for the (3^1R)-**6** (742 nm) was also more bathochromically shifted compared to that of the (3^1S)-**6** stereoisomer (718 nm). Notably, in such partially self-assembled systems a variety of aggregates with different size and geometry may prevail which can exhibit quite distinct CD spectra. For this reason, UV/Vis and CD spectra do not always properly match together in such cases. In addition to investigations on the self-assembly of pure (3^1R)-**6** and (3^1S)-**6** epimers, the mixtures of these epimers were also studied by UV/Vis spectroscopy. For this purpose, stock solutions of the epimers in THF were mixed in different ratios and added to *n*-hexane for the formation of aggregates. To achieve the highest possible amount of aggregates compared to monomers, solutions containing only 0.5 vol % THF were used. To make the different shifts and forms of aggregation bands noticeable, the absorption spectra (not shown) were normalized.[105] The higher was the percentage of (3^1S)-**6**, the further bathochromically shifted was the main aggregate Q_y band. In several previous publications it was reported that the aggregation modes of 3^1R and 3^1S epimers of BChls are quite distinct.[109-114]As in the case of ZnChl **6** epimers, earlier studies on BChl *c* and *e* revealed a larger bathochromic shift for the aggregate band of *S* epimers.[109,112] Compared to earlier studies on BChl *c* and *e*, a more pronounced bathochromic shift for the Q_y aggregate band for (3^1S)-**6** was observed. Thus, for aggregate bands of 3^1R-BChl *c* and 3^1S-BChl *c* absorption maxima at 703 nm and 750 nm respectively, were observed in concentrated dichloromethane solutions.[109] For the epimers of BChl *e* in cyclohexane, the 3^1R-BChl exhibited the Q_y absorption maximum at 706 nm and the *S* epimer at 717 nm.[112] Two previous independent studies showed that the addition of small amounts of the corresponding *S* epimers to solutions of *R* epimers of BChl *c* and *e* afforded aggregates with further bathochromically displaced Q_y absorption bands than those observed in the case of pure *R* epimers.[112,113] These observations were considered to be supportive for the bacteriochlorophyll double-tube model, in which the outer layer is formed preferentially by *R* epimers and the inner by *S* epimers. However, mixing experiments with the epimeric ZnChls (3^1R)-**6** and (3^1S)-**6** did not show any such effect. Furthermore, it was previously reported that a methyl group at the 3^1 position suppresses aggregation, whereas an additional methyl group at this position (tertiary alcohol) has no further influence. Thus, the

observation that the 3^1 methyl group in ZnChl **6** has a strong influence on the aggregation behavior and prevents formation of extended aggregates was in accordance with previous studies.

The 3^1-methoxy-functionalized ZnChl **2** has the structural features to form 1D π-stacks instead of the tubular nanostructures of **1** and **3-5** due to the absence of 3^1-hydroxy group and by virtue of π-π interactions and coordination of 3^1-methoxy group to the central zinc ion.[104] The self-assembly properties of ZnChl **2** in solution were investigated by UV/Vis spectroscopy. To gain insight into the self-assembly process, temperature-dependent UV/Vis spectroscopic measurements of ZnChl **2** were performed in cyclohexane/*n*-hexane (1:1) at a temperature range from 7 °C to 31 °C in 2 °C intervals (Figure 18a). The absorption spectra of ZnChl **2** in cyclohexane/*n*-hexane (1:1) (Figure 18a) revealed a pronounced bathochromic shift of the Q_y-band upon self-assembly from 646 nm (monomers) to 727 nm (aggregates), which is very characteristic for a J-type excitonic coupling resulting from spatial interactions of the transition dipole moments of the aggregated chromophores. The temperature-dependent UV/Vis absorption spectrum in Figure 18a shows that with increasing temperature the Q_y-band of ZnChl **2** aggregates at 727 nm decreases, while the Q_y-band of monomers at 646 nm increases. Upon subsequent cooling of the sample, the Q_y-band of aggregates at 727 nm reappears, confirming the reversibility of aggregate formation. It is to be noted that the Q_y-band of ZnChl **2** aggregates is 13 nm less red shifted compared with that of rod-shaped aggregates of ZnChl **1** which indicates that the supramolecular order of **2** is quite distinct from that observed for ZnChl **1** aggregates.

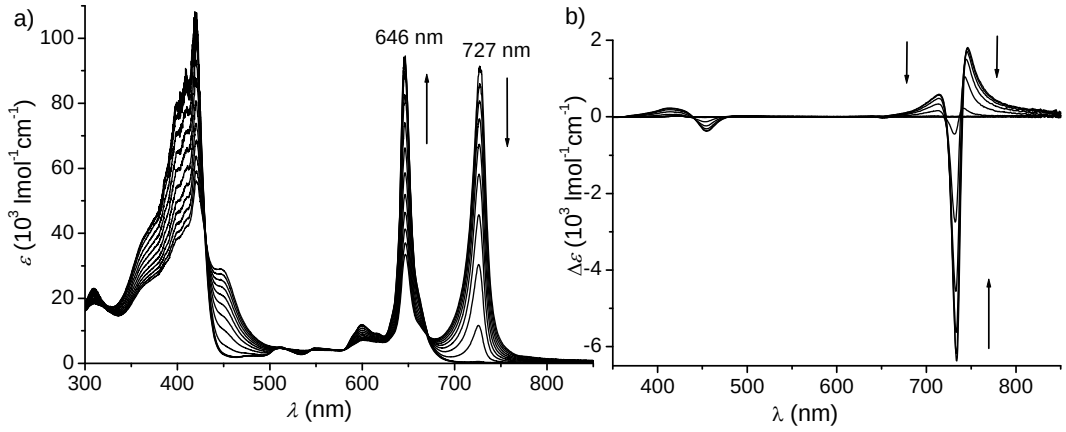

Figure 18. Temperature-dependent a) UV/Vis ($c = 2 \times 10^{-5}$ mol L^{-1}) and b) CD ($c = 1.7 \times 10^{-5}$ mol L^{-1}) spectra of ZnChl **2** in cyclohexane/*n*-hexane (1:1). The initial temperature of 7 °C was gradually increased in 2 °C steps up to 31 °C and the sample was equilibrated at each temperature for 1 h prior to measurements. Arrows indicate the changes upon increasing temperature. Inset in (a): the decrease of the Q_y band of aggregates at 727 nm and the increase of the monomer band at 646 nm upon increasing temperature. Inset in (b): magnification of the CD signals. Reprinted from ref. 104, with permission from Wiley-VCH Verlag GmbH & Co. KGaA.

Aggregates of methoxy ZnChl **2** in cyclohexane/*n*-hexane (1:1) showed a pronounced induced CD effect (Figure 18b) due to chiral excitonic coupling of transition dipole moments, a strong cotton effect at the chlorin Q_y absorption bands with two positive and one negative maxima. With increasing temperature, the induced CD effect decreases and the positive maximum at longer wavelength is shifted from 746 nm to 741 nm. This shift can be taken as an evidence for the existence of large polymeric ZnChl **2** aggregates rather than dimeric aggregates. To further elucidate the structural features and molecular ordering of self-assembled layers of **2**, scanning tunneling microscopy (STM) measurements were performed with aggregate solution of **2** on conductive and atomically flat surfaces such as highly oriented pyrolytic graphite (HOPG). In STM images of ZnChl **2** (Figure 19), two different types of well-ordered lamellae could be observed depending upon the concentration of aggregate solutions. In samples prepared from a less concentrated (c = 10^{-7} mol L^{-1}) ZnChl **2** aggregate solution, broad lamellae (L_I = 2.8 ± 0.1 nm) and small lamellae (l_I = 1.9 ± 0.1 nm) are observed (phase I with a periodicity of P_I = 4.7 nm) (Figure 19).

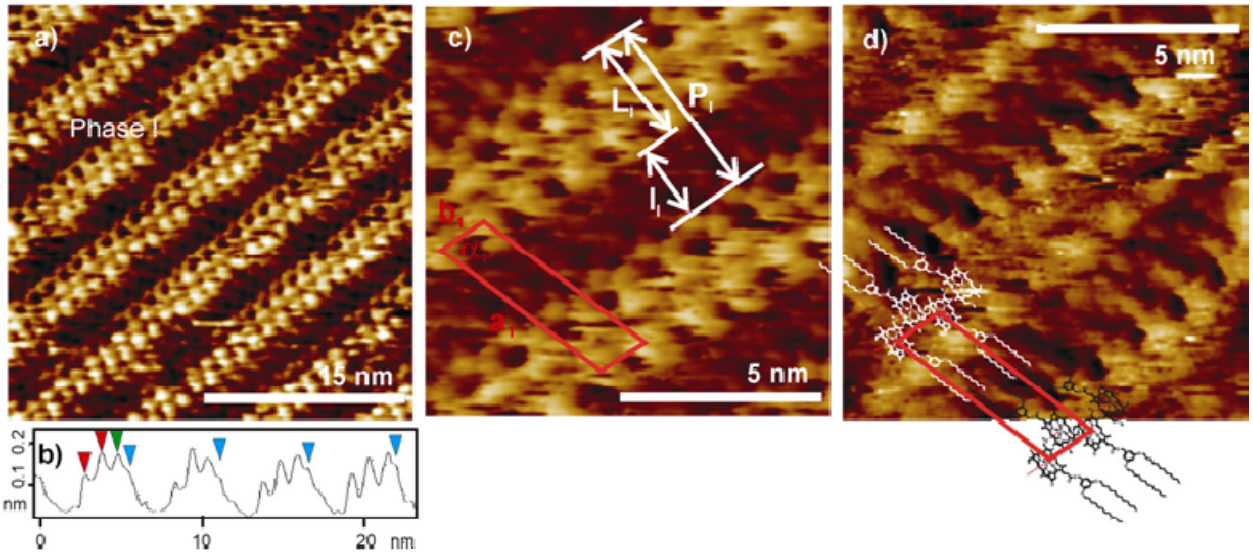

Figure 19. STM image of phase I arrangement of ZnChl **2**: (a) High resolution image (bias voltage: -900 mV, tunnel current: 5 pA). (b) Average cross section of four rows in image (a). (c) STM image of a magnified area of (a); the main measured dimensions are plotted and the red rectangle corresponds to the unit cell of the lattice of phase I. (d) In comparison to (c), the imaging parameters are optimized for better visualization of the alkyl chains of zinc chlorin **2** (bias voltage: -1100 mV, tunnel current: 500 fA); the proposed model for the arrangement of **2** molecules in phase I is depicted in (d). Reprinted from ref. 104, with permission from Wiley-VCH Verlag GmbH & Co. KGaA.

In contrast to phase I, in STM images of phase II (Figure 20), the bright lamellae structure is broader (L_{II} = 3.6 ± 0.2 nm in phase II compared to L_I = 2.8 ± 0.1 nm in phase I). Measured lattice constants of phase II are marked in Figure 20 as a_2 = 5.7 ± 0.2 nm, b_2 = 1.2 ± 0.1 nm, and α_2 = 70°. Based on the observed dimensions, a model for the aggregate of ZnChl **2** in phase II is

proposed in Figure 20. According to this model, double stacks of parallel-oriented ZnChl **2** molecules are arranged in a way in which the alkyl chains of one stack are all arranged in the same direction. As in phase I, the neighboring double stacks in phase II are connected by interdigitated alkyl chains. The proposed models for the aggregates in phase I and II developed on the basis of the above-mentioned STM analysis are schematically illustrated in Figure 21. Figure 22 summarises the different semisynthetic zinc chlorin aggregates that are formed based on their structural variations discussed in this section.

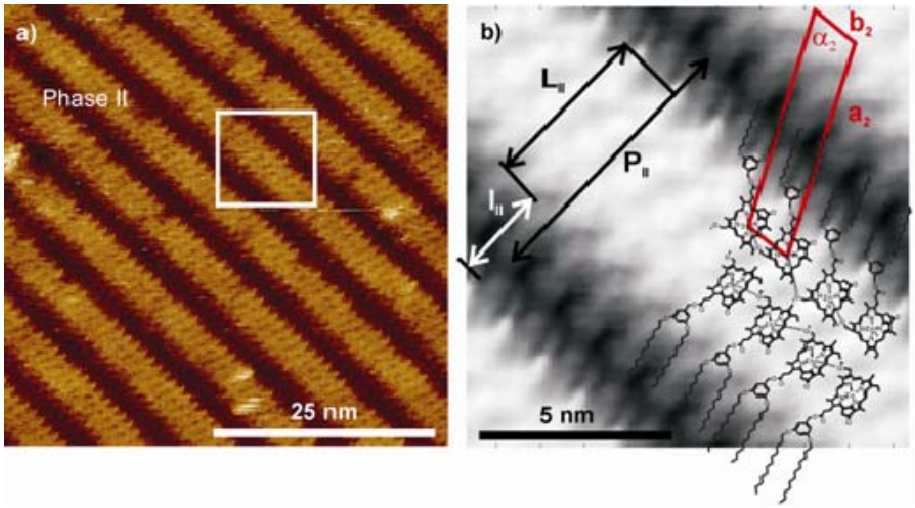

Figure 20. STM image of phase II arrangement of ZnChl **2**: (a) Bias voltage: -2700 mV, tunnel current: 500 fA, (b) image with measured dimensions for phase II obtained by correlation averaging (148 times) of a window marked in (a) with a white rectangle and a proposed structure model for the arrangement of ZnChl **2** in phase II. The red rectangle corresponds to the unit cell of the lattice of phase II. Schematic representation of the structural models proposed for the surface arrangement of π-stacked aggregates of ZnChl **2** in phase II. In both phases, the chlorin cores (green rectangles) are tilted with respect to the HOPG surface. Reprinted from ref. 104, with permission from Wiley-VCH Verlag GmbH & Co. KGaA.

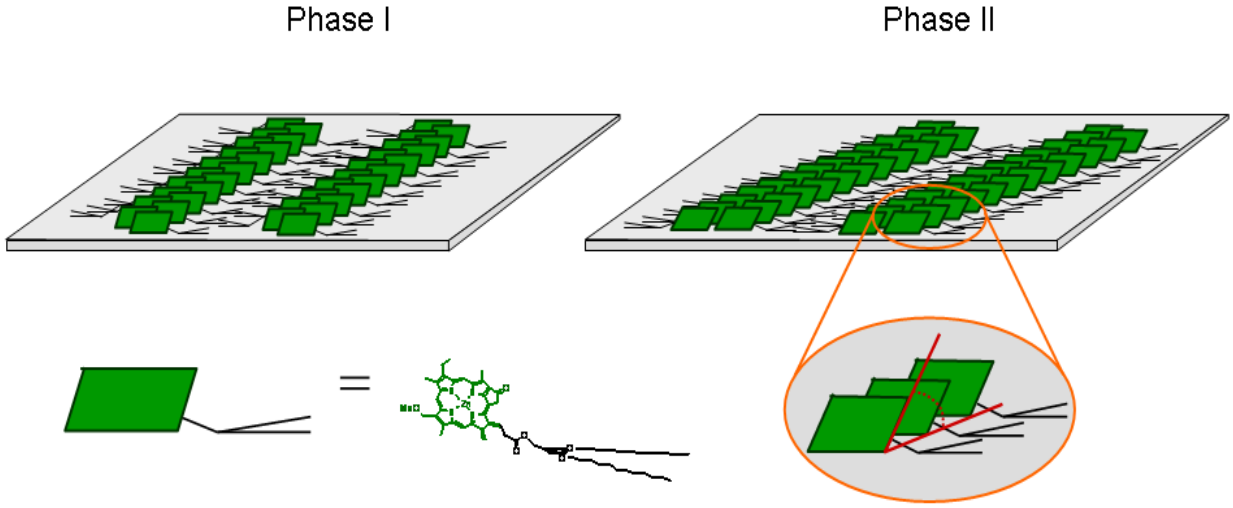

Figure 21. Schematic representation of the structural models proposed for the surface arrangement of π-stacked aggregates of ZnChl **2** in phase I (left) and phase II (right). In both phases, the chlorin cores (green rectangles) are tilted with respect to the HOPG surface. This tilt is visualized in a magnified section of phase II (bottom, right). Reprinted from ref. 104, with permission from Wiley-VCH Verlag GmbH & Co. KGaA.

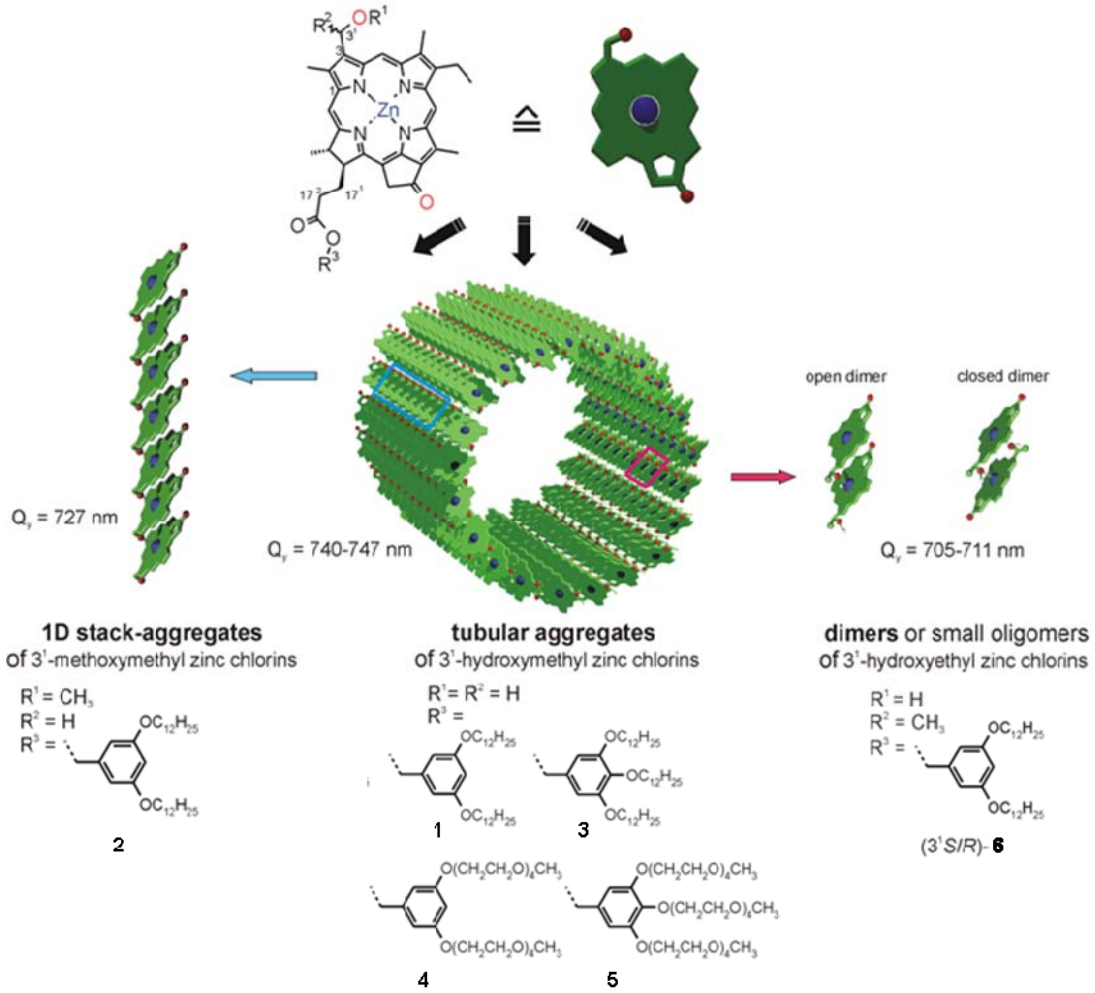

Figure 22. Schematic illustration of the self-assembled aggregate structures formed from zinc chlorins **1**-**6**. Left: 3^1-methoxy zinc chlorins **2** form one-dimensional π-stacked aggregates. Middle: 3^1-hydroxy zinc chlorins with solubility promoting side chains (**1**, **3** and **4**, **5**) form tubular structures. Right: 3^1-hydroxyethyl zinc chlorins ((3^1*S*/*R*)-**6**) for studying the influence of chirality on aggregation, prefer the formation of small oligomeric aggregates (adapted from Ph.D Thesis V. Huber 2007, ref 68).

2.6.2. Functional semisynthetic zinc chlorin aggregates

The rod aggregates formed from self-assembly of semisynthetic zinc chlorins are also excellent functional model systems for energy transport thereby closely mimicking the natural chlorosomal LH systems. Despite the fact that BChl *c* and ZnChl assemblies are very efficient in harvesting blue and red light of the solar spectrum, they cannot utilize the significant green region. Hence, biomimetic LH systems based on ZnChl with covalently linked naphthalene diimide (NDI) dyes (Figure 23) were synthesized that could act as light harvesting chromophores in the green region, thereby covering the "green gap". These ZnChl-NDI dyads and triads self-assembled into rod antennae in cyclohexane/tetrachlomethane (1%) by non-covalent interactions of the ZnChl units while the appended NDI dyes did not aggregate at the periphery of the rod antennae. Self-assembly of multichromophoric arrays based on covalently linked ZnChl-NDI

dyads **7**, **8** and, triad ZnChl-NDINN-NDINO **9** containing additional NDI chromophores to cover the green and orange fractions of solar light, were studied by UV/Vis, CD (Figure 24) and stationary fluorescence spectroscopy.[107,108]

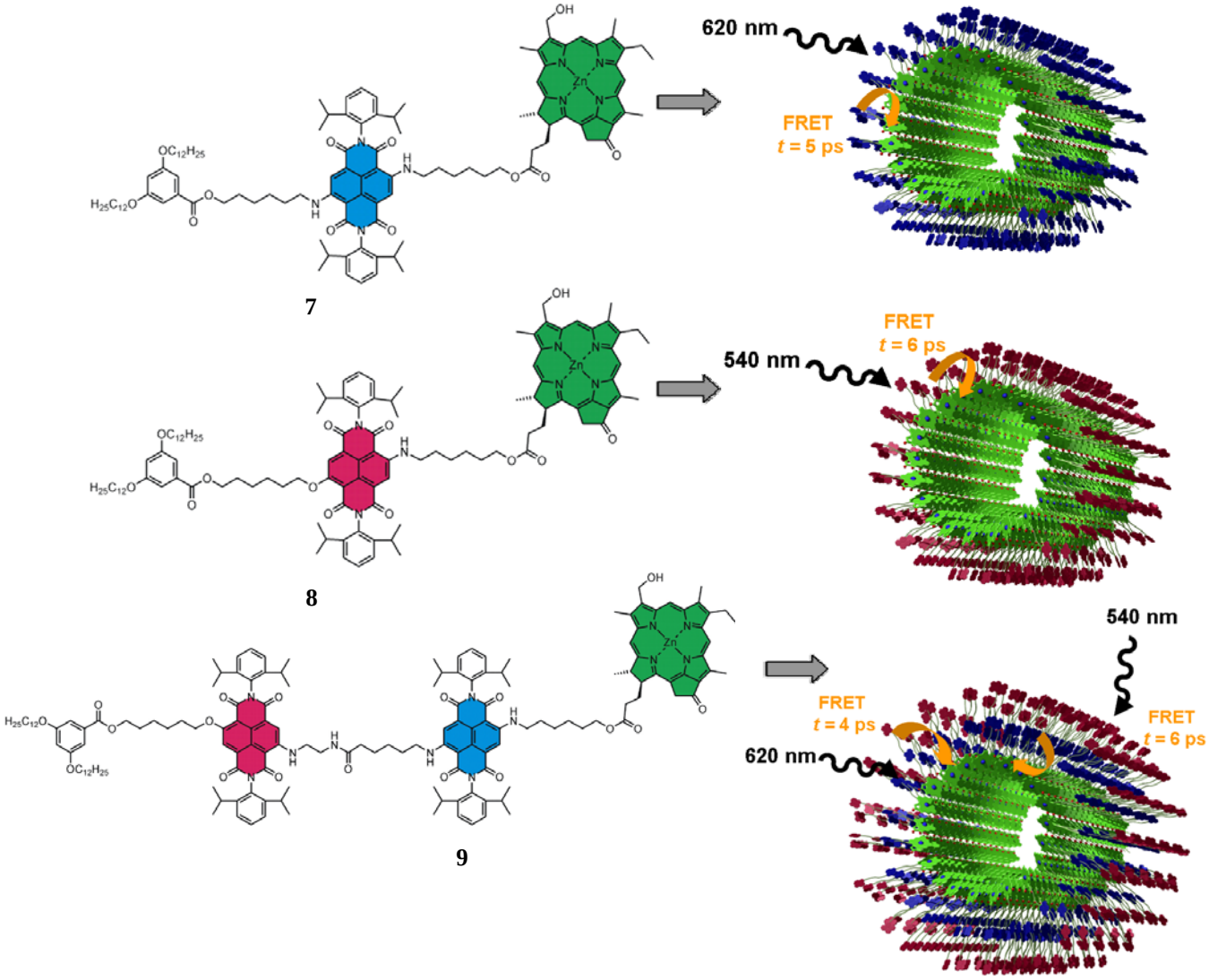

Figure 23. Zinc chlorin-NDI dyads **7**, **8** and triad **9** and a schematic representation of their self-assembly into rod-like nanostructures in non-polar solvents. Reprinted from ref. 107,108, with permission from the American Chemical Society and adapted from Ph.D Thesis C. Röger 2007, ref 67.

The photophysical behavior of aggregate solutions of **7**, **8** and **9** was investigated by time-resolved fluorescence experiments. These experiments revealed that upon selective photoexcitation of blue or pink NDI units of **7**, **8**, and **9** monomers, their excitation energy is quantitatively conveyed to the ZnChl chromophores on a picosecond time scale (7-25 ps). For aggregates of **7**, **8**, and **9** energy transfer processes from peripheral NDIs to the inner green ZnChl rod antenna were observed, showing even faster energy transfer time constants (5-6 ps). [107,108] Therefore, the "green gap" was bridged by the attached NDI antenna chromophores, providing dye aggregates whose light-harvesting efficiency for the absorption of terrestrial

sunlight is increased by up to 63% compared to the parent ZnChl or natural BChl *c* rod aggregates. These systems were thus highly efficient ultrafast LH self-organized multichromophoric antennae mimicking natural LH systems.[107,108]

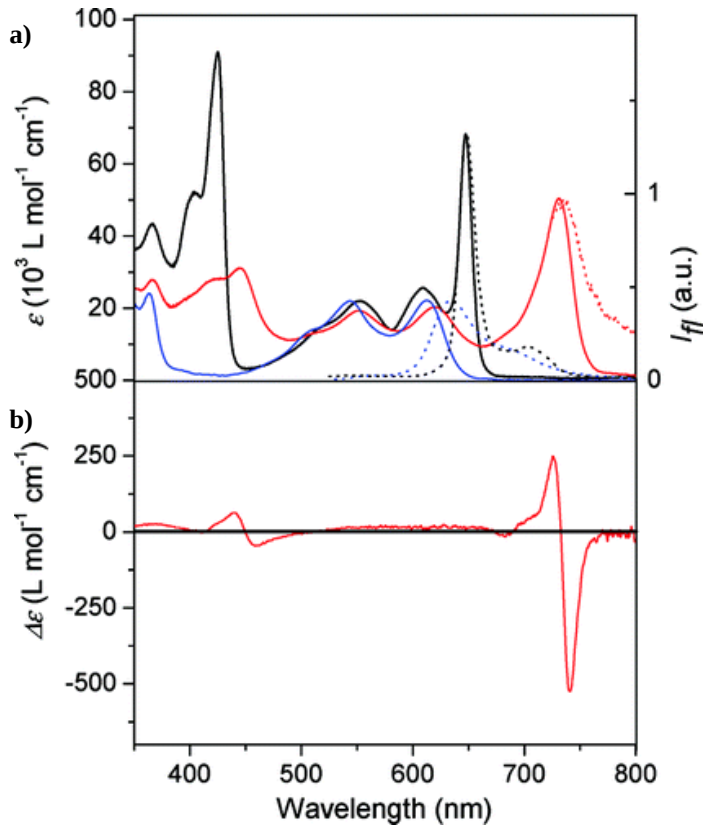

Figure 24. a) UV/Vis spectra (solid lines) and normalized fluorescence spectra (dotted lines) of triad **9** monomers in THF (black, λ_{ex} = 510 nm) and of triad **9** aggregates (red, λ_{ex} = 540 nm) in cyclohexane/tetrachloromethane (100:1); b) CD spectrum of triad **9** aggregates in cyclohexane/tetrachloromethane (100:1) (red). Reprinted from ref. 107 with permission from the American Chemical Society.

2.7. Conclusion

The present introductory chapter gives an overview on the detailed structural aspects of photosynthetic LH systems of purple bacteria and more importantly, on chlorosomal LH systems of green sulphur and non-sulphur bacteria. The structural developments and refinements of chlorosomal superstructure provided till-date are discussed. The functions of such LH systems arise due to the precise spatial disposition of the BChl dyes in the assemblies that have potential for supramolecular photonic and electronic applications. By virtue of their favorable redox properties, chlorin aggregates should also be well suited for charge carrier transport. However, till date, charge transport properties of synthetic mimic of chlorosomes i.e., aggregates of semisynthetic zinc chlorins have not been investigated and structure-property relationship have not been elucidated. The concepts presented herein i.e., elucidation of chlorophyll aggregate

structures by combination of different spectroscopic (UV/Vis, CD), scanning probe microscopy (AFM, STM), electron microscopy (TEM, STEM, SEM) and the utilization of these nanoaggregates as functional material for charge transport, are the major objectives of this work. The pertinent results will be described in subsequent chapters.

2.8. References and notes

(1) *Electronic Materials: the Oligomer Approach* Wiley-VCH, Weinheim, 1998.

(2) *Semiconducting Polymers: Chemistry, Physics and Engineering*; Hadziioannou, G., van Hutten P. F., Eds.; Wiley-VCH: Weinheim, 2000.

(3) Forrest, S. R.; Thompson, M. E. *Chem. Rev.* **2007**, *107*, 923–925 and articles published in this thematic issue of *Chem. Rev.* (**2007**, *107*, Issue 4).

(4) Coropceanu, V.; Cornil, J.; da Silva, D. A.; Olivier, Y.; Silbey, R.; Brédas, J. L. *Chem. Rev.* **2007**, *107*, 926–952.

(5) Grozema, F. C.; Houarner-Rassin, C.; Prins, P.; Siebbeles, L. D. A.; Anderson, H. L. *J. Am. Chem. Soc.* **2007**, *129*, 13370–13371.

(6) Warman, J. M.; de Haas, M. P.; Dicker, G.; Grozema, F. C.; Piris, J.; Debije, M. G. *Chem. Mater.* **2004**, *16*, 4600–4609.

(7) Würthner, F.; Chen, Z.; Hoeben, F. J. M.; Osswald, P.; You, C.-C.; Jonkheijm, P.; van Herrikhuyzen, J.; Schenning, A. P. H. J; van der Schoot, P. P. A. M.; Meijer, E. W.; Beckers, E. H. A.; Meskers, S. C. J.; Janssen, R. A. J. *J. Am. Chem. Soc.* **2004**, *126*, 10611–10618.

(8) Xiao, S. X.; Myers, M.; Miao, Q.; Sanaur, S.; Pang, K. L.; Steigerwald, M. L.; Nuckolls, C. *Angew. Chem., Int. Ed.* **2005**, *44*, 7390–7394.

(9) Schmidt-Mende, L.; Fechtenkötter, A.; Müllen, K.; Moons, E.; Friend, R. H.; MacKenzie, J. D. *Science* **2001**, *293*, 1119–1122.

(10) Lehn, J. M. *Supramolecular Chemistry: Concepts and Perspectives*; VCH: Weinheim, 1995.

(11) Schenning, A.; Meijer, E. W. *Chem. Commun.* **2005**, 3245–3258.

(12) Hoeben, F. J. M.; Jonkheijm, P.; Meijer, E. W.; Schenning, A. *Chem. Rev.* **2005**, *105*, 1491–1546.

(13) Meijer, E. W.; Schenning, A. *Nature* **2002**, *419*, 353–354.

(14) Percec, V.; Glodde, M.; Bera, T. K.; Miura, Y.; Shiyanovskaya, I.; Singer, K. D.;

Balagurusamy, V. S. K.; Heiney, P. A.; Schnell, I.; Rapp, A.; Spiess, H. W.; Hudson, S. D.; Duan, H. *Nature* **2002**, *419*, 384–387.

(15) Wilson, T. M.; Tauber, M. J.; Wasielewski, M. R. *J. Am. Chem. Soc.* **2009**, *131*, 8952–8957.

(16) Sergeyev, S.; Pisula, W.; Geerts, Y. H. *Chem. Soc. Rev.* **2007**, *36*, 1902–1929.

(17) Adam, D.; Schuhmacher, P.; Simmerer, J.; Häussling, L.; Siemensmeyer, K.; Etzbach, K. H.; Ringsdorf, H.; Haarer, D. *Nature* **1994**, *371*, 141–143.

(18) van de Craats, A. M.; Warman, J. M.; de Haas, M. P.; Adam, D.; Simmerer, J.; Haarer, D.; Schuhmacher, P. *Adv. Mater.* **1996**, *8*, 823–826.

(19) Simpson, C. D.; Wu, J. S.; Watson, M. D.; Müllen, K. *J. Mater. Chem.* **2004**, *14*, 494–504.

(20) Wu, J. S.; Pisula, W.; Müllen, K. *Chem. Rev.* **2007**, *107*, 718–747.

(21) Feng, X. L.; Marcon, V.; Pisula, W.; Hansen, M. R.; Kirkpatrick, J.; Grozema, F.; Andrienko, D.; Kremer, K.; Müllen, K. *Nat. Mater.* **2009**, *8*, 421–426.

(22) Guo, X. F.; Xiao, S. X.; Myers, M.; Miao, Q.; Steigerwald, M. L.; Nuckolls, C. *Proc. Natl. Acad. Sci. U. S. A.* **2009**, *106*, 691–696.

(23) Eichhorn, H. *J. Porphyrins Phthalocyanines* **2000**, *4*, 88–102.

(24) Wicklein, A.; Lang, A.; Muth, M.; Thelakkat, M. *J. Am. Chem. Soc.* **2009**, *131*, 14442–14453.

(25) Debije, M. G.; Chen, Z. J.; Piris, J.; Neder, R. B.; Watson, M. M.; Müllen, K.; Würthner, F. *J. Mater. Chem.* **2005**, *15*, 1270–1276.

(26) Chen, Z.; Baumeister, U.; Tschierske, C.; Würthner, F. *Chem.–Eur. J.* **2007**, *13*, 450–465.

(27) Chen, Z.; Stepanenko, V.; Dehm, V.; Prins, P.; Siebbeles, L. D. A.; Seibt, J.; Marquetand, P.; Engel, V.; Würthner, F. *Chem.–Eur. J.* **2007**, *13*, 436–449.

(28) Warman, J. M.; Van de Craats, A. M. *Mol. Cryst. Liq. Cryst.* **2003**, *396*, 41–72.

(29) Lemaur, V.; Da Silva Filho, D. A.; Coropceanu, V.; Lehmann, M.; Geerts, Y.; Piris, J.; Debije, M. G.; Van de Craats, A. M.; Senthilkumar, K.; Siebbeles, L. D. A.; Warman, J. M.; Brédas, J. L.; Cornil, J. *J. Am. Chem. Soc.* **2004**, *126*, 3271–3279.

(30) Lehmann, M.; Kestemont, G.; Aspe, R. G.; Buess-Herman, C.; Koch, M. H. J.; Debije, M. G.; Piris, J.; de Haas, M. P.; Warman, J. M.; Watson, M. D.; Lemaur, V.; Cornil, J.; Geerts, Y. H.; Gearba, R.; Ivanov, D. A. *Chem.–Eur. J.* **2005**, *11*, 3349–3362.

(31) Rosen, B. M.; Wilson, D. A.; Peterca, M.; Imam, M. I.; Percec V. *Chem. Rev.* **2009**, *109*, 6275–6540.

(32) Percec, V. *Chem. Rev.* **2009**, *109*, 4961–4962.

(33) Rosen, B. M.; Peterca, M.; Morimitsu, K.; Dulcey A. E.; Leowanawat, P.; Resmerita, A.; Imam M. R.; Percec V. *J. Am. Chem. Soc.*, **2011**, *133*, 5135–5151.

(34) Hill, J. P.; Jin, W. S.; Kosaka, A.; Fukushima, T.; Ichihara, H.; Shimomura, T.; Ito, K.; Hashizume, T.; Ishii, N.; Aida, T. *Science* **2004**, *304*, 1481–1483.

(35) Yamamoto, Y.; Fukushima, T.; Suna, Y.; Ishii, N.; Saeki, A.; Seki, S.; Tagawa, S.; Taniguchi, M.; Kawai, T.; Aida, T. *Science* **2006**, *314*, 1761–1764.

(36) Yamamoto, Y.; Zhang, G. X.; Jin, W. S.; Fukushima, T.; Ishii, N.; Saeki, A.; Seki, S.; Tagawa, S.; Minari, T.; Tsukagoshi, K.; Aida, T. *Proc. Natl. Acad. Sci. U. S. A.* **2009**, *106*, 21051–21056.

(37) Hizume, Y.; Tashiro, K.; Charvet, R.; Yamamoto, Y.; Saeki, A.; Seki, S.; Aida, T. *J. Am. Chem. Soc.* **2009**, *132*, 6628–6629.

(38) Schouten, P. G.; Warman, J. M.; Dehaas, M. P.; Fox, M. A.; Pan, H. L. *Nature* **1991**, *353*, 736–737.

(39) Kim, J. Y.; Bard, A. J. *Chem. Phys. Lett.* **2004**, *383*, 11–15.

(40) Fox, M. A.; Grant, J. V.; Melamed, D.; Torimoto, T.; Liu, C. Y.; Bard, A. J. *Chem. Mater.* **1998**, *10*, 1771–1776.

(41) Liu, C. Y.; Pan, H. I.; Fox, M. A.; Bard, A. J. *Science* **1993**, *261*, 897–899.

(42) Gregg, B. A.; Fox, M. A.; Bard, A. J. *J. Phys. Chem.* **1990**, *94*, 1586–1598.

(43) Kassi, H.; Hotchandani, S.; Leblanc, R. M. *Appl. Phys. Lett.* **1993**, *62*, 2283–2285.

(44) Kassi, H.; Leblanc, R. M.; Hotchandani, S. *Physica Status Solidi B-Basic Research* **2000**, *220*, 931–939.

(45) Grozema, F. C.; Tonzani, S.; Berlin, Y. A.; Schatz, G. C.; Siebbeles, L. D. A.; Ratner, M. A. *J. Am. Chem. Soc.* **2009**, *131*, 14204–14205.

(46) Pullerits, T.; Sundström, V. *Acc. Chem. Res.* **1996**, *29*, 381–389.

(47) Percec, V.; Heck, J.; Johansson, G.; Tomazos, D.; Ungar, G. *Macromolecular Symposia* **1994**, *77*, 237–265.

(48) Klug, A. *Angew. Chem., Int. Ed.* **1983**, *22*, 565–582.

(49) Beljonne, D.; Curutchet, C.; Scholes, G. D.; Silbey, R. J. *J. Phys. Chem. B* **2009**, *113*, 6583–6599.

(50) Doust, A. B.; Wilk, K. E.; Curmi, P. M. G.; Scholes, G. D. *J. Photochem. Photobiol. a-*

Chemistry **2006**, *184*, 1–17.

(51) Balaban, T. S.; Tamiaki, H.; Holzwarth, A. R. *Supramolecular Dye Chemistry* **2005**, *258*, 1–38.

(52) McDermott, G.; Prince, S. M.; Freer, A. A.; Hawthornthwaite-lawless, A. M.; Papiz, M. Z.; Cogdell, R. J.; Isaacs, N. W. *Nature* **1995**, *374*, 517–521.

(53) Scheuring, S.; Sturgis, J. N.; Prima, V.; Bernadac, A.; Lévy, D.; Rigaud, J. L. *Proc. Natl. Acad. Sci. U. S. A.* **2004**, *101*, 11293–11297.

(54) Bahatyrova, S.; Frese, R. N.; Siebert, C. A.; Olsen, J. D.; van der Werf, K. O.; van Grondelle, R.; Niederman, R. A.; Bullough, P. A.; Otto, C.; Hunter, C. N. *Nature* **2004**, *430*, 1058–1062.

(55) Hu, X. C.; Schulten, K. *Physics Today* **1997**, *50*, 28–34.

(56) Yu, L. H.; Lindsey, J. S. *J. Org. Chem.* **2001**, *66*, 7402–7419.

(57) Beatty, J. T.; Overmann, J.; Lince, M. T.; Manske, A. K.; Lang, A. S.; Blankenship, R. E.; Van Dover, C. L.; Martinson, T. A.; Plumley, F. G. *Proc. Natl. Acad. Sci. U. S. A.* **2005**, *102*, 9306–9310.

(58) Bryant, D. A.; Costas, A. M. G.; Maresca, J. A.; Chew, A. G. M.; Klatt, C. G.; Bateson, M. M.; Tallon, L. J.; Hostetler, J.; Nelson, W. C.; Heidelberg, J. F.; Ward, D. M. *Science* **2007**, *317*, 523–526.

(59) Saga, Y.; Shibata, Y.; Ltoh, S.; Tamiaki, H. *J. Phys. Chem. B* **2007**, *111*, 12605–12609.

(60) Würthner, F.; Kaiser, T. E.; Saha-Möller C. R. *Angew. Chem., Int. Ed.* **2011**, *50*, 3376–3410.

(61) Wakao, N.; Yokoi, N.; Isoyama, N.; Hiraishi, A.; Shimada, K.; Kobayashi, M.; Kise, H.; Iwaki, M.; Itoh, S.; Takaichi, S.; Sakurai, Y. *Plant and Cell Physiology* **1996**, *37*, 889–893.

(62) Davydov, A. S. *Theory of Molecular Excitons*; Plenum Press: New York, 1971.

(63) Czlikkely, V.; Forsterling, H. D.; Kuhn, H. *Chem. Phys. Lett.* **1970**, *6*, 11–14.

(64) Czikklely, V.; Forsterling, H. D.; Kuhn, H. *Chem. Phys. Lett* .**1970**, *6*, 207–210.

(65) Emerson, E. S.; Conlin, M. A.; Rosenoff, A. E.; Norland, K. S.; Rodrigue, H.; Chin, D.; Bird, G. R. *J. Phys. Chem.* **1967**, *71*, 2396–2403.

(66) Bohn, P. W. *Annu. Rev. Phys. Chem.* **1993**, *44*, 37–60.

(67) Röger C.; Dissertation, Universität Würzburg, 2007.

(68) Huber, V.; Dissertation, Universität Würzburg, 2007.

(69) Watanabe, T.; Kobayashi, M. in *Chlorophylls*; Scheer, H., Ed.; CRC Press: Boca Raton, US, 1991; pp 288–315.

(70) Campbell, N. *Biologie*; Spektrum Akademischer Verlag Heidelberg, Berlin, Oxford, **1997**.

(71) Gouterman, M. *J. Mol. Spectroscopy* **1961**, *6*, 138–163.

(72) Gouterman, M.; Snyder, L. C.; Wagniere, G. H. *J. Mol. Spectrosc.* **1963**, *11*, 108–127.

(73) Holzwarth, A. R.; Schaffner, K. *Photosyn. Res.* **1994**, *41*, 225–233.

(74) Nozawa, T.; Ohtomo, K.; Suzuki, M.; Nakagawa, H.; Shikama, Y.; Konami, H.; Wang, Z. Y. *Photosyn. Res.* **1994**, *41*, 211–223.

(75) Wang, Z. Y.; Umetsu, M.; Kobayashi, M.; Nozawa, T. *J. Phys. Chem. B* **1999**, *103*, 3742–3753.

(76) Wang, Z. Y.; Umetsu, M.; Kobayashi, M.; Nozawa, T. *J. Am. Chem. Soc.* **1999**, *121*, 9363–9369.

(77) Cohenbazire, G.; Pfennig, N.; Kunisawa, R. *J. Cell Biol.* **1964**, *22*, 207–225.

(78) Staehelin, L. A.; Golecki, J. R.; Fuller, R. C.; Drews, G. *Arch. Microbiology* **1978**, *119*, 269–277.

(79) Staehelin, L. A.; Golecki, J. R.; Drews, G. *Biochimica Et Biophysica Acta* **1980**, *589*, 30–45.

(80) Sprague, S. G.; Staehelin, L. A.; Dibartolomeis, M. J.; Fuller, R. C. *J. Bacteriology* **1981**, *147*, 1021–1031.

(81) Pšenčík, J.; Ikonen, T. P.; Laurinmaki, P.; Merckel, M. C.; Butcher, S. J.; Serimaa, R. E.; Tuma, R. *Biophys. J.* **2004**, *87*, 1165–1172.

(82) Nozawa, T.; Nishimura, M.; Hatano, M.; Sato, M. *Bull. Chem. Soc. Japan* **1993**, *66*, 692–697.

(83) Nozawa, T.; Suzuki, M.; Ohtomo, K.; Morishita, Y.; Konami, H.; Madigan, M. T. *Chem. Lett.* **1991**, 1641–1644.

(84) Nozawa, T.; Ohtomo, K.; Suzuki, M.; Morishita, Y.; Madigan, M. T. *Chem. Lett.* **1991**, 1763–1766.

(85) Balaban, T. S.; Holzwarth, A. R.; Schaffner, K.; Boender, G. J.; de Groot, H. J. M. *Biochemistry* **1995**, *34*, 15259–15266.

(86) van Rossum, B. J.; Steensgaard, D. B.; Mulder, F. M.; Boender, G. J.; Schaffner, K.; Holzwarth, A. R.; de Groot, H. J. M. *Biochemistry* **2001**, *40*, 1587–1595.

(87) de Boer, I.; Matysik, J.; Amakawa, M.; Yagai, S.; Tamiaki, H.; Holzwarth, A. R.; de Groot, H. J. M. *J. Am. Chem. Soc.* **2003**, *125*, 13374–13375.

(88) de Boer, I.; Matysik, J.; Erkelens, K.; Sasaki, S.; Miyatake, T.; Yagai, S.; Tamiaki, H.; Holzwarth, A. R.; de Groot, H. J. M. *J. Phys. Chem. B* **2004**, *108*, 16556–16566.

(89) Tamiaki, H.; Holzwarth, A. R.; Schaffner, K. *J. Photochem. Photobiol.,* B **1992**, *15*, 355–360.

(90) Steensgaard, D. B.; Wackerbarth, H.; Hildebrandt, P.; Holzwarth, A. R. *J. Phys. Chem. B* **2000**, *79*, 2105–2120.

(91) Kakitani, Y.; Nagae, H.; Mizoguchi, T.; Egawa, A.; Akiba, K.; Fujiwara, T.; Akutsu, H.; Koyama, Y. *Biochemistry* **2006**, *45*, 7574–7585.

(92) Mizoguchi, T.; Ogura, K.; Inagaki, F.; Koyama, Y. *Biospectroscopy* **1999**, *5*, 63–77.

(93) Mizoguchi, T.; Sakamoto, S.; Koyama, Y.; Ogura, K.; Inagaki, F. *Photochem. Photobiol.* **1998**, *67*, 239–248.

(94) Kakitani, Y.; Koyama, Y.; Shimoikeda, Y.; Nakai, T.; Utsumi, H.; Shimizu, T.; Nagae, H. *Biochemistry* **2009**, *48*, 74–86.

(95) Hohmann-Marriott, M. F.; Blankenship, R. E.; Roberson, R. W. *Photosyn. Res.* **2005**, *86*, 145–154.

(96) Saga, Y.; Tamiaki, H. *J. Bioscience and Bioengineering* **2006**, *102*, 118–123.

(97) Oostergetel, G. T.; Reus, M.; Chew, A. G. M.; Bryant, D. A.; Boekema, E. J.; Holzwarth, A. R. *FEBS Letts* **2007**, *581*, 5435–5439.

(98) Ganapathy, S.; Oostergetel, G. T.; Wawrzyniak, P. K.; Reus, M.; Chew, A. G. M.; Buda, F.; Boekema, E. J.; Bryant, D. A.; Holzwarth, A. R.; de Groot, H. J. M. *Proc. Natl. Acad. Sci. U. S. A.* **2009**, *106*, 8525– 8530.

(99) Balaban, T. S.; Linke-Schaetzel, M.; Bhise, A. D.; Vanthuyne, N.; Roussel, C.; Anson, C. E.; Buth, G.; Eichhöfer, A.; Foster, K.; Garab, G.; Gliemann, H.; Goddard, R.; Javorfi, T.; Powell, A. K.; Rösner, H.; Schimmel, T. *Chem.–Eur. J.* **2005**, *11*, 2268–2275.

(100) Tamiaki, H.; Amakawa, M.; Shimono, Y.; Tanikaga, R.; Holzwarth, A. R.; Schaffner, K. *Photochem. Photobiol.* **1996**, *63*, 92–99.

(101) Kunieda, M.; Tamiaki, H. *J. Org. Chem.* **2009**, *74*, 5803–5809.

(102) Saga, Y.; Nakagawa, T.; Miyatake, T.; Tamiaki, H. *Chem. Lett.* **2009**, *38*, 882–883.

(103) Kunieda, M.; Tamiaki, H. *J. Org. Chem.* **2009**, *74*, 8437–8440.

(104) Huber, V.; Lysetska, M.; Würthner, F. *Small* **2007**, *3*, 1007–1014.

(105) Huber, V.; Sengupta, S.; Würthner, F. *Chem.–Eur. J.* **2008**, *14*, 7791–7807.

(106) Huber, V.; Katterle, M.; Lysetska, M.; Würthner, F. *Angew. Chem., Int. Ed.* **2005**, *44*, 3147–3151.

(107) Röger, C.; Miloslavina, Y.; Brunner, D.; Holzwarth, A. R.; Würthner, F. *J. Am. Chem. Soc.* **2008**, *130*, 5929–5939.

(108) Röger, C.; Müller, M. G.; Lysetska, M.; Miloslavina, Y.; Holzwarth, A. R.; Würthner, F. *J. Am. Chem. Soc.* **2006**, *128*, 6542–6543.

(109) Chiefari, J.; Griebenow, K.; Griebenow, N.; Balaban T. S.; Holzwarth, A. R.; Schaffner, K. *J. Phys. Chem.* **1995**, *99*, 1357–1365.

(110) Tamiaki, H.; Takeuchi, S.; Tsudzuki, S.; Miyatake, T.; Tanikaga, R. *Tetrahedron* **1998**, *54*, 6699–6718.

(111) Balaban, T. S.; Tamiaki, H.; Holzwarth, A. R.; Schaffner, K. *J. Phys. Chem. B* **1997**, *101*, 3424–3431.

(112) Steensgaard, D. B.; Wackerbarth, H.; Hildebrandt, P.; Holzwarth, A. R. *J. Phys. Chem. B* **2000**, *104*, 10379–10386.

(113) Mizoguchi, T.; Hara, K.; Nagae, H.; Koyama, Y. *Photochem. Photobiol.* **2000**, *71*, 596–609.

(114) Yagai S.; Miyatake, T.; Shimono, Y.; Tamiaki, H. *Photochem. Photobiol.* **2001**, *73*, 153–163.

Chapter 3

Zinc Chlorin Rod and Stack Assemblies: Investigations on Structural and Charge Transport Properties

Semisynthetic 3^1-hydroxy zinc chlorins (ZnChls) **1**-**3**-OH and 3^1-methoxy ZnChls **1**-, **2**-OMe self-assemble into tubular and stack aggregates respectively. Solution aggregation studies of these two types of aggregates i.e., tubular and stack aggregates, have been performed by UV/Vis, circular dichroism (CD), dynamic light scattering (DLS) and electron microscopy (EM) techniques to provide detailed insights into the aggregate structure. Convincing evidence was obtained for tubular rod assemblies of 3^1-hydroxy ZnChl **3**-OH by EM studies for the first time. The microstructures of these two types of aggregates in the solid state, particularly that of **1**-OMe have been assessed by a combination of solid-state magic angle spinning (MAS) NMR, X-ray powder diffraction and molecular modelling, all converging towards a unique three-dimensional packing of the π-stacks of **1**-OMe in the solid state. Finally, charge transport properties of these aggregates have been studied by pulse radiolysis time-resolved microwave conductivity (PR-TRMC) technique and supramolecular structure-charge transport relationship have been elucidated in detail. Efficient charge transport is found in these aggregates and charge transport is strongly influenced by aggregate structures and presence of central zinc ion. Furthermore, thermally activated charge carrier transport with maximum charge carrier mobilities of upto ~ 0.1 cm^2/Vs are observed for tubular aggregates of 3^1-hydroxy ZnChl **1**-OH. The corresponding stack aggregates of 3^1-methoxy ZnChl **1**-OMe have comparatively higher charge carrier mobility of upto 0.28 cm^2/Vs. Such highly ordered superstructures constructed from semisynthetic zinc chlorins possessing efficient charge transporting capabilities are of interest for (bio)supramolecular electronics.

The following measurements have been performed by collaborating groups:
Solid-state NMR measurements were performed by Dr. Swapna Ganapathy in the group of Prof. Dr. Huub J. M. de Groot at University of Leiden. X-ray diffraction data were obtained by Dr. Ute Baumeister at Universität Halle. Charge carrier mobility measurements and theoretical study on optical properties were performed by Dr. Sameer Patwardhan in the group of Prof. Dr. Laurens D. A. Siebbeles at Technical University of Delft. Conductive AFM measurement was performed by Dr. Daniel Ebeling in the group of Prof. Dr. Lifeng Chi at Universität Münster.

3.1. Introduction

Biosupramolecular materials possessing intriguing electronic properties have attracted considerable interest in the past years.[1-4] Complex superstructures have been designed using construction principles or building blocks from nature with the expectation that architectural complexity would commensurate with functional sophistication given in biological systems.[2,3,4] Nanostructures with specific shapes, dimensions and desirable surface properties prepared from biological or biomimetic building blocks could in principle emulate some of the architectural features prevalent in natural supramolecular systems. Their environment adaptation can be compared to biological systems such as proteins and membranes, and therefore could bridge the gap between synthetic polymers on one hand and biological structures on the other hand.[5] In addition, it is possible to control the structure and function of these supramolecular architectures by altering environmental conditions such as temperature, solvent and concentration, features not accessible with classical covalent polymers and small molecules.[4,5]

Naturally occurring architectures such as secondary and tertiary structure of proteins, cyclic chlorophyll arrays in light-harvesting (LH) complexes, and the π-stacked structure of DNA often provide inspiration for rational design of motifs promising for biosupramolecular electronics. Nevertheless, when considering the size and well-defined superstructures of biological systems, fully artificial systems featuring equal complexity are scarce.[1,2] DNA is an excellent natural archetype for charge carrier transport in one-dimensional polymers, and indeed direct electrical transport measurements through DNA single polymers, bundles and networks have been reported extensively.[1b,2]

The increased knowledge of intermolecular non-covalent interactions has culminated in an impressive control over molecular self-assembly and consequently on their applications. Representative examples of self-organizing organic materials relevant for (opto)electronic applications are discotic liquid crystals (DLCs) based on triphenylenes,[6] hexabenzocoronenes (HBCs),[7] porphyrins,[8] and phthalocyanines[9] as well as unconventional self-assembled architectures based on dendrons.[10] One of the key parameters that determines the performance of organic materials in (opto)electronic devices such as organic solar cells, light emitting diodes and thin fim transistors is their intrinsic charge carrier mobility. It is well established that the mobility of charge carriers is intimately related to the supramolecular organization[11] of these materials.[12,13,14,15] Hence combination of efficient self-assembly of biomolecules or

biomimetic building blocks and high charge carrier mobilities of their assemblies are prerequisites for biosupramolecular electronics. In the pioneering work of Aida and co-workers, amphiphilic HBCs functionalized with variety of substituents that self-assemble into nanotubes and possessing excellent electronic properties have been reported.[16a-c] Dendrimer-appended porphyrins and phthalocyanines have also been investigated as bioinspired functional materials for charge and energy transport.[16d,e] However, supramolecular electronics based on true biomolecules are relatively scarce.[1,2]

As discussed in Chapter 2, the chlorosomal antennae[17,18] of green sulphur and non-sulphur bacteria are fascinating examples of biosupramolecular dye assemblies that are constructed from ~ 250,000 bacteriochlorophyll (BChl) *c*, *d*, or *e* pigments,[19] where non-covalent interactions hold the pigments in proper geometrical arrangement without the stabilization by protein networks.[20] The non-covalent interactions, namely, the central metal-3^1-OH coordination, π-π overlap between tetrapyrroles, and 3^1-OH-13^1C=O hydrogen bonding, bind the stacks together into tubular architectures and provide exciton delocalization pathway. These antenna systems are responsible for capturing and transporting light energy with quantum efficiencies close to unity.[21,22] Although the exciton transport properties of chlorosomal assemblies have been confirmed,[23] and the redox properties of the constituent BChls suggest that charge carrier transport should be possible, reports on such studies are rather scarce.[24]

To derive a better understanding of chlorosomal LH systems, Tamiaki et al. developed a model zinc chlorin (ZnChl) compound which is a BChl *d* analogue that forms extended dye aggregates and replicates the aggregation behavior of BChl *c* in non-polar solvents.[25] As discussed in the introductory Chapter 2 (State of Knowledge, section 2.7), it has been demonstrated that self-assembly process of BChl *c*, *d*, and *e* into tubular architectures can be mimicked by using semisynthetic ZnChls that are pre-programmed for tubular mode of self-assembly,[26,27] i.e., possessing 3^1-OH group, a central metal ion, and 13^1 C=O moieties along the Q_y axis, and containing at least 2 or more extended alkyl chains **1**-OH (Figure 1) or other chromophores.[28,29] On the other hand, if the 3^1-hydroxy group is substituted by a 3^1-methoxy functionality in ZnChl **1**-OMe (Figure 1), self-assembly into ordered one-dimensional (1D) π-stacks (Figure 2) on conductive and atomically flat highly oriented pyrolytic graphite (HOPG) surface was revealed by atomic force microscopy (AFM) and scanning tunneling microscopy (STM) studies.[30]

Detailed optical spectroscopy (UV/Vis, CD) and scanning probe microscopy (i.e., AFM and STM) have already provided convincing evidence for the formation of extended rod-like aggregates for 3^1-hydroxy and stacks for 3^1-methoxy ZnChls with distinct spectral differences in solution and surface organization patterns as discussed in Chapter 2.

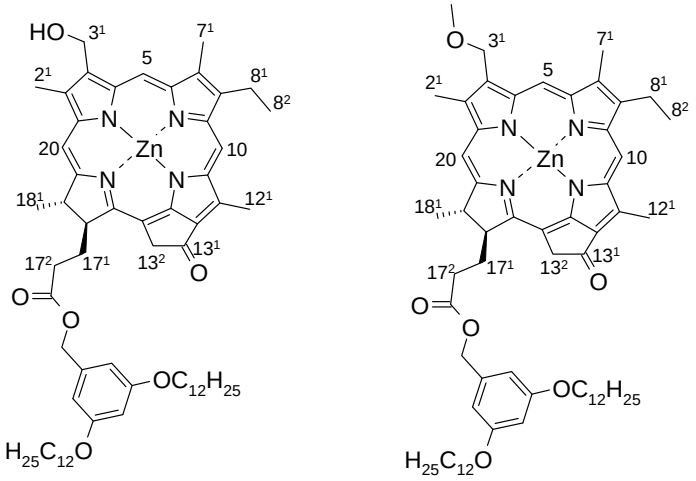

1-OH **1**-OMe

Figure 1. Chemical structures of 3^1-hydroxy and 3^1-methoxy zinc chlorins (ZnChls) **1**-OH and **1**-OMe.

However, clear microscopic evidence has not been obtained for tubular assemblies of 3^1-hydroxy ZnChls to date. In order to provide insights into aggregation mode, aggregation studies in solution have been performed by UV/Vis, CD and dynamic light scattering (DLS). The aggregate morphology of 3^1-hydroxy zinc chlorins has been intensively investigated by electron microscopic techniques. For the first time, detailed EM studies such as transmission electron microscopy (TEM) and scanning transmission electron microscopy (STEM) provided unequivocal evidence for tubular aggregates of 3^1-hydroxy ZnChls.

A detailed understanding of the short- and long-range packing behavior of these dyes in solution and more importantly in solid-state is of high importance considering the potential utility of such closely spaced 1D π-stacks and layered assemblies for supramolecular electronics. Suitable single crystals for a complete X-ray crystal structure analysis are currently not available for these microcrystalline materials because of size inhomogenities. This led us to explore the utilization of solid-state magic angle spinning (MAS) NMR in combination with powder X-ray diffraction (XRD), solution NMR, molecular modelling, and DFT calculations to provide precise information about the three-dimensional (3D) packing of these chromophores in the bulk solid state.

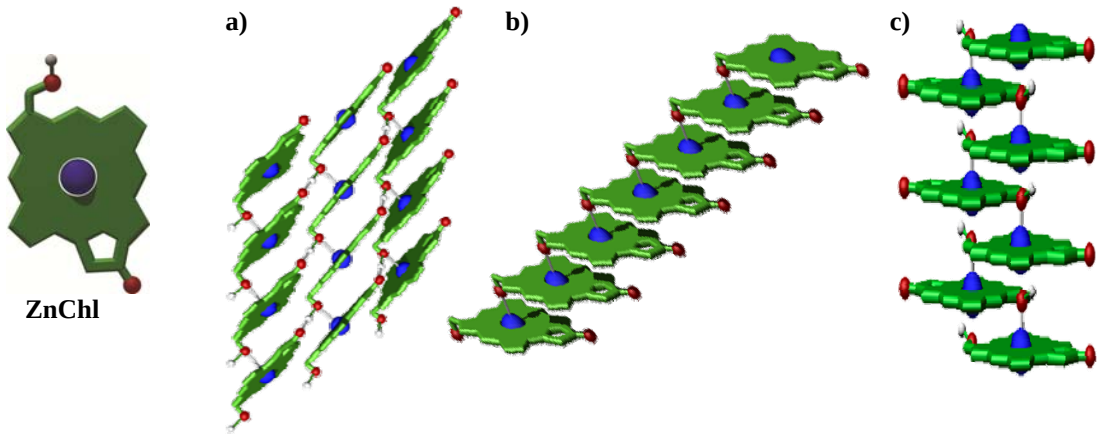

Figure 2. Schematic representation of proposed structural models for zinc chlorins: a) section of a rod/tube aggregate (3^1-OH ZnChls) and b, c) stack aggregate (3^1-OMe ZnChls) derived from spectroscopic and microscopic investigations; a) representation of intermolecular interactions: π-π stacking, zinc-oxygen coordination (indicated by grey lines) and interstack hydrogen bonding (indicated by green lines); b) parallel stack model and c) antiparallel monomer stack model indicating the intermolecular interactions, namely π-π stacking, zinc-oxygen coordination applicable for 3^1-OMe ZnChls.

The goal of this chapter is to establish the detailed packing behavior of aggregates of 3^1-hydroxy ZnChls (tubular assemblies)[26,27] and 3^1-methoxy ZnChls (stack assemblies)[30] in solution and in solid state and the investigation of their charge transport and conducting properties in order to explore the suitability of these assemblies for biosupramolecular electronics. Towards this goal, charge transport properties of aggregates of 3^1-hydroxy and 3^1-methoxy ZnChls in solid state have been investigated by an electrodeless technique, pulse radiolysis-time resolved microwave conductivity (PR-TRMC) experiments.[31,32] Efficient charge transport has been observed in these aggregates in solid state and the observed differences in charge transport properties for these two types of ZnChls are rationalized in terms of very distinct structural motifs of their self-assemblies, i.e. tubular for 3^1-OH and stacked for 3^1-OMe functionalized ZnChls. For the aggregates of 3^1-OH ZnChls, charge carrier mobilities upto 0.07 cm^2/Vs have been observed while the aggregates of corresponding 3^1-OMe ZnChls exhibit very high charge carrier mobilities of 0.28 cm^2/Vs, the latter being the highest value known to date for chlorophyll derivatives.

3.2. Results and Discussions

3.2.1. Synthesis and sample preparation

ZnChls **1**-**3**-OH were synthesized starting from Chl *a*, which was extracted from cyanobacteria *Spirulina platensis*[33,34] according to the synthetic route outlined in Scheme 1. Chl *a* was converted into pheophorbide *a* (pheo *a*) according to literature procedure.[27] Subsequently, the 3^1-vinyl group was transformed into corresponding diol with osmium tetroxide, followed by oxidative cleavage by sodium periodate to afford the respective formyl derivative and the latter was further hydrolyzed with conc. hydrochloric acid (HCl) that afforded the corresponding chlorin carboxylic acid. This was followed by its esterification with the respective dodecyloxybenzyl alcohols and with tetraethyleneoxybenzyl alcohols in the presence of coupling reagent dicyclohexylcarbodiimide (DCC), 4-dimethylaminopyridine (DMAP), 4-(dimethylamino)pyridinium-*p*-toluenesulfonate (DPTS) and *N*-ethyldiisopropyl-amine in dry dichloromethane as solvent,[27] afforded the corresponding esters with yields of 51-76%.[27] Selective reduction of the formyl groups into alcohols were carried out with borane-*tert*-butylamine complex with a yield of 68-73%. Finally, the metalation step with methanolic zinc acetate in tetrahydrofuran (THF) afforded the ZnChls **1**, **2**, **3**-OH as turquoise green solids with 73-75% yields.[27] The intermediates and final products were purified by silica gel column chromatography, and subsequently by high performance liquid chromatography (HPLC) separation and characterized by ^{1}H NMR spectroscopy, MALDI-TOF mass spectra and/or high resolution mass spectrometry (HRMS).

A slightly different synthetic route was employed for the methoxy ZnChls **1**, **2**-OMe. The pheo *a* was transformed into 3^1-methoxypheo *a* according to the literature method.[30] The acidic hydrolysis of 3^1-methoxypheo *a* with concentrated HCl and subsequent esterification of the 3^1-methoxy chlorin carboxylic acid with the respective alcohols afforded the free base esterified products with yields of 68-73%. The final metalation of the free base compounds with $Zn(OAc)_2$ in methanol yielded the target building block ZnChls **1**, **2**-OMe with yields of 61-68%. The intermediate compounds and the final zinc chlorins were purified by silica gel column chromatography and subsequently by reverse-phase HPLC, and were characterized by ^{1}H NMR, MALDI-TOF mass spectra and/or HRMS.

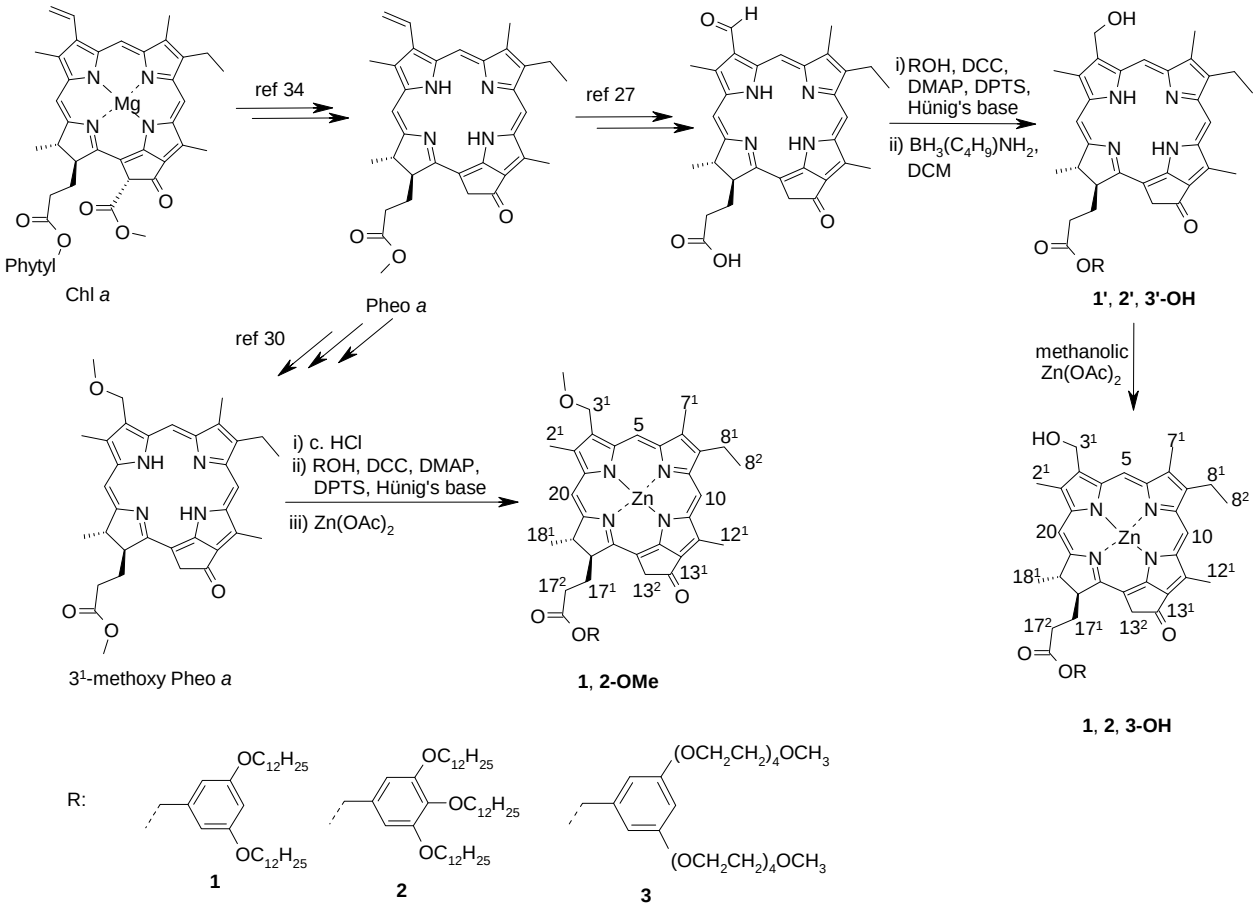

Scheme 1. Synthetic scheme for 3^1-hydroxy ZnChls and 3^1-methoxy functionalized ZnChls **1**-**3**-OH and **1**-, **2**-OMe studied in this chapter.

To prepare samples for solid-state MAS NMR measurements and PR-TRMC measurements, the HPLC purified ZnChl derivatives were dissolved in a minimum amount of THF or dichloromethane (~ 1 equiv.) and ~ 10 equiv. of *n*-hexane was added to each to prepare the aggregates in solution. The solvent was partially removed under vacuum with a rotary evaporator, and the solutions were frozen and lyophilized for ~ 1-2 days to transform the aggregates into free-flowing powders. These aggregated samples were used subsequently for solid-state MAS NMR and PR-TRMC measurements.

The solution aggregation behavior of these ZnChls **1**-OH/**1**-OMe have been discussed in detail in Chapter 2.[26,27,30] Like BChl *c* assemblies in chlorosomes for which a tubular structure has been proposed,[26,27] 3^1-hydroxy zinc chlorins **1**-OH and **2**-OH showed similar spectral characteristics with their Q_y-band bathochromically shifted from 648 nm in THF (monomers) to 741 nm in *n*-heptane or *n*-hexane containing 0.5% v/v of THF as a result of J-type excitonic

coupling.[27] On the other hand, the absorption spectra of ZnChl **1**-OMe in cyclohexane/*n*-hexane (1:1)[30] revealed a less pronounced bathochromic shift of the Q_y-band from 646 nm (monomers) to 727 nm (aggregates) compared to that of **1**-OH upon self-assembly indicating that the aggregate structures of 3^1-methoxy and 3^1-hydroxy ZnChls are distinct.

3.2.2. Solution aggregation of 3^1-hydroxy and 3^1-methoxy zinc chlorins in solution

For the construction of complex self-assembled structures, it is crucial to unravel the self-assembly pathway of aggregate formation.[35,36,37] The application of spectroscopy in combination with scattering and microscopic techniques often provides a reasonable way of explaining the self-assembly mechanism pathways. The thermodynamics of linear supramolecular polymerization can be either isodesmic or cooperative/anti-cooperative.

Isodesmic (i.e., equal association constant for all step) self-assembly[38,39] has been reported for quasi one-dimensional self-assembly of organic molecules and is indeed operative in many supramolecular polymers.[40,41,42] On the other hand, cooperative self-assembly has been described by a modified isodesmic model in which all, but the first association constants are assumed to be equal. This model has its limitation since it assumes that only the first non-covalent assembly step is different from all the other steps. In biological systems however, cooperative self-assembly of proteins has been described by a nucleation-growth model, which is characterized by the unfavorable formation of nuclei of a critical size immediately succeeded by a favorable elongation process which leads to stable self-assembled structure. In the isodesmic model, the Gibbs free energy (ΔG) of monomer addition is independent of the degree of polymerization, whereas in the cooperative[35,36] or anti-cooperative polymerization models, the ΔG of monomer addition will increase or decrease following the formation of an oligomeric nucleus, respectively.

Self-assembly of 3^1-hydroxy zinc chlorins (rod aggregates)

Temperature-dependent UV/Vis and CD were performed to characterize the reversibility of self-assembly behavior of ZnChl **1**-OH as discussed in Chapter 2. For this purpose, ZnChls were dissolved in di-*n*-butyl ether in a UV/Vis cuvette followed by the

addition of the nonpolar solvent *n*-heptane (di-*n*-butyl ether: *n*-heptane 1:4) and the temperature was adjusted to 15 °C by a Peltier element. Prior to each measurement, the solutions were allowed to equilibrate for 1.5 h at the measuring temperature to ensure a stationary state. With increasing temperature the Q_y band of the aggregates at 741-742 nm decreases and the monomer band at 648 nm increases. These spectral changes reveal that the aggregates dissociate at higher temperature into monomers. Upon cooling to the initial temperature of 15 °C, the Q_y band was completely recovered, which is indicative of the reversibility of the aggregation process (Figure 3a). Curve fitting to the Boltzmann function led to a sigmoidal behavior which is indicative of an isodesmic mechanism of aggregation (Figure 3b). To fit the *T*-dependent absorption, the data were normalized to obtain the degree of aggregation, α, and fitted to the isodesmic model, in which α is approximated by equation 1. In this equation, T_m is the melting temperature defined as the temperature for which $\alpha = 0.5$, ΔH is the molar enthalpy release related to the formation of non-covalent intermolecular interactions and *R* is the gas constant.

$$\alpha(T) \cong \frac{1}{1+\exp\left(-0.908\Delta H\frac{T-Tm}{RTm^2}\right)} \tag{1}$$

The mole fraction of the aggregated species $\alpha_{agg}(T)$ at each temperature was estimated according to equation 2

$$\alpha(T) = \frac{\varepsilon(T)-\varepsilon_{max}}{\varepsilon_{agg}-\varepsilon_{max}} \tag{2}$$

with $\alpha_{agg}(T)$ being the mole fraction of aggregated molecules at each temperature, and $\varepsilon(T)$, ε_{agg}, and ε_{mon} being the apparent absorption coefficients of the aggregate at temperature T, the absorption coefficient of the aggregate, and the monomer, respectively. The absorption coefficients of pure monomer ε_{mon} and aggregate ε_{agg} were determined by extrapolation of the measured apparent absorption coefficients to their asymptotic values at high and low temperatures. Inserting the degree of aggregation into equation 3 yields the average stack length, DP_N, as well as the equilibrium constant at the temperature of measurement, $K(T)$.

$$DP_N = \frac{1}{\sqrt{1-\alpha(T)}} = \frac{1}{2}+\frac{1}{2}\sqrt{4K(T)c_T+1} \tag{3}$$

The gradual stack growth with decreasing temperature is characteristic of isodesmic assembly (Tables 1, 2). Higher *K* values imply that higher DP_N values are obtained at lower

temperature, e.g. at 288 K (Figure 3c, e). The average K_e value at 288 K is 5.3×10^6 M^{-1} (and values of 5.7×10^6 M^{-1} at 448 nm and 4.8×10^6 M^{-1} at 741 nm) is determined by *T*-dependent UV/Vis spectroscopy by monitoring the aggregate bands at 448 nm and 741 nm. Also, by plotting the logarithm of K_a versus the reciprocal temperature (Van't Hoff plot, Figure 3d, f), ΔH values of -49.4 kJmol^{-1} and -52.3 kJmol^{-1} (average value of 50.9 kJmol^{-1}) and ΔS values of -0.0446 kJ mol^{-1} K^{-1} and -0.0528 kJ mol^{-1} K^{-1} (average value of -0.0487 kJ mol^{-1} K^{-1}) were obtained by monitoring the aggregate bands at 741 nm and 448 nm respectively.

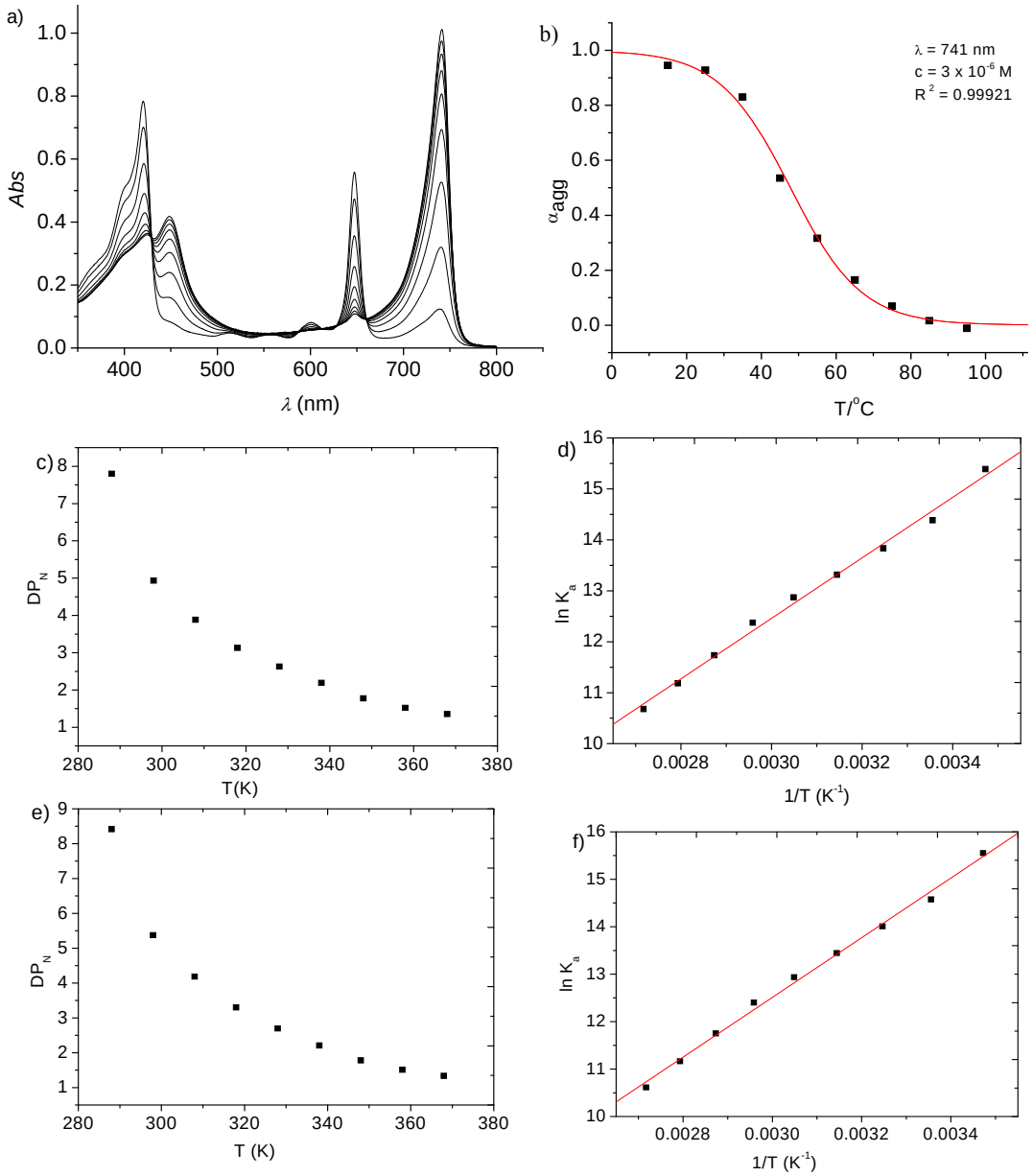

Figure 3. a) Temperature dependent UV/Vis absorption spectra of **1**-OH in dibutylether/*n*-heptane (3×10^{-6} M); b) corresponding α vs *T* plot at aggregate band at 741 nm; c) DP_N vs *T*; d) ln *K* vs 1/*T* (Vant Hoff's plot) at 741 nm and e) DP_N vs *T* and f) ln *K* vs 1/*T* (Vant Hoff's plot) at aggregate band at 448 nm for aggregates of ZnChl **1**-OH.

These results indicate that self-assembly is enthalphically driven process and entropically disfavored. Gibbs free binding energy is -37.1 kJ/mol and -36.5 kJ/mol at 448 nm and 741 nm respectively. Decrease in DP_N values with increasing temperature is also indicative of isodesmic self-assembly.

Table 1. Thermodynamic parameters K_a (M^{-1}), DP_N, ΔG obtained from monitoring the aggregate band at 448 nm from temperature-dependent self-assembly of ZnChl **1**-OH (c = 3.1 × 10^{-6} M, dibutylether/*n*-heptane = 1:4 vol %) based on the isodesmic model.

T (K)	DP_N	K_a ($Lmol^{-1}$)	$1/T$ (1/K)	ln K_a
288	8.4	5.7×10^6	0.00347	15.6
298	5.4	2.1×10^6	0.00336	14.6
308	4.2	1.2×10^6	0.00325	14.1
318	3.3	6.9×10^5	0.00314	13.5
328	2.7	4.2×10^5	0.00305	12.9
338	2.2	2.4×10^5	0.00296	12.5
348	1.8	1.3×10^5	0.00287	11.8
358	1.5	7.0×10^4	0.00279	11.2
368	1.3	4.1×10^4	0.00272	10.6

Table 2. Thermodynamic parameters K_a (M^{-1}), DP_N, ΔG obtained from monitoring the aggregate band at 741 nm from temperature-dependent self-assembly of ZnChl **1**-OH (c = 3.1 × 10^{-6} M, dibutylether/*n*-heptane = 1:4 vol %) based on the isodesmic model.

T (K)	DP_N	K_a ($Lmol^{-1}$)	$1/T$ (1/K)	ln K_a
288	7.8	4.8×10^6	0.00347	15.4
298	4.9	1.7×10^6	0.00336	14.4
308	3.9	1.0×10^6	0.00325	13.8
318	3.1	6.1×10^5	0.00314	13.3
328	2.6	3.9×10^5	0.00305	12.9
338	2.2	2.3×10^5	0.00296	12.4
348	1.8	1.3×10^5	0.00287	11.7
358	1.5	7.2×10^4	0.00279	11.2
368	1.4	4.3×10^4	0.00272	10.7

To substantiate the formation of extended assemblies of ZnChl **1**-OH in deuterated *n*-hexane/THF (1%), diffusion ordered spectroscopy (DOSY) NMR measurements were performed. However, extremely broad ^{1}H NMR signals were obtained for these aggregates thereby preventing structural elucidation by NMR.

Self-assembly of 3[1]-methoxy zinc chlorins (stack aggregates):

To study the self-assembly mechanism of ZnChl **1**-OMe, temperature-dependent UV/Vis measurements in cyclohexane/*n*-hexane (1:1) were performed (Figure 4a) between 282 K and 305 K. The Q_y absorption band of ZnChl **1**-OMe is shifted bathochromically to 727 nm in cyclohexane/*n*-hexane (1:1), which reversibly disappears at higher temperature.[30] The melting curves are non-sigmoidal and non-linear curve fitting of degree of aggregation with Boltzmann function at multiple aggregate wavelengths of the temperature-dependent UV/Vis spectra showed non-sigmoidal behavior (Figure 4b) and thus can not be explained by isodesmic model. Hence, a cooperative nucleation-elongation pathway might be operable.

Meijer and co-workers have delineated the nucleation-elongation-cooperative aggregation process by thermodynamical considerations. They used a modified nucleation-growth model, originally developed by Oosawa and Kasai, to describe the cooperative self-assembly of organic π-conjugated molecules into 1D helical fibers.[43] In this model,[35] a highly active state is in equilibrium with a weakly active state of supramolecular polymer formation. For thermodynamic isodesmic model of supramolecular polymerization, a sigmoidal relationship between the degree of aggregation and temperature is observed, whereas in a nucleated cooperative helical growth model, a non-sigmoidal relationship between the degree of aggregation and temperature is observed. Only in the active state, a supramolecular polymer elongates to form long, one-dimensional objects. In the inactive state the molecules first need to undergo activation (i.e. nucleation) and the equilibrium constant for this activation process from the inactive to the activated state is given by K_a and during elongation every step is governed by a dimensionless equilibrium constant K_e. The temperature at which activation occurs is defined as the elongation temperature, T_e, and at temperatures higher than T_e, the system is in the nucleation regime, whereas for temperatures below T_e, the system is in the elongation regime.

The relevant thermodynamic data can be obtained by fitting the degree of aggregation ϕ_n with the equation for the elongation domain according to Meijer to equation 4, where h_e is the molar enthalpy for self-assembly, and T_e is the temperature at which elongation process sets in and R is the gas constant. For the cooperative helical growth model, T_e can be viewed as the temperature at which a complete turn of a helix is formed. First the degree of

aggregation obtained from UV/Vis spectra in the elongation regime ($T < T_e$) is modeled, using equation 4.

$$\phi_n = \phi_{SAT}\left(1-\exp\left[\frac{-h_e}{RT_e^{\,2}}(T-T_e)\right]\right) \tag{4}$$

Above equation contains three parameters (P1, P2, P3), namely, the parameter ϕ_{SAT} (P1), which is introduced to ensure that the parameter $\phi_n/\phi_{SAT,}$ does not exceed unity following the constraint that the degree of aggregation ϕ_n cannot exceed unity, the molecular enthalpy release due to non-covalent interactions during elongation, h_e (P2) and the elongation temperature T_e (P3). At temperatures above the elongation temperature T_e i.e., in the nucleation regime, the fraction of aggregated molecules is described by equation 5.

$$\phi_n = K_a^{\,1/3}\exp\left[\left(2/3K_a^{\,-1/3}-1\right)\frac{h_e}{RT_e^{\,2}}(T-T_e)\right] \tag{5}$$

where, the only unknown parameter is the K_a value, which can be obtained by fitting the experimentally found degree of aggregation for temperatures above T_e. The K_a value obtained from equation 5 can then be substituted in equation 6 or its simplified form in equation 7 to obtain the average size of the stacks at all the temperatures. The temperature-dependence of the number-averaged degree of polymerization, $<N_n>$ is thus given by equations 6 and 7.

$$\langle N_n\rangle = \frac{1}{\sqrt{K_a}}\sqrt{\frac{1-\exp\left(\frac{-h_e}{RT_e^2}(T-T_e)\right)}{\exp\left(\frac{-h_e}{RT_e^2}(T-T_e)\right)}} \tag{6}$$

or, $$\langle N_n\rangle = \frac{1}{\sqrt{K_a}}\sqrt{\frac{\phi_n}{1-\phi_n}} \tag{7}$$

At the elongation temperature, the length of the stack averaged over the nucleated species, $\langle N_n(T_e)\rangle$ is given by equation 8.

$$\langle N_n(T_e)\rangle = \frac{1}{K_a^{\,1/3}} \tag{8}$$

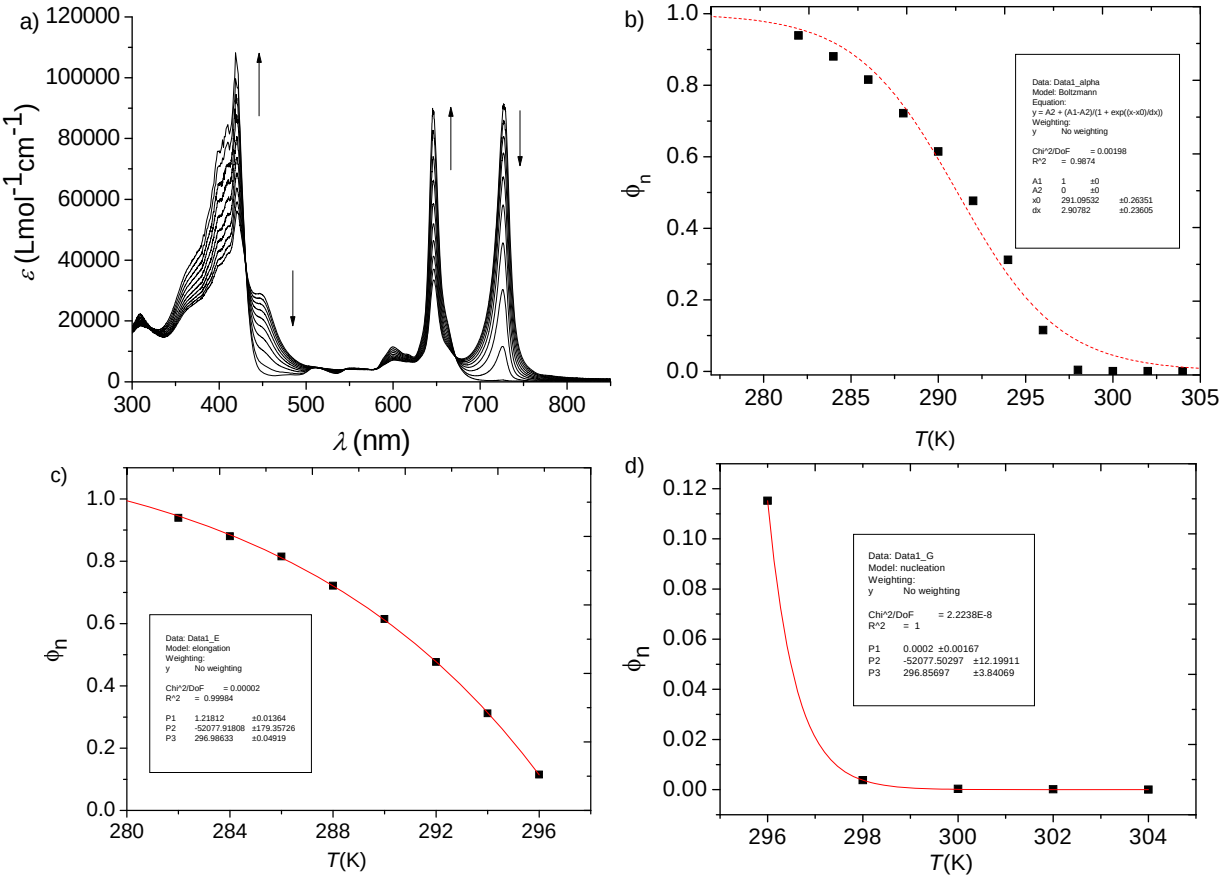

Figure 4. a) Temperature-dependent UV/Vis spectra of **1**-OMe in cyclohexane/*n*-hexane (1:1) ($c = 2 \times 10^{-5}$ M); b) degree of aggregation ϕ_n vs T plot at 727 nm (red dashed line shows the Boltzmann distribution function) showing a non-sigmoidal behavior of aggregation of **1**-OMe; c) Fitting of the experimental ϕ_n with temperature upto the elongation temperature (~ 297 K) with thermodynamic elongation equation 4 of Meijer model; fit parameters P1: ϕ_{SAT}, P2: enthalpy release of self-assembly (h_e), P3: elongation temperature (T_e); d) Fitting of degree of aggregation ϕ_n at temperatures higher than T_e with nucleation equation 5 of Meijer model, fit parameters P1: nucleation constant (K_a), P2: enthalpy release of self-assembly (h_e), P3: elongation temperature (T_e).

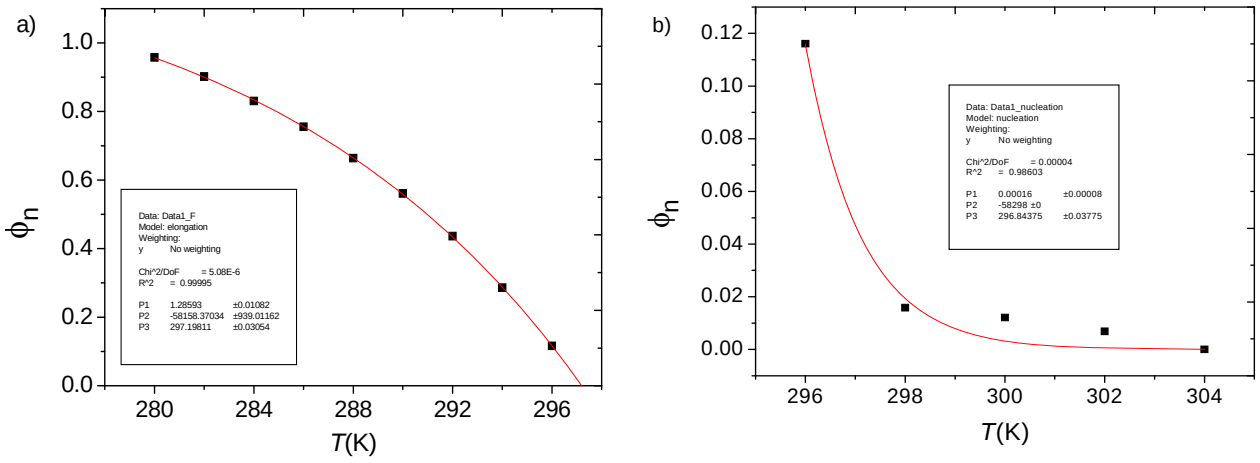

Figure 5. a) Non-linear fitting of degree of aggregation i.e., ϕ_n with temperature at 719 nm upto the elongation temperature (~ 297.7 K) with thermodynamic elongation equation of Meijer model; Parameters P1: ϕ_{SAT}, P2: enthalpy release of self-assembly (h_e), P3: elongation temperature (T_e); b) Fitting of ϕ_n at temperatures higher than elongation temperature with nucleation equation of the Meijer model, fit parameters P1: nucleation constant (K_a), P2: enthalpy release of self-assembly (h_e), P3: elongation temperature (T_e).

The thermodynamic nucleation growth model based on temperature-dependent UV/Vis studies thus provide information on the enthalpy release during self-assembly, elongation temperature, stack length at the elongation temperature and the temperature-dependence of stack growth. It is important to note that a high degree of cooperativity is expressed in a small K_a value and leads to a larger nucleus before elongation starts.

From the fits to elongation and nucleation equations (Figures 4c, d and 5), two temperature regimes could be distinguished: the nucleation and the elongation regime, which are separated by the elongation temperature. Normalizing the temperature-dependent UV/Vis absorption data allowed to model the elongation regime of the self-assembly process (Figure 4c, 5a). An enthalpy value h_e, of -73 kJ mol^{-1} (at aggregate wavelength of 727 nm), -89 kJ mol^{-1} (at 719 nm) and -43 kJ mol^{-1} (at 448 nm) were obtained, indicating that self-assembly is an enthalpically driven process. The average elongation temperature (T_e) at these aggregate wavelengths was 297.7 K. On the basis of fits to the nucleation equation (Figure 4d, 5b) at wavelengths of 727 nm and 719 nm, ZnChl **1**-OMe is found to self-assemble in a highly cooperative fashion with K_a values of 1.6×10^{-4} and 2×10^{-4}. Using equation 7, the average stack length at 282 K is 311, and using equation 8, stack length obtained at nucleation temperature is 17 and 18.4 for these two K_a values. This indicates that the nucleating species is much larger than a dimeric unit. The temperature-dependent stack lengths evaluated for nucleation constants K_a of 1.6×10^{-4} and 2×10^{-4} are presented in Table 3. It is to be noted from the fits (Figures 4d, 5b) that the stacks lengths rapidly decrease at temperatures higher than the elongation temperature of~ 297 K.

Table 3. Temperature-dependence of stack lengths at two different nucleation constants K_a values obtained from the fit to Nucleation equation.

Temperature (K)	$<N_n>$ (for $K_a = 1.6 \times 10^{-4}$)	$<N_n>$ (for $K_a = 2 \times 10^{-4}$)
282	311	275.6
284	214.7	190.3
286	166.2	147.3
288	127.3	112.8
290	99.8	88.5
292	75.5	66.9
294	53.2	47.1
296	28.5	25.2

Figure 6a shows the CD spectra of **1**-OMe measured at temperatures of 280 K to 302 K. To ensure that self-assembly was under thermodynamic control, a slow cooling rate of 2 ^{o}C/hour was applied. Temperature-dependent CD measurements revealed intense CD signals at 713 nm (+), 733 nm (-) and 747 nm (+) that decreased upon increasing temperature. Such appearance of a pronounced CD signal is directly related to the formation of helical ordered one-dimensional aggregates. When molar ellipticity at these three wavelengths (713 nm, 733 nm, 747 nm) is plotted with temperature, the melting curves obtained are non-sigmoidal and reveal a highly cooperative self-assembly process. Furthermore, a steep rise in the molar ellipticity value occurs at elongation temperature at which the rapid growth of the π-stacks starts (Figure 6b). Using equation 4, the elongation regime of the normalized molar ellipticity data (i.e., for temperatures below T_e) could be fitted accurately with the elongation equation and the enthalpy values, h_e of -94.3 kJ/mol, 170.9 kJ/mol and -197 kJ/mol were obtained at 713 nm, 733 nm and 747 nm, respectively (Table 4). No deviations in the data from the model were observed at low temperatures, indicating that over the whole temperature range only linear, one-dimensional growth of stacks takes place. A very sharp transition in the molar ellipticity around elongation temperature T_e (~ 290.2 K) was observed, indicative of a high degree of cooperativity in the self-assembly process. However, data points at temperatures above the elongation temperature could not be fitted satisfactorily to the nucleation equation 5 because of the fluctuations in data points and the nucleation constant K_a was not obtainable from the CD measurements.

The elongation temperature T_e of ~ 297 K determined from the UV/Vis data corresponds well with that obtained from the CD data (~ 290 K), revealing that both CD and UV/Vis spectroscopy are probing the same helical cooperative self-assembly process of **1**-OMe into helical 1D stacks. However, an intermediate non-helical state or nucleating species could not be observed. It should be noted that the T_e values of ~ 297.7 K and ~ 290.2 K obtained from UV/Vis and CD respectively, are relatively similar while the enthalpy values h_e obtained from fitting the molar ellipticity of CD spectra with elongation equation are much larger compared to those in UV/Vis at least at two different wavelengths. For ZnChl **1**-OMe, the onset in the degree of aggregation, ϕ_n, around T_e, is more gradual in UV/Vis compared to that observed in CD. This effect can be attributed to the fact that CD spectroscopy is highly sensitive to stack growth and length unlike UV/Vis hence sharp change in the stack length around the nucleation-elongation transition regime is reflected in much higher enthalpy values

obtained by curve-fitting of the CD spectra. Consequently, the sharp changes at the elongation temperature led to a large fluctuation in the data points in the nucleation regime and hence could not be fitted with satisfactory accuracy to the nucleation equation.

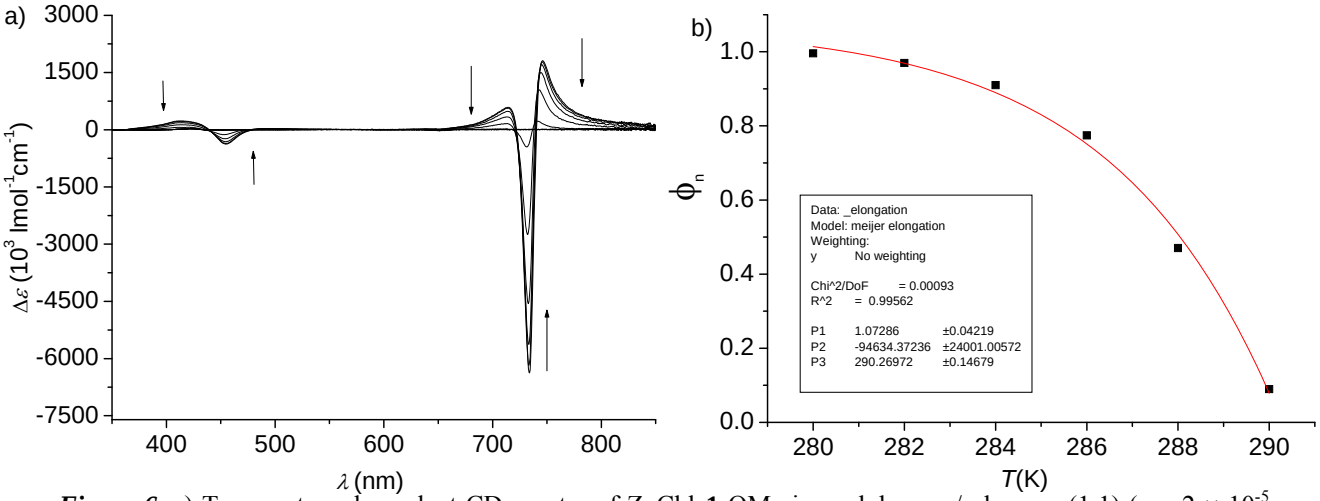

Figure 6. a) Temperature-dependent CD spectra of ZnChl **1**-OMe in cyclohexane/*n*-hexane (1:1) ($c = 2 \times 10^{-5}$ M); b) Fitting of degree of aggregation ϕ_n with temperature upto the elongation temperature (~ 290.2 K) at 713 nm with thermodynamic elongation equation of Meijer model; Parameters P1: ϕ_{SAT}, P2: enthalpy release, P3: elongation temperature. Fitting of the experimental data points at temperatures higher than elongation temperature with nucleation equation of the Meijer model did not lead to a satisfactory fit.

Table 4. Fit values for thermodynamic parameters, enthalpy h_e and elongation temperature T_e obtained from the curve fitting of UV/Vis and CD spectra with elongation equation for 3^1-methoxy ZnChl **1**-OMe.

Absorption maxima (nm)	h_e (kJ/mol)	T_e (K)
719 (UV)	-89.575	297.16
728 (UV)	-73.221	297.01
448 (UV)	-43.428	299.06
713 (CD(+))	-94.634	290.10
733 (CD(-))	-170.964	290.19
747 (CD(+))	-197.005	290.23

Meijer and co-workers have described self-assembly mechanism of C3-symmetrical trialkylbenzene-1,3,5-tricarboxamides,[36] oligo(p-phenylene vinylene) (OPV) derivatives functionalized with chiral side chains capped on one end by a tridodecyloxybenzene and on the other by a ureidotriazine tailored for self-complementary fourfold hydrogen bonding,[43] and OPV substituted hexaarylbenzene derivatives [44] into 1D aggregates using the thermodynamic nucleation-elongation model. These OPV derivatives and trialkylbenzene-1,3,5-tricarboxamide derivatives[36] self-assemble into 1D right-handed chiral superstructures in apolar solvents via a highly cooperative pathway. Indeed, for all these systems, very small

values of K_a (~10^{-4}-10^{-6}) have been obtained. For trialkylbenzenetriamides,[36] K_a values of ~ 4.2-0.6 × 10^{-5} were obtained and average stack lengths of ~ 500-5000 were obtained. For OPVs,[43,44] K_a values of 2.0-0.15 ×10^{-4} were obtained. Moreover, self-assembly in all these systems is found to be enthalpy driven. Notably, using this model, the K_e values have not been reported for these systems.

Theoretical studies on optical properties of stack assemblies of 1-OMe[a]: The optical properties of the π-stacks of ZnChl **1**-OMe have been studied theoretically using an exciton theory description and the relationship of optical properties to supramolecular organization was established.[45] The exciton coupling between ZnChls was calculated using a transition density formalism, making it possible to distinguish stereochemical differences that arise from facial orientations of chiral ZnChls in the aggregate. The presence of intense features in CD spectra generally indicates an ordered structure in which the transition dipoles have a single-handed helical orientation. It is shown that the inherent chirality of ZnChls and their precise stereochemical orientation is important to correctly interpret the experimental CD spectra. The effect of increasing temperature is to break the excitonically coupled aggregated chromophores into smaller aggregates, and eventually into isolated chromophores. As a result, the intensity of both absorption and CD spectra reduces upon increasing temperature. Interestingly, the shape and position of CD signal do not change with temperature, which indicates that the spectral shift and shape are not sensitive to size of the aggregates or the supramolecular structure but rather depend on the primary structure that consists of presumably coordinated stack of zinc chlorins. In Chapter 2, it has been discussed that extended π-stacks of **1**-OMe are probably formed by zinc-oxygen coordination as indicated by the "edge-on" Phase I (analogous to antiparallel model) and Phase II (analogous to parallel model) stacking patterns on HOPG surface. In section 3.2.5, detailed solid state NMR studies will be discussed which indeed revealed that self-assembly of **1**-OMe is driven primarily by zinc-oxygen coordination, with the antiparallel stacking mode being the preferable arrangement. Thus, for the theoretical modelling of CD spectra, antiparallel arrangement of molecules in the stacks is considered. The non-planar chlorin macrocycle posseses asymmetric centres at C17, C18 positions and the metal centre of chlorin is an additional stereocentre that can adopt two diastereotopic configurations, namely α and β, depending

[a]This section is written based on the results from reference 45 and the theoretical study has been performed by Dr. Sameer Patwardhan in the group of Prof. Dr. L. D. A. Siebbeles at the Technical University of Delft.

upon its ligation from the opposite and same side of the 17-propionic ester group, respectively. Considering two distinct π-faces of chlorins, namely, α and β face, four different combinations of facial dimers that can lead to extended stacks are possible. The helical conformations required for calculation of CD spectra were generated by considering three conformations of the antiparallel model (A, B, C, shown in Figure 7), with different facial orientations of ZnChl with respect to their neighbors.

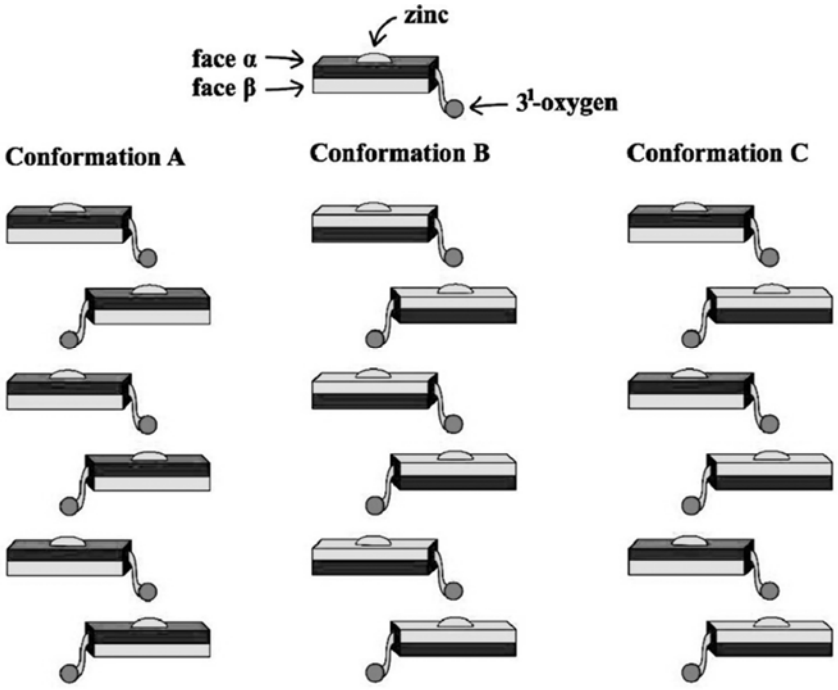

Figure 7. Different possible stacked conformations formed by zinc chlorins **1**-OMe.

The rotational freedom for the four coordinated facial dimers ($F_\beta \rightarrow F_\alpha$ in conformation A, $F_\alpha \rightarrow F_\beta$ in conformation B, $F_\beta \rightarrow F_\beta$ and $F_\alpha \rightarrow F_\alpha$ in conformation C) varies because of the steric hindrance imposed by the substituents at the 17 and 18 positions. As a result, the rotational flexibility in the different conformations varies. Taking these steric restrictions into account, the allowed rotational angles for the four coordinated dimers are as follows: $F_\alpha F_\beta \rightarrow F_\alpha F_\beta$ (0° to 180°), $F_\beta F_\alpha \rightarrow F_\beta F_\alpha$ (-145° to 35°), $F_\alpha F_\beta \rightarrow F_\beta F_\alpha$ (-145° to 35°), and $F_\beta F_\alpha \rightarrow F_\alpha F_\beta$ (0° to 180°). A rotational twist was introduced around the coordinate bonds into the antiparallel model between consecutive molecules. Using a theoretical methodology, the ground- and excited-state densities and transition densities were obtained. These densities were used to calculate the absorption and CD spectra of the aggregate for these three different conformations and distinct differences in the exciton coupling for the different conformations of the stack were

obtained.[45] The exciton coupling is sensitive to the twist angle between neigboring molecules which means that the UV/Vis and CD spectra also depend on the twist angle. In the CD spectrum, the effect is much more pronounced, especially the intensity. The calculated CD spectra for conformations A and B at a single equilibrium twist angle consist of a single bisignate curve that is either +/- or negative -/+. Therefore, conformations A and B could not account for the experimentally observed CD spectra (+/-/+) having two positive and one negative maxima. In conformation C, the physicochemical environment for consecutive neighbors is different because of distinct facial orientations $F_\beta \rightarrow F_\beta$ and $F_\alpha \rightarrow F_\alpha$. As a result, it is reasonable that different equilibrium twist angles might exist between consecutive pairs of molecules. Therefore, the spectral properties of the stack were investigated by assigning two different twist angles to consecutive neighbors. Upon introducing two twist angles, the UV/Vis spectrum splits into two parts that have appreciable oscillator strength. Both of these parts give rise to a bisignate curve in the CD spectrum. It was found that for alternating twist angles of 0° ($F_\alpha F_\beta \rightarrow F_\beta F_\alpha$) and 110° ($F_\beta F_\alpha \rightarrow F_\alpha F_\beta$), the relative intensities of the maxima and the shape of the CD spectrum in experimental spectra is reproduced best in the presence of disorder. Further data obtained from these calculations indicate that two alternating twist angles are necessary along the stack of chlorins in order to account for the shape (+/-/+) of the experimental CD spectrum. This means that subsequent chlorins in the stack should be distinct from each other, such as, for instance, in conformation C. A possible variation of conformation C that might be consistent with these theoretical results might be the initial formations of a closed dimeric species, as proposed by Nozawa and co-workers (discussed in Chapter 2) that might assemble in a subsequent step into extended stacked structures by π-π interactions without involvement of coordinative bonds between oxygen and zinc.

From these results and based on thermodynamic spectroscopic data, a nucleation-elongation pathway that suggests remarkable degree of cooperativity is proposed. The 1D helical stack aggregates probably assemble further into 2D assemblies. However, any dimeric species intermediate to the monomers and extended aggregates was not observable experimentally by UV/Vis and CD studies. Notably, DOSY NMR measurements of ZnChl **1**-OMe in deuterated *n*-hexane/cyclohexane (1:1) exhibited extremely broad signals thereby preventing structural elucidation. However, it is indicative of presence of large aggregates in solution. Information regarding aggregate size distribution in solution have been obtained by

complementary dynamic light scattering (DLS) technique, as discussed in detail in the next section.

3.2.3. Dynamic light scattering measurements of rod and stack aggregates

Dynamic light scattering (DLS) technique is commonly used to determine the sizes of sub micrometric dispersed particles by measuring their diffusion coefficients. In this technique, the rates of diffusion of particles (supramolecular aggregates in the present case) depend on temperature and viscosity of the fluid and the particle size.[46] The particles undergoing Brownian motion are detected and analyzed by illuminating with laser and measuring the scattered light. The time-dependent fluctuations in the scattering intensity is used to determine the translational diffusion coefficient (D), and subsequently the hydrodynamic radius of the polymers. Large particles move slowly and cause slow intensity fluctuations at the detector. Conversely, small particles move faster and cause rapid intensity fluctuations. Thus, the fluctuations in intensity contain information about the rate of diffusion of the particles. In order to calculate the diffusion coefficient and therefore the particle size from the changing light intensity signal, the signal is mathematically transformed into the so called autocorrelation function (ACF). If the ACF at time τ has a high value, there is a strong correlation between the intensity at any instant compared to that at a later time τ. The intensity is related to the pattern of the particle positions and a higher correlation between the intensity at two different times implies that particles have not diffused very far. Thus, an ACF that remains at high magnitudes for long time intervals indicates large slowly moving particles. The autocorrelation functions for aggregates of ZnChl **1**-OH at two different angles (28^{o}, 63^{o}) are shown (Figure 8) and a sigmoidal behavior is observable.

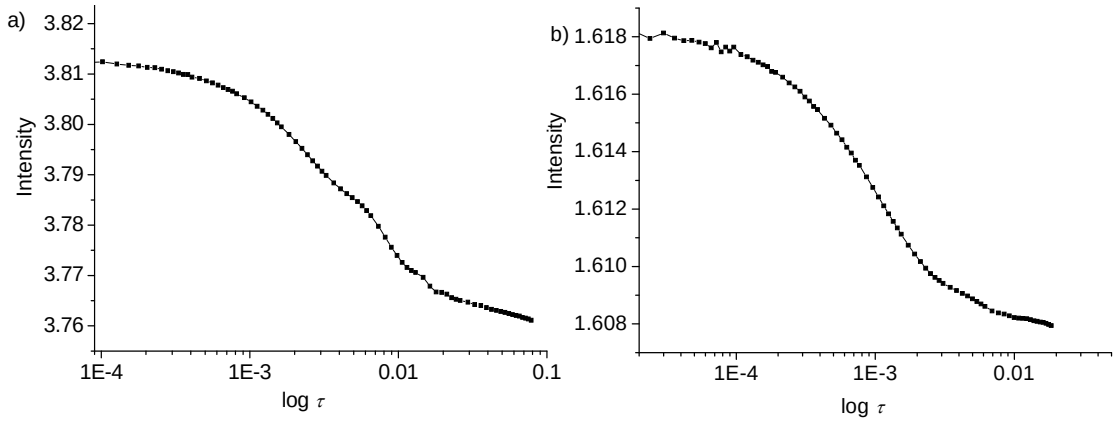

Figure 8. Autocorrelation functions (ACF) for the aggregates of ZnChl **1**-OH in *n*-hexane containing 0.5 % THF ($c = 3 \times 10^{-6}$ M) obtained from dynamic light scattering (DLS) measurements at scattering angles of a) 28.8° and b) 63.8°.

DLS measurement data are analyzed by two methods i.e. unimodal distribution and size distribution processor (SDP) analysis. The unimodal analysis provides the particle mean size and the polydispersity index (PI) of the particle size distribution. The mean is based on cumulant fittings and polydispersity index of the size distribution. For PI values less than 0.1, the sample is considered monomodal (i.e., narrow particle size distribution), whereas for values over 0.3, the sample is considered polydisperse.[46] A relatively broad distribution of sizes and a comparatively high degree of polydispersity is expected for supramolecular polymers in solution in which rapid dynamic equilibrium between free and self-assembled species takes place. The limitation of the unimodal analysis is that it is less accurate for complex size distributions. The unimodal distribution results (at six scattering angles with three repetitions at each angle) obtained for ZnChls **1**-OH and **1**-OMe yielded average PI values of 1.29 and 1.03 respectively, which indicate significantly high polydispersity (broadness in size distribution) for both of these aggregates. For highly polydisperse supramolecular polymers of ZnChls **1**-OH and **1**-OMe, the SDP analysis is more accurate as it provides particle size distribution in terms of intensity, weight and number distributions (Figure 9, 10). In the intensity distribution histogram (Figure 9a), the magnitude of each peak is proportional to the percent of total scattered intensity due to the particles. The variation of intensity with changes in scattering angles account for anisotropy of aggregates and their non-spherical and rather one-dimensional shape.

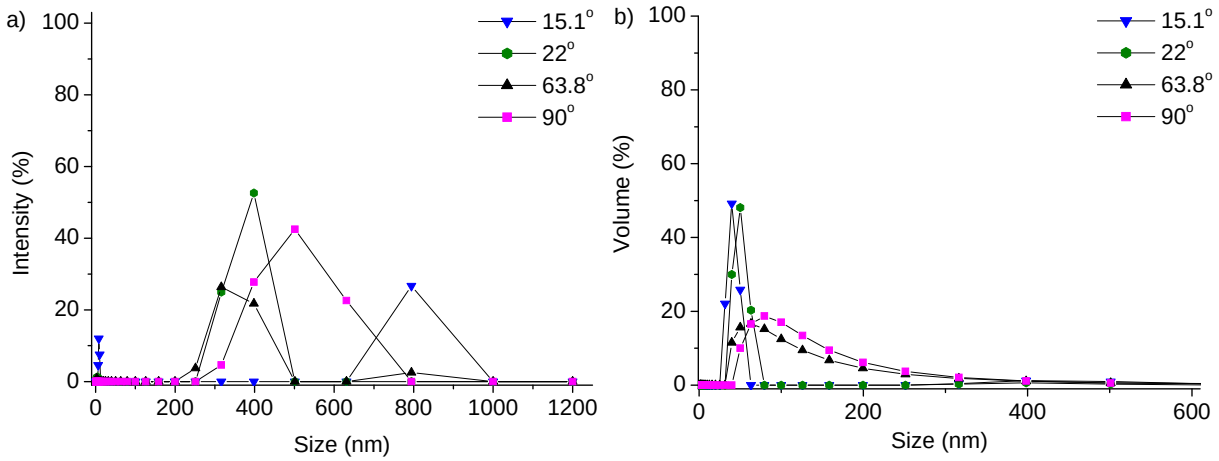

Figure 9. a) Intensity distribution and b) volume distribution of aggregates of **1**-OH in *n*-hexane containing THF (0.5 %) ($c = 3 \times 10^{-6}$ M) obtained from DLS measurements.

Volume distribution (Figure 9b) gives the relative volume of particles of each size in the sample. Intensity results are dependent on scattering angles whereas volume results are not. Number percentage distributions are determined by dividing the volume percentage results by cubed diameter of the particles in the distribution shown in Figure 10.

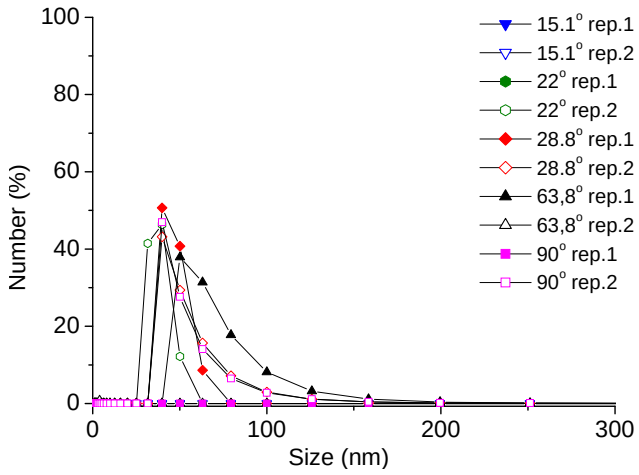

Figure 10. Number distribution of aggregates of ZnChl **1**-OH in *n*-hexane containing 0.5 % THF ($c = 3 \times 10^{-6}$ M) obtained by DLS measurements.

The unimodal distribution provides a very rough estimate of the size of aggregates in solution. The mean diffusion coefficient obtained from the DLS measurements was 1.77×10^{-12} m^2/s. Using Stokes Einstein equation, $r = k_B T/6\pi\eta D$, where r is the hydrodynamic radius, k_B is the Boltzmann constant, T is the temperature of measurement, η is the viscosity of the solvent and D is the diffusion coefficient of the particles in solution. Taking into account the viscosity of the solvent as 0.0042 poise, k_B as 1.38×10^{-23} J/K, and D as 1.77×10^{-12} m^2/s

determined from DLS measurement, the hydrodynamic radius *r* was estimated to be 291 nm. Thus, the results indicate that size of aggregates of ZnChl **1**-OH in solution is very large.

In order to compare the size in solution for the corresponding 3^1-methoxy ZnChl **1**-OMe, angle-dependent dynamic light scattering was measured with aggregate solution of ZnChl **1**-OMe in *n*-hexane/cyclohexane (1:1) and the results are described below. The autocorrelation function (ACF) at different angles showed a usual sigmoidal behaviour (Figure 11) and the SDP analysis was used to obtain the intensity, volume and number distribution as shown below. As for the rod aggregates of ZnChl **1**-OH, the intensity distribution shows a strong angle dependence which is indicative of the polydispersity and anisotropic one-dimensional nature of the aggregates. Moreover, size of aggregates in solution was found to be very large. In the intensity distribution histogram (Figure 12a), the magnitude of each peak is proportional to the percent of total scattered intensity due to the particles.

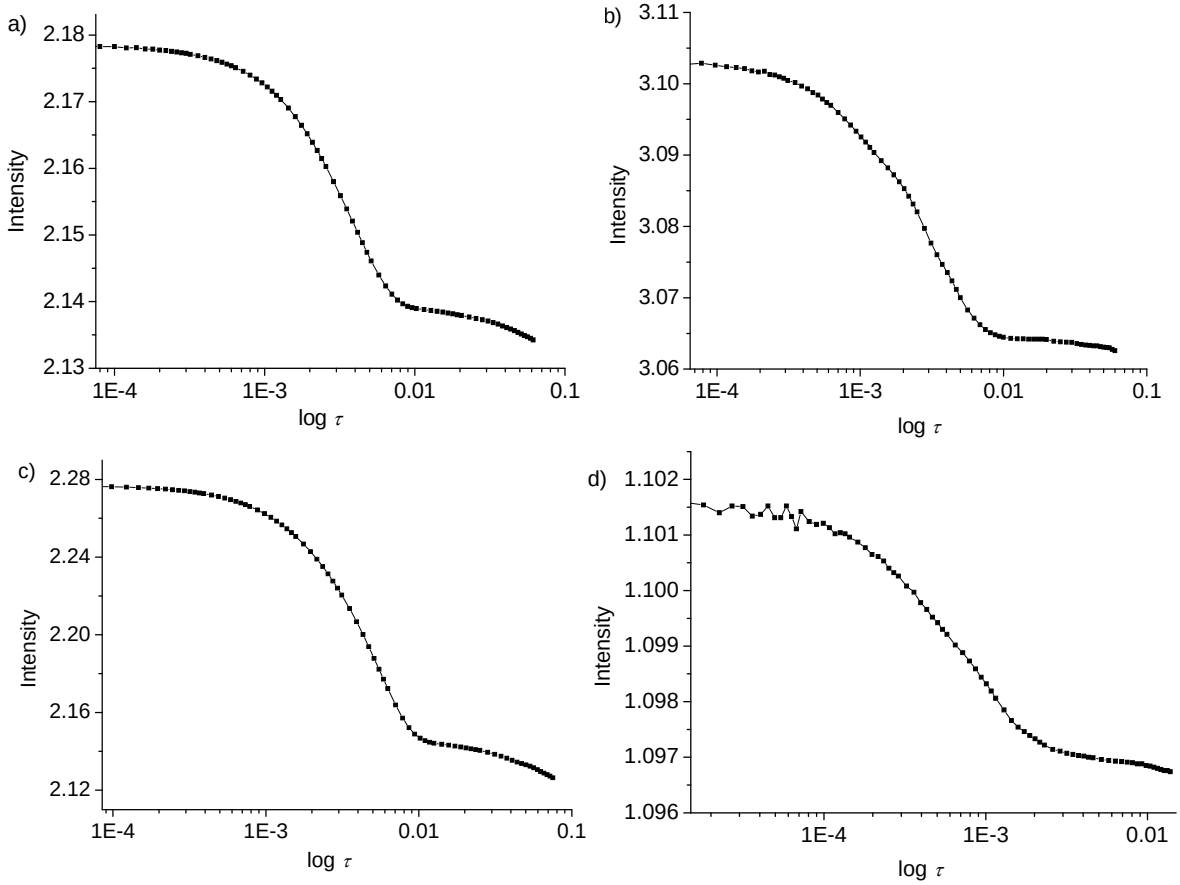

Figure 11. Autocorrelation functions (ACF) for the aggregates of ZnChl **1**-OMe in *n*-hexane:cyclohexane (1:1) ($c = 2 \times 10^{-5}$ M) obtained from dynamic light scattering (DLS) measurements at four different scattering angles a) 15.1°, b) 22.0°, c) 28.8 and d) 63.8°.

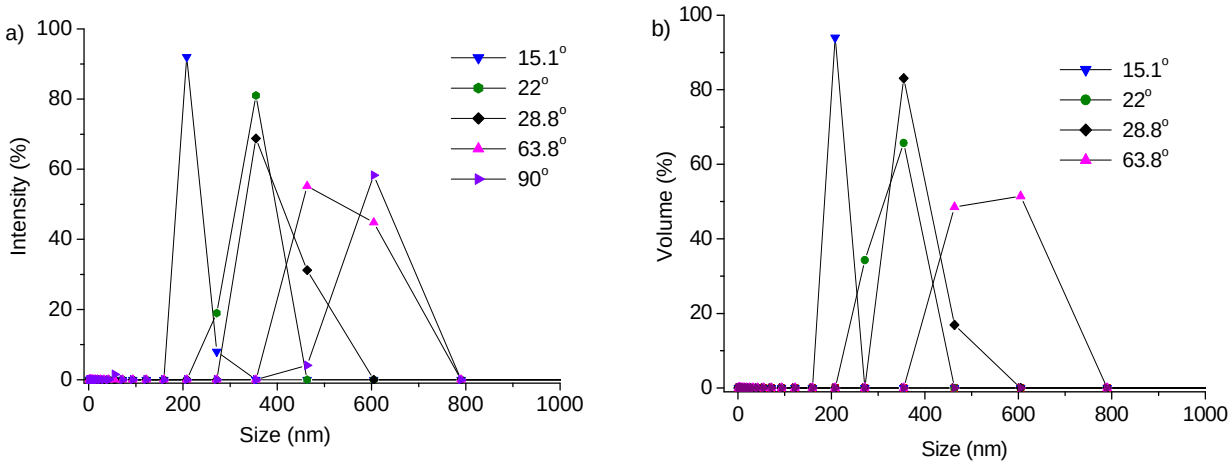

Figure 12. a) Intensity distribution and b) volume distribution of aggregates of ZnChl **1**-OMe in *n*-hexane:cyclohexane (1:1) ($c = 2 \times 10^{-5}$ M) obtained from DLS measurements.

Volume distribution (Figure 12b) provides the relative volume of particles of each size in the sample. Figure 13 shows the number distribution for the aggregates of ZnChl **1**-OMe.

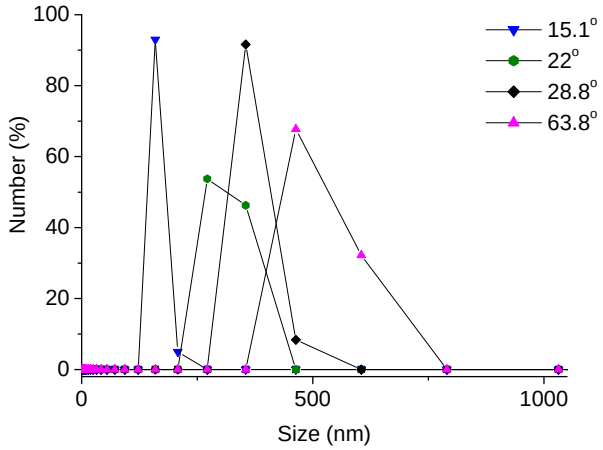

Figure 13. Number distribution of aggregates of ZnChl **1**-OMe in *n*-hexane:cyclohexane (1:1) ($c = 2 \times 10^{-5}$ M) obtained from DLS measurements.

The SDP analysis which provides a distribution of aggregates based on size, intensity and volume is more accurate. Nevertheless, the unimodal distribution can give a very rough estimate of the size of aggregates in solution. The mean diffusion coefficient obtained from the DLS measurements was 6.1×10^{-12} m^2/s. Using Stokes Einstein equation, $r = k_B T/6\pi\eta D$, where r is the hydrodynamic radius, k_B is the Boltzmann constant, T is the temperature of measurement, η is the viscosity of the solvent and D is the diffusion coefficient of the particles in solution. Taking into account the viscosity of the solvent mixture as 0.0042 poise, k_B as 1.38×10^{-23} J/K, and D as 6.1×10^{-12} m^2/s determined from DLS measurement, the

hydrodynamic radius *r* was rougly estimated to 84.3 nm. Thus, the result is consistent with our proposition that size of aggregates of ZnChl **1**-OMe is also large in the given solution.
DLS measurements were performed for ZnChl **3**-OH aggregates in water/methanol (99:1) and the ACF obtained at six different angles showed the usual sigmoidal behavior (ACF at angles of 10.6^{o} and 90^{o} are shown in Figure 14). The results obtained from SDP analysis are shown in Figures 15 and 16. The unimodal distribution results (at six scattering angles with two repeatations at each angle) obtained for ZnChls **3**-OH yielded average PI values of 1.3, which indicate significantly high polydispersity (broadness in size distribution) for these aggregates.

As for all the rod aggregates of 3^{1}-hydroxy zinc chlorins, the intensity distribution for ZnChl **3**-OH shows a strong angle dependence which is indicative of the polydispersity and anisotropic one-dimensional nature of the aggregates. Moreover, size of aggregates in solution was found to be very large. In the intensity distribution histogram (Figure 15a), the magnitude of each peak is proportional to the percent of total scattered intensity due to the particles. Volume distribution (Figure 15b) provide the relative volume of particles of each size in the sample. Figure 16 shows the number distribution for the aggregates of ZnChl **3**-OH.

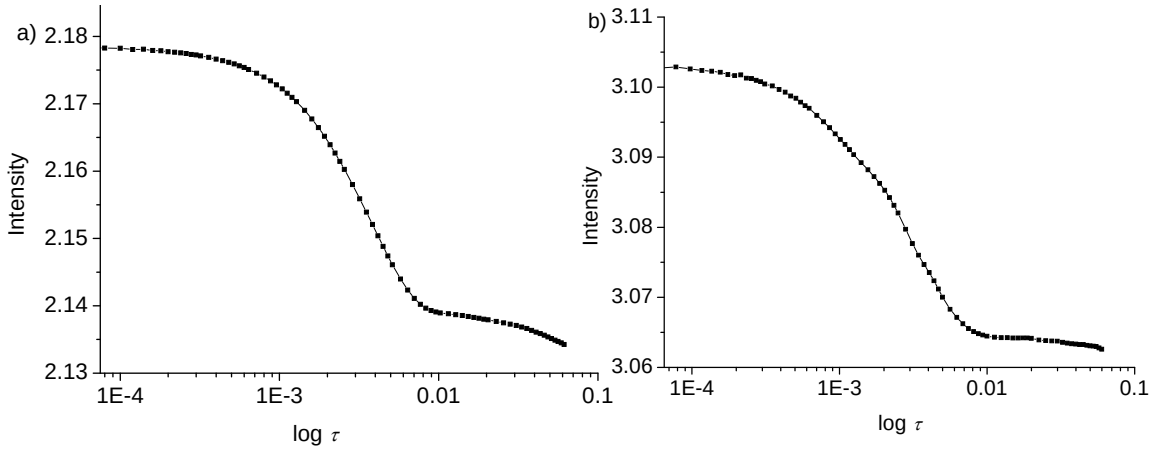

Figure 14. Autocorrelation functions (ACF) for the aggregates of ZnChl **3**-OH in water:methanol (100:1) (c = 1 × 10^{-5} M) obtained from dynamic light scattering (DLS) measurements at scattering angles of a) 10.6^{o} and b) 90^{o}.

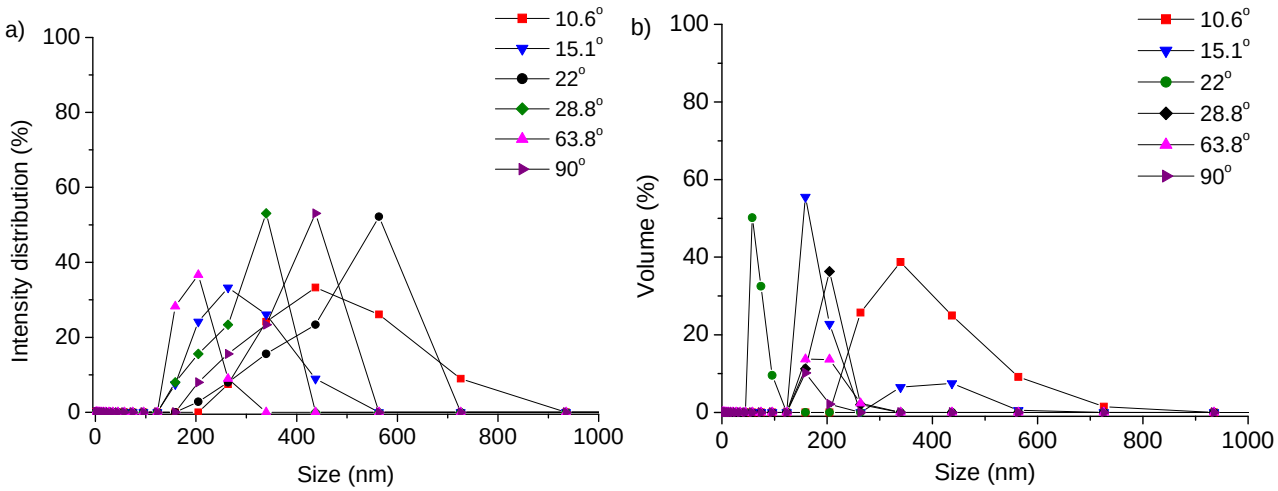

Figure 15. a) Intensity distribution and b) volume distribution of aggregates of ZnChl **3**-OH in water:methanol (100:1) ($c = 1 \times 10^{-5}$ M) obtained from DLS measurements at different scattering angles.

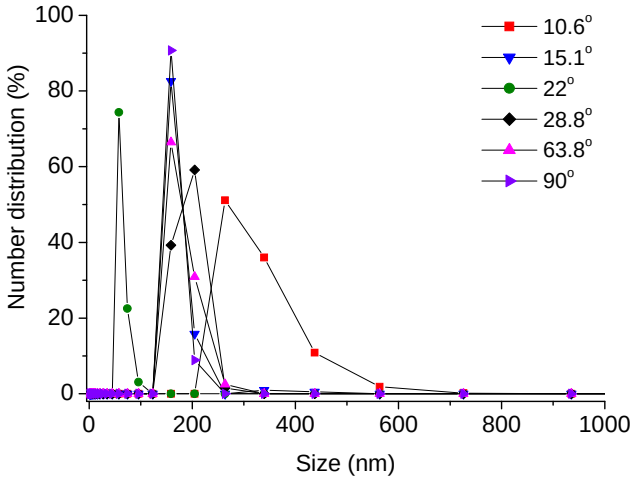

Figure 16. Number distribution of aggregates of ZnChl **3**-OH in water:methanol (100:1) ($c = 1 \times 10^{-5}$ M) obtained from DLS measurements at different scattering angles.

The SDP analysis which provides a distribution of aggregates based on size, intensity and volume is more accurate. Nevertheless, the unimodal distribution can give a very rough estimate of the size of aggregates in solution. The mean diffusion coefficient obtained from the DLS measurements was 2.5×10^{-13} m^2/s. Using Stokes Einstein equation, $r = k_B T/6\pi\eta D$, where r is the hydrodynamic radius, k_B is the Boltzmann constant, T is the temperature of measurement, η is the viscosity of the solvent and D is the diffusion coefficient of the particles in solution. Taking into account the viscosity of the solvent mixture as 0.0089 poise, k_B as 1.38×10^{-23} J/K, and D determined from DLS measurement, the hydrodynamic radius r was rougly estimated to be 981 nm, which indicates that size of aggregates of ZnChl **3**-OH is indeed very large in the given solution.

3.2.4. Electron microscopic studies of 3^1-hydroxy zinc chlorins

As discussed in Chapter 2, electron microscopy[47] is an important technique that has been extensively used for the structural characterization of natural chlorosomal assemblies.[48,49] Whereas scanning probe techniques, such as STM and AFM, are the most important tools for the imaging of surface-associated nanostructures, transmission electron microscopy (TEM) is the technique of choice for the analysis of core-shell structure and morphology of self-assemblies in solution. In the case of organic materials, which are relatively translucent to electron beams, drying is often combined with negative staining, which artificially enhances contrast for visualization of the nanostructures. Strongly electron scattering heavy-metal compounds, such as uranyl acetate, are added as contrasting agent to the dried sample specimen. Alternatively, a near-native solvated state can be preserved by cryogenic vitrification and subsequent imaging of the nanostructures by low-dose cryogenic TEM (cryo-TEM). In order to elucidate the core-shell structure of the chlorosomal assemblies and converge upon the tube-like model of the BChl *c* assemblies, cryo-electron microscopy has been utilized extensively.[47-50] In this section, the electron microscopic studies for the 3^1-hydroxy zinc chlorins that form the rod-like aggregates in solution are discussed in detail. Different electron microscopic techniques such as transmission electron microscopy (TEM) and scanning transmission electron microscopy (STEM) have been used to elucidate the hollow tubular structures of 3^1-hydroxy ZnChl aggregates in solution.

Transmission electron microscopy (TEM): In order to obtain information about the core-shell structure of tube-like aggregates of 3^1-hydroxy zinc chlorins, TEM measurements were performed for aggregates of 3^1-hydroxy ZnChls **1**-, **2**-, **3**-OH. For ZnChls **1**- and **2**-OH, the aggregates were prepared in THF/*n*-hexane (1:100) or THF/*n*-heptane (1:100). For ZnChl **3**-OH, the aggregates were prepared in THF/water (1:100) and methanol/water (1:100). Most importantly, the samples could be stained by a negative staining agent of 0.5 % aqueous uranyl acetate. The samples were prepared by drop casting an aggregate solution onto carbon-coated copper grid, dried and stained with uranyl acetate and TEM measurements were performed at an accelerating voltage of 80 kV. For ZnChl **3**-OH aggregates, long tubular aggregates could be observed with diameters of ~ 6-7 nm and lengths varying largely from 300-400 nm upto as long as 10 μm. Furthermore, some of the aggregates were intertwined and formed bundles of tubes as evident from the TEM micrographs. Figures 17-19 show the

TEM micrographs of ZnChl **3**-OH aggregates showing tubular aggregates with high polydispersity in length but uniform diameters of ~ 5-6 nm.

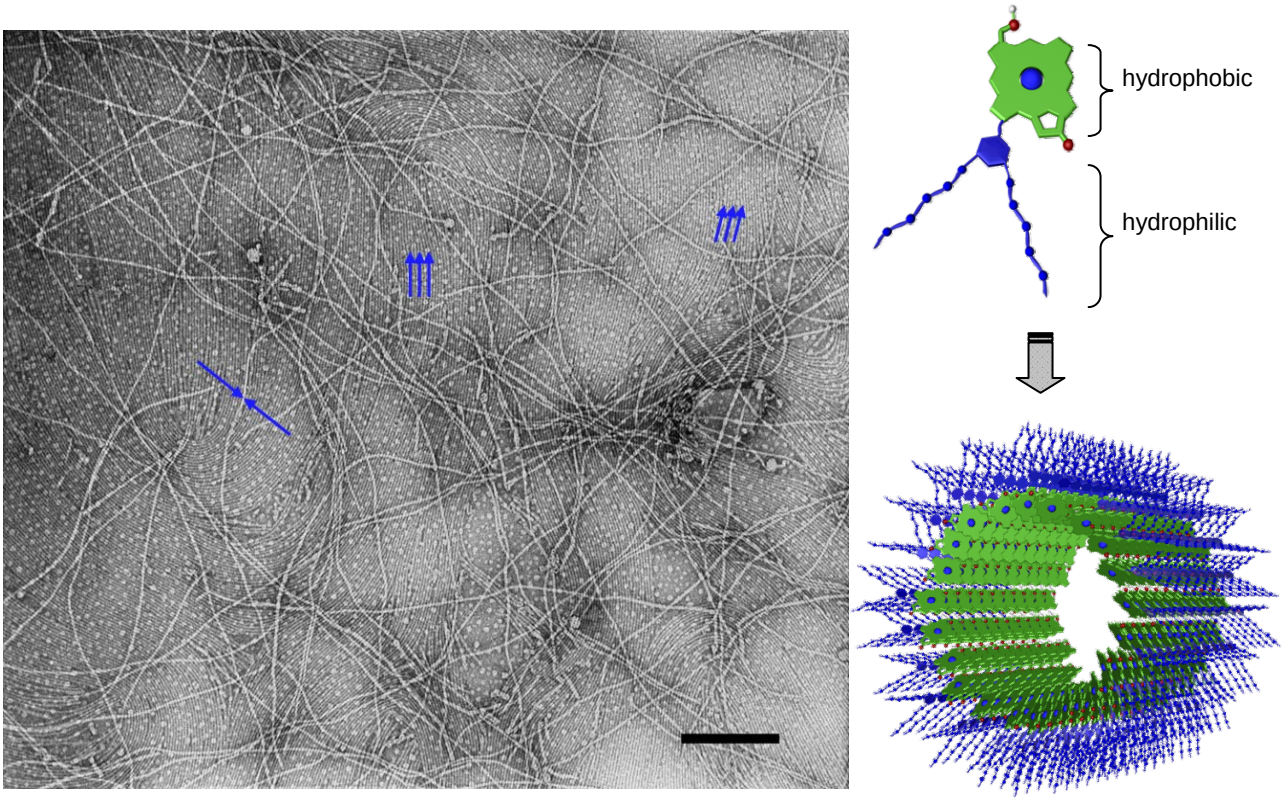

Figure 17. TEM micrograph of ZnChl **3-OH** aggregates in water/methanol (100:1) solution with 0.5 % aqueous uranyl acetate staining at accelerating voltage of 80 kV. Scalebar is 200 nm. Blue arrows indicate densely packed layer of nanotubes having the same orientation and the nanotube thickness of ~ 6nm.

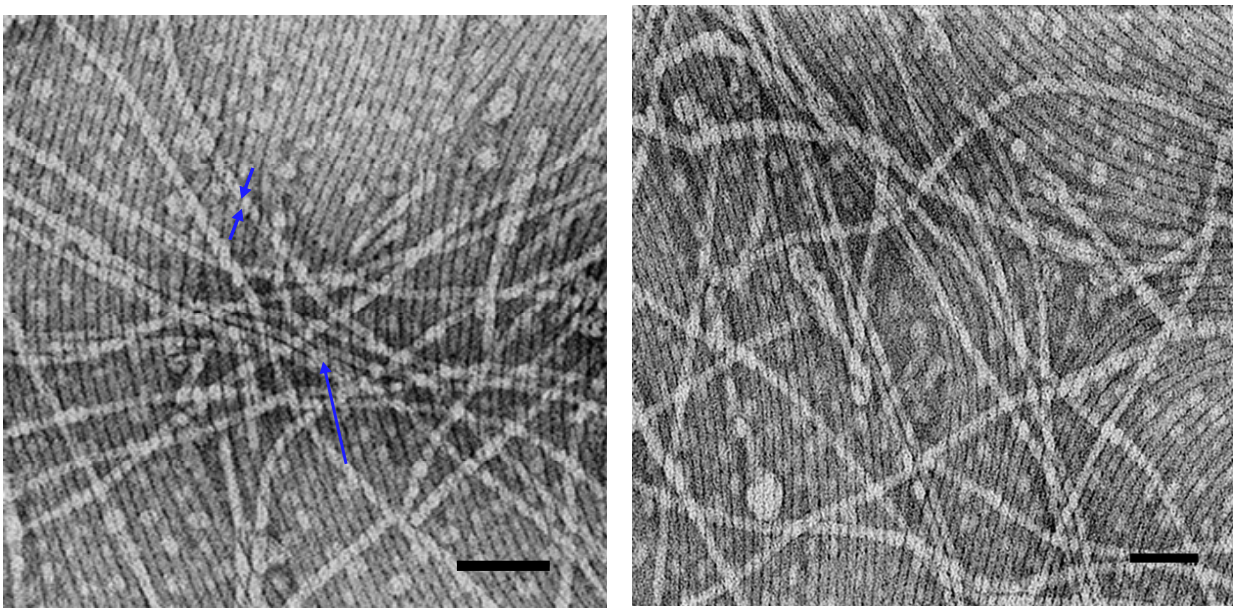

Figure 18. TEM micrograph of ZnChl **3**-OH aggregates in water/methanol (100:1) solution with 0.5 % aqueous uranyl acetate staining at accelerating voltage of 80 kV. Scalebar is 100 nm. Blue arrows indicate layers of densely packed nanotubes.

All the nanotubular assemblies have same diameters of 5-6 nm and electron micrographs of ZnChl **3**-OH (Figures 18, 19) reveal multiple layers of nanotubes obtained with the first densely packed nanotube layer with same horizontal orientation and the subsequent nanotubes lying on top of it. The measured diameter of ~ 5-6 nm of these biomimetic zinc chlorin aggregates is in excellent agreement with electron microscopy data of BChl *c* rod aggregates in chlorosomes (*Chloroflexus aurantiacus*, diameter ~ 5-6 nm) and thus complied with the tubular model postulated by Holzwarth and Schaffner as discussed in Chapter 2.

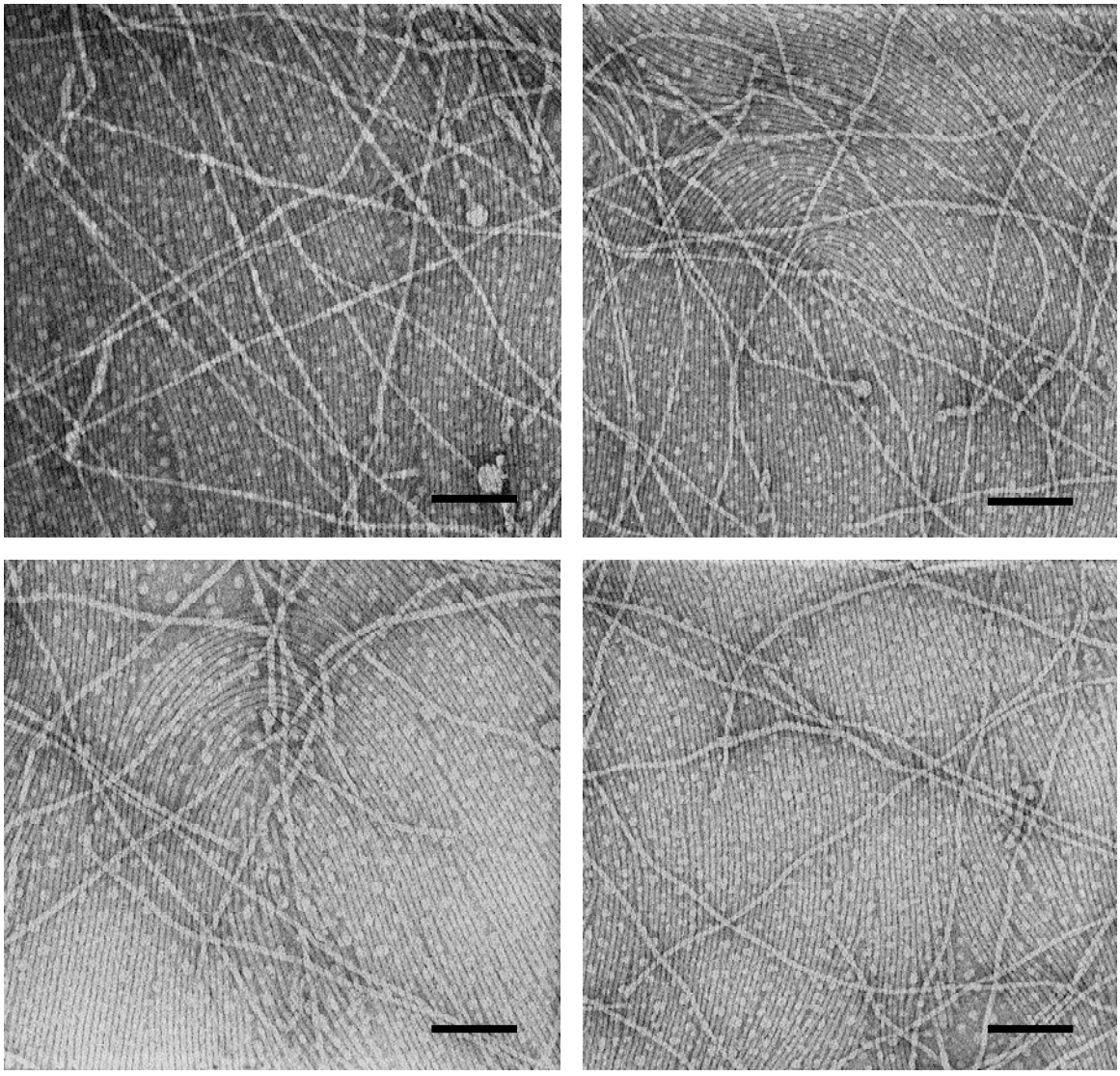

Figure 19. TEM micrographs of ZnChl **3**-OH aggregates in water/methanol (100:1) solution with 0.5 % aqueous uranyl acetate staining at accelerating voltage of 80 kV. Scalebar is 100 nm in all the figures.

Scanning electron microscopy is another sequential imaging microscopic technique that can be used in reflection or transmission mode, the latter known as scanning transmission electron

microscopy (STEM). These tubular aggregates of zinc chlorin **3**-OH have been characterized by STEM as described in next section.

Scanning transmission electron microscopy (STEM): Scanning transmission electron microscopy (STEM) is a technique closely related to SEM that uses electron beams to image a sample. As in the SEM, secondary or backscattered electrons can be used for imaging in STEM; but higher signal levels and better spatial resolution are obtainable by detecting the transmitted electrons in STEM. It works on the same principle as that of the normal scanning electron microscopy (SEM), by forming a focused beam of electrons that is scanned over the sample while the desired signal is collected to form an image. STEM measurements of ZnChl **3**-OH enabled visualization of very long highly ordered nanotubular assemblies with diameters of ~ 5-6 nm for individual aggregates as observed by TEM. Furthermore, bundles of aggregates could also be observed throughout (Figure 20). The aggregates were highly polydisperse with lengths varying from 200-300 nm upto 1-10 μm.

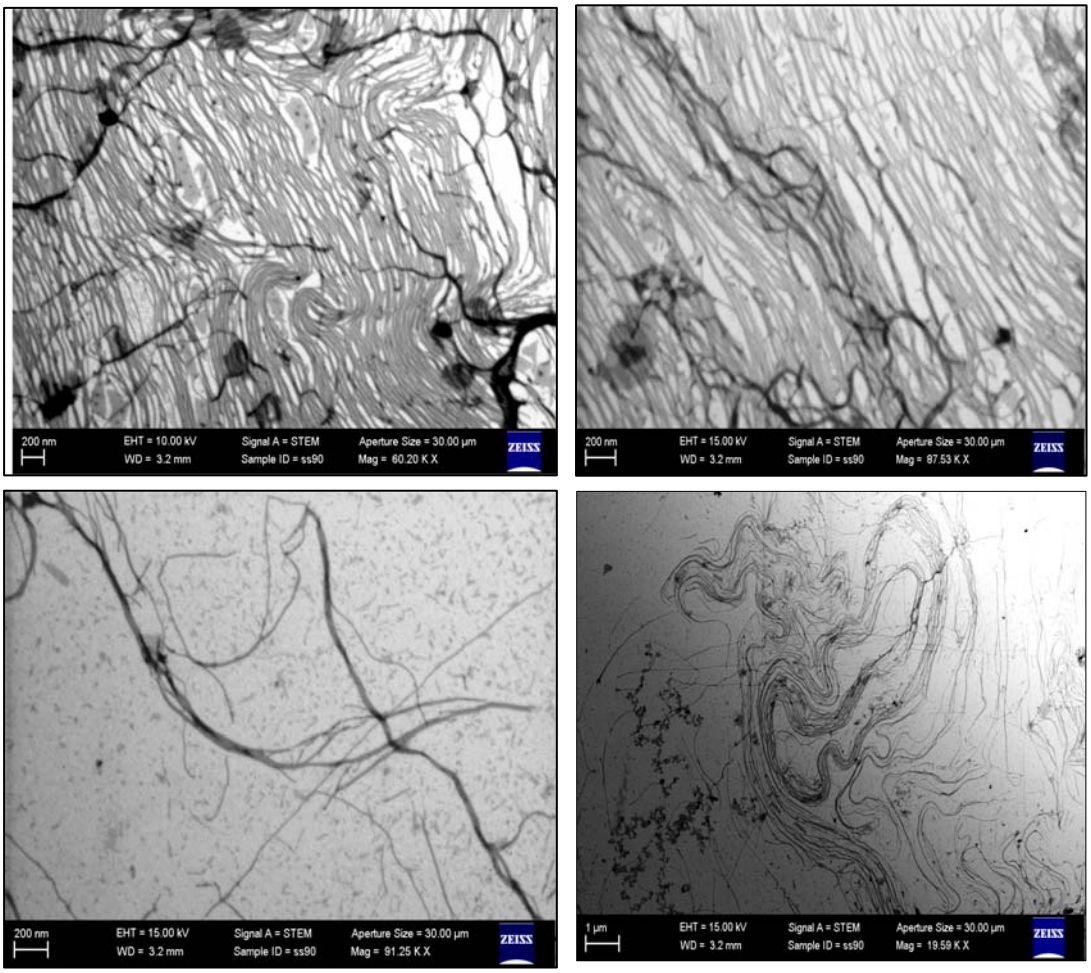

Figure 20. STEM micrographs of zinc chlorin **3**-OH aggregates in water/methanol (100:1) solution with 0.5 % aqueous uranyl acetate staining at accelerating voltages (EHT) of 10 kV and 15 kV. Scalebars are indicated in respective figures.

On the other hand, TEM studies with aggregates of ZnChl **1**-OH and **2**-OH in non-polar solvent were not successful apparently because of the aqueous staining agent being less effective in organic solvent mixture, sufficient contrast could not be achieved. However, STEM studies of these aggregates enabled visualization of fibrous aggregates with diameters in good agreement to those observed by AFM studies. However, from STEM micrographs, it was not possible to conclude upon whether these aggregates were (hollow) tubular.

3.2.5. Solid-state packing of 3^1-hydroxy and 3^1-methoxy compounds

Recently, solid-state MAS NMR has been successfully developed and used for structure determination of uniformly enriched compounds or multiple spin clusters in solid type biological systems,[51,52,53] disordered systems, and polypeptides. For solid-state NMR studies of chlorosomes or aggregated BChls in literature, ^{13}C and ^{15}N enriched starting materials have been used.[54,55,56,57] While labeling of biological systems is routinely performed, isotope enrichment of semisynthetic systems is more difficult to achieve. This is attributed to the fact that firstly, a large fraction of labeled material is lost in a multi-step synthesis or derivatization process, and secondly, chemical structure determination at each step with labelled sample is highly impractical and difficult. In such cases, it is more practical and economical to adopt a method to study unlabeled samples. Here, aggregates of unlabelled ZnChls **1**-OH and **1**-OMe have been studied by solid-state NMR, powder XRD technique and molecular modelling studies and a precise structural arrangement could be proposed based on these studies.

To resolve the structural arrangement of ZnChl tubular and stacked assemblies in solid state, ZnChls **1**-OH and **1**-OMe aggregates were studied using MAS NMR combined with molecular modelling and ring-current shift calculations. The aggregation shifts (i.e., difference of the chemical shifts in solid state and the shifts of monomers in solution) for the aggregates in solid were measured by cross polarisation magic angle spinning (CP MAS) NMR and by heteronuclear ^1H-^{13}C correlation (HETCOR) NMR spectroscopy at Leiden University.[b] This technique has previously been applied for studying aggregated BChls and chlorosomes.[55-57] The ^1H shifts were first resolved by 2D heteronuclear ^1H-^{13}C dipolar correlation experiments and thereby the proton aggregation shifts were determined. Access to

[b] Solid-state NMR measurements were performed by Dr. Swapna Ganapathy in the group of Prof. Dr. Huub J. M. de Groot at the University of Leiden.

the proton chemical shifts of aggregated chlorins allows accurate probing of ring current effects that can be related to the short-range stacking of chlorin macrocycles. This is possible because the building blocks **1**-OH and **1**-OMe are moderately sized, unsaturated molecules of low symmetry. For the highly ordered and closely spaced stacks of **1**-OH and **1**-OMe, all of the resonances of the chlorin macrocycle could be assigned and analyzed to resolve their microstructures. Quantum mechanical calculations were then performed to quantitatively reproduce the observed ring currents for two proposed models discussed in Chapter 2, namely parallel[58] and antiparallel[59] stacking. In this way, the combination of MAS NMR, molecular modelling and DFT based ring current shift calculations provided a quantitative basis to determine the stacking patterns that ZnChls **1**-OH and **1**-OMe adopt at the molecular level. Complimentary X-ray diffraction data for ZnChl **1**-OMe provided a packing model of these dyes in the solid state that substantiates the three-dimensional organization of the chlorin subunits.

To obtain monomer chemical shifts, ZnChl dyes **1**-OH and **1**-OMe were dissolved in the coordinating solvents THF-d_8 and pyridine-d_5, respectively. In the case of ZnChl **1**-OMe pyridine-d_5 was chosen for enhanced solubility after it was confirmed that the chemical shifts exhibit negligible changes compared to those in a THF-d_8 solution. The ^{1}H monomer chemical shifts for ZnChl compounds **1**-OH and **1**-OMe are listed in Table 5 ($\sigma^{H}_{\mathbf{1}\text{-OH,liq}}$, $\sigma^{H}_{\mathbf{1}\text{-OMe,liq}}$). The aggregation shifts that are observed in the ZnChl aggregates relative to their monomers in solution provide important information about the stacking of the molecules. Aggregation shifts or ring-current shifts are defined as chemical shifts in the solid state relative to the monomer shifts in solution. In particular the ^{1}H shifts are an accurate probe of the secondary fields induced by the aromatic rings. The monomeric ^{1}H assignment was obtained from ^{1}H solution NMR experiments. Figure 21 shows the 2D heteronuclear ^{1}H-^{13}C spectrum for ZnChls **1**-OH and **1**-OMe where the assignments are indicated in panels a-d in Figure 21. Moreover, the single set of peaks without significant broadening is detected for **1**-OH and **1**-OMe, which implies a local packing order with unique structural environments for every molecule. The 3^1-OH and 3^1-OMe resonances for ZnChls **1**-OH and **1**-OMe respectively, could not be observed, possibly because of some form of dynamics (or inefficient cross-polarization). The solid-state proton shift values ($\sigma^{H}_{1\text{-OH,i}}$ and $\sigma^{H}_{1\text{-OMe,i}}$) as well as aggregation shifts for **1**-OH and **1**-OMe ($\Delta\sigma^{H}_{1\text{-OH,i}}$ and $\Delta\sigma^{H}_{1\text{-OMe,i}}$) have been listed in Table 5. Significant upfield aggregation shifts are observed, both for ZnChls **1**-OH and **1**-OMe. From Table 5, it

is evident that the aggregation shifts are highest for 3^1 protons indicative of the fact that these protons experience strongest ring currents from neighbouring aromatic rings. Very high ring current shifts are observed also for protons at 5, 2^1 and 12^1 positions for both ZnChls **1**-OH and **1**-OMe.

Table 5. ^{1}H solution (σ_{liq}^{H}) and experimental solid-state chemical shifts (σ_i^{H}) of ZnChls **1**-OH and **1**-OMe, as well their aggregation shifts $\Delta\sigma_i^{H} = \sigma_i^{H}-\sigma_{liq}^{H}$.

position	σ^{H} **1**-OH,i	σ^{H} **1**-OH,liq	$\Delta\sigma^{H}$ **1**-OH,i	σ^{H} **1**-OMe,i	σ^{H} **1**-OMe,liq	$\Delta\sigma^{H}$ **1**-OMe,i
5	3.7	9.5	-5.8	3.3	9.3	-6.0
10	6.6	9.6	-3.0	8.8	9.6	-0.8
17	3.1	4.3	-1.2	5.1	4.2	0.9
18	3.1	4.5	-1.4	5.1	4.4	0.7
20	5.3	8.5	-3.2	7.4	8.4	-1.0
2^1	-3.1	3.3	-6.4	-1.8	3.3	-5.1
3^1	-2.5	5.7	-8.2	-2.6	5.6	-8.2
7^1	1.7	3.3	-1.6	2.6	3.3	-0.7
8^1	2.2	3.8	-1.6	3.8	3.7	0.1
8^2	0.4	1.7	-1.3	2.0	1.7	0.3
12^1	-2.9	3.7	-6.6	-2.3	3.7	-6.0
13^2	3.0	5.1	-2.1	4.7	5.1	-0.4
17^1	1.2	2.3	-1.1	2.4	1.9	0.5
17^2	1.2	2.3	-1.1	2.4	1.9	0.5
18^1	1.1	1.8	-0.7	2.4	1.7	0.7

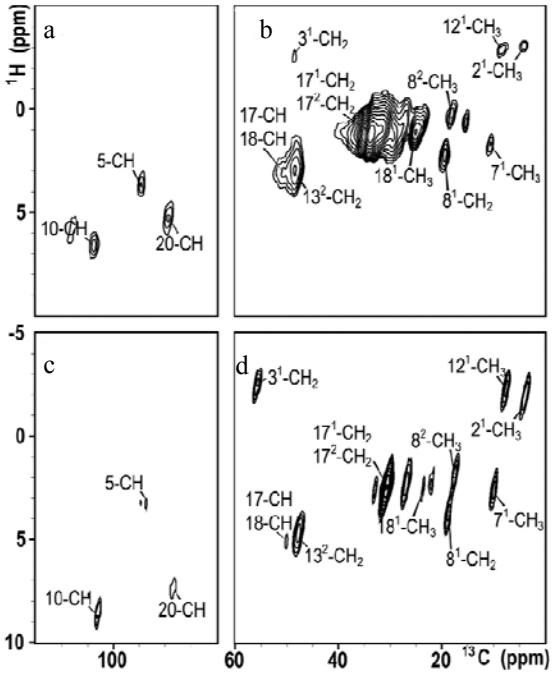

Figure 21. Contour plot sections of heteronuclear ^{1}H-^{13}C MAS NMR HETCOR dipolar correlation spectra of ZnChls **1**-OH (panels a and b) and **1**-OMe (panels c and d) recorded in a field of 17.6 T employing a spinning rate of 13 kHz and sample temperatures of 298 K. The partial assignments of the correlations from the chlorin rings are indicated.

In order to explain these aggregation shift patterns, structural models of coordinating ZnChls for **1**-OH and **1**-OMe were built in Hyperchem 7 and optimized by MM+ on the basis of the previously published AFM and STM results and literature known models (discussed in Chapter 2).[26,27,30] The first model is called the *parallel* stack model in which the arrangement of the chlorin cores is directed by the coordination of hydroxy or methoxy groups to the zinc ions, and the alkyl chains of one stack are all oriented in the same direction, whereas the second is the *antiparallel* monomer stack model in which the alkyl chains of neighboring ZnChls are oriented in opposite directions (Figure 22).[60,61] The terms parallel and antiparallel refer to the mutual orientation of the Q_y transition dipoles. These models have been selected because the tubular aggregates of ZnChl **1**-OH are thought to be built from the basic parallel stack motif. On the other hand, ZnChl **1**-OMe has been shown to aggregate with either the antiparallel stack motif or the parallel stack motif on surface (analogous to Phase I and Phase II STM structures discussed in Chapter 2). For simplifying the modelling, the 17-3,5-bis-dodecyloxybenzylalcohol tail has been replaced by a 17-methyl group and the 8-ethyl is replaced by an 8-methyl group. For ZnChls **1**-OH and **1**-OMe, a parallel stack model with five molecules each was constructed and optimized using molecular mechanics with an MM+ force field. The terminal chlorin was capped with a methanol molecule as the fifth ligand in order to prevent structural distortion. To investigate the possibility of H-bonding between stacks, larger aggregates of **1**-OH were built by placing multiple stacks together with their 3^1-OH group of one stack within H-bonding distance of the 13^1C=O of the adjacent stack followed by geometry optimization by MM+ calculation.

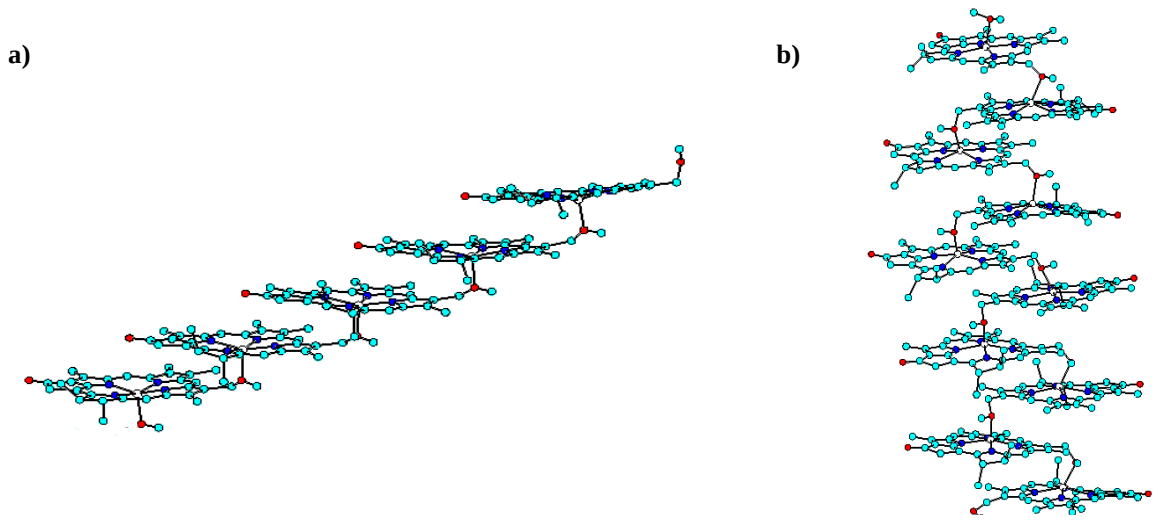

Figure 22. Schematic models used for ring-current shift calculations a) parallel-stack model and b) antiparallel stack model constructed both for ZnChls **1**-OH and **1**-OMe compounds.

In this way, an additional twenty molecule aggregate of four pentamer stacks was optimized for ZnChl **1**-OH. The inter-stack H-bond network remained intact on optimization. Due to the presence of the methoxy functionality at 3^1 position in ZnChl **1**-OMe, H-bonding is not possible and only a single parallel stack comprising of ten zinc chlorin **1**-OMe molecules was optimized. Similarly, to optimize the *antiparallel* stack model for **1**-OH and **1**-OMe, an initial stack of six molecules was constructed for each of them. Geometry optimization revealed that these structures were very unstable as single stacks. A second six molecule stack was added for both ZnChls **1**-OH and **1**-OMe in the inter-stack H-bonding arrangement for ZnChl **1**-OH and with the methoxy functionalities pointing towards the 13^1-C=O of the adjacent stack for ZnChl **1**-OMe. Upon optimization, energetically stable aggregates were obtained for both compounds. This confirms that a stabilization mechanism probably operates for multiple stacks to promote aggregation. Similar mechanism has been explained in the literature for the parallel stack model.[58]

From a correlation plot (Figure 23) comparing the solid state chemical shifts of ZnChls **1**-OH and **1**-OMe with their monomer shifts in solution, it is clear that the ^{1}H aggregation shifts are particularly pronounced for 2^1, 3^1, 12^1 and 5 positions.

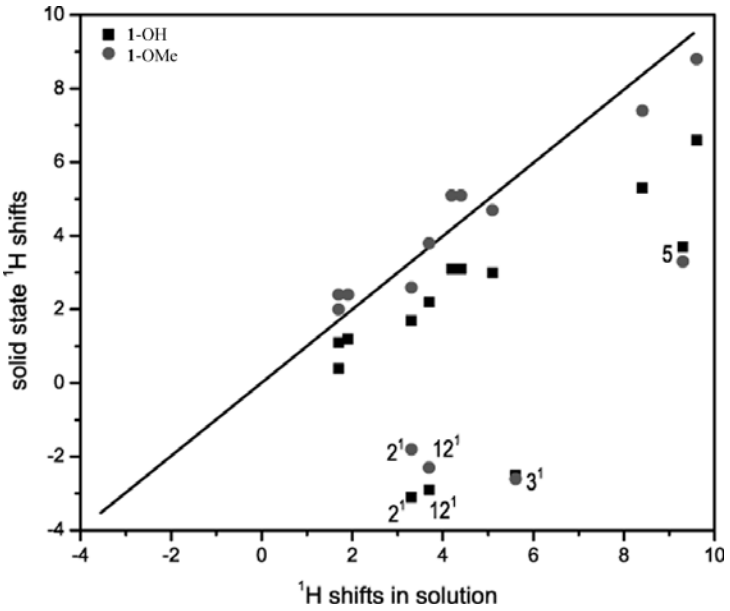

Figure 23. Chemical shift correlation plots for ZnChls **1**-OH and **1**-OMe. The ^{1}H shifts in the solid samples **1**-OH and **1**-OMe are plotted against the monomer shifts in THF-d_8 and pyridine-d_5 solution. The solid lines represent the diagonals. ^{1}H signals (positions 2^1, 3^1, 12^1, 5) are indicated that show a large upfield shift in the solid relative to the monomer in solution.

^{1}H ring-current shifts were calculated for ZnChls **1**-OH and **1**-OMe in the antiparallel (Figure 24) and parallel stack models (Figure 25) and they are listed in Table 6. The ^{1}H aggregation shifts are dominated by ring-current effects, in line with observations in other chlorin aggregates and are useful for resolving the structure.[53,54] The magnitude of the aggregation shifts for ZnChls **1**-OH and **1**-OMe are very similar, which indicates that the pattern of stacking and the stacking motif is very similar for both ZnChls **1**-OH and **1**-OMe in the solid, despite a pronounced difference at the 3^{1}-position, i.e., OH with H-bonding capability for ZnChl **1**-OH, and without it for ZnChl **1**-OMe. The importance of the hydrogen bonding has been questioned before, since extended stacks were found for simplified artificial BChl mimics due to packing by hydrophobic interactions without the assistance of hydrogen bonding.[62] The absence of the -OH resonance in the chemical shift data of ZnChl **1**-OH is well in line with previous studies on Mg-chlorin aggregates of biological origin and semisynthetic Cd-chlorins reported by de Groot and co-workers.[53,54] Apparently the -OMe resonance was also missing indicating that it has a similar role in ZnChl **1**-OMe compared with the -OH moiety in ZnChl **1**-OH. The ring current shifts observed experimentally were also reproduced for the parallel stack model and the aggregation shifts are depicted as circles for values less than -3 ppm in Figures 24 and 25, where the circles have a radius proportional to the magnitude of aggregation shifts.

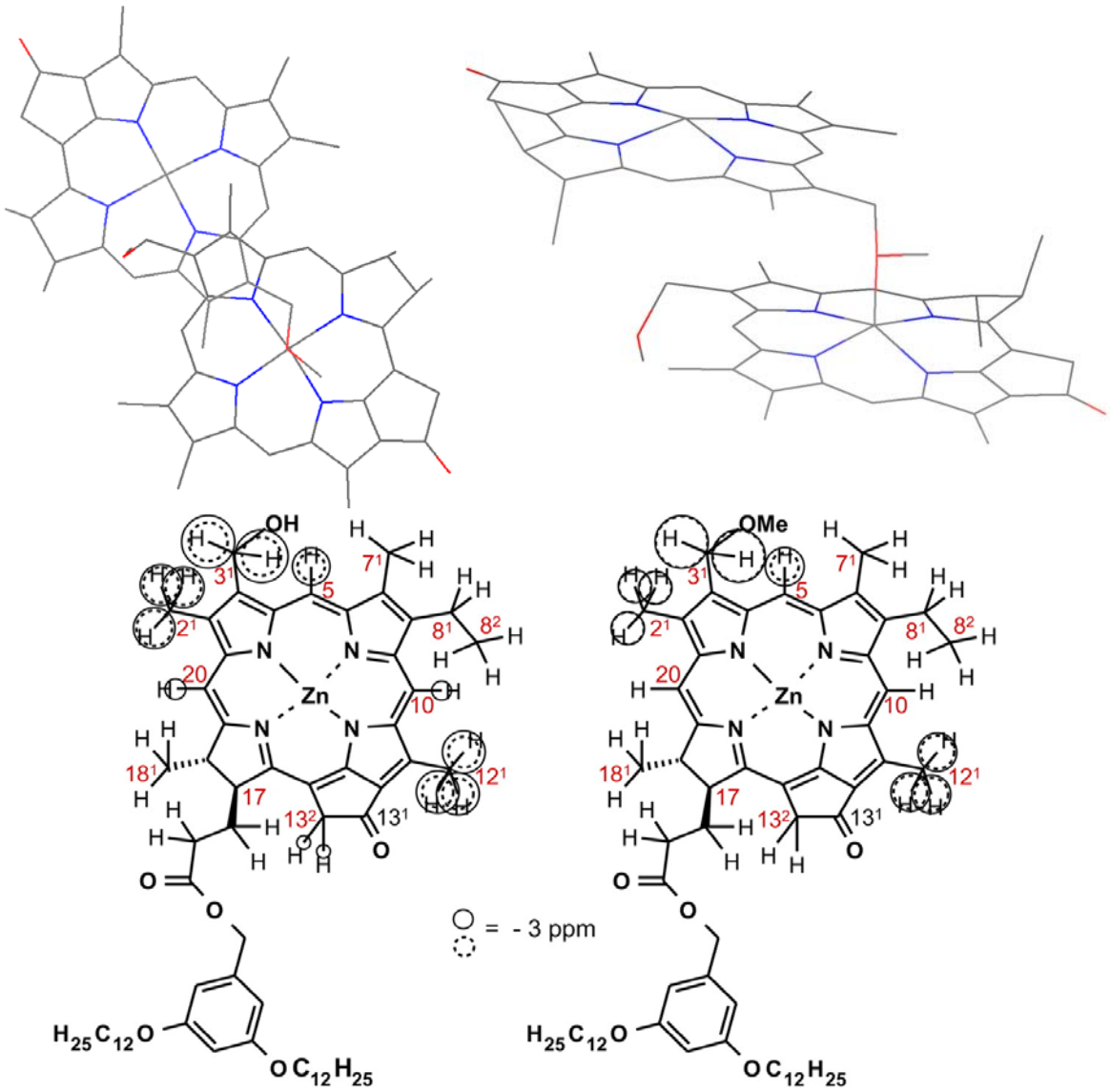

Figure 24. Top: Geometry optimized antiparallel model with two molecules top view and side view; Bottom: Detected ^{1}H upfield aggregation shifts of aggregated ZnChls **1**-OH and **1**-OMe relative to their monomers in THF-d_8 and pyridine-d_5, respectively, are shown as solid grey circles. Calculated ring-current shifts (DFT calculations) for **1**-OH and **1**-OMe in the antiparallel stack model are shown as dashed black circles. Values less than -3 ppm are depicted. The circles have a radius proportional to the magnitude of the shift.

Contribution of the bonding and non-bonding interactions were evaluated to elucidate the precise pigment organization in solid state. It was observed that for both ZnChls **1**-OH and **1**-OMe, the contribution from the non-bonding interactions or the van der Waals interaction increases ~ four to five times from a single stack to a two stack aggregate. As a result, for the antiparallel stack model both for ZnChls **1**-OH and **1**-OMe, the increased π-π overlap on increased aggregate size led to an energetically cooperative stabilization mechanism in an extended space filling structure.

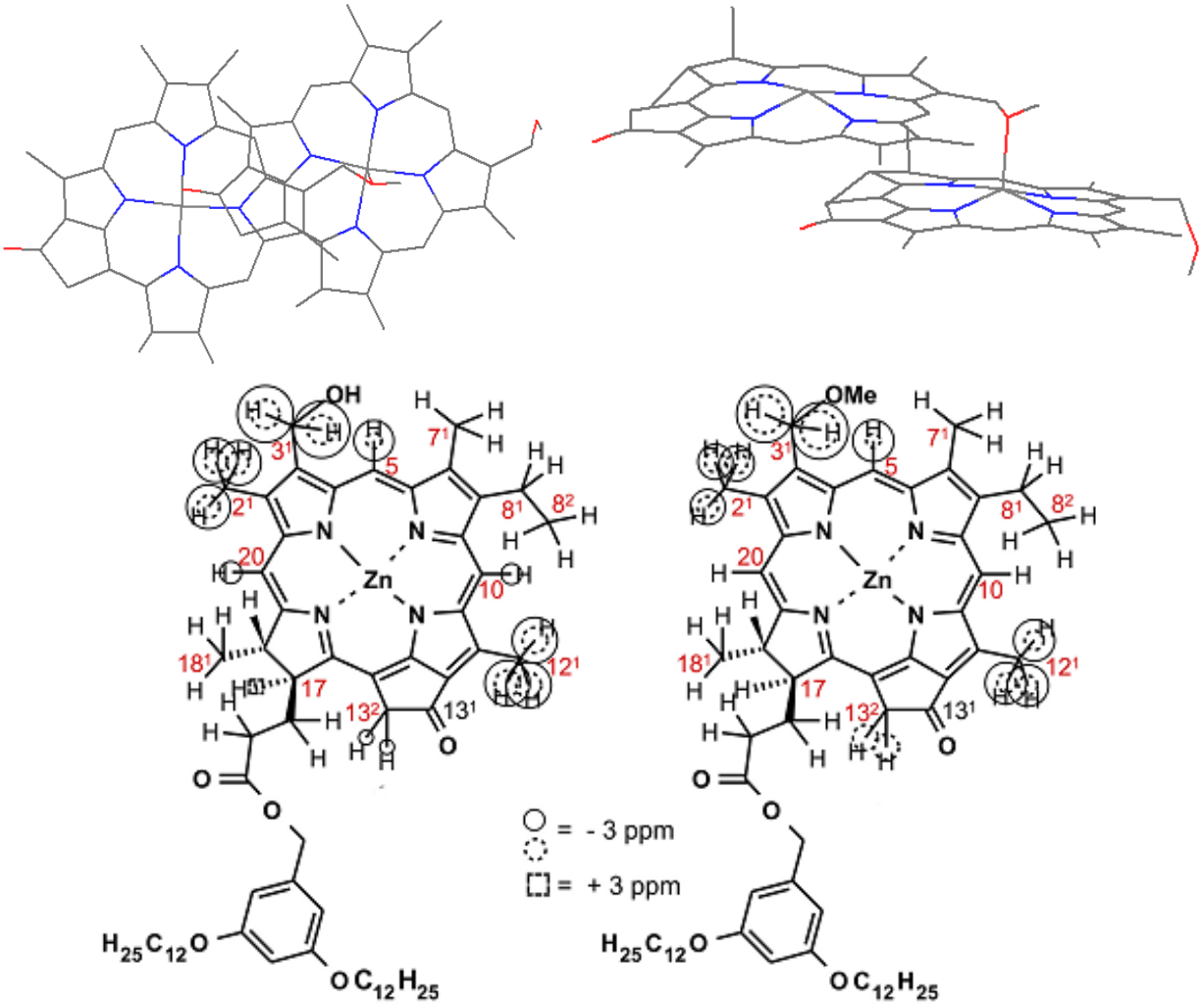

Figure 25. Top: Geometry optimized parallel model top view and side view; Detected ^{1}H upfield aggregation shifts of aggregated ZnChls **1**-OH and **1**-OMe relative to their monomers in THF-d_8 and pyridine-d_5, respectively, are shown as solid grey circles. Calculated ring-current shifts (DFT calculations) for **1**-OH and **1**-OMe in the parallel stack model are shown as dashed black circles. Values less than -3 ppm are depicted. The circles have a radius proportional to the magnitude of the shift.

From the differences between the experimental and the calculated ring-current shifts for the two models (i.e., the parallel and the antiparallel model for both the ZnChls **1**-OH and **1**-OMe compounds) (Table 6), the aggregation shifts of ZnChl **1**-OMe were in very good quantitative agreement with the calculated shifts for the antiparallel stack arrangement (Table 7). On the other hand, the calculated ring-current shifts for ZnChl **1**-OH are only in semi-quantitative agreement with the observed aggregation shifts for the parallel stack model. However, they reproduce the essential features, particularly the combination of very strong aggregation shifts in the 3-CH_2 region and significant 12^1-CH_3 shifts. The magnitude of the aggregation shifts observed for the 12^1-CH_3 protons for both ZnChls **1**-OH and **1**-OMe in the antiparallel arrangement precludes their existence as individual one-dimensional π-stacks in the solid

state. This is because in a single antiparallel stack there is no significant ring overlap in the region of 12^1-CH_3 that could cause such a strong upfield shift (see models in Figures 24 and 25). Overlap with chlorins from adjacent stacks is thus essential.

Table 6. Calculated ring current shifts $\Delta\sigma^{H}_{calc}$ (ppm) for ZnChls **1**-OH and **1**-OMe, each in the parallel stack (P) and antiparallel stack (A) models.

position	$\Delta\sigma^{H}_{\mathbf{1}\text{–OH},calc}$ (P)	$\Delta\sigma^{H}_{\mathbf{1}\text{–OMe},calc}$ (P)	$\Delta\sigma^{H}_{\mathbf{1}\text{–OH},calc}$ (A)	$\Delta\sigma^{H}_{\mathbf{1}\text{–OMe},calc}$ (A)
5	-2.0	-1.8	-4.2	-4.3
10	-0.3	-0.2	1.5	0.3
17	2.1	-0.1	1.1	-0.2
18	1.3	-0.3	1.1	-0.1
20	-0.6	-0.1	0.7	-1.2
2^1	-2.9	-2.7	-5.5	-5.0
3^1	-3.7	-4.9	-6.0	-8.0
7^1	0.4	0.0	-0.7	-0.3
8^1	0.4	0.4	1.3	1.4
12^1	-3.3	-2.5	-4.8	-5.2
13^2	-0.5	-3.3	1.7	0.2
17^1	0.9	-0.1	1.6	-0.1
17^2	-	-	-	-
18^1	1.2	0.2	1.5	0.1

As a result, two or three dimensional network like structures where several antiparallel stacks are in close proximity is envisaged. Also, the dodecyl chains constitute an important factor for the supramolecular organization of the 1D π-stacks of ZnChl **1**-OMe and their stabilization in solid state. On HOPG the lamellar arrangement is most probably favored due to the strong intermolecular interaction of alkyl chains with graphite. Probably the interdigitation of tails between adjoining stacks plays an important role in stabilizing the extended lamellar structure that is observed on surfaces, in contrast with the extended H-bonding present in the natural BChl stacks. Similarly, in the solid state, the alkyl chains play crucial role in space filling leading to overall stabilization of the aggregate structures.

Table 7. Difference of the experimental ($\Delta\sigma$) and calculated ($\Delta\sigma_{calc}$) ring current shifts (ppm) (by DFT calculation) for ZnChl **1**-OH and **1**-OMe, each in the parallel stack (P) and antiparallel stack (A) models.

position	$\Delta\sigma^{H}_{i,\mathbf{1}\text{–OH}} - \Delta\sigma^{H}_{\mathbf{1}\text{–OH,calc}}$ (P)	$\Delta\sigma^{H}_{i,\mathbf{1}\text{–OH}} - \Delta\sigma^{H}_{\mathbf{1}\text{–OH,calc}}$ (A)	$\Delta\sigma^{H}_{i,\mathbf{1}\text{–OMe}} - \Delta\sigma^{H}_{\mathbf{1}\text{–OMe,calc}}$ (P)	$\Delta\sigma^{H}_{i,\mathbf{1}\text{–OMe}} - \Delta\sigma^{H}_{\mathbf{1}\text{–OMe,calc}}$ (A)
5	-3.8	-1.6	-4.2	-1.7
10	-2.7	-1.5	-0.6	-1.0
17	-3.3	-2.3	1.0	-1.1
18	-2.7	-2.5	1.0	0.8
20	-2.6	-3.9	-0.9	-2.2
2^1	-3.5	-0.9	-2.4	-0.1
3^1	-4.5	-2.2	-3.3	-0.2
7^1	-2.0	0.9	-0.7	-0.4
8^1	-2.0	-2.9	-0.3	1.3
8^2				
12^1	-3.3	-1.8	-3.5	-0.8
13^2	-1.6	-3.8	2.9	-0.6
17^1	-2.0	-2.7	-0.4	0.6
17^2	-	-	-	-
18^1	-1.9	-1.2	0.5	0.6

The aggregates of ZnChl **1**-OH was also modelled in the closed dimer model, which has been discussed in the literature.[58,59] Calculation of the ring-current shifts revealed a substantial mismatch that allowed the elimination of this packing model (Figure 26). Moreover, ZnChls **1**-OH and **1**-OMe show an aggregate bathochromic shift of the Q_y bands of ~ 80-100 nm in non-polar solvents,[26,30] and such larger shifts are unlikely for dimer aggregates. Since similar solvent combinations are used to obtain aggregates in solid state, closed dimer aggregates are unlikely. It has been discussed in section 3.2.2 that ZnChl **1**-OH self-assemble into extended aggregates via an isodesmic pathway whereas **1**-OMe self-assemble by a highly cooperative nucleation-elongation pathway. No intermediate dimeric species was observable in both cases. Moreover, DLS studies and very broad solution NMR signals of these aggregates indicated very large aggregate sizes rather than dimers in solution. Based on these considerations, the closed dimer model could be safely eliminated.

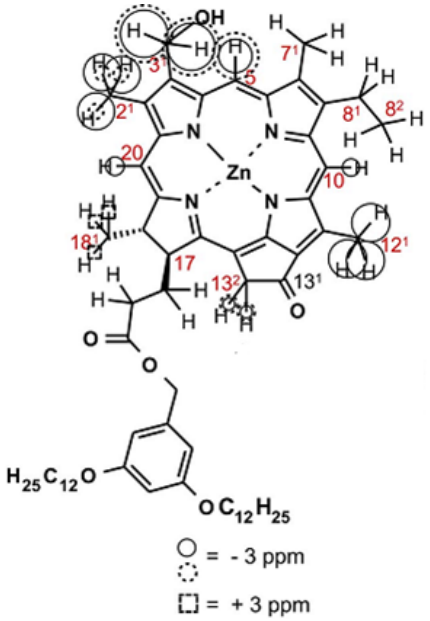

Figure 26. Detected ^{1}H upfield aggregation shifts of aggregated ZnChl **1**-OH relative to their monomers in THF-d_8. Calculated ring-current shifts for **1**-OH in the closed dimer model are shown as dashed black circles whereas solid circles represent the experimentally observed ring current shifts.

Powder X-ray diffraction[c]: To gain further insight into the 3D packing of π-stacked ZnChl **1**-OMe in the solid state, XRD was measured for ZnChl **1**-OMe at 80 °C and at RT and shown in Figure 27. Both diffraction patterns show non-equidistant and very sharp reflections in the small and wide angle regions which confirm a highly ordered three-dimensional arrangement of these dyes. In addition, the wide angle scattering at 80 °C shows a diffuse part with its maximum at about 4.5 Å ($2\theta \approx 20°$), which could be attributed to a partially liquid-like packing of the 17^2-dodecyl chains. The small-angle reflections could be indexed with satisfactory accuracy on a primitive two-dimensional rectangular unit cell with lattice constants a = 28.6 Å and b = 32.3 Å (*cf.* experimental and calculated d spacings in Table 8). The three strongest reflections in the wide-angle region are also numbered (reflections 9-11). The sharp peak at 2θ = 26° (reflection 11) indicates a definite long-range order in the structure of the ZnChl **1**-OMe with intervals of 3.4 Å. This value is characteristic of densely π-stacked dyes and corresponds to the inter-planar distance of the zinc chlorins in the direction perpendicular to the two-dimensional cell. This assumption is supported by the literature known π-π distances in crystals of stacked zinc porphyrins (3.46 Å).[63, 64] A comparison with the dimensions measured for the packing obtained from the MM+ optimized antiparallel stack model shows that twice the distance between the ZnChl **1**-OMe molecules

[c] X-ray diffraction data was measured by Dr. Ute Baumeister, Universität Halle.

along the stacking direction is a periodic one and can be considered as the third dimension $h = d_{(\text{reflection 11})} = 6.8$ Å in an orthorhombic 3D unit cell with a volume of $V_E = a \times b \times h = 6.28$ nm^3. On the other hand, one molecule of ZnChl **1**-OMe in the crystalline state has an approximate volume of 1.47 nm^3 estimated according to the volume increment method of Immirzi and Perini.[65] Thus, the unit cell should contain four molecules of ZnChl **1**-OMe with a molecular volume of 1.57 nm^3, a reasonable value for the less dense phase at 80 ^{o}C which is also consistent with the packing model. Using the lattice parameters from the hyperchem models used for NMR ring current shift calculations, it could be indexed as 201, and in the packing model, the Zn atoms occupy this lattice plane comparatively densely. A possible space group consistent with these considerations could be proposed as $P2_122_1$. As can be seen in Figure 27, however, the strongest reflections were only slightly changed in position and intensity (reflections 1, 2, 3, 9, 10, 11). Thus, even though the space group symmetry might be different at room temperature, the principal packing mode for the π-stacks appears to be the same as observed at 80 °C where the alkyl chains are partially molten and the material transforms into a less ordered soft crystalline phase. Figure 28 shows the antiparallel stack model as derived from NMR studies and MM+ calculations and a schematic depiction of the corresponding 3D packing model that was derived from the XRD data collected at 80°. It was however not possible to uniquely index the XRD pattern at ambient temperature.

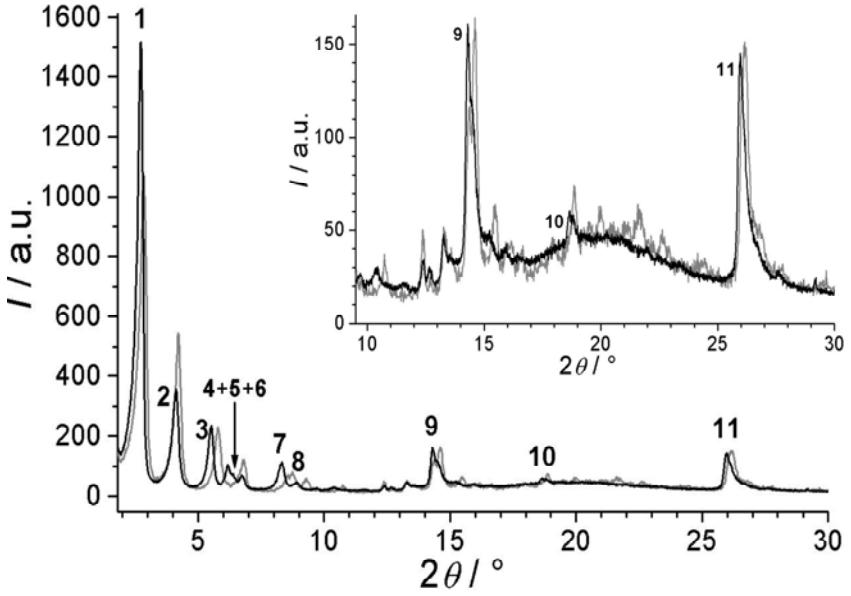

Figure 27. Powder X-ray diffraction pattern of ZnChl **1**-OMe at ambient temperature (grey lines) and at 80 °C on heating (black lines). Inset shows an enlarged plot of the wide angle range; numbers indicate the reflection numbers for the pattern at 80 °C used in Table 4.

Table 8. Assignment of the powder X-ray pattern of small and wide angle reflections of ZnChl **1**-OMe for a primitive two-dimensional rectangular lattice with lattice constants a = 14.3 Å and b = 64.6 Å; experimental (d_{exp}) and calculated (d_{calc}) d values; *hk*: assigned indices; d_{exp}-d_{calc} (Å): error of the calculated d values.

Reflection number	2Θ (°)	d_{exp}(Å)	hk	d_{calc} (Å)	d_{exp}-d_{calc} (Å)
1	2.73	32.4	02	32.3	0.1
2	4.11	21.5	03	21.5	0.0
3	5.51	16.0	04	16.1	-0.1
4	6.16	14.3	10	14.3	0.0
5	6.40	13.8	11	14.0	-0.2
6	6.74	13.1	12	13.1	0.0
7	8.30	10.6	06	10.8	-0.2
			14	10.7	-0.1
8	8.89	9.9	15	9.6	0.3
9	14.4	6.2			
10	18.7	4.7			
11	26.0	3.4			

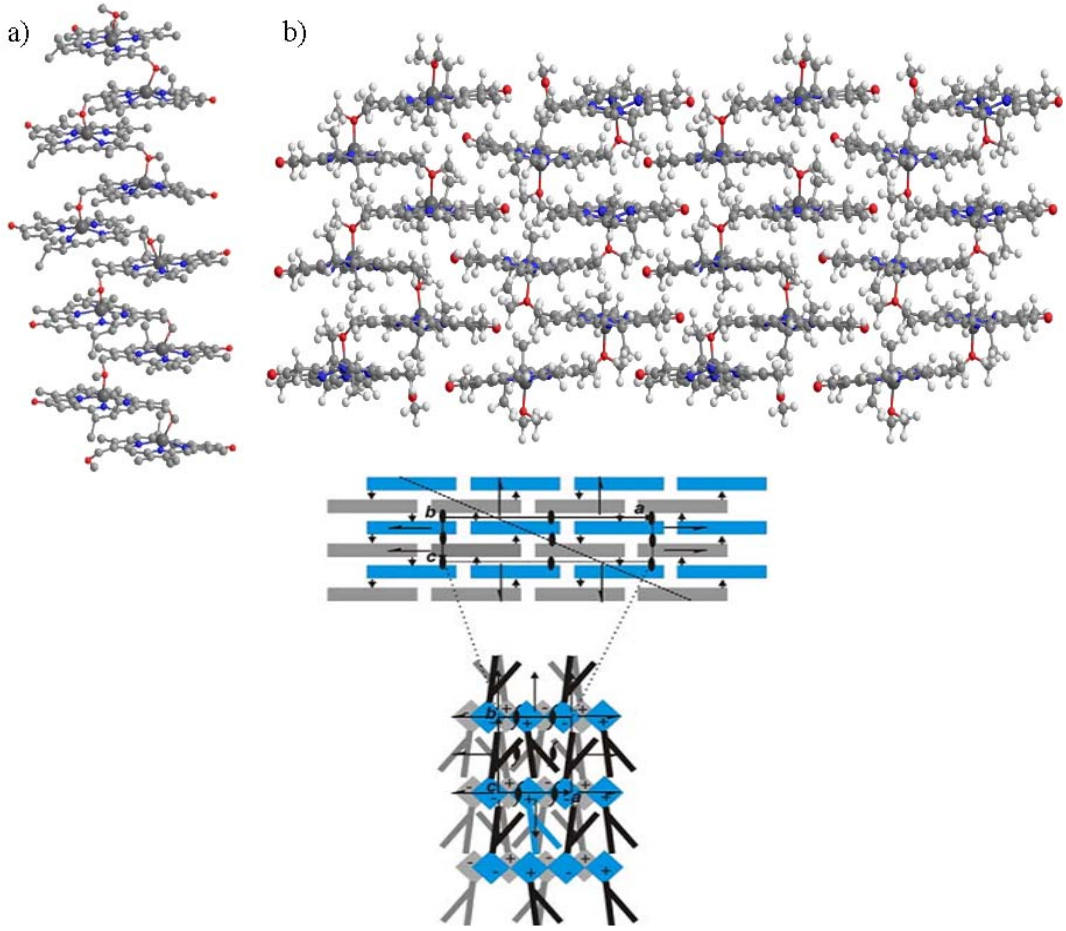

Figure 28. Proposed 3D packing of ZnChl **1**-OMe in an alternating antiparallel stack arrangement: a) Antiparallel single stack and b) multiple antiparallel stack model of **1**-OMe derived from MM+ calculations; c) schematic representation of a possible packing obtained by combination of NMR and X-ray data with unit cell axes a, b, and c in projections along b (top) and c (bottom). The arrows and +/- signs, respectively, show the direction of the O–Zn coordinative bond within an individual stack. Additionally, the symmetry elements for this packing (space group $P2_122_1$) are shown. The dashed line indicates a lattice plane parallel to (201), which is comparatively densely occupied by Zn atoms in this model.[66]

Followed by detailed structural studies on ZnChl tubular and stacked aggregates, their charge transport properties were investigated in detail in order to explore the suitability of these assemblies for biosupramolecular electronics.

3.2.6. Charge carrier mobility of zinc chlorin rod and stack aggregates

One of the key parameters that determines the performance of organic materials in (opto)electronic devices is their intrinsic charge carrier mobility.[15,31,32,67] The charge carrier mobilities of aggregates of ZnChls were measured using the PR-TRMC technique,[d] which has been used to determine charge carrier mobilities in a large number of organic materials in the past.[31,32] PR-TRMC is a contact-free technique that is not affected by space-charge effects and can be applied to bulk materials as well as to single polymer chains in solution.[31,32] With this technique, the charges are directly generated in the bulk, their transport properties are probed on a very local spatial scale and the charges trapped by impurities or structural defects are not responsive. Charge transport properties depend on (supra)molecular organization and long-range order inside the material. PR-TRMC measurements have been performed for the 3^1-hydroxy and 3^1-methoxy ZnChl aggregates and their intrinsic charge carrier mobilities have been obtained. In addition to the charge carrier mobility, useful information about the morphology of the sample can be deduced from the decay kinetics of the conductivity transients in the two aggregates.

PR-TRMC measurements were performed on the 3^1-hydroxy ZnChls **1**-OH, **2**-OH, **3**-OH and the 3^1-methoxy ZnChls **1**-OMe, **2**-OMe. The difference in the solid state, solution aggregate structures of **1**-OH and **1**-OMe have strong consequences on their charge transport properties and distinct differences in the charge carrier dynamics in these materials could be observed. In Figure 29, comparison of the radiation-induced conductivity change in ZnChls **1**-OH and **1**-OMe is shown. In this figure, the changes in conductivity per unit of the energy deposited by the electron pulse ($\Delta\sigma$/D) are plotted as a function of time. The conductivity of the sample increases upon irradiation with 10 ns pulse due to the creation of mobile charge carriers. Subsequently, the charge carriers either recombine or get trapped resulting in reduction of conductivity that eventually goes to zero. There are distinct differences in the magnitude of the conductivity signal and the conductivity lifetimes for the 3^1-hydroxy and 3^1-

[d] Charge carrier mobilities were measured by Dr. Sameer Patwardhan in the group of Prof. Dr. Laurens D. A. Siebbeles at the Technical University of Delft.

methoxy ZnChls (Figure 29). For the 3^1-hydroxy ZnChl **1**-OH, relatively low but long living conductivity transient was obtained, while the corresponding 3^1-methoxy ZnChl **1**-OMe exhibit much higher but shorter living signals (Figure 29a). Similar trends in the PR-TRMC transients were observed for the zinc chlorin pair of **2**-OH/**2**-OMe (Figure 29b) although the conductivities were lower for the **2**-OH/**2**-OMe pair compared to those of **1**-OH/**1**-OMe.

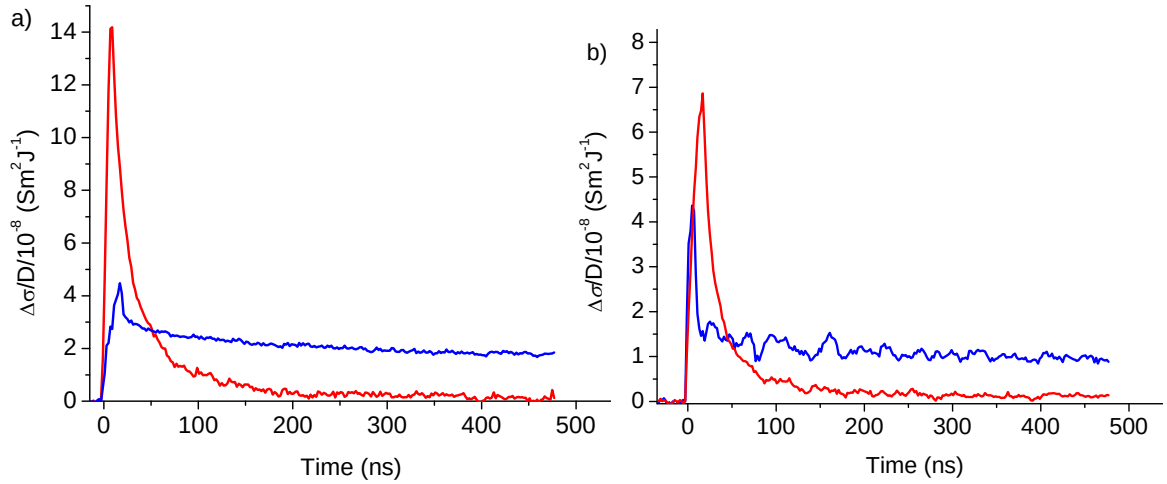

Figure 29. Transient change in conductivity of ZnChls a) **1**-OH (blue line) and **1**-OMe (red line) and b) **2**-OH (blue lines) and **2**-OMe (red lines) upon irradiation with a 10 ns electron pulse.

The temporal decay of the conductivity results from either a decrease in the mobility of the charge carriers due to localization at domain boundary or trapping sites, or from a decrease in the concentration of charge carriers via charge recombination.[68] The decay of the radiation-induced conductivity with time is plotted for different electron pulse duration in Figure 30 for ZnChls **1**-OH and **1**-OMe. The decay of electro-generated charge carriers is first-order mono-exponential for compound **1**-OH (rod) and half-life for conductivity signal is of the order of few microseconds (Figure 30a). Similar behavior is found for discotic liquid crystals (DLCs) that form one dimensional columns of aromatic cores surrounded by hydrophobic side chains.[31,32] This may suggest that in the 3^1-hydroxy ZnChls, the decay of the conductivity occurs mostly due to slow trapping of the charges along the tubular aggregates and the subsequent recombination takes place via tunneling through the surrounding insulating hydrocarbon mantle, as observed for several DLCs. On the other hand, second order effects are present in conductivity transients of **1**-OMe where much faster moving charges recombine on the timescale of ten(s) of nanoseconds (Figure 30b). Theoretical investigation predicts that second order effects are very pronounced only for two- and three-dimensional networks but not for one-dimensional columnar systems.[32] This suggests that the stacks in **1**-OMe also form

two- or three-dimensional network in solid state, which is consistent with the proposed solid-state aggregate structure discussed earlier, whereas the 3^1-hydroxy zinc chlorins forms one dimensional tubular structures.

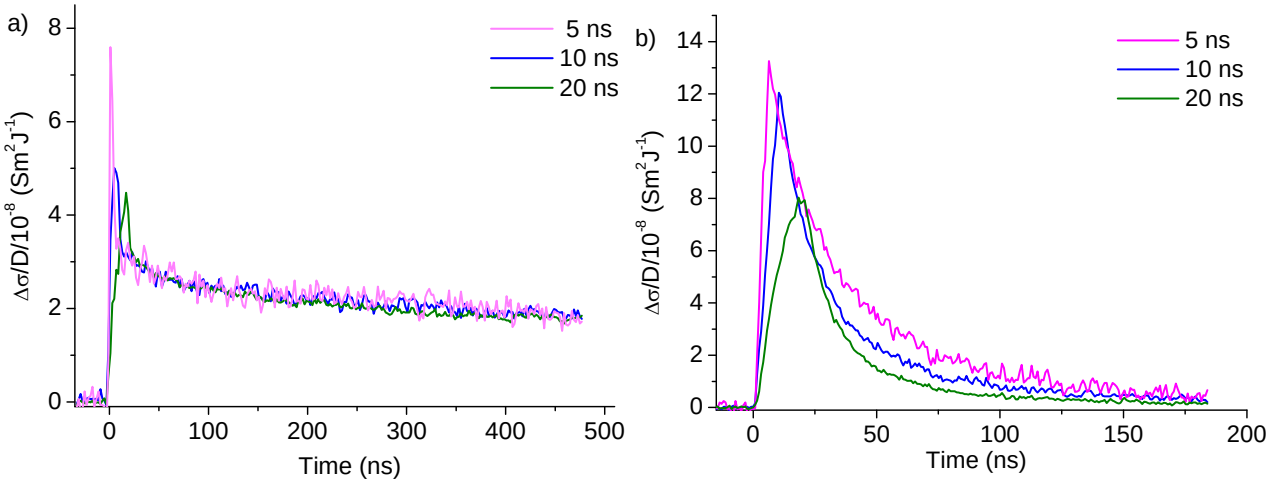

Figure 30. Transient change in conductivity for ZnChls **1**-OH and **1**-OMe for varying electron pulse durations (5, 10 and 20 ns).

In order to estimate the charge carrier mobility from the conductivity, the concentration of charges that were generated by irradiation must be known. Although this can not be directly determined, a good estimate of the concentration of charge pairs (electrons and holes) can be made by using a charge scavenging model that has previously been applied for DLCs.[31] In this way the concentration of charge pairs at the end of the irradiation pulse is obtained and hence the sum of the mobility of the positive and negative charges can be estimated. The charge carrier mobility values obtained for ZnChls **1-3** are listed in Table 9. In both cases the mobilities in the 3^1-OMe compounds (1D stacks) are higher than the corresponding 3^1-OH counterparts (rods). Moreover, the mobilities are comparable or higher than structurally related tetrapyrrole counterparts porphyrin and phthalocyanine liquid crystalline materials.[8,9]

Charge transfer integral is an important parameter that determines the charge transport properties of organic materials.[15,31,32] The primary stacking in zinc chlorin J-aggregates is directed by local interactions such as coordination of 3^1-oxygen to the zinc ion which reduces the charge transfer integral due to the lateral shift of cores with respect to each other. At the same time it reduces lateral and twist motion of cores presumably due to zinc-oxygen coordination. In spite of these structural constraints, the charge mobilities that are obtained for ZnChls are very high, comparable to those of DLCs (from 10^{-3} upto 1.0 cm^2/Vs for HBCs).

Table 9. Room temperature charge carrier mobilities of ZnChls **1**-**3**-OH and **1**, **2**-OMe.

ZnChl	**1**-OH	**1**-OMe	**2**-OH	**2**-OMe	**3**-OH
Charge carrier mobility (cm^2/Vs)	0.07	0.28	0.05	0.08	0.04

In order to explore the possible effect of intermolecular coordination of the oxygen atom at 3^1-position to the zinc ion on the charge carrier mobility, conductivity measurements were performed for ZnChl **1**-OH that contains zinc ion and the corresponding free-base chlorin **1'**-OH as reference compound. The presence of the coordination has a distinct effect on the charge carrier mobility as evident from the conductivity transients of **1**-OH and **1'**-OH shown in Figure 31. The mobility of charges in **1**-OH (~ 0.07 cm^2/Vs) is significantly higher than the corresponding free-base chlorin (~ 0.01 cm^2/Vs). Surprisingly, the lifetime of conductivity transient is long for both compounds, i.e., ~ 1.37 µs and ~3 µs for **1**-OH and **1'**-OH, respectively, at room temperature. The appreciable charge mobility value of the latter indicates that stacking of chlorin cores prevail inspite of the fact that the building blocks lack the central metal ion. This is in line with the fact that for ZnChl **1**-OH (and **1**-OMe), the stabilization of self-assembled structures is predominated by π-stacking and hydrophobic interactions.[65] The lower mobility of **1′**-OH can be attributed to higher disorder within the aggregate as a result of the absence of zinc-oxygen coordination.

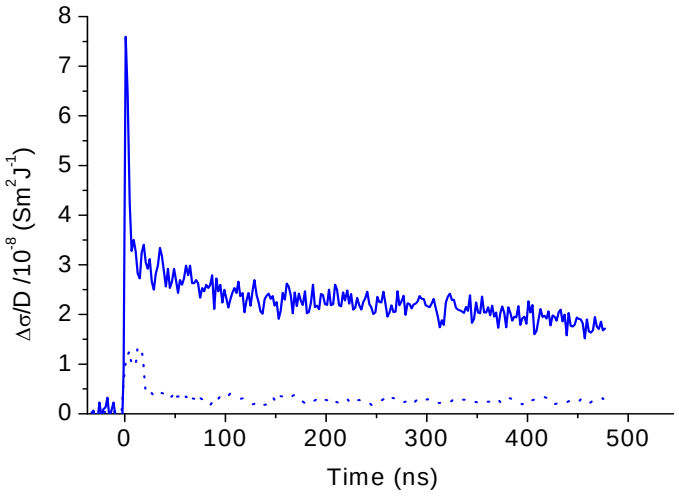

Figure 31. Transient change in conductivity for zinc chlorin **1**-OH (solid line) and corresponding free-base chlorin **1'**-OH (dotted line) upon irradiation with 10 ns electron pulse.

The temperature-dependent charge carrier mobilities for 3^1-hydroxy ZnChls **1-3**-OH are tabulated in Table 10 in the sequence of temperature steps taken while performing the experiment and plotted in Figure 32. The charge carrier mobilities were found to gradually increase with temperature pointing towards a thermally activated charge hopping along the zinc chlorin tubular aggregates. For ZnChls **1**-OMe, **2**-OMe compounds the charge carrier mobility for the fresh samples were considerably higher than those for the OH derivatives, however, the mobility values decreased upon annealing the samples. Charge carrier mobilities are directly related to the size and planarity of aromatic cores.[67] Considering that ZnChls **1-3** OH and **1**, **2**-OMe have moderately sized and non-planar chlorin cores as well as significant amounts of electronically inactive material in form of two or three dodecyl or polyethyleneglycol side chains, the charge carrier mobilities obtained for these aggregates are appreciably high. Previously, hole mobilities of the order of 10^{-4}-10^{-5} cm^2/Vs were determined in microcrystalline Chl *a* with time of flight measurments.[24] In the framework of disorder formalism of Bässler and co-workers, maximum hole mobility of 0.002 cm^2/Vs for microcrystalline Chl *a* was predicted in the absence of disorder. The charge carrier mobility values observed for ZnChl tubular and stack aggregates are thus two order of magnitude higher compared to those of microcrystalline Chl *a*.[24]

Table 10. Temperature-dependent charge carrier mobilities of ZnChls **1**- **3**-OH obtained from PR-TRMC measurements.

Temp. (^oC)	Charge carrier mobility, μ (cm^2/Vs) **1**-OH	Temp. (^oC)	Charge carrier mobility, μ (cm^2/Vs) **2**-OH	Temp. (^oC)	Charge carrier mobility, μ (cm^2/Vs) **3**-OH
20	0.0678	25	0.0391	25	0.0287
0	0.0593	0	0.0391	-25	0.0170
-20	0.0516	-25	0.0391	25	0.0276
-40	0.0471	-50	0.0370	50	0.0340
-60	0.0438	0	0.0411	100	0.0425
-40	0.0464	50	0.0514	25	0.0287
-20	0.0508	100	0.0617		
0	0.0568	25	0.0411		
20	0.0651	25	0.0391		
40	0.0734	0	0.0391		
60	0.0801				
80	0.0902				
100	0.1209				
80	0.1067				
60	0.0886				

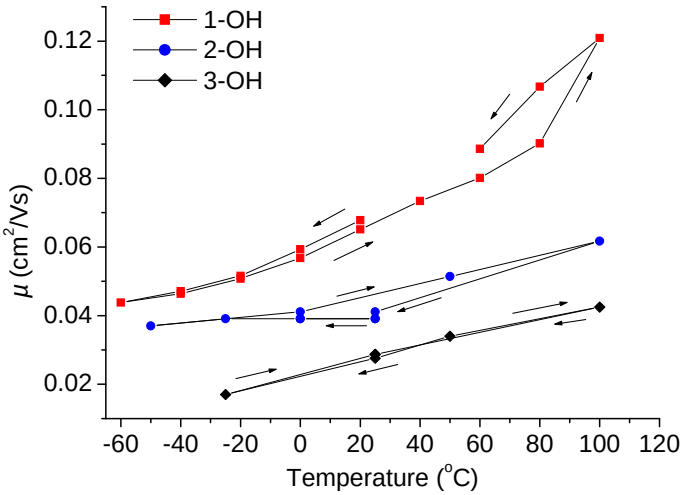

Figure 32. Temperature-dependent charge carrier mobilities of 3[1]-hydroxy ZnChls **1**-, **2**-, **3**-OH indicative of thermally activated transport of charge carriers. Arrows indicate the temperature sequence in which mobility measurements have been performed.

3.2.7. Supramolecular chlorin nanowires: Conductive AFM measurement

Supramolecular one-dimensional assemblies in the length scale of 10-100 nm are promising to serve as nanoelectronic components. However, it is challenging to develop methodologies to connect such assemblies to electrodes in order to construct nanocircuits. For the first time, direct electrical transport was measured in tubular assemblies of ZnChl **3**-OH employing a special operation mode of AFM namely, conductive AFM or I-AFM (*current*-AFM)[e] that offers a direct method to measure the electrical conductivity of single nanowires. Electrical characterization was performed on isolated ZnChl nanotubular assemblies on a non-conductive substrate with conductive AFM technique. Owing to its hydrophilicity, it was possible to align the tubular aggregates of ZnChl **3**-OH onto non-conductive substrates such as mica or silicon oxide. Consequently, single nanotubes of ZnChl **3**-OH could be adsorbed on silicon oxide surface by spin-coating aggregates of **3** in water/methanol (100:1) and the measurements were performed in air. Interestingly, deposition of ZnChl **3**-OH aggregates onto insulating surfaces such as silicon wafer allowed the contacting of single ZnChl **3**-OH nanowires by a conductive polymer PEDOT:PSS and consequently the analysis of the electronic properties of these tubular aggregates. The topography was measured in contact mode AFM with a conductive tip. During scanning a bias voltage was applied between the conductive polymer and the conductive AFM tip and the resulting current which flows between tip and sample was measured with an external current amplifier. From the current

[e]Conductive AFM measurement was performed by Dr. Daniel Ebeling in the group of Prof. Dr. Lifeng Chi at Universität Münster.

image (Figure 33a), it is evident that a current (~ 1-2 pA) flows through the nanorods of ZnChl when electrically contacted to the conductive polymer.

In the next step, the conductivity of the zinc chlorin nanowires could be quantified and the current images of the conductive nanowires could be analyzed in detail. Figure 33b shows the current image of the performed measurement and the analysis is shown in Figure 33c. Current values of ~ 1-3 pA were measured at every point of the single nanotubes and the conductivity of these wires could be calculated. For this purpose the current was analyzed as a function of length of the nanotube (Figure 33b) and the resistance could be calculated according to Ohm's law (Figure 33c). Since the resistance of a conductive (cylindrical) wire is proportional to its length according to the equation $R = L/\sigma A$ where R is the resistance, σ is the conductivity, L is the length of the wire and A is the area of the cross section of a cylindrical structure, σA could be calculated from the obtained slope of plot of R vs L. For ZnChl **3**-OH, TEM has provided convincing evidence for tubular aggregates hence a tubular model has been considered for the evaluation of the conductivity of these aggregates. Considering an average diameter of 6 nm and hence a radius of ~ 3 nm for the nanotubes of ZnChl **3**-OH, the cross section area, A could be calculated and conductivity value (σ) of 0.3 S/m could be obtained for ZnChl **3**-OH aggregates. It was also possible to analyze other isolated nanowires of ZnChl **3**-OH which showed high conductivities of ~ 0.2-0.5 S/m. These results confirm the substantial charge transport properties observed in bulk for the aggregates of ZnChl **3**-OH. This is the first example of direct electrical conductance measurement in semisynthetic zinc chlorin tubular assemblies.

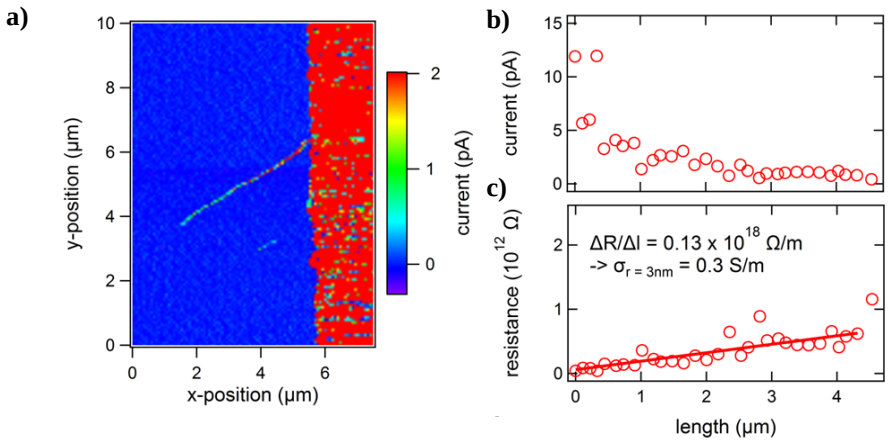

Figure 33. a) Topography image (7.5 * 10 µm²) of ZnChl **3**-OH nanowire adsorbed to a silicon oxide surface. The nanowire is electrically connected to a thin layer of conductive polymer (PEDOT:PSS) in the right part of the image. b) Measured current and c) resistance of the nanowire as a function of its length. The slope of the resistance is used to determine the conductivity of the nanowire assuming a radius of 3 nm of the wire. AFM parameter: I-AFM mode, scan rate: 0.5 Hz, sample bias: 0.5 V, Cantilever: PPP-CONTPt, Nanosensors.

Despite the highly efficient charge transport observed in the aggregates of semisynthetic ZnChls, there is currently no clear understanding of the mechanism which might control the mobility of charge carriers through these superstructures. However, the results reveal that charge carrier transport is highly favored in one-dimensional tubular aggregates of 3^1-hydroxy ZnChls as well as in stacks formed by 3^1-methoxy ZnChls. In 3^1-methoxy ZnChls, interstack charge migration presumably takes place and higher charge carrier mobilities as well as faster charge recombination are observed compared to 3^1-hydroxy ZnChls. In light of all the studies and the above discussion, it can be concluded that highly efficient charge transport observed both in the 3^1-hydroxy and 3^1-methoxy functionalized zinc chlorins is strongly dependent on supramolecular structures.

3.3. Conclusions

To summarize, semisynthetic 3^1-hydroxy ZnChls **1**-OH–**3**-OH and 3^1-methoxy ZnChls **1**-OMe, **2**-OMe self-assemble into tubular and stacked assemblies, respectively (Figure 34). Temperature-dependent UV/Vis and CD studies indicated distinct aggregation mechanisms i.e., isodesmic pathway for rod/tubular aggregates and cooperative nucleation elongation pathway for stack aggregates and DLS studies indicate large aggregate sizes in solution. Furthermore, well-defined hollow tubular assemblies could be visualized for ZnChl **3**-OH by electron microscopy i.e., TEM and STEM for the first time.

Based on thermodynamic considerations of self-assembly, ZnChl **1**-OMe can be proposed to self-assemble in a highly cooperative fashion into extended 1D stacks, which probably assemble further into 2D structures in solution. No intermediate (dimeric) species between monomer and extended aggregates was observable. The optical properties of **1**-OMe were studied theoretically by calculation of exciton couplings using a transition density formalism. This study suggested that the inherent chirality and precise stereochemical orientation of ZnChls influence the observed CD spectra and pointed to a structure with distinct helicity and alternative twist angles of 0 ^{o}C and 110 ^{o}C between neighboring molecules. The extended structures of **1**-OMe are indeed evident from detailed studies on solid state packing behavior of ZnChl **1**-OMe. The specific aim was to resolve the packing of ZnChls in the solid state by means of an effective method that combines proton chemical

shifts obtained from solid state MAS NMR, solution monomer shifts, molecular modelling and DFT calculations. The experimental aggregation shifts of ZnChls **1**-OH and **1**-OMe were well reproduced by ring-current shift calculations for the antiparallel stacking mode. From powder XRD of **1**-OMe, a molecular volume of 3.14 nm^3 was obtained and a unit cell that can accommodate two molecules arranged in the antiparallel fashion. Consequently, the local antiparallel model could be extended to a 3D periodic packing arrangement (Figure 34).

Finally, charge transport properties of aggregates of 3^1-hydroxy ZnChls **1**-**3**-OH and 3^1-methoxy ZnChls **1**, **2**-OMe have been investigated in solid state by PR-TRMC technique. Stack aggregates of 3^1-methoxy ZnChl possess very high charge carrier mobilities up to ~ 0.28 cm^2/Vs at RT, whereas corresponding tubular aggregates of 3^1-hydroxy ZnChls possess charge carrier mobilities of ~ 0.07 cm^2/Vs-0.1 cm^2/Vs. One-dimensional charge transport is facilitated in tubular assemblies of 3^1-hydroxy zinc chlorins. Whereas, in 3^1-methoxy zinc chlorins, interstack charge migration presumably takes place and higher charge carrier mobilities as well as faster charge recombination are observed compared to 3^1-hydroxy zinc chlorins (Figure 34).

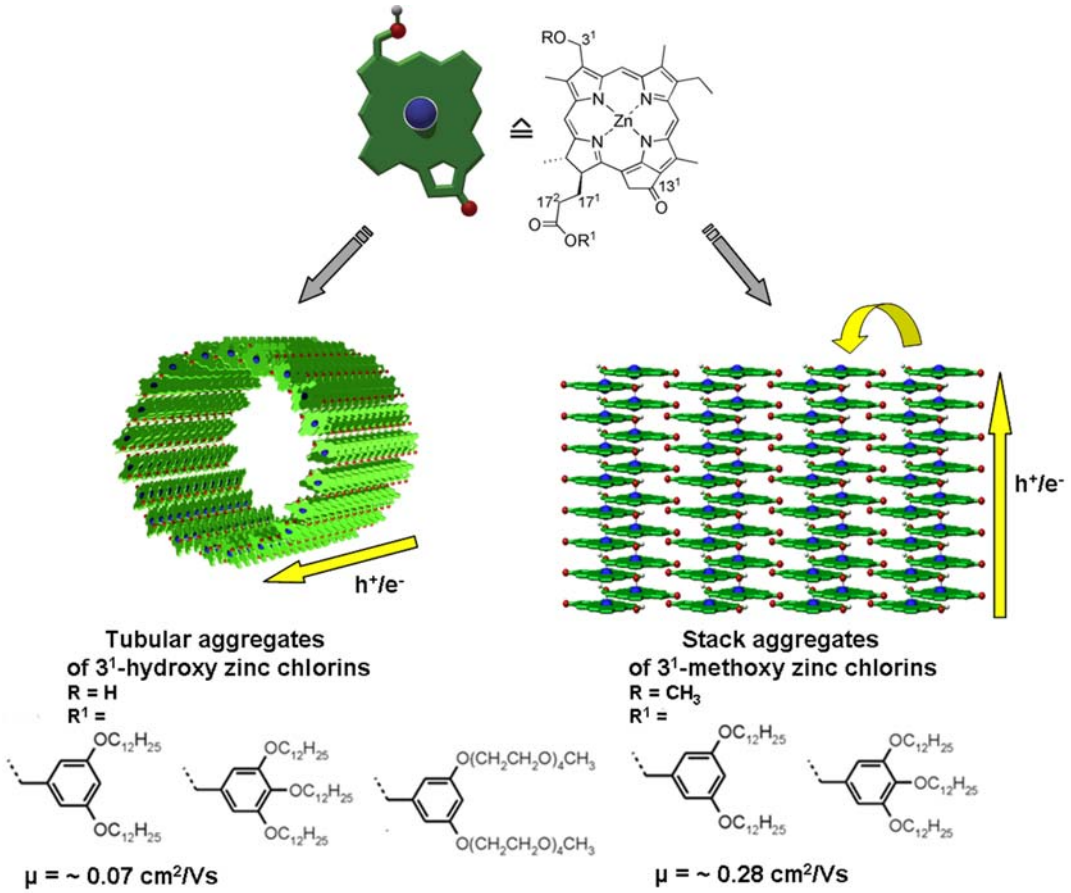

Figure 34. Schematic representation of summarised aggregate structures of 3^1-hydroxy and 3^1-methoxy ZnChls and the respective charge transport properties of these aggregates.

The charge transport properties (mobilities, life-times and decay kinetics) correspond well with the higher crystallinity of ZnChl **1**-OMe stacks derived from various spectroscopic, crystallographic, scanning probe microscopic and electron microscopic studies. Electrical characterization was performed on isolated nanotubes of ZnChl **3**-OH on non-conductive substrate with conductive AFM technique. These nanowires were found to conduct charges efficiently over micrometer length scale, with a very high conductivity of ~ 0.3 S/m that varies linearly with the length of the wires.

Our findings in this chapter have revealed profound structure-function correlation of ZnChl tubular and stack assemblies that should contribute to the knowledge base prerequisite for bottom-up fabrication of supramolecular electronic devices. Utilization of these dye assemblies, for instance, in field effect transistors, is thus conceivable in the future.

3.4. Experimental section

Reagents and Solvents: All the reagents and chemicals commercially obtained from Merck, Acros, Aldrich or Fluka were used as such without further purification.

Thin Layer Chromatography (TLC): TLC experiments were performed on aluminium plates, which were coated with silica gel 60 F254 and a concentration zone, purchased from Merck KGaA (Hohenbrunn, Germany).

Melting Points: Melting points were determined using a Olympus Bx41 polarization microscope (Olympus GmbH, Hamburg, Germany) equipped with a heating stage (THMS 600, Linkam, Great Britain) and are uncorrected.

Column Chromatography: Flash and normal pressure column chromatography were done using silica gel Si60 (mesh size 0.032-0.063 mm) from Merck KGaA (Hohenbrunn, Germany) as stationary phase. The eluents are mentioned in the respective procedures. Column chromatography of chlorin derivatives was carried out in a darkened hood.

High Performance Liquid Chromatography (HPLC): Analytical HPLC was performed on a system (PU 2080 PLUS) with a photodiode array detector (MD 2015) from JASCO equipped with a ternary gradient unit (LG 2080–02) and line degasser (DG-2080-533). Semipreparative HPLC was performed on a system (PU 2080 PLUS) with a photodiode array detector (UV 2077 PLUS) from JASCO. HPLC grade solvents (Rectapur) from VWR

(Darmstadt, Germany) were used. Reverse phase columns obtained from Macherey-Nagel (Germany) (analytical: EC 250/4.6 NUCLEODUR 100-5 C18 ec, pre-column: CC 8/4 NUCLEODUR 100-5 C18 ec; semipreparative: SP 250/21 NUCLEODUR 100-7 C18 ec, pre-column semipreparative: SP 50/21 NUCLEODUR 100-7 C18 ec).

Mass Spectrometry (MS): The high resolution electron spray ionisation (ESI) mass spectra were measured with a Bruker Daltonics Micro TOF Focus instrument.

UV/Vis Spectroscopy: All spectroscopic measurements were performed in pure spectroscopic grade solvents (Merck UVASOL) in 0.5 cm or 1 cm quartz glass cuvettes. Studies for the monomers and aggregates of zinc chlorins were performed in water free solvents *n*-hexane, *n*-di-butyl ether and THF (dried and distilled over sodium). The UV/Vis spectra were measured with a PE Lambda 40 P instrument from Perkin Elmer GmbH (Rodgau, Germany) under ambient conditions. Molar extinction coefficients ε were calculated according to Lambert-Beer's law and are referred to respective monomers.

NMR measurements: The ^{1}H NMR solution spectra were recorded at 25 °C with a 400-MHz spectrometer (Bruker). Chemical shifts (δ) are relative to TMS. The monomer ^{1}H shifts were determined in coordinating solvents, for zinc chlorin **1**-OH in THF-d_8 and for zinc chlorin **1**-OMe in pyridine-d5. Zinc Chlorin **1**-OMe has enhanced solubility in pyridine-d5 than in THF-d8. To prepare bulk samples for the solid-state NMR measurements, the HPLC purified dyes were dissolved in a minimum amount of THF and dichloromethane, respectively, and 10 equiv. of *n*-hexane was added to each to form the aggregates in solution. The aggregates were precipitated at 0 °C, solvents were removed under vacuum with a rotary evaporator. The solids were dissolved in dioxane and the frozen solutions were lyophilized for 2–3 days to transform the aggregates into solid powders that can be packed tightly in the NMR rotors. All MAS NMR experiments were performed with a Bruker AV-750 spectrometer equipped with a 4-mm triple resonance MAS probe head, using a ^{13}C radio frequency of 188.6 MHz and a sample temperature of 298 K. A spinning frequency of 13 kHz ± 5Hz was used for the 2D ^{1}H-^{13}C heteronuclear correlation experiments. The ^{1}H spins were decoupled during acquisition using the two-pulse phase modulation (TPPM) scheme. Two-dimensional ^{1}H-^{13}C heteronuclear correlation datasets were obtained by using the frequency-switched Lee-Goldburg (FSLG) experiment, by using a short cross-polarisation (CP) time of 256 μs and a ^{1}H 90° pulse of 3.1 μs. The ^{1}H chemical shift scale was calibrated from a FSLG spectrum of solid tyrosine HCl salt. For each of 256 steps in the indirect ^{1}H dimension, 1536

^{13}C scans were accumulated. All geometry optimizations were done using molecular mechanics in Hyperchem 7 with MM+ force field and used a Polak-Ribiere conjugate gradient algorithm with a gradient convergence criterion of 0.01 kcal/mol.

Dynamic light scattering (DLS): DLS measurements were performed at 25 °C on a N5 Submicron Particle Size Analyzer, Beckman Coulter, using a 25 mW helium-neon laser (632.8 nm). Sample solutions were filtered into a dust-free vial through a 0.45 mm hydrophobic polytetrafluoroethylene (PTFE) filter. Data were collected at a scattering angle of 10.6^o, 15.1^o, 22^o, 28.8^o, 63.8^o and 90^o and analyzed with a photon correlation spectroscopy (PCS) control software.

Transmission electron microscopy (TEM): TEM measurements were performed on a Siemens Elmiskop 101 Electron Microscope at the Biocenter of Würzburg University, operating at an acceleration voltage of 80 kV. For the observation of aggregates, a drop of sample suspension was placed on 300-mesh formvar copper grids coated with carbon. About 2 min after the deposition, the grid was tapped with filter paper to remove solvent (i.e., organic solvent or water) to yield a thin film with a thickness of typically about 100 nm. Staining was performed by addition of a drop of aqueous solutions of uranyl acetate (0.5 %) onto the copper grid. After 1 min, the surface water on the grid was removed by tapping with filter paper.

Scanning transmission electron microscopy (STEM): STEM images of the sample were recorded using a ZEISS Ultra Plus scanning transmission electron microscope. The samples (on carbon coated copper grids stained with uranyl acetate as used in TEM) were imaged with accelerating voltages (EHT) of 18-19 kV indicated in the respective STEM images.

Pulse-radiolysis time-resolved conductivity (PR-TRMC) measurements: Conductivity measurements were performed on solid samples (30 mg) in a Persplex container. The samples were placed in microwave cells consisting of a rectangular waveguide with inner dimensions of 3.55×7.00 mm^2 that was short-circuited with a metal end plate. The materials were uniformly ionized with a nanosecond pulse of 3 MeV electrons from a Van-de-Graff accelerator. The energy absorbed by the sample was accurately known from dosimetry and leads to the formation of charge carrier pairs with concentrations of $\sim 10^{21}$ m^{-3}. If the charge carriers formed by ionization are mobile, the sample conductivity will increase upon irradiation. The change in conductivity of the sample was measured as a function of time by

monitoring the decrease in microwave power reflected by the cell. The conductivity increases during the irradiation pulse due to the formation of mobile charge carriers. After the pulse, the conductivity decays because of trapping and/or recombination of positive and negative charges. From the value of the conductivity at the end of the pulse, an estimate of the charge carrier mobility may be obtained if the concentration of charge carriers generated by irradiation is known. Accurate estimates of the charge carrier concentrations generated by pulse radiolysis can be made for discotic materials as described previously. The PR-TRMC technique is described more extensively in recent reviews.[31,32]

Conductive AFM: Conductive AFM measurement was performed at Universität Münster. As a sample substrate a silicon wafers with 100 nm oxide layer were used to guarantee a high electrical isolation. The thin conductive top layer consists of PEDOT:PSS (poly(3,4-ethylenedioxythiophene):poly(4-styrenesulphonate), Sigma-Aldrich Chemie GmbH, Germany) and was obtained as 1.3 wt % dispersion in H_2O. After diluting to 0.2 wt % this dispersion was spin coated with ≈ 4000 min^{-1} to the substrate to yield a film thickness of 10-15 nm. For the scratching of coated substrates cantilevers with high spring constants (PPP-NCHR, Nanosensors) and high loading forces were used. After the scratching procedure the nanowires were spin coated to those substrates by dropping 10 µl of the nanowire solution to the rotating sample ≈ 4000 min^{-1}.

General synthesis of zinc chlorin compounds

13^2-Demethoxycarbonyl-pheophorbide *a* methyl ester (Pheo *a*): The starting material of all the synthesized zinc chlorins is 13^2-demethoxycarbonyl-pheophorbide *a* methyl ester (Pheo *a*), which is synthesized from natural chlorophyll *a* according to a literature known procedure.[34] The provision of chlorophyll *a* was made by soxlet-extraction of dried algae *Spirulina platensis*. The extraction was performed with 800 g of algae and extracted for 2-3 days with acetone (1.5-2 L). After removal of acetone at a rota evaporator, a dark green oily residue was obtained, which was refluxed with collidin (200 mL) for 6 h, afterwards collidin was removed under vacuum (30 mbar) and the residue was cooled to room temperature immediately. Subsequently, the residue was dissolved in methanol (200 mL) and cooled to 5 °C and 20% sulphuric acid (150 mL) was added to it. After stirring for 12 h at RT, and diethyl ether (500

mL) was added and the pH of the aqueous phase was adjusted to 6-7 by careful addition of saturated aqueous sodium hydrogen carbonate ($NaHCO_3$) solution. The product was repeatedly extracted with diethyl ether and the united organic phases were washed with water. The organic layer was dried over sodium sulphate, followed by filtration and the solvent was removed at a rotor evaporator. The crude product so obtained was purified on a silica gel column using *n*-pentane as the eluent to get rid of the carotenoids and plant oils. Diethyl ether was used as eluent to obtain the desired Pheo *a*. The latter has the tendency to aggregate on the column, thus the aggregated portions were collected from column with the help of a spatula and washed with diethyl ether and after filtration, solvent was removed under vacuum. About 3-4 g Pheo *a* was obtained starting fromm 800 g of algae, which was then characterized by NMR, UV/Vis spectroscopy and mass spectrometry.[34]

Acidic ester hydrolysis: Pheo *a* or its derivatives were dissolved in little amounts of THF and subsequently concentrated hydrochloric acid (5-10 mL) was added. After 5-6 h stirring at RT under argon atmosphere, the reaction mixture was poured into saturated aqueous $NaHCO_3$ solution and solid $NaHCO_3$ was added to adjust the pH to 6-7. The resulting carboxylic acids were extracted with dichloromethane (CH_2Cl_2) and the solution was dried with sodium sulphate. After removal of drying agent by filtration, the solvent was removed by rotary evaporation and the crude product was purified by column chromatography with CH_2Cl_2/methanol mixtures. The analytical data for the obtained chlorin carboxylic acids are in accordance with those reported in literature.[69]

Esterification of chlorin carboxylic acids: The free carboxylic acids at 17^2-position of chlorins were esterified with the respective alcohols using dried coupling reagents. Chlorin carboxylic acids were dissolved in as little as possible amounts of dry dichloromethane and vacuum dried coupling reagents DCC (dicyclohexylcarbodiimide), DMAP (4-dimethylaminopyridine), and DPTS (4-dimethylaminopyridinium-*p*-toluolsulfonate) were added in the presence of *N*-ethyldiisopropylamine (Hünigs base). After stirring at RT for 6 hours under dark, the resulting 17^2 esters were purified by silica gel column chromatography.

Oxidation reaction: The 3^1-vinyl group of chlorins was converted into the corresponding diol with a catalytic amount of OsO_4, followed by oxidative cleavage of the diol by sodium periodate ($NaIO_4$). The respective 3^1-vinyl chlorin was at first dissolved in THF, followed by the addition of little amounts of a 1:1 mixture of water and acetic acid and then a catalytic amount of osmium tetroxide (1-2 small crystals; due to the toxicity of osmium

tetroxide, weighing was avoided) was added. Subsequently, the reaction mixture was stirred at RT under argon atmosphere, and the reaction was monitored by thin layer chromatography. When significant amounts of diol-intermediate was formed after 1-1.5 h, a saturated aqueous sodium periodate solution was added dropwise by a syringe pump (5-10 mL/h) within 2-4 h. Thereby a color change from olive green to the grey diol intermediate and then finally to brown 3^1-aldehyde was observed. Afterwards, water (100 mL) and diethyl ether (100 mL) were added and the acetic acid was neutralized with saturated aqueous $NaHCO_3$ solution. The product was extracted with diethyl ether (3 × 100 mL) and washed several times with water (50 mL), and finally dried over sodium sulphate. After filtration of the drying agent the solvent was removed at the rota evaporator.

Reduction reaction: The 3^1-formyl group of chlorins was selectively reduced to the corresponding primary alcohol with 10 equivalents of borane-*t*-butylamine complex BH_3(*t*-Bu)NH_2 reagent. The respective 3^1-formyl chlorin was dissolved in THF, followed by the addition of the boron reagent and the mixture was stirred at RT under argon atmosphere. The color of the reaction mixture changed from dark brown to olive green, indicating the formation of the 3^1-hydroxy chlorin derivative. To the reaction mixture, diethyl ether (100 mL) and water (50 mL) were added and the amine complex was neutralized with saturated aqueous ammonium chloride solution (20 mL). The organic phases were washed several times with water and dried over sodium sulphate. The desiccant was filtered off and the solvent was removed under vacuum to afford the 3^1-hydroxymethyl chlorin derivatives.

Metalation reaction: The metalation of chlorins was carried out in THF and with a saturated methanolic zinc acetate solution and by stirring for 2-3 h at RT under argon atmosphere. The incorporation of zinc ion into chlorin center leads to a color change from olive green to turquoise blue. To terminate the reaction, water (100 mL) and ether (100 mL) were added. After adding a saturated aqueous $NaHCO_3$ solution (100 mL) for the neutralization of the acetate, the mixture was washed with water at least 4 times to remove the excess amount of zinc acetate. The organic phase was dried over sodium sulphate, the desiccant was filtered off and the solvent was then removed at a rotary evaporator to afford the zinc chlorins. The synthesis and characterization details of compounds **1**-OH, **2**-OH, **3**-OH and **1**-OMe have been published previously.[27,30] Hence, the characterization data for compounds in last two steps are provided.

3-Devinyl-3-hydroxymethyl-13^2-demethoxycarbonyl-pheophorbide *a* (3,5-bis-dodecyloxy)benzylester (**1**'-OH): According to the general procedure for reduction reaction, chlorin (80 mg, 0.0805 mmol) was dissolved in CH_2Cl_2 (10 mL), followed by the addition of borane-*t*-butylamine complex (70 mg, 0.8048 mmol) and the reaction mixture was stirred for 1 h at RT. The reaction mixture was extracted according to the general procedure and the olive grey product **1**'-OH was purified by column chromatography on silica gel column with a solvent mixture of CH_2Cl_2/methanol (9:1), and subsequently by semipreparative HPLC; obtained yield: 59.2 mg, 0.0593 mmol, 73%; literature yield: 50.1 mg, 0.06 mmol, 74%. Analytical HPLC: **1**'-OH eluted after 8.7 min at a flow of 1 mL/min with solvent mixture methanol/CH_2Cl_2 (7:3). M.p.: 51-54 °C; ^{1}H NMR (400 MHz, $CDCl_3$, 25 °C): δ = 9.50 (s, 1H, 10-H), 9.45 (s, 1H, 5-H), 8.56 (s, 1H, 20-H), 6.34 (s, 3H, 2'-H, 4'-H, 6'-H), 5.89 (s, 2H, 3^1-H), 5.23 (d, ^2J = 19.8 Hz, 1H, 13^2-H), 5.05 (d, ^2J = 19.7 Hz, 1H, 13^2-H), 4.99 (d, ^2J = 12.4 Hz, 1H, 1''-H), 4.88 (d, ^2J = 12.4 Hz, 1H, 1''-H), 4.48 (dq, ^3J = 7.3 Hz, ^3J = 2.0 Hz, 1H, 18-H), 4.29 (td, ^3J = 8.3 Hz, ^3J = 2.3 Hz, 1H, 17-H), 3.84-3.78 (m, 4H, α-H), 3.72-3.66 (q, ^3J = 7.6 Hz, 2H, 8^1-H), 3.66 (s, 3H, 12^1-H), 3.40 (s, 3H, 2^1-H), 3.26 (s, 3H, 7^1-H), 2.73-2.53 and 2.37-2.25 (m, 4H, 17^1-H, 17^2-H), 1.77 (d, ^3J = 7.3 Hz, 3H, 18^1-H), 1.69-1.63 (m, 7H, β-H, 8^2-H), 1.35-1.21 (m, 36H, 18 × CH_2), 0.88 (t, ^3J = 7.1 Hz, 6H, ω-H), 0.24 (s, 1H, NH), -1.83 (s, 1H, NH); HRMS (ESI): *m*/*z* calcd for $C_{63}H_{89}N_4O_6$ $[M+H]^+$: 997.6782, found: 997.6776.

3-Devinyl-3-hydroxymethyl-13^2-demethoxycarbonyl-pheophorbide *a* (3,5-bis-dodecyloxy)benzylester zinc complex (**1**-OH): According to the general procedure for metalation, chlorin **1**'-OH (59 mg, 0.0556 mmol) was dissolved in a little amount of THF (6 mL) followed by the addition of saturated methanolic zinc acetate solution and was stirred at RT. The reaction mixture was extracted according to the general procedure with CH_2Cl_2 instead of diethyl ether and purified by column chromatography with an eluting solvent mixture of CH_2Cl_2/methanol (9:1), and further purified using semipreparative HPLC; obtained yield: 40 mg, 0.0378 mmol, 63.7%; literature yield: 40.3 mg, 0.04 mmol, 75%. Analytical HPLC: **1**-OH was eluted after 6.25 min at a flow of 1 mL/min with solvent mixture of methanol/CH_2Cl_2 (7:3). M.p.: 241 °C; ^{1}H NMR (400 MHz, [D_8] THF, 25 °C): δ = 9.57 (s, 1H, 10-H), 8.59 (s, 1H, 5-H), 8.34 (s, 1H, 20-H), 6.40 (d, ^4J = 2.3 Hz, 2H, 2'-H, 6'-H), 6.32 (t, ^4J = 2.2 Hz, 1H, 4'-H), 5.71 (d, ^3J = 5.8 Hz, 2H, 3^1-H), 5.11 (d, ^2J = 19.5 Hz, 1H, 13^2-H),

5.00-4.92 (m, 3H, 13^2-H, 1''-H), 4.53 (dq, ^3J = 7.2 Hz, ^3J = 2.1 Hz, 1H, 18-H), 4.40 (t, ^3J = 5.8 Hz, 1H, 3^1-OH), 4.31 (td, ^3J = 8.3 Hz, ^3J = 2.3 Hz, 1H, 17-H), 3.84 (m, 6H, α-H, 8^1-H), 3.61 (s, 3H, 12^1-H), 3.31 (s, 3H, 2^1-H), 3.29 (s, 3H, 7^1-H), 2.74-2.59 and 2.36-2.26 (m, 4H, 17^1-H, 17^2-H), 1.78 (d, ^3J = 7.3 Hz, 3H, 18^1-H), 1.71-1.63 (m, 7H, 8^2-H, β-H), 1.40-1.22 (m, 36H, 18 × CH_2), 0.88 (t, ^3J = 6.9 Hz, 6H, ω-H); HRMS (ESI): *m*/*z* calcd for $C_{63}H_{86}N_4O_6Zn$ $[M]^+$: 1058.5839, found: 1058.5833; UV/Vis (THF): λ_{max} (ε_{max}) = 648 nm (90,000 M^{-1} cm^{-1}).

3-Devinyl-3-hydroxymethyl-13^2-demethoxycarbonyl-pheophorbide *a* (3,4,5-tris-dodecyloxy)benzylester (**2**'-OH): To a solution of formyl chlorin (150 mg, 0.1273 mmol) in CH_2Cl_2, borane-*t*-butylamine complex (110.7 mg, 1.2733 mmol) was added and stirred for 1.5 h at RT. The reaction mixture was extracted as described in the general procedure for reduction. The olive grey reduced product **2**'-OH was purified by column chromatography by eluting with a mixture of diethyl ether/*n*-pentane (3:2), and was further purified by semipreparative HPLC; obtained yield: 101 mg, 0.0839 mmol, 67.2%; literature yield: 102 mg, 0.09 mmol, 68%. Analytical HPLC: **2**'-OH was eluted after 6.8 min at a flow of 1 mL/min with a solvent mixture of methanol/CH_2Cl_2 (3:2). M.p.: 104-106 ° C; ^{1}H NMR (400 MHz, $CDCl_3$, TMS, 25 °C): δ = 9.50 (s, 1H, 10-H), 9.45 (s, 1H, 5-H), 8.49 (s, 1H, 20-H), 6.25 (s, 2H, 6'-H, 2'-H), 5.90 (m, 2H, 3^1-H), 5.25 (d, ^2J = 19.8 Hz, 1H, 13^2-H), 5.08 (d, ^2J = 19.8 Hz, 1H, 13^2-H), 4.91 (d, ^2J = 12.1 Hz, 1H, 1''-H), 4.67 (d, ^2J = 12.3 Hz, 1H, 1''-H), 4.48 (dq, ^3J = 7.3 Hz, ^3J = 2.1 Hz, 1H, 18-H), 4.30 (td, ^3J = 8.1 Hz, ^3J = 2.4 Hz, 1H, 17-H), 3.78-3.56 (m, 11H, α-H, 8^1-H, 12^1-H), 3.29 (s, 3H, 2^1-H), 3.19 (s, 3H, 7^1-H), 2.75-2.68 and 2.54-2.27 (m, 4H, 17^1-H, 17^2-H), 1.69 (d, ^3J = 7.3 Hz, 3H, 18^1-H), 1.68-1.56 (m, 9H, β-H, 8^2-H), 1.18-1.14 (m, 54H, 27 × CH_2), 0.79 (m, 9H, ω-H), 0.26 (s, 1H, NH), -1.80 (s, 1H, NH); HRMS (ESI): *m*/*z* calcd for $C_{75}H_{113}N_4O_7$ $[M+H+Na]^+$: 1203.8441, found: 1203.8423.

3-Devinyl-3-hydroxymethyl-13^2-demethoxycarbonyl-pheophorbide *a* (3,4,5-tris-dodecyloxy)benzylester zinc complex (**2**-OH): According to the general procedure for metalation, 3^1-hydroxy chlorin **2**'-OH (80 mg, 0.0677 mmol) dissolved in THF (6 mL) followed by the addition of a saturated methanolic zinc acetate solution (12 mL). After 2 h reaction time, the mixture was worked up according to the general procedure, and the resulting turquoise product was purified by column chromatography by using *n*-

pentane/diethyl ether (3:2), and further purified by semipreparative HPLC; obtained yield: 62.2 mg, 0.0498 mmol, 73.4%; literature yield: 62.2 mg, 0.05 mmol, 73%. Analytical HPLC: **2**-OH eluted after 9 min at a flow of 1 mL/min with solvent mixture of methanol/CH_2Cl_2 (7:3). M.p.: 187-189 °C; ^{1}H NMR (400 MHz, [D_5] pyridine, $CDCl_3$, 25 °C): δ = 9.62 (s, 1H, 10-H), 9.48 (s, 1H, 5-H), 8.40 (s, 1H, 20-H), 6.52 (s, 2H, 6'-H, 2'-H), 5.91 (s, 2H, 3^1-H), 5.23 (d, ^2J = 19.6 Hz, 1H, 13^2-H), 5.08 (d, ^2J = 19.7 Hz, 1H, 13^2-H), 5.02 (d, ^2J = 12.0 Hz, 1 H, 1''-H), 4.96 (d, ^2J = 12.0 Hz, 1H, 1''-H), 4.42 (dq, ^3J = 7.3 Hz, ^3J = 2.2 Hz, 1H, 18-H), 4.23 (td, ^3J = 7.9 Hz, ^3J = 2.4 Hz, 1H, 17-H), 3.93 (m, 6H, α-H), 3.77 (q, ^3J = 7.6 Hz, 2H, 8^1-H), 3.73 (s, 3H, 12^1-H), 3.32 (s, 3H, 2^1-H), 3.20 (s, 3H, 7^1-H), 2.63-2.02 (m, 4H, 17^1-H, 17^2-H), 1.79-1.71 (m, 12H, 18^1-H, β-H, 8^2-H), 1.50-1.21 (m, 54H, 27 × CH_2), 0.91 (m, 9H, ω-H); HRMS (ESI): *m*/*z* calcd. for $C_{75}H_{110}N_4O_7Zn$ $[M+Na]^+$: 1265.7720, found: 1265.7558; UV/Vis (THF): λ_{max} (ε_{max}) = 648 nm (92 000 M^{-1} cm^{-1}).

3-Devinyl-3-hydroxymethyl-13^2-demethoxycarbonyl-pheophorbide *a* (3',5'-bis-(2-(2-[2-(2-methoxy-ethoxy)-ethoxy]-ethoxy)-ethoxy))benzyl ester (**3**'-OH): The synthesis and characterization is in accordance with literature.[27]

3-Devinyl-3-hydroxymethyl-13^2-demethoxycarbonyl-pheophorbide *a* (3',5'-bis-(2-(2-[2-(2-methoxy-ethoxy)-ethoxy]-ethoxy)-ethoxy))benzyl ester zinc complex (**3**-OH): The synthesis and characterization is in accordance with literature.[27]

3-Devinyl-3^1-methoxymethyl-13^2-demethoxycarbonyl-3,5-bis-dodecylalkoxybenzylester-pheophorbide *a* (**1**'-OMe): A mixture of 3^1-methoxypheo *a* (85 mg, 0.1539 mmol) and 6 mL conc. HCl was stirred under argon atmosphere for 2 h at room temperature and afterwards ice water (20 mL) and 20 mL of methylene chloride (CH_2Cl_2) were added. After neutralization with $NaHCO_3$, the organic layer was separated, washed with water (2 × 20 mL) and dried over Na_2SO_4. The CH_2Cl_2 solution was evaporated under vacuum and purified by column chromatography (CH_2Cl_2/THF/MeOH 6:2:2). Without further purification the carboxylic acid (mg, mmol) was used for esterification with 3,5-didodecylalkoxybenzylalcohol (183 mg, 0.3847 mmol) by employing DCC (158.7 mg, 0.7695 mmol), DMAP (57. 3 mg, 0.4617 mmol), DPTS (135.9 mg, 0.4617 mmol) and *N*-ethyldiisopropylamin (66 µL) as activating reagents in dry CH_2Cl_2 (3 mL) at room temperature under an argon atmosphere for 2 h. The

crude reaction mixture was purified by column chromatography (diethyl ether/*n*-pentane 70:30) and successively by HPLC (methanol/CH_2Cl_2 7:3) to afford 3^1-methoxy-benzylesterpheo *a* as an olive green solid obtained yield: 113 mg, 0.1116 mmol, 73%); literature yield: 91 mg, 60%. ^{1}H NMR (400 MHz, $CDCl_3$, 25 °C, TMS): δ = 9.53 (s, 1H, 10-H), 9.45 (s, 1H, 5-H), 8.54 (s, 1H, 20-H), 6.38 (d, ^4J(H,H) = 2.1 Hz, 2H, 2′-H, 6′-H), 6.33 (t, ^4J(H,H) = 2.3 Hz, 1H, 4′-H), 5.77 (s, 2H, 3^1-H), 5.26 (d, ^2J(H,H) = 19.8 Hz, 1H, 13^2-CH_2), 5.09 (d, ^2J(H,H) = 19.8 Hz, 1H, 13^2-CH_2), 5.01 (d, ^2J(H,H) = 12.3 Hz, 1H, 1″-H), 4.94 (d, ^2J(H,H) = 12.4 Hz, 1H, 1″-H), 4.48 (dq, ^3J(H,H) = 7.2 Hz, ^3J(H,H) = 2.0 Hz, 1H, 18-H), 4.30 (td, ^3J(H,H) = 8.7 Hz, ^3J(H,H) = 2.5 Hz, 1H, 17-H), 3.76 (t, ^{3}J(H,H) = 6.6 Hz, 4H, α-H), 3.64 (q, ^3J(H,H) = 7.7 Hz, 2H, 8^1-H), 3.61(s, 3H, 12^1-H), 3.60 (s, 3H, 3^1-OMe), 3.35 (s, 3H, 2^1-H), 3.19 (s, 3H, 7^1-H), 2.70-2.50 and 2.30-2.12 (m, 4H, 17^1-H, 17^2-H), 1.71 (d, ^3J(H,H) = 7.3 Hz, 3H, 18^1-H), 1.65-1.56 (m, 7H, β-H, 8^2-H), 1.37-1.21 (m, 36H, CH_2), 0.79 (t, ^3J = 6.9 Hz, 6H, ω-H), 0.64 (s, 1H, NH), -1.79 (s, 1H, NH); HRMS (ESI): 1011.6935 $[M+H]^+$ (calcd for $C_{64}H_{91}N_4O_6$: 1011.6938).

Zinc3-devinyl-3^1-methoxymethyl-13^2-demethoxycarbonyl-3,5-bis-dodecylalkoxy benzylester pheophorbide *a* (**1**-OMe): 3^1-methoxy-benzylesterpheo *a* (100 mg, 0.0891 mmol) was dissolved in 4 mL tetrahydrofurane (THF) and a saturated methanolic zinc acetate dehydrate solution (5 mL) was added to it. After stirring for 2 h under argon, CH_2Cl_2 (20 mL) was given into this mixture and then washed with water (4× 20 mL). The organic phase was dried over Na_2SO_4, evaporated under vacuum and the resulting crude product was purified by HPLC (methanol/CH_2Cl_2 7:3) to afford zinc chlorin **1**-OMe as a turquoise green solid with a melting point of 167 °C. obtained yield: 73.2 mg, 0.0681 mmol, 69%; literature yield: 66 mg, 68%. ^{1}H NMR (400 MHz, $CDCl_3$, 1 drop of [D_5]pyridine, 25 °C, TMS): δ = 9.45 (s, 1H, 10-H), 8.90 (s, 1H, 5-H), 8.38 (s, 1H, 20-H), 6.31 (d, ^4J(H,H) = 2.1 Hz, 2H, 2′-H, 6′-H), 6.28 (t, ^4J(H,H) = 2.2 Hz, 1H, 4′-H), 5.61 (s, 2H, 3^1-H), 5.15 (d, ^2J(H,H) = 19.6 Hz, 1H, 13^2-CH_2), 5.04 (d, ^2J(H,H) = 19.7 Hz, 1H, 13^2-CH_2), 4.85 (d, ^2J(H,H) = 12.2 Hz, 1H, 1″-H), 4.78 (d, ^2J(H,H) = 12.2 Hz, 1H, 1″-H), 4.45 (dq, ^3J(H,H) = 7.3 Hz, ^3J(H,H) = 2.2 Hz, 1H, 18-H), 4.21 (td, ^3J(H,H) = 8.1 Hz, ^3J(H,H) = 2.7 Hz, 1H, 17-H), 3.80 (t, ^3J(H,H) = 6.6 Hz, 4H, α-H), 3.68 (q, ^3J(H,H) = 7.4 Hz, 2H, 8^1-H), 3.57 (s, 3H, 12^1-H), 3.17 (s, 3H, 3^1-OMe), 3.12 (s, 3H, 2^1-H), 3.03 (s, 3H, 7^1-H), 2.64-2.53 and 2.35-2.19 (m, 4H, 17^1-H, 17^2-H), 1.82-1.62 (m, 10H, 18^1-H, 8^2-H, β-H), 1.35-1.25 (m, 36H, CH_2), 0.87 (t, ^3J = 6.9 Hz, 6H, ω-H); UV/Vis (THF): λ_{max}

(ε_{max}) = 648 nm (93 000 L mol^{-1} cm^{-1}); HRMS (ESI): 1072.5985 [M^+] (calcd for $C_{64}H_{88}N_4O_6Zn$: 1072.5995).

3-devinyl-3^1-methoxymethyl-13^2-demethoxycarbonyl-3,4,5-tris-dodecylalkoxy-benzylester pheophorbide *a* (**2**'-OMe): A mixture of 3^1-methoxypheo *a* and 6 mL conc. HCl was stirred under argon atmosphere for 2 h at room temperature and afterwards ice water (20 mL) and 20 mL of CH_2Cl_2 were added. After neutralization with $NaHCO_3$, the organic layer was separated, washed with water (2 × 20 mL) and dried over Na_2SO_4. The CH_2Cl_2 solution was evaporated under vacuum and purified by column chromatography (CH_2Cl_2/THF/MeOH 6:2:2). Without further purification the carboxylic acid (40 mg, 0.0724 mmol) was used for esterification with 3,4,5-tridodecylalkoxybenzylalcohol (71.6 mg, 0.1086 mmol) followed by further addition of DCC (74.7 mg, 0.3623 mmol), DMAP (27 mg, 0.2172 mmol), DPTS (64 mg, 0.2172 mmol) and *N*-ethyldiisopropylamin (30 µL) as activating reagents in dry CH_2Cl_2 (3 mL) at room temperature under an argon atmosphere for 2 h. The crude reaction mixture was purified by column chromatography (diethyl ether/*n*-pentane 70:30) and successively by HPLC (methanol/CH_2Cl_2 7:3) to afford 3^1-methoxy-benzylesterpheo *a* as an olive green solid. obtained yield: 58.8 mg, 0.0492 mmol, 68%. ^{1}H NMR (400 MHz, $CDCl_3$, 25 °C, TMS): δ = 9.50 (s, 1H, 10-H), 9.46 (s, 1H, 5-H), 8.50 (s, 1H, 20-H), 6.24 (d, ^4J(H,H) = 2.1 Hz, 2H, 2′-H, 6′-H), 5.89 (s, 2H, 3^1-H), 5.25 (d, ^2J(H,H) = 19.8 Hz, 1H, 13^2-CH_2), 5.08 (d, ^2J(H,H) = 19.8 Hz, 1H, 13^2-CH_2), 4.91 (d, ^2J(H,H) = 12.1 Hz, 1H, 1″-H), 4.67 (d, ^2J(H,H) = 12.2 Hz, 1H, 1″-H), 4.47 (dq, ^3J(H,H) = 7.2 Hz, ^3J(H,H) = 2.0 Hz, 1H, 18-H), 4.29 (td, ^3J(H,H) = 8.0 Hz, ^3J(H,H) = 2.5 Hz, 1H, 17-H), 3.78-3.56 (m, 11H, α-H, 8^1-H, 12^1-H), 3.29 (s, 3H, 2^1-H), 3.19 (s, 3H, 7^1-H), 2.75-2.68 and 2.54-2.27 (m, 4H, 17^1-H, 17^2-H), 1.69 (d, ^3J(H,H) = 7.3 Hz, 3H, 18^1-H), 1.74-1.56 (m, 9H, β-H, 8^2-H), 1.20-1.14 (m, 54H, CH_2), 0.79 (m, 9H, ω-H), 0.26 (s, 1H, NH) , -1.80 (s, 1H, NH); MS (MALDI-TOF, matrix: DCTB) for $C_{76}H_{114}N_4O_7$ calcd value: 1196.74, found value: 1196.67 [M+H^+].

3-devinyl-3^1-methoxymethyl-13^2-demethoxycarbonyl-3,4,5-tris-dodecylalkoxy-benzylester-pheophorbide *a* (**2**-OMe): 3^1-methoxy-benzylesterpheo *a* (40 mg, 0.0334 mmol) was dissolved in 4 mL tetrahydrofuran (THF) and a saturated methanolic zinc acetate dehydrate solution (2 mL) was added to it. After stirring for 6 h under argon, CH_2Cl_2 (20 mL) was given into this mixture and then washed with water (6 × 20 mL). The organic phase was

dried over Na_2SO_4, evaporated under vacuum and the resulting crude product was purified by HPLC (methanol/CH_2Cl_2 70:30) to afford zinc chlorin **2**-OMe as a turquoise green solid. yield: 25.7 mg, 0.0204 mmol, 61%. ^{1}H NMR (400 MHz, $CDCl_3$, 1 drop of [D_5]pyridine, 25 °C, TMS): δ = 9.50 (s, 1H, 10-H), 9.46 (s, 1H, 5-H), 8.50 (s, 1H, 20-H), 6.24 (d, ^4J(H,H) = 2.1 Hz, 2H, 2′-H, 6′-H), 5.89 (s, 2H, 3^1-H), 5.25 (d, ^2J(H,H) = 19.8 Hz, 1H, 13^2-CH_2), 5.08 (d, ^2J(H,H) = 19.8 Hz, 1H, 13^2-CH_2), 4.91 (d, ^2J(H,H) = 12.2 Hz, 1H, 1″-H), 4.67 (d, ^2J(H,H) = 12.2 Hz, 1H, 1″-H), 4.47 (dq, ^3J(H,H) = 7.3 Hz, ^3J(H,H) = 2.2 Hz, 1H, 18-H), 4.29 (td, ^3J(H,H) = 8.1 Hz, ^3J(H,H) = 2.7 Hz, 1H, 17-H), 3.78-3.56 (m, 11H, α-H, 8^1-H, 12^1-H), 3.29 (s, 3H, 2^1-H), 3.19 (s, 3H, 7^1-H), 2.75-2.68 and 2.54-2.27 (m, 4H, 17^1-H, 17^2-H), 1.69 (d, ^3J(H,H) = 7.3 Hz, 3H, 18^1-H), 1.74-1.56 (m, 9H, β-H, 8^2-H), 1.20-1.14 (m, 54H, CH_2), 0.79 (m, 9H, ω-H); MS (MALDI-TOF, matrix: DCTB) for $C_{76}H_{112}N_4O_7Zn$ calculated value: 1257.78, found value: 1257.82 for [$M+H^+$].

3.5. References and notes

(1) a) Shinwari, M. W.; Deen, M. J.; Starikov, E. B.; Cuniberti, G. *Adv. Funct. Mater.* **2010**, *20*, 1865–1883; b) Kumar, A.; Sevilla, M. D. *Chem. Rev.* **2010**, *110*, 7002–7023.

(2) a) Genereux, J. C.; Wuerth, S. M.; Barton J. K. *J. Am. Chem. Soc.* **2011**, *133*, 3863–3868; b) Genereux, J. C.; Barton, J. K. *Chem. Rev.* **2010**, *110*, 1642–1662; c) Grozema, F. C.; Tonzani, S.; Berlin, Y. A.; Schatz, G. C.; Siebbeles, L. D. A.; Ratner, M. A. *J. Am. Chem. Soc.* **2009**, *131*, 14204–14205; d) Guo, X.; Gorodetsky, A.; Hone, J.; Barton, J. K.; Nuckolls C. *Nat. Nanotech.* **2008**, *3*, 163–167; e) Porath, D.; Bezryadin, A.; de Vries, S.; Dekker, C. *Nature* **2000**, *403*, 635–638.

(3) a) Matile, S.; Jentzsch, A. V.; Montenegro, J.; Fin, A. *Chem. Soc. Rev.* **2011**, *40*, 2453–2474; b) Bhosale, R.; Misek, J.; Sakai, N.; Matile, S. *Chem. Soc. Rev.* **2010**, *39*, 138–149; c) Sakai, N.; Bhosale, R.; Emery, D.; Mareda, J.; Matile, S. *J. Am. Chem. Soc.* **2010**, *132*, 6923–6925; d) Bhosale, R.; Perez-Velasco, A.; Ravikumar, V.; Kishore, R. S. K.; Kel, O.; Gomez-Casado, A.; Jonkheijm, P.; Huskens, J.; J. Maroni, P.; Borkovec, M.; Sawada, T.; Vauthey, E.; Sakai, N.; Matile, S. *Angew. Chem. Int. Ed.* **2009**, *48*, 6461–6464.

(4) a) Uhlenheuer, D. A.; Petkau, K.; Brunsveld, L. *Chem. Soc. Rev.* **2010**, *39*, 2817–2826; b) Stupp, S. I. *Nano Letters* **2010**, *10*, 4783–4786; c) Tovar, J. D.; Rabatic, B.

M.; Stupp, S. I. *Small* **2007**, *3*, 2024–2028; d) Hirschberg, J.; Brunsveld, L.; Ramzi, A.; Vekemans, J.; Sijbesma, R. P.; Meijer, E. W. *Nature* **2000**, *407*, 167–170; e) Sijbesma, R. P.; Beijer, F. H.; Brunsveld, L.; Folmer, B. J. B.; Hirschberg, J.; Lange, R. F. M.; Lowe, J. K. L.; Meijer, E. W. *Science* **1997**, *278*, 1601–1604.

(5) a) Palermo, V.; Schwartz, E.; Finlayson, C. E.; Liscio, A.; Otten, M. B. J.; Trapani, S.; Müllen, K.; Beljonne, D.; Friend, R. H.; Nolte, R. J. M.; Rowan, A. E.; Samorì, P. *Adv. Mater.* **2010**, *22*, E81–E88; b) Braun, P. V.; Osenar, P.; Stupp, S. I. *Nature* **1996**, *380*, 325–328.

(6) Kumar, S. *Liq. Cryst.* **2005**, *32*, 1089–1113.

(7) Wu, J. S.; Pisula, W.; Müllen, K. *Chem. Rev.* **2007**, *107*, 718–747.

(8) a) Eichhorn, H. *J. Porphyrins Phthalocyanines* **2000**, *4*, 88–102; b) Kimura, M.; Saito, Y.; Ohta, K.; Hanabusa, K.; Shirai, H.; Kobayashi, N. *J. Am. Chem. Soc.* **2002**, *124*, 5274–5275; c) Li, L.; Kang, S.-W.; Harden, J.; Sun, Q.; Zhou, X.; Dai, L.; Jakli, A.; Kumar, S.; Li, Q. *Liq. Cryst.* **2008**, *35*, 233–239.

(9) a) Hatsusaka, K.; Ohta, K.; Yamamoto, I.; Shirai, H. *J. Mater. Chem.* **2001**, *11*, 423–433; b) van der Pol, J. F.; Neeleman, E.; Zwikker, J. W.; Nolte, R. J. M.; Drenth, W.; Aerts, J.; Visser, R.; Picken, S. J. *Liq. Cryst.* **1989**, *6*, 577–592.

(10) a) Rosen, B. M.; Wilson, C. J.; Wilson, D. A.; Peterca, M.; Imam, M. R.; Percec, V. *Chem. Rev.* **2009**, *109*, 6275–6540; b) Duzhko, V.; Aqad, E.; Imam, M. R.; Peterca, M.; Percec, V.; Singer, K. D. *App. Phys. Lett.* **2008**, 92, 11312-1–11312-3; c) Percec, V.; Glodde, M.; Bera, T. K.; Miura, Y.; Shiyanovskaya, I.; Singer, K. D.; Balagurusamy, V. S. K.; Heiney, P. A.; Schnell, I.; Rapp, A.; Spiess, H. W.; Hudson, S. D.; Duan, H. *Nature* **2002**, *419*, 384–387.

(11) de Greef, T. F. A.; Smulders, M. M. J.; Wolffs, M.; Schenning, A. P. H. J.; Sijbesma, R. P.; Meijer, E. W. *Chem. Rev.* **2009**, *109*, 5687–5754.

(12) a) Hoeben, F. J. M.; Jonkeijm, P.; Meijer, E. W.; Schenning, A. P. H. J. *Chem. Rev.* **2005**, *105*, 1491–1546; b) Schenning, A. P. H. J.; Meijer, E. W. *Chem. Commun.* **2005**, 3245–3258; c) Würthner, F.; Chen, Z.; Hoeben, F. J. M.; Osswald, P.; You, C.-C.; Jonkheijm, P.; van Herrikhuyzen, J.; Schenning, A. P. H. J.; van der Schoot, P. P. A. M.; Meijer, E. W.; Beckers, E. H. A.; Meskers, S. C. J.; Janssen, R. A. J. *J. Am. Chem. Soc.* **2004**, *126*, 10611–10618.

(13) Brédas, J. L.; Beljonne, D.; Coropceanu, V.; Cornil, J. *Chem. Rev.* **2004**, *104*, 4971–5003.

(14) a) Forrest, S. R.; Thomson, M. E. *Chem. Rev.* **2007**, *107*, 923–925, and the articles published in this thematic issue of *Chem. Rev.* (**2007**, *107*, Issue 4); b) Coropceanu, V.; Cornil, J.; da Silva, D. A.; Olivier, Y.; Silbey, R.; Brédas, J. L. *Chem. Rev.* **2007**, *107*, 926–952.

(15) Grozema, F. C.; Siebbeles, L. D. A. *Int. Rev. Phys. Chem.* **2008**, *27*, 87–138.

(16) a) Yamamoto, Y.; Zhang, G.; Jin, W.; Fukushima, T.; Ishii, N.; Saeki, A.; Seki, S.; Tagawa, S.; Minari, T.; Tsukagoshi, K.; Aida, T. *Proc. Natl. Acad. Sci. U. S. A.* **2009**, *106*, 21051–21056; b) Yamamoto, Y.; Fukushima, T.; Suna, Y.; Ishii, N.; Saeki, A.; Seki, S.; Tagawa, S.; Taniguchi, M.; Kawai, T.; Aida, T. *Science* **2006**, *314*, 1761–1764; c) Hill, J. P.; Jin, W.; Kosaka, A.; Fukushima, T.; Ichihara, H.; Shimomura, T.; Ito, K.; Hashizume, T.; Ishii, N.; Aida, T. *Science* **2004**, *304*, 1481–1483; d) Li, W.-S.: Aida, T. *Chem. Rev.* **2009**, *109*, 6047–6076; e) Jiang, D. L.; Aida, T. *Prog. Polym. Sci.* **2005**, *30*, 403–422.

(17) a) Frigaard, N. U.; Chew, A. G. M.; Li, H.; Maresca, J. A.; Bryant, D. A. *Photosyn. Res.* **2003**, *78*, 93–117; b) Blankenship, R. E.; Matsura, K. *Light-Harvesting Antennas in Photosynthesis* (Eds.: B. R. Green, W. W. Parson), Kluwer Academic Publishers, Dordrecht, **2003**, pp. 195–217; c) Olson, J. M. *Photochem. Photobiol.* **1998**, *67*, 61–75; d) Blankenship, R. E.; Olson, J. M.; Miller, M. *Anoxygenic Photosynthetic Bacteria* (Eds.: R. E. Blankenship, M. T. Madigan, C. E. Bauer), Kluwer Academic Publishers, Dordrecht, **1995**, pp. 399–435.

(18) Bryant, D. A.; Garcia Costas, A. M.; Maresca, J. A.; Gomez Maqueo Chew, A.; Klatt, C. G; Bateson, M. M.; Tallon, L. J.; Hostetler, J.; Nelson, W. C.; Heidelberg, J. F.; Ward, D. M. *Science* **2007**, *317*, 523–526.

(19) Saga, Y.; Shibata, Y.; Ltoh, S.; Tamiaki, H. *J. Phys. Chem. B*, **2007**, *111*, 12605–12609.

(20) a) Prokhorenko, V. I.; Holzwarth, A. R.; Müller, M. G.; Schaffner, K.; Miyatake, T.; Tamiaki, H. *J. Phys. Chem. B* **2002**, *106*, 5761–5768; b) Prokhorenko, V. I.; Steensgaard, D. B.; Holzwarth, A. F. *Biophys. J.* **2000**, *79*, 2105–2120; c) Savikhin, S.; van Noort, P. I.; Zhu, Y.; Lin, S.; Blankenship, R. E.; Struve, W. S. *Chem. Phys.* **1995**, *194*, 245–258; d) Brune, D. C.; King, G. H.; Infosino, A.; Steiner, T.; Thewalt, M. L. W.; Blankenship, R. E. *Biochemistry* **1987**, *26*, 8652–8658.

(21) a) Montaño, G. A.; Bowen, B. P.; LaBelle, J. T.; Woodbury, N. W.; Pizziconi, V. B.; Blankenship, R. E. *Biophys. J.* **2003**, *85*, 2560–2565; b) Savikhin, S.; Zhu, Y. W.; Blankenship, R. E.; Struve, W. S. *J. Phys. Chem.* **1996**, *100*, 3320–3322.

(22) Martinez-Planells, A.; Arellano, J. B.; Borrego, C. A.; López-Iglesias, C.; Gich, F.; Garcia-Gil, J. S. *Photosynth. Res.* **2002**, *71*, 83–90.

(23) a) Scholes, G. D.; Rumbles, G. *Nat. Mater.* **2006**, *5*, 683–696; b) Pšenčík, J.; Ma, Y. -Z.; Arellano, J. B.; Hála, J.; Gillbro, T. *Biophys. J.* **2003**, *84*, 1161–1179.

(24) a) Kassi, H.; Leblanc, R. M.; Hotchandani, S. *Physica Status Solidi B-Basic Research* **2000**, *220*, 931–939; b) Kassi, H.; Hotchandani, S.; Leblanc, R. M. *App. Phys. Lett.* **1993**, *62*, 2283–2285.

(25) Tamiaki, H.; Holzwarth, A. R.; Schaffner, K. *J. Photochem. Photobiol. B-Biology* **1992**, *15*, 355–360.

(26) Huber, V.; Katterle, M.; Lysetska, M.; Würthner, F. *Angew. Chem., Int. Ed.* **2005**, *44*, 3147–3151.

(27) Huber, V.; Sengupta, S.; Würthner, F. *Chem.–Eur. J.* **2008**, *14*, 7791–7807.

(28) Röger, C.; Muller, M. G.; Lysetska, M.; Miloslavina, Y.; Holzwarth, A. R.; Würthner, F. *J. Am. Chem. Soc.* **2006**, *128*, 6542–6543.

(29) Röger, C.; Miloslavina, Y.; Brunner, D.; Holzwarth, A. R.; Würthner, F. *J. Am. Chem. Soc.* **2008**, *130*, 5929–5939.

(30) Huber, V.; Lysetska, M.; Würthner, F. *Small* **2007**, *3*, 1007–1014.

(31) Warman, J. M.; Van de Craats, A. M. *Mol. Cryst. Liq. Cryst.* **2003**, *396*, 41–72.

(32) Warman, J. M.; de Haas, M. P.; Dicker, G.; Grozema, F. C.; Piris, J.; Debije, M. G. *Chem. Mater.* **2004**, *16*, 4600–4609.

(33) Tamiaki, H.; Amakawa, M.; Shimono, Y.; Tanikaga, R.; Holzwarth, A. R.; Schaffner, K. *Photochem. Photobiol.* **1996**, *63*, 92–99.

(34) Smith, K. M.; Goff, D. A.; Simpson, D. J. *J. Am. Chem. Soc.* **1985**, *107*, 4946–4954.

(35) Smulders, M. M. J.; Nieuwenhuizen, M. M. L.; de Greef, T. F: A.; van der Schoot, P.; Schenning, A. P. H. J.; Meijer, E. W. *Chem.–Eur. J.* **2010**, *16*, 362–367.

(36) Smulders, M. M. J.; Schenning, A. P. H. J.; Meijer E. W. *J. Am. Chem. Soc.* **2008**, *130*, 606–611.

(37) Zhao, D.; Moore, J. S. *Org. Biomol. Chem.* **2003**, *1*, 3471–3491.

(38) Ciferri, A. *Macromol. Rapid Commun.* **2002**, *23,* 511–529.

(39) Dudowicz, J.; Freed, K. F.; Douglas, J. F. *J. Chem. Phys.* **2003**, *119*, 12645–12666.

(40) Oosawa, F.; Kasai, M. *J. Mol. Biol.* **1962**, *4*, 10–21.

(41) Goldstein, R. F.; Stryer, L. *Biophys. J.* **1986**, *50*, 583–599.

(42) Van der Schoot, P. In *Supramolecular Polymers*, 2nd ed.; Ciferri, A., Ed.; Taylor & Francis: London, 2005.

(43) Jonkheijm, P.; van der Schoot, P.; Schenning, A. P. H. J.; Meijer, E. W. *Science* **2006**, *313*, 80–83.

(44) Tomović, Z.; van Dongen, J.; George, S. J.; Xu, H.; Pisula, W.; Leclère, P.; Smulders, M. M. J.; De Feyter, S.; Meijer, E. W.; Schenning A. P. H. J. *J. Am. Chem. Soc.* **2007**, *129*, 16190–16196.

(45) Patwardhan, S.; Sengupta, S.; Würthner, F.; Siebbeles, L. D. A.; Grozema F. C. *J. Phys. Chem. C* **2010**, *114*, pp. 20834–20842.

(46) Berne, B. J.; Pecora, R. *Dynamic Light Scattering*; Wiley: NewYork, 1976.

(47) Friedrich, H.; Frederik, P. M.; With, G. de; Sommerdijk N. A. J. M. *Angew. Chem., Int. Ed.* **2010**, *49*, 7850–7858.

(48) a) Cohen-Bazire, G.; Pfennig, N.; Kunisawa, R. *J. Cell Biol.* **1964**, *22*, 207–225; b) Staehelin, L. A.; Golecki, J. R.; Fuller, R. C.; Drews, G. *Arch. Microbiol.* **1978**, *119*, 269–277.

(49) a) Oostergetel, G. T.; van Amerongen, H.; Boekema E. J. *Photosynth. Res.* **2010**, *104*, 245–255; b) Staehelin, L. A.; Golecki, J. R.; Drews, G. *Biochim. Biophys. Acta* **1980**, *589*, 30–45.

(50) a) Ganapathy, S.; Oostergetel, G. T.; Wawrzyniak, P. K.; Reus, M.; Chew, A. G. M.; Buda, F.; Boekema, E. J.; Bryant, D. A.; Holzwarth, A. R.; de Groot, H. J. M. *Proc. Natl. Acad. Sci. U. S. A.* **2009**, *106*, 8525–8530; b) Oostergetel, G. T.; Reus, M.; Chew, A. G. M.; Bryant, D. A.; Boekema, E. J.; Holzwarth, A. R. *FEBS Lett.* **2007**, *581*, 5435–5439.

(51) Balaban, T. S.; Holzwarth, A. R.; Schaffner, K.; Boender, G.-J.; de Groot, H. J. M. *Biochemistry* **1995**, *34*, 15259–15266.

(52) Holzwarth, A. R.; Müller, M. G.; Griebenow, K. *J. Photochem. Photobiol. B* **1990**, *5*, 457–465.

(53) Kakitani, Y.; Koyama, Y.; Shimoikeda, Y; Nakai, T; Utsumi, H.; Shimizu, T.; Nagae, H. *Biochemistry* **2009**, *48*, 74–86.

(54) van Rossum, B. J.; Förster, H.; de Groot, H. J. M. *J. Magnetic Resonance* **1997**, *124*, 516–519.

(55) de Boer, I.; Matysik, J.; Amakawa, M.; Yagai, S.; Tamiaki, H.; Holzwarth, A. R.; de Groot, H. J. M. *J. Am. Chem. Soc.* **2003**, *125*, 13374–13375.

(56) de Boer, I.; Matysik, J.; Erkelens, K.; Sasaki, S.; Miyatake, T.; Yagai, S.; Tamiaki, H.; Holzwarth, A. R.; de Groot, H. J. M. *J. Phys. Chem. B* **2004**, *108*, 16556–16566.

(57) Van Rossum, B. -J.; Steensgaard, D. B.; Mulder, F. M.; Boender, G. J.; Schaffner, K.; Holzwarth, A. R.; de Groot, H. J. M. *Biochemistry* **2001**, *40*, 1587–1595.

(58) Holzwarth, A. R.; Schaffner, K. *Photosyn. Res.* **1994**, *41*, 225–233.

(59) Nozawa, T.; Ohtomo, K.; Suzuki, M.; Nakagawa, H.; Shikama, Y.; Konami, H.; Wang, Z. Y. *Photosyn. Res.* **1994**, *41*, 211–223.

(60) Wang, Z. Y.; Umetsu, M.; Kobayashi, M.; Nozawa, T. *J. Phys. Chem. B* **1999**, *103*, 3742–3753.

(61) Mizoguchi, T.; Ogura, K.; Inagaki, F.; Koyama, Y. *Biospectroscopy* **1999**, *5*, 63–77.

(62) Jochum T.; Reddy C. M.; Eichhöfer A.; Buth G.; Szmytkowski J.; Kalt H.; Moss D.; Balaban T. S. *Proc. Natl. Acad. Sci. U. S. A.* **2008**, *105*, 12736–12741.

(63) Balaban, T. S.; Linke-Schaetzel, M.; Bhise, A. D.; Vanthuyne, N.; Roussel, C.; Anson, C. E.; Buth, G.; Eichhöfer, A.; Forster, K.; Garab, G.; Gliemann, H.; Goddard, R.; Javorfi, T.; Powell, A. K.; Rösner, H.; Schimmel, T. *Chem.–Eur. J.* **2005**, *11*, 2267–2275.

(64) Manickam, M.; Belloni, M.; Kumar, S.; Varshney, S. K.; Rao, D. S. S.; Ashton, P. R.; Preece, J. A.; Spencer, N. *J. Mater. Chem.* **2001**, *11*, 2790–2800.

(65) Immirzi, A.; Perini, B. *Acta Crystallographica Section A* **1977**, *33*, 216–218.

(66) Ganapathy, S.; Sengupta, S.; Wawrzyniak, P. K.; Huber, V.; Buda, F.; Baumeister, U.; Würthner, F.; de Groot, H. J. M. *Proc. Natl. Acad. Sci. U. S. A.* **2009**, *106*, 11472–11477.

(67) van de Craats, A. M.; Warman, J. M. *Adv. Mater.* **2001**, *13*, 130–133.

(68) Schouten, P. G.; Warman, J. M.; Gelinck, G. H.; Copyn, M. J. *J. Phys. Chem.* **1995**, *99*, 11780–11793.

(69) Wasielewski, M. R.; Svec, W. A. *J. Org. Chem.* **1980**, *45*, 1969–1974.

Chapter 4

Dendron Functionalized Zinc Chlorins: Tuning Two-Dimensional Packing and Liquid Crystals as Functional Material for Charge Transport

A series of zinc chlorin dyes **1-3** have been synthesized functionalized with second generation dendritic wedge units at their 17^2-positions. Depending on the dendron wedge shapes, compounds **1-3** spontaneously self-assemble into linear rows and cyclic nanostructures on highly oriented pyrolitic graphite (HOPG) surface, studied by scanning probe microscopy (SPM). Compound **2** was found to exhibit liquid crystalline (LC) behavior in the condensed phase and its mesomorphic properties have been characterized by differential scanning calorimetry (DSC), polarisation optical microscopy (POM), powder X-ray diffraction (XRD). Combination of powder XRD, scanning tunneling microscopy (STM) and atomic force microscopy (AFM) revealed the formation of nano-segregated well-ordered columnar tubular superstructures consisting of five molecules in the column stratum. The self-assembled columns are further self-organized into a two-dimensional oblique unit cell lattice. Semiconducting behavior of **1-3** have been studied by pulse-radiolysis time-resolved microwave conductivity (PR-TRMC) method and charge carrier mobility values of ~ 10^{-2} cm^2/Vs have been observed. Such organized columnar superstructures constructed from semisynthetic zinc chlorin **2** are reminiscent of the tubular organization of the bacteriochlorophylls in the light-harvesting chlorosomal antennae of green sulphur bacteria.

X-ray diffraction data were obtained by Dr. Ute Baumeister at Universität Halle and charge carrier mobility measurements were performed by Dr. Sameer Patwardhan in the group of Prof. Dr. Laurens D. A. Siebbeles at the Technical University of Delft.

4.1. Introduction

The field of organic electronics and optoelectronics has witnessed tremendous progress in the last decade.[1-3] During this time, supramolecular electronics has been emerged based on self-assembled functional π-conjugated materials.[4-9] In particular, columnar discotic liquid crystals (DLCs)[10-14] have evolved as the new generation of organic semiconducting materials by virtue of their anisotropic charge transport abilities and high charge carrier mobilities,[15-25] and provided prospects for their utilization in photovoltaic devices[26] and field effect transistors.[27,28] The processability inherent to DLCs offer possibilities to control column orientation and morphology of thin films, at length scales from macroscopic to molecular dimensions, and to obtain defect-free large-area thin devices. Ever since the first DLCs were observed for hexa(alkanoyloxy)benzenes, representative DLCs based on a broad class of π-conjugated materials such as triphenylenes,[29,30] hexabenzocoronenes (HBCs),[19,20] contorted HBCs,[27,28] phthalocyanines,[31-40] porphyrins,[23,33,41] perylene bisimides,[16,42-46] coronenes,[47] porphycenes[48-50] have been developed, and intensively investigated with regard to their applications in (opto)electronics.

In the context of photovoltaic[51-54] and electronic applications,[23] porphyrinoid liquid crystalline (LC) materials have been of prime interest due to their large π-electron systems, favorable redox and photochemical properties and thermal stability. They constitute a valuable structural motif for the construction of metallomesogens[55] and various types of mesomorphism, from calamitic, lamellar to discotic, are obtainable by alteration of substituents and/or substituted positions. In many cases, zinc coordination has been applied and shown to provide an improved stability to porphyrin based mesophases compared to the related free base porphyrins.

Natural systems often provide the inspiration for the hierarchical ordering of dyes/pigments into functional supramolecular architectures. During the course of evolution, nature has developed chlorosomes,[56-58] the light-harvesting apparatus of green sulphur bacteria (phylum *Chlorobi*), some filamentous anoxygenic phototrophs of the phylum *Chloroflexi* and in the recently discovered aerobic phototroph, *Candidatus* Chloracidobacterium thermophilum.[59] Chlorosomes are fascinating examples of natural dye assemblies, constructed from ~250,000 bacteriochlorophyll (BChl) *c*, *d*, or *e* pigments, where vital non-covalent interactions without the assistance of a protein scaffold, hold the pigments in proper geometrical arrangement for optimal and rapid excitation energy transfer.[60-62] BChl assemblies show very high exciton mobilities,[60,62,63] which make these aggregates interesting for applications in photonic devices.

Moreover, the redox properties associated with chlorin dyes suggest that these dye aggregates might also be well suited for charge carrier transport although no studies on this topic could be found in the literature. Owing to its outstanding excitonic, optical and redox properties, the chlorosomal superstructure is thus extremely appealing for the rational design of self-assembling, biomimetic functional material, for example, soft/liquid crystalline material based on chlorophylls.

Generally, symmetrical substitutions along the porphyrin macrocycle, usually involving three substitution patterns, namely, octa-β-alkyl substitution, 5,15-di- or 5,10,15,20-tetra-meso-substitutions, are very facile. A large number of meso tetrakis-substituted porphyrins are reported which mostly form columnar mesophases, while few of them are known to form lamellar mesophases. On the other hand, octakis-substituted porphyrins tend to form columnar hexagonal mesophases, whereas 5,15-bis-substituted porphyrins form smectic mesophases.[23,32] Phthalocyanines also offer numerous synthetic possibilities, in which a wide range of metal ions can be coordinated and upto 16 hydrogens of the macrocycle can be replaced by functional groups.[23] Dendrimer appended porphyrins and phthalocyanines, designed and investigated as functional material for energy transport, have been reviewed recently.[64,65] Although porphyrins, phthalocyanines and related compounds constitute an intensively investigated class of building blocks suitable for the construction of metallomesogens,[55,66,67] to the best of our knowledge, metallomesogens based on (bacterio)chlorophyll derivatives, in particular biomimetic chlorin macrocycles, are to-date unprecedented.

The most common concepts for discotic mesophase formation,[10,11,14,68] i.e., facile introduction of long alkyl chains in a symmetric fashion along the periphery of an aromatic core, e.g. positions 5, 10, 15, 20 of a porphyrin macrocycle, is difficult to apply in chlorins owing to its structural complexity. Unlike porphyrins, the chlorin macrocycle lacks structural symmetry by virtue of a five-membered isocyclic phorbin ring, and a reduced double bond at C17, C18 positions with asymmetric centres at these two positions.[56] While the reactivity of chlorin is similar to those of structurally related porphyrins, the reduced pyrrole ring lowers the stability and induces non-planarity in the chlorin ring. As a result of these structural features, the metal centre of chlorin becomes an additional stereocentre that can adopt two diastereotopic configurations, namely α and β depending upon its ligation from the opposite and same side of the 17-propionic ester group, respectively.[56] Because of these very distinct structural features, a different synthetic strategy has to be adopted to achieve mesophases based on metallochlorin dyes.

In this work, we have developed such a strategy on the basis of the "dendron wedge concept" introduced by Percec and coworkers.[69] Depending upon the dendron wedge shape, branching and generation number, monodendrons described as tapers, half disks, disks, cones, half spheres or spheres are known to form supramolecular liquid crystals that self-organize further into lamellar, columnar or cubic macroscopic lattices.[69] Polyaromatic Percec-type dendrons have provided access to complex supramolecular architectures with well-defined shapes, pronounced surface organization,[69] promising electronic properties[70] and potential for nanoscale device-fabrication.[69]

Thus, in this work, zinc chlorin (hereafter ZnChl) compounds **1-3** (Scheme 1), containing Percec-type second generation dendritic wedges, namely (3,4-3,5)12G2-CH_2OH, (3,4-3,4,5)12G2-CH_2OH and (3,4,5-3,4,5)12G2-CH_2OH at their 17^2-position have been synthesized and their bulk phase properties have been investigated. ZnChl **2** has been found to exhibit LC behavior. To our knowledge, any functional LC material based on semisynthetic chlorophyll derivative has not been reported so far. The mesomorphic properties and structural arrangement of the LC phases have been investigated in detail by differential scanning calorimetry (DSC), polarisation optical microscopy (POM), powder X-ray diffraction (XRD), atomic force microscopy (AFM) for bulk sample and scanning probe microscopy (SPM i.e., AFM and STM) for thin films. Furthermore, intrinsic charge carrier mobilities of ZnChls **1-3** in solid-state have been investigated by pulse radiolysis-time resolved microwave conductivity (PR-TRMC) experiments.

4.2. Results

Synthesis and characterization of 3^1-methoxy zinc chlorin bearing second generation dendritic side chain residue: The synthetic route to the dendritic ZnChls **1-3** is outlined in Scheme 1. Chl *a* was extracted from cyanobacterium *Spirulina Platensis* and was converted to pheophorbide *a* (pheo *a*) according to literature procedures.[71-73] The latter compound was transformed into 3^1-methoxypheo *a*[72] and was further hydrolyzed with conc. hydrochloric acid into the corresponding 17^2-carboxylic acid derivative. The latter was esterified, in the presence of coupling reagents dicyclohexylcarbodiimide (DCC), 4-dimethylaminopyridine (DMAP), 4(dimethylamino)pyridinium-*p*-toluenesulfonate (DPTS) and *N*,*N*-ethyldiisopropylamine in dry dichloromethane (DCM) as solvent, with second generation dendritic alcohols (3,4-3,5)dodecyloxybenzyl alcohol (termed as (3,4-3,5)12G2-CH_2OH), (3,4-3,4,5)dodecyloxybenzyl alcohol (termed as (3,4-3,4,5)12G2-CH_2OH) and (3,4,5-

3,4,5)dodecyloxybenzyl alcohol (termed as (3,4,5-3,4,5)12G2-CH_2OH) which afforded the free base chlorin compound **1a-3a** with yields of 58-66%. The second generation dendritic alcohols (3,4-3,5)12G2-CH_2OH, (3,4-3,4,5)12G2-CH_2OH and (3,4,5-3,4,5)12G2-CH_2OH were synthesized according to the convergent stepwise synthetic method developed by Percec and co-workers.[74] The final step involved the metalation of the free base compounds **1a-3a** with saturated solution of $Zn(OAc)_2$ in methanol and in THF as solvent, that afforded the target building block ZnChls **1-3** with yields of 63-72%. The intermediates and final products were purified by silica gel column chromatography, followed by HPLC purifications and characterized by ^1H NMR spectroscopy and high-resolution mass spectrometry (HRMS) and MALDI TOF mass spectrometry.

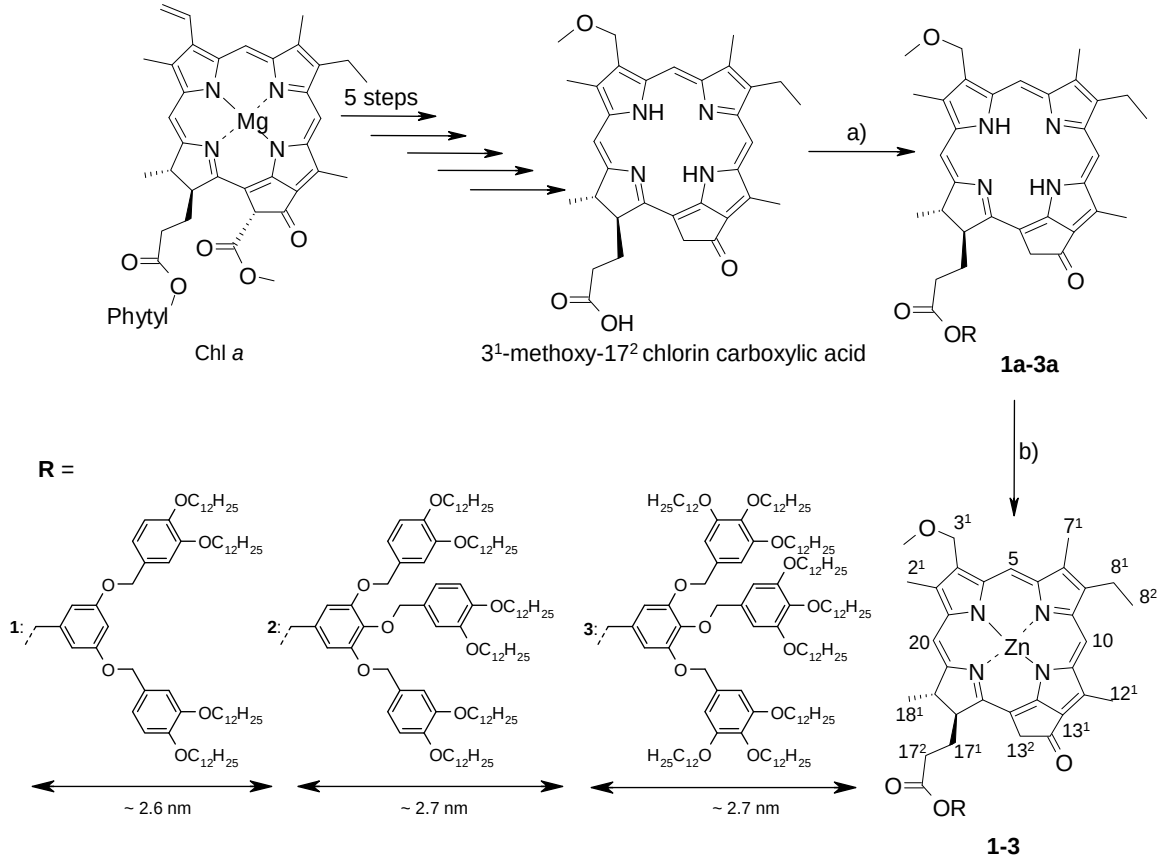

Scheme 1. Synthesis of ZnChls **1-3**: a) DCC, DMAP, DPTS, *N*,*N*-ethyldiisopropylamine, dry CH_2Cl_2, RT, 3–4 h, ROH, 58-66% yield; b) $Zn(OAc)_2$, MeOH, THF, RT, 3 h, 63-72% yield.

4.2.1. Liquid crystalline zinc chlorin

4.2.1.1. Differential scanning calorimetry (DSC): The thermotropic behavior of ZnChls **1-3** were investigated by differential scanning calorimetry (DSC) experiment. The transition temperatures and the associated enthalpy changes were determined by DSC at the heating rates and cooling rates of 10 ^oC/min. ZnChls **1** and **3** melted upon heating upto 130 ^oC and did

not show any phase transition behavior. The DSC thermogram of ZnChl **2** (Figure 1) shows the first phase transition at a temperature of 34.8 °C with a melting enthalpy of ΔH_m = 19.83 kJ/mol and the clearing point temperature to the isotropic phase was obtained at 137 °C (ΔH_c = 23.7 kJ/mol). Upon cooling down from the isotropization temperature (137 °C), a phase transition at 110 °C (28.8 kJ/mol) was observed which corresponds to the transformation from isotropic to the LC phase, followed by another transition at 10.5 °C (18.1 kJ/mol).

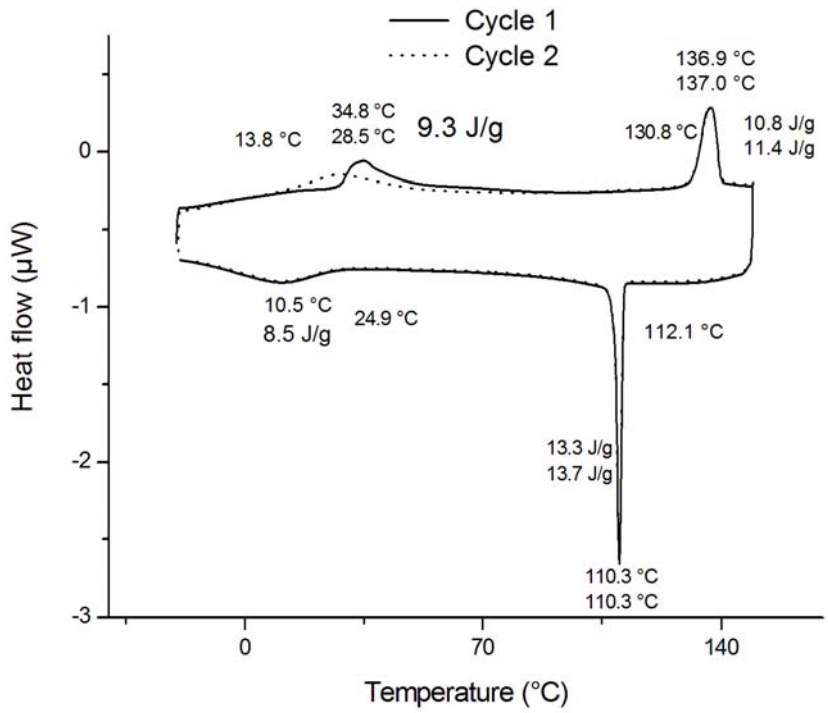

Figure 1. Differential scanning calorimetry thermogram of ZnChl **2**. The heating rates were 10 °C/min whereas the cooling rates were 0.4 °C/min. The first (solid line) and second (dotted line) heating and cooling cycles are indicated.

The thermal processes were reversible and almost identical in subsequent cycles as evident from the first and second heating and cooling cycles, which is indicative of the formation of a stable enantiotropic mesophase. The enthalpies of transitions are relatively higher than those obtained for typical LC phases,[75] indicating a considerably higher degree of order within the mesophase. For several zinc porphyrin and zinc phthalocyanine based liquid crystals, the mesophase clearing temperatures and enthalpies of transitions vary over a wide range depending upon the substituents and/or substituted positions.[13,14,23]

4.2.1.2. Polarisation optical microscopy (POM): Liquid crystals are anisotropic phases and exhibit a variety of characteristic birefringent textures,[12] that result from the symmetry-dependent elasticity of the LC phases, in combination with defects, surface conditions, thickness and cooling rate of the sample under investigation. ZnChl **2** was investigated for the

temperature-dependent texture formation under the crossed polarizers of the optical polarization microscope provided with a heating stage. It was first heated upto 137 °C till it melted and upon cooling down from the isotropic liquid state, spherulitic textures could be observed under the crossed polarizers of the optical polarization microscope (Figure 2a). Upon repeated melting and cooling of the sample, similar spherulitic textures could be reproduced. Such spherulitic textures are especially typical for columnar LC phases.[12] The liquid crystal columns were sufficiently cohesive and could be aligned with external stimulus like mechanical shear. Shearing of the sample with two glasses sandwiching it gave rise to complete removal of the well-developed spherulitic textures, replaced by non-specific highly birefringent and nearly homogeneously aligned textures (Figure 2b).

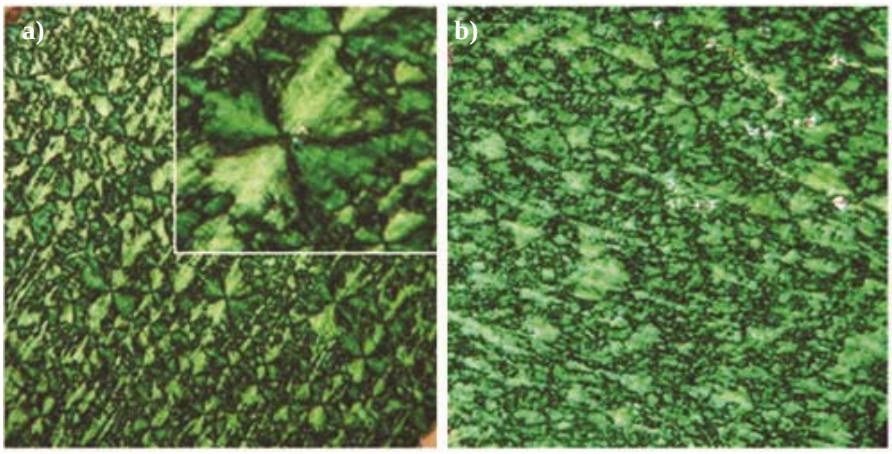

Figure 2. Images of textures observed for the liquid crystalline ZnChl **2** observed under the crossed polarizers of optical polarization microscope a) before shearing and b) after shearing; inset in (a) shows an expanded region of the spherulitic textures.

This indicates that liquid crystal columns are lying predominantly parallel to the glass substrate along the direction of the shear. Similar examples for alignment of dendron based columnar liquid crystals on surface by mechanical shearing and other alignment techniques have been reported previously.[13,69,76,77]

4.2.1.3. Atomic force microscopy (AFM) measurements under temperature control: The one-dimensional columnar features of ZnChl **2** could be verified by atomic force microscopy (AFM) studies performed on bulk sample. To gain insight into the morphological changes of **2** with variations in temperature, the sheared sample from the POM measurement was used for temperature-dependent AFM measurement after removal of the upper glass plate (Figure 3). Upon heating to 130 ^{o}C, the sample became almost fluidic and imaging of the morphology was difficult to be accomplished with AFM (Figure 3a). The sample was then heated upto its melting point and slowly cooled down and AFM was recorded at different temperatures. While cooling down gradually from the isotropic melt to 100 ºC, at the rate of c

a. 0.6 ºC/min, long bundles of fibrillar structures were formed on the glass surface (Figure 3b). Upon cooling down further to room temperature (Figure 3c and d), these fibrillar structures were maintained covering the whole area without specific differences. Figure 3e shows the cross section of the blue line in Figure 3c and the fibrillar structures were found to have an average width of ~ 10 ± 2 nm. As described in the POM investigation, ZnChl **2** has LC property and thus, these fibrillar structures correspond to the cylindrical columns of the liquid crystals that are aligned parallel to the glass substrate as illustrated in Figure 3f. Previous literature examples have described direct visualization of organized assemblies of dendrimers on surfaces,[69] where shear-induced alignment has been applied.[78] The ability of these cylindrical columns of the LC phases to self-assemble in aligned macroscopic structures, combined with their controlled stiffness should be favorable for their utilization in nano (opto)electronics.[19,20]

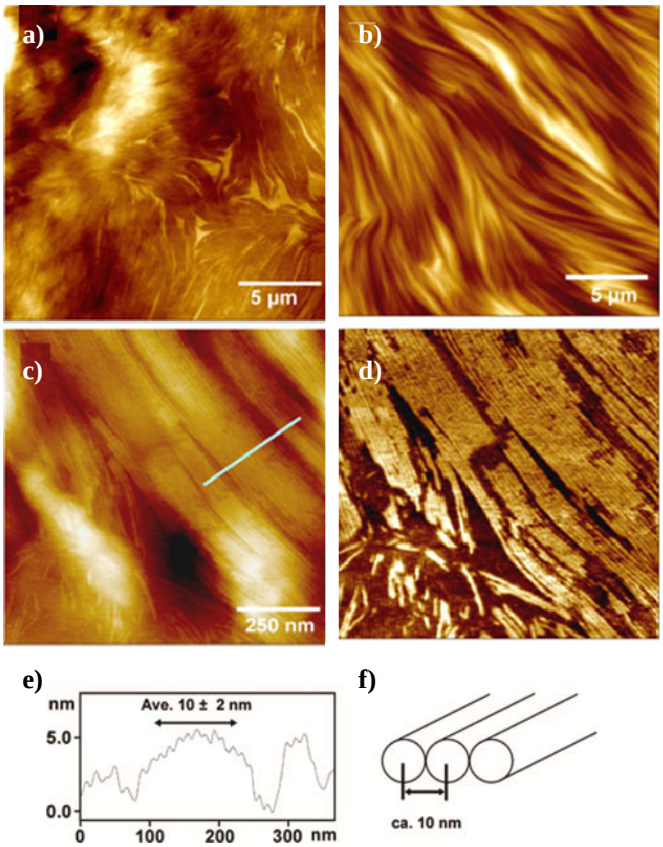

Figure 3. AFM images for ZnChl **2** on glass surface a) upon heating to 130 °C , b) upon cooling down from the isotropic melt to 100 °C and, c), d) to RT; a-c) Height images; d) Phase image of c; e) cross section of the blue line in (c), indicating that ten aligned fibres have a width of 102 nm, i.e, an average column width of ~ 10 nm; f) pictorial representation of aligned columns with average column diameter, i.e., center-to-center distance of ca.10 nm.

4.2.1.4. Powder X-ray diffraction (XRD): To obtain insights into the molecular ordering of the LC phases, powder XRD was measured for bulk sample of ZnChl **2** at 115 °C upon cooling from the isotropic melt. Generally, the small angle diffraction regime provides

information about the crystalline lattice and symmetry and the long range organization whereas, the wide angle diffraction regime provides information on the short-range arrangement inside the structural elements.[12,79] The powder XRD pattern of a powder like sample of ZnChl **2** is shown in Figure 4. The small angle reflections (Figure 4c, d, reflections 1-11 in Table 1) obtained for ZnChl **2** were no harmonics of each other, indicating the existence of no simple layer structure but a two-dimensional rather long-range ordered arrangement of the molecules within the LC phases. Moreover, the sharpness of the reflections can be attributed to an ordered mesophase structure. In the wide angle region (Figure 4a, b), ZnChl **2** exhibited a slightly broadened peak at 2Θ = 25.4 (reflection no. 14 in Figure 4b, Table 1), which is indicative of a medium- to long-range order with intervals of 3.5 Å, which is characteristic of the stacked π-π distances, generally found in the crystals of zinc porphyrins (3.46 Å) and other π-stacked compounds.[80,81] The broad and diffused halo obtained at 4.6 Å (2Θ = 19.2) in the wide angle region (reflection no.13 in Figure 4b, Table 1) could be attributed to the liquid-like disordered packing of the alkyl chains of the dendrons.[82,83] A second slightly broadened reflection in the wide-angle region at 6.3 Å (2Θ = 14.0) (reflection no. 12 in Figure 4b, Table 1) could probably be attributed to inter-columnar correlations. The small angle reflections (Figure 4c, d, reflections 1-11 in Table 1) could be indexed to a tentative oblique lattice (Figure 5) and alternatively to a centered rectangular lattice (*c*2*mm*) (Table 2, Figure 6), although the latter arrangement seems less likely. The best self-consistency of X-ray data set and its correlation with other experimental data could be reached for the 2D oblique lattice.

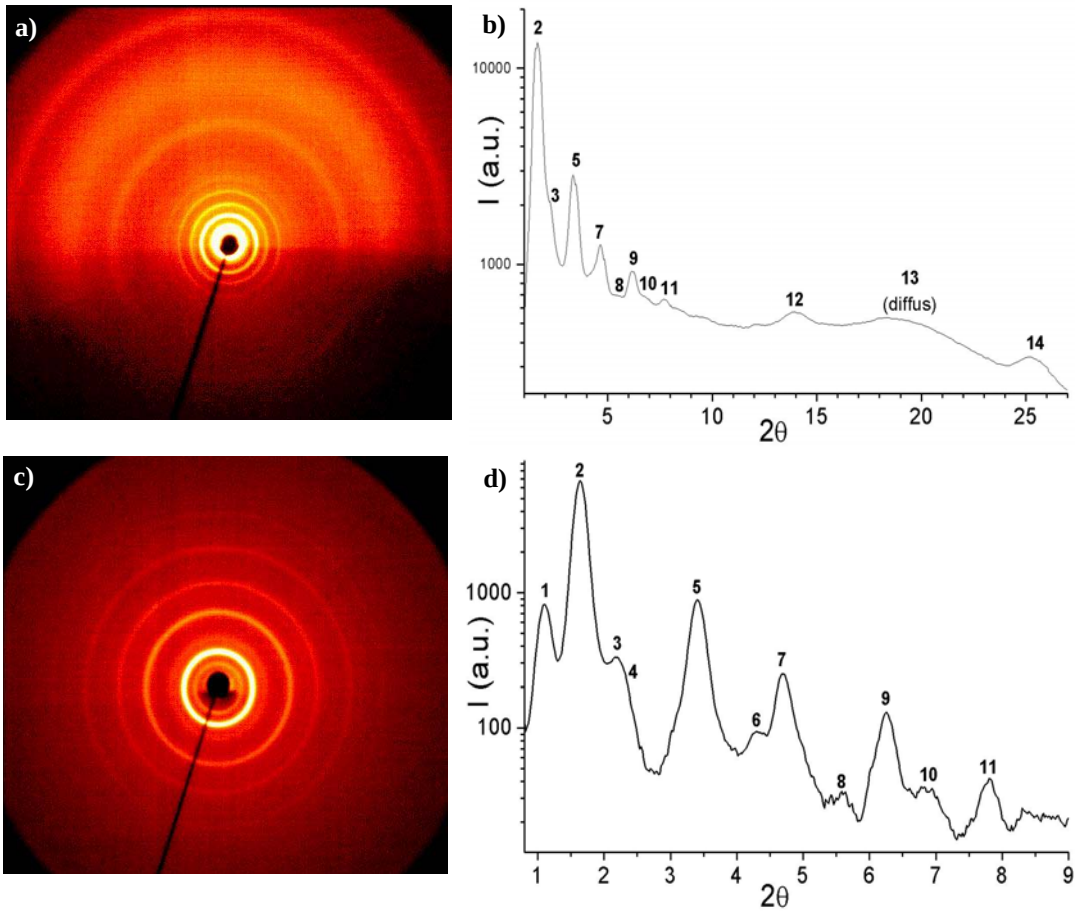

Figure 4. X-ray diffraction patterns for a powder-like sample of ZnChl **2** at 115 °C upon cooling: a, b) wide angle region, c, d) small angle region; a, c) original patterns, b, d) θ scans; numbers indicate the reflections used in Table 1.

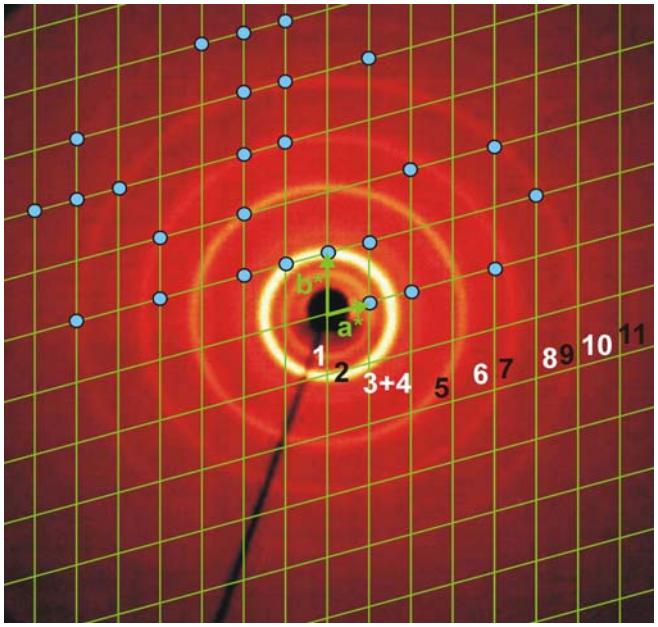

Figure 5. Indexing of the small angle reflections in the powder X-ray diffraction pattern of ZnChl **2** at 115°C to a 2D oblique lattice with lattice constants a = 83.5 Å , b = 56.9 Å, γ = 106.0°; numbers indicate reflections 1-11 in Table 1.

Table 1. Observed small and wide angle reflections in the powder X-ray diffraction pattern of ZnChl **2** at 115°C.

Reflection number	I^a	$2\theta^b$ (°)	$d_{obs}{}^c$ (Å)	hk^d	$d_{calc}{}^e$ (Å)	d_{obs} - $d_{calc}{}^f$ (Å)
1	m	1.10	80.3	10	80.3	0.0
2[g]	vs	1.64	53.8	01	54.7	0.0
2a[g]	vs	1.61	54.7	-11	52.4	0.6
2b[g]	vs	1.66	53.0	11	40.3	-0.2
3	m	2.20	40.1	20	40.1	0.0
				- 21	37.7	0.3
4	w	2.32	38.0	-22	26.2	-0.3
5	s	3.40	25.9	- 41	20.8	-0.3
6	vw	4.32	20.5	22	20.2	0.3
				40	20.1	0.4
				-13	18.9	-0.1
7	m	4.70	18.8	-42	18.8	0.0
				-23	18.6	0.2
				42	14.4	0.3
8	vw	6.01	14.7	51	14.4	0.3
				-53	14.1	0.0
9	m	6.25	14.1	-24	14.2	-0.1
				-14	14.1	0.0
				-61	13.9	0.2
				14	12.9	-0.1
10	vw	6.91	12.8	-63	12.6	0.2
				-15	11.3	0.0
11	w	7.79	11.3	-64	11.2	0.1
				-73	11.2	0.1
				-35	11.3	0.0
				-25	11.4	-0.1
12	m	14.0	6.3			
13	diff.	19.2	4.6			
14	m	25.4	3.5			

[a] *I*: estimated relative intensity, intensities of peaks are represented as vs: very strong, s: strong, m: medium, w: weak ; vw: very weak, diffus: diffused. [b] 2θ : diffraction angle. [c] d_{obs} : *d* value calculated according to Bragg's equation; indexing of the small angle reflections (numbers 1 – 11) on a 2D oblique lattice with lattice constants *a* = 83.5 Å, *b* = 56.9 Å, γ = 106.0°. [d] *hk* : assigned indices. [e] d_{calc} (Å): calculated *d* spacings. [f] d_{obs} - d_{calc} (Å): difference between experimentally observed (d_{obs}) and calculated (d_{calc}) *d* spacings. [g] The very strong peak 2 in Figure 5 may be interpreted as a single reflection 2 or as two strongly overlapping ones 2a and 2b.

The experimental and calculated *d* spacings for primitive 2D oblique lattice indexing, with lattice constants *a* = 83.5 Å, *b* = 59.4 Å and γ = 106°, were in reasonably good agreement (d_{obs} - d_{calc}, Table 1). For a 2D oblique lattice there are no particular reflection conditions[12]

hence, all peaks (*hk*) are allowed as shown in Table 1. Moreover, a 2D oblique lattice corresponds to tilted columns with column cross sections that are non-circular.[12] The powder X-ray diffraction pattern for ZnChl **2** could also be indexed alternatively to a rectangular centered unit cell lattice with lattice parameters a = 107.6 Å, b = 120.6 Å.

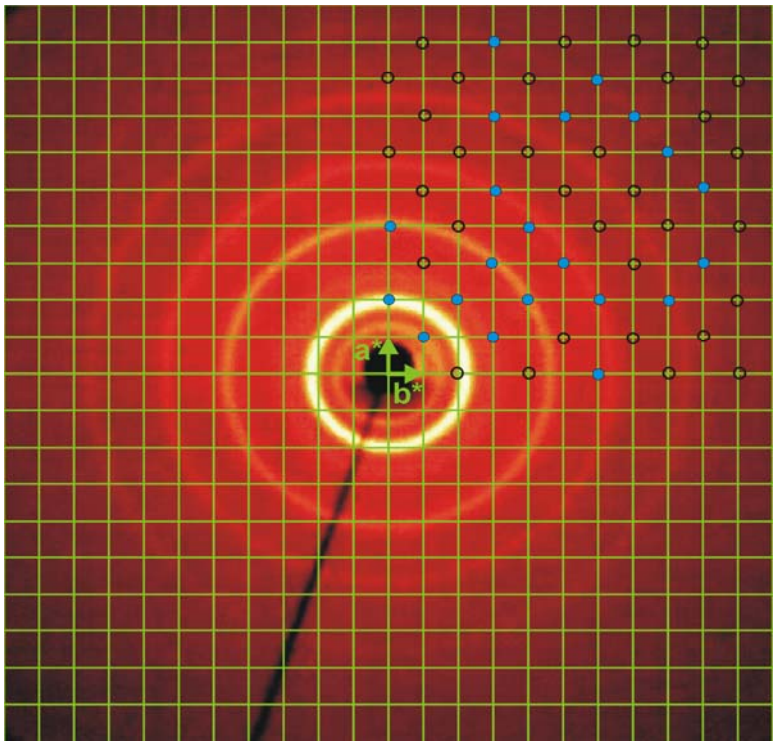

Figure 6. Indexing of small angle reflections in the powder X-ray diffraction pattern of ZnChl **2** at 115 °C to a 2-dimensional centered rectangular lattice (*c*2*mm*) with lattice constants a = 107.6 Å, b = 120.6 Å.

Table 2. Alternative indexing of the small angle reflections in the powder X-ray diffraction pattern of ZnChl **2** at 115 °C to a 2D centered rectangular lattice (*c*2*mm*) with lattice constants a = 107.6 Å, b = 120.6 Å.

Reflection number	I[a]	2θ[b] (°)	d_{obs}[c] (Å)	hk[d]	d_{calc}[e] (Å)	d_{obs} - d_{calc}[f] (Å)
1	m	1.101	80.3	11	80.3	0.0
2	vs	1.614	53.8	20	53.8	0.0
3	m	2.201	40.1	22	40.1	0.0
4	w	2.322	38.0	13	37.7	0.3
5	s	3.409	25.9	40	26.9	-1.0
				24	26.3	-0.4
				33	26.7	-0.8
6	vw	4.320	20.5	44	20.1	0.4
				06	20.1	0.4
				35	20.0	0.5
7	m	4.706	18.8	26	18.8	0.0
				53	19.0	-0.2
				-42	18.8	0.0
8	vw	6.011	14.7	28	14.5	-0.2
9	m	6.258	14.1	73	14.4	-0.3
10	vw	6.912	12.8	75	13.0	-0.2
				39	12.6	0.2
11	w	7.790	11.3	68	11.5	-0.2
				77	11.5	-0.2
				93	11.5	-0.2
				59	11.4	-0.1
				86	11.2	0.1

[a]I: estimated relative intensity, intensities of peaks are represented as vs: very strong, s: strong, m: medium, w: weak ; vw: very weak; [b]2θ: diffraction angle; [c]d_{obs}: experimentally observed d value; [d]hk: assigned indices; [e]d_{calc}: calculated d value; [f]d_{obs} - d_{calc} (Å): difference between experimentally observed (d_{obs}) and calculated (d_{calc}) d spacings.

Once the two-dimensional lattice for the columnar arrangement of the mesophases of ZnChl **2** was established, the question arises of how many molecules might be present within the column stratum. In order to estimate the number of molecules within the column stratum, the volume of the repeat unit was calculated. Taking the intracolumnar repeat distance of the chlorin cores (d = 3.5 Å) as the height h, the volume of the repeating unit ($V_{cell} = a \times b \times \sin\gamma \times h$) estimated was 15984.8 Å^3 (Table 3). The molecular volume of ZnChl **2** in the crystalline state ($V_{mol,cr}$) was calculated to be 3121.6 Å^3, according to the volume increment method of

Immirzi and Perini,[84] which indicates that there exist five molecules of **2** in the column stratum, for a calculated density as in the crystalline state ($n_{cr} = V_{cell}/V_{mol,cr}$, Table 3). For comparison, the estimated molecular volume of **2** in the isotropic liquid state (3972.9 Å^3) would indicate the existence of four molecules in the column stratum in the liquid state ($n_{liq} = V_{cell}/V_{mol,liq}$, Table 3).

Table 3. Comparison of lattice parameters obtained from powder X-ray diffraction for 2D oblique lattice and STM for ZnChl **2**; molecular volume of **2** in the crystalline phase, $V_{mol,cr}$[a] = 3121.6 Å^3, Molecular volume of **2** in the isotropic liquid state, $V_{mol,liq}$[b] = 3972.9 Å^3. See section 4.3 also for the STM discussion.

Indexing	a[c] (Å)	b[c] (Å)	h[d] (Å)	γ/α[c] (°)	V_{cell}[e] (Å^3)	n_{cr}[f]	n_{liq}[g]	A_{cell}[h] (Å^2)	n_{Acell}[i]	n_{in}[j]	ρ_{calc}[k]
hexagonal (STM)	73.7	73.7	–	120	–	–	–	4704.0	6.0	6	–
oblique (XRD)	83.5	56.9	3.5	106	15984.8	5.1	4.0	4567.1	5.9	6	1.33

[a]$V_{mol,cr}$: volume of molecule **2** for a density as in the crystalline state estimated from the incremental system by Immirzi and Perini (V_{Zn} roughly estimated from the atomic radius); [b]$V_{mol,liq}$: volume of molecule **2** for a density as in the liquid state estimated according to $V_{mol,liq} = V_{mol,cr} \times 0.7/0.55$, where 0.7 and 0.55 are the average packing coefficients in the crystal and isotropic liquid respectively; [c]a, b, γ: lattice parameters for XRD and a, b, α: lattice parameters for STM; [d]h: height of the repeating unit, h = 3.5 Å from the outer X-ray reflection (reflection no. 14, Table 1); [e]V_{cell} : volume of the 3D repeating unit, $V_{cell} = a \times b \times \sin\gamma \times h$; [f]$n_{cr}$: number of molecules in the repeating unit for a density as in the crystalline state calculated from $V_{mol,cr}$ according to $n_{cr} = V_{cell}/V_{mol,cr}$; [g]$n_{liq}$: number of molecules in the repeating unit for a density as in the liquid state calculated from $V_{mol,liq}$ according to $n_{liq} = V_{cell}/V_{mol,liq}$; [h]$A_{cell}$: area of the 2D unit cell, $A_{cell} = a \times b \times \sin\gamma$ for XRD and $A_{cell} = a \times b \times \sin\alpha$ for STM; [i]n_{Acell}: number of molecules in the unit cell calculated roughly from A_{cell} according to $n_{Acell} = A_{cell}/A_{mol,STM}$ with $A_{mol,STM} = A_{hexcell,STM}/n_{hexcell,STM}$ = 4704 Å^2/6 ≈ 780 Å^2; [j]n_{in}: integer number of molecules in the repeating unit; [k]ρ_{calc}: density calculated from the cell parameters and n_{in} according to the relationship $\rho_{calc} = n_{in} \times M/(V_{cell} \times N_A)$, where M is the molar mass of compound **2** (2130.46 g/mol).

It is noteworthy to discuss the inter-columnar distance (i.e., lattice parameter a of the 2D oblique lattice) of 83.5 Å (8.35 nm) obtained from powder XRD pattern that is smaller than the measured column width of ~10 nm by AFM visualization. Similar results have been obtained for self-organized dendronized poly(phenylacetylenes) where column diameters determined in the bulk by XRD were slightly smaller than the column widths measured by AFM on HOPG substrate.[85,86] Rationale for such differences in the column widths observed by AFM on HOPG and XRD in bulk was provided in terms of epitaxy of the peripheral alkyl tails on surface leading to formation of more flattened oblate structures on HOPG.[86,87] Likewise in our own work on liquid-crystalline perylene bisimides bearing trialkylphenyl side chains we have observed this phenomenon.[88] In the present case, the slight discrepancy in

column diameters obtained from AFM on glass substrate and XRD in bulk could be attributed as in the case of perylene bismides, to a denser packing in the bulk phase owing to the interdigitation of alkyl chains from neighboring columns.

Thus, based on powder XRD and solid-state AFM measurement at heating stage, tilted columnar arrangement for the LC phases of ZnChl **2** with non-circular column cross sections consisting of ~ five molecules per column stratum seems most plausible. Tilted mesophases of porphyrins and phthalocyanines have been reported previously in the literature.[23] The influence of central metal has also been elucidated for several mesophases based on octa-(*p*-alkoxyphenyl) phthalocyanines, where the metal free derivatives tend to form hexagonal mesophases exclusively, whereas the metallated derivatives formed tilted rectangular mesophases.[23] Notably, metal ions like Zn^{2+}, Co^{2+} or Cu^{2+} are known to stabilize the columnar mesophases of phthalocyanines and increase their tendency to arrange into tilted columnar phases.[23]

4.2.2. Two-dimensional surface organization of dendritic zinc chlorins

The two-dimensional self-assembly of ZnChls **1-3** was investigated by scanning probe microscopy (SPM) on HOPG surface. Figure 7 shows the AFM images of ZnChls **1-3** on HOPG spin coated from solutions in tetrahydrofuran (THF) at ~ 5×10^{-5} M concentration. In all the three cases, no large aggregates could be observed on the surface but layers with interesting structural features were observable. For ZnChl **1** containing dendron (3,4)-3,5-12G2CH_2, linearly ordered striations with a width of 4.8 ± 0.3 nm were observed in the layers (Figure 7a). In contrast, ZnChl **3** containing dendron (3,4,5)-3,4,5-12G2CH_2 did not form any ordered structures within the layers (Figure 7c). Pleasingly, ZnChl **2**, which has a dendron of intermediate size to that of **1** and **3**, was found to form highly ordered cyclic structures with a center-to-center distance of 7.6 ± 0.3 nm between neighboring circular arrays (Figure 7b). These results clearly indicate that the 2D packing behavior of these zinc chlorins on HOPG is dependent on the dendron wedge shapes. The dendron substituent of **1** has the smallest wedge in the series leading to formation of linearly ordered structures. In ZnChl **2**, the dendron group acts as an effective wedge for the formation of cyclic self-assembled structures, and both wedges in **1** and **2** can adopt planar orientations that lead to better interaction of the aromatic chlorin cores with the graphite surface, rendering their visualization as layers with distinct features by AFM (Figure 7d, e). In contrast, ZnChl **3** might have a conic shape, as schematically illustrated in Figure 7f, owing to the large number of alkyl chains in the

periphery, and it is apparently disadvantageous for the planarization on graphite surfaces, thereby leading to disordered structures.

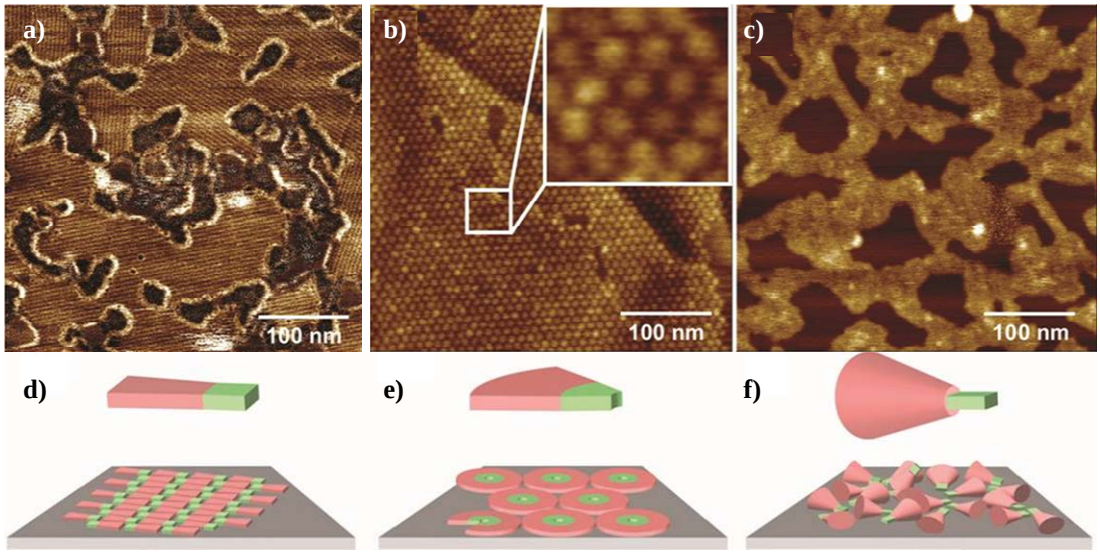

Figure 7. (a-c) AFM images of ZnChls **1-3** on HOPG; a) Phase image of **1**, (b and c) height images of **2** and **3**, respectively. (Inset in b) Magnification of a section in b. (d-f) Schematic illustrations of zinc chlorins **1-3** and their self-assembled structures on surfaces, respectively.

To obtain more insight into the molecular ordering of dyes on HOPG surfaces, STM investigations were performed with ZnChls **1-3**. For ZnChl **1**, lamellar structures were observed at the phenyloctane–HOPG interface (Figure 8a). A closer look at this high resolution STM image reveals that within the lamellae, circular brighter spots (indicated by green circles) ordered in an antiparallel fashion and feeble bright areas (indicated by pink ellipses) beside these spots were present. In the dark areas, striations with six lines in a repeat unit were observed. Generally, aromatic moieties in STM images are detected at higher tunneling current than those of alkyl chains; and the aromatic units appear brighter than that for alkyl groups, because of higher tunnelling efficiency.[89,90] Thus, in STM image of **1**, the brighter spots could be attributed to chlorin cores, the feeble bright areas to phenyl rings of the dendron, and the striations in the dark trough to alkyl chains of the dendrons (Figure 8). Accordingly, a tentative model for the molecular arrangement of **1** in the lamellae is illustrated in Figure 8b. The unit cell parameters of this arrangement (marked in Figure 8c) are $a = 2.65 \pm 0.10$ nm, $b = 9.40 \pm 0.19$ nm, and $\alpha = 92 \pm 2^{\circ}$. Notably, chlorin dyes may adopt two different molecular orientations, namely "face-on" and "edge-on", on the surfaces.[72,91-94] Not only chlorin dyes which are non-planar molecules, but other planar aromatic compounds, particularly phthalocyanine and porphyrin derivatives also tend to orient on surface in both fashions. Based on the above-mentioned STM investigations, we propose that "face-on"

orientation prevails for ZnChl **1**, and the chlorin cores adopt an offset arrangement where the dendrons of neighboring zinc chlorins are oriented in opposite directions (Figure 8f). The alkyl chains of ZnChl **1** of the neighboring rows are interdigitated at the dark trough, and three out of four alkyl chains of each ZnChl molecule were in contact with graphite surface as revealed by six lines observed for the repeat unit in STM current image of **1**. In the dark troughs 6 lines (indicated by blue arrows) could be seen in a repeat unit marked by green arrows in Figure 8d. The distance between the neighboring lines is 0.44 ± 0.02 nm, which is typical for adjacent alkyl chains on HOPG. Therefore, these lines in a repeat unit can be attributed to 6 alkyl chains that adsorb to the graphite surface (Figure 8d).

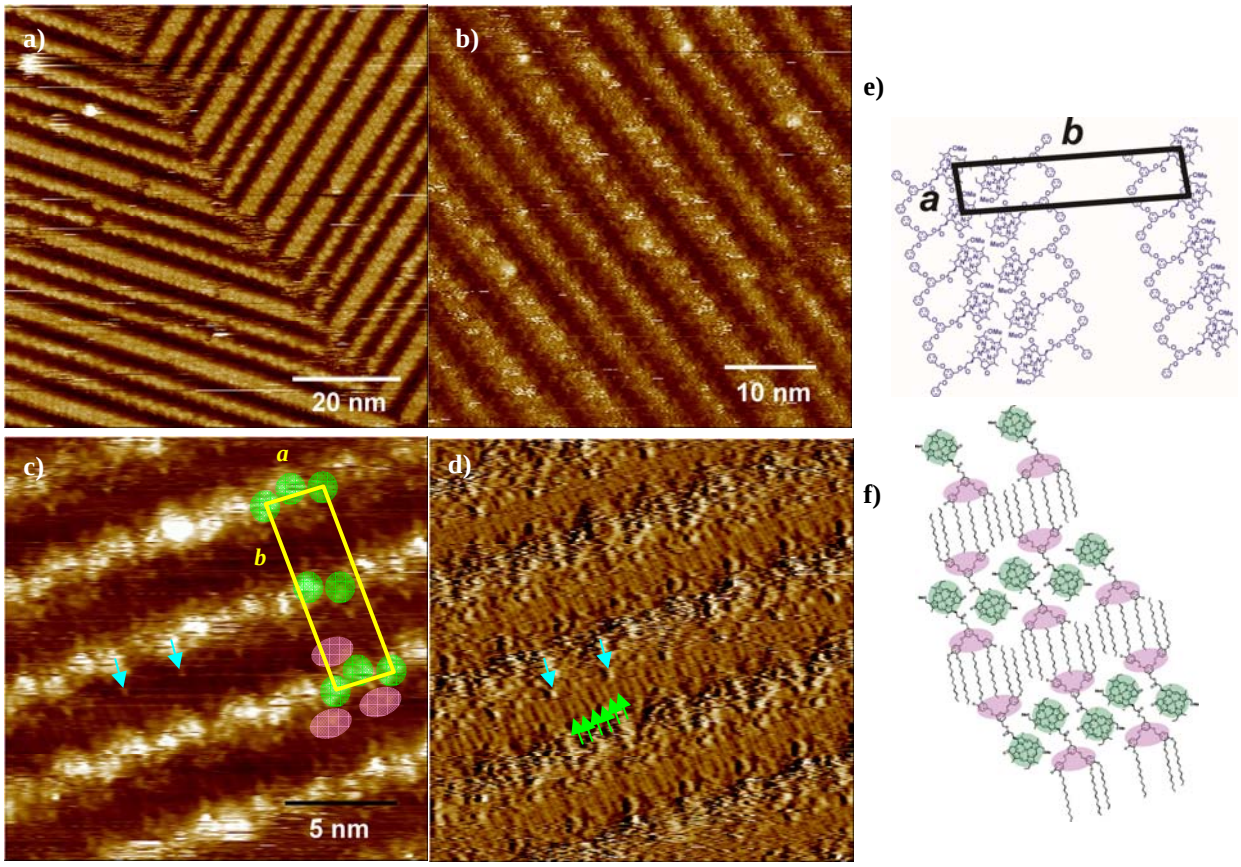

Figure 8. STM images (a-d) and the tentative model (e and f) of self-assembled **1** at the phenyloctane solution-HOPG interface; a-c) Height images; d) Current image of (c); a) E_{bias} = -1500 mV, I = 6 pA; b) E_{bias} = -900 mV, I = 5 pA; c) E_{bias} = -900 mV, I = 50 pA; e) "Double spot" row aggregate structures for ZnChl **1**; f) antiparallel row structures for ZnChl **1**.

For ZnChl **2** containing six alkyl chains in the dendron, two different self-assembled structures were observed at the solution–HOPG interface depending on the concentration (Figure 9). STM images of a solution of zinc chlorin **2** in 1-phenyloctane/octanoic acid (1:1) mixture on HOPG showed highly ordered cyclic structures with hexagonal packing (Figure 9a) similar to that observed for this ZnChl by AFM (see Figure 7b). The center-to-center

distance between the neighboring cyclic structures is 7.4 nm, which is in good agreement with the value (7.6 ± 0.3 nm) observed for cyclic structures of **2** on HOPG in air by AFM. Moreover, a single cyclic structure consist of six ZnChl **2** molecules, as six brighter spots corresponding to the chlorin cores can be seen in STM image (Figure 9a, inset). A schematic illustration for the structural order of ZnChl **2** cyclic arrays is shown in Figure 9c, and a unit cell is marked in Figure 9a with unit cell parameters $a = b = 7.37 \pm 0.08$ nm and $\alpha = 60 \pm 5°$ that are in good agreement with a hexagonal packing.

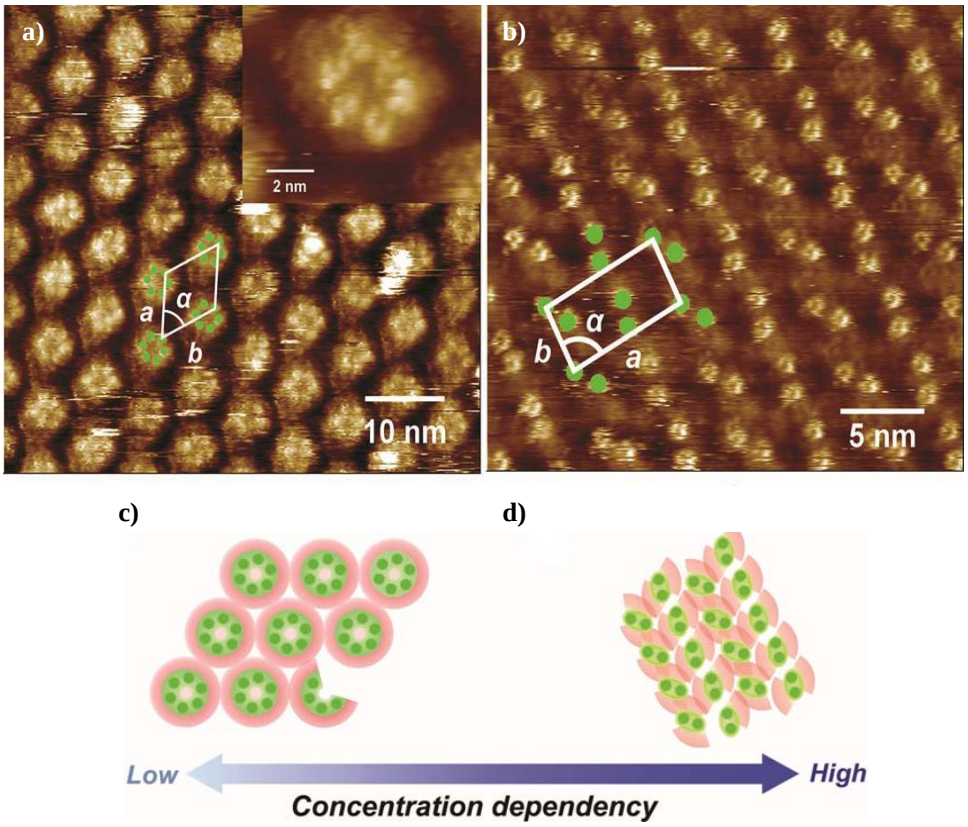

Figure 9. STM images of self-assembly of ZnChl **2** on HOPG surface at different concentrations in a 1:1 mixture of 1-phenyloctane and octanoic acid (a and b) and schematic illustrations of the corresponding molecular arrangements (c and d). (a) 1×10^{-5} M solution; STM conditions: V_{bias} = -1.8 V and I = 5 pA. (b) 2×10^{-5} M solution; STM conditions: V_{bias} = -1.5 V and I = 6 pA. (Inset in a) Magnified image of the cyclic hexameric structure.

The fact that the chlorin core does not possess any additional functional groups, e.g. hydroxy groups to stabilize 2D structures, it is reasonable to propose that these cyclic structures are established solely by the steric hindrance imposed by the dendron wedges depending upon their 2D spatial demands. In addition, the centers of hexameric cyclic structures appear to possess holes while the alkyl chains of dendrons are surrounding the chlorin cores as indicated by the dark areas in the STM image.

At higher concentrations (2×10^{-5} to ~ 5×10^{-5} M) of ZnChl **2** in 1-phenyloctane/octanoic acid (1:1) mixture, linear structures could be observed at the solution–HOPG interface. From the high resolution image in Figure 9b it is evident that the bright rows are composed of dimeric units of ZnChl **2** with two orientations, and in neighboring linear structures the dimeric units are aligned alternately, as schematically illustrated in Figure 9d. The center-to-center distance in the dimers is approximately 1.4 nm. A unit cell is marked in Figure 9b, and the parameters are $a = 7.2 \pm 0.1$ nm, $b = 3.9 \pm 0.2$ nm, and $\alpha = 85 \pm 5°$.

The formation of two different types of self-assembled structures of dendritic ZnChl **2** depending on concentrations could be explained in terms of molecular packing at the interface by considering areas of molecules in unit cells. The unit cell areas divided by the number of molecules per unit cell in linear structures and in cyclic structures are estimated as 7.0 nm^2 and 7.8 nm^2, respectively. The linear structures have slightly smaller area per molecule, compared to that of the cyclic structures, implying that the molecular packing density is higher in the former. As a result, the molecular packing changes at the interface due to variation of the concentration. At lower concentration of ZnChl **2**, cyclic structures with "face-on" molecular orientation were formed, whereas upon increasing adsorbate concentration at the interface, ZnChls **2** adopted densely packed dimeric linear structures. Recently, De Feyter and co-workers have reported such concentration dependency for self-assembled structures at the solution-solid interface.[95,96] This points out that the delicate balance of interactions between solvent, molecule and substrate is important for the construction of supramolecular 2D structures at the interface. The formation of self-assembled structures of ZnChls **1** and **2** was thus largely governed by the spatial demands of the peripheral dendron wedges attached to the 17^2-position of ZnChls.

4.2.3. Charge transport properties of Zinc Chlorins 1-3

The intrinsic charge carrier mobilities of ZnChls **1-3** in the solid state were obtained from pulse radiolysis-time resolved microwave conductivity (PR-TRMC) measurements. It is shown that the charge transport properties of these materials depend strongly on the structure of the dendron side chain, which is indicative of the difference in their supramolecular structures. In order to check thermal stability of the materials towards charge transport, PR-TRMC measurements were performed for freshly prepared samples and sample annealed at 100 ºC (Table 4). The charge carrier mobilities of ZnChls **1** and **2** (~ 0.005 $cm^2V^{-1}s^{-1}$) are significantly smaller than 3^1-methoxy compounds studied previously. Interestingly, these

compounds retained their stable morphologies of the freshly prepared samples towards charge transport. On the contrary, the charge transport properties of ZnChl **3** are similar to the 3^1-methoxy compounds studied in Chapter 3; it exhibits a high charge carrier mobility that decreases by a factor of two after annealing.

The intrinsic charge carrier mobility of ZnChl **2** in the solid-state was measured by PR-TRMC technique[15,21] for the temperature range between -20 °C and 100 °C (Table 5). The sum of charge carrier mobility (electrons and holes) was determined and appreciable charge carrier mobilities (~10^{-3}-10^{-2} cm^2/Vs) were obtained from these experiments. The first order decay and long lifetimes (>150 ns) of the PR-TRMC transients suggest charge recombination via intercolumnar tunneling through the insulating hydrocarbon mantles, similar to that observed for several columnar DLCs.[15,21,24,25,97] The mobility values are appreciable, considering the fact that chlorin units are moderately sized non-planar aromatic cores of lower symmetry. Moreover, the mobilities were not very sensitive to temperature variations and no abrupt mobility changes at the crystal-liquid crystal phase transition at around 20 ^oC and upon approaching the liquid crystal-isotropic phase transition (~ 100 ^oC) (Table 5) were observed. This probably indicates that no appreciable change in the organization of aromatic chlorin cores occur in the experimentally accessible temperature range. The lifetime of the radiation induced conductivity obtained from PR-TRMC provides a good indication of the morphology of a sample. The conductivity lifetime obtained for ZnChls **1** and **2** were found to be very long (> 150 ns for **1** and > 1 ms for **2**), and the decay followed first order kinetics, the behavior being characteristic of DLCs. The long lifetime of ZnChl **2** suggests that charge recombination occurs via intercolumnar tunneling through the insulating hydrocarbon mantle separating the tubular columns. The conductivity lifetime for ZnChl **3** was found to be much shorter than for **1** and **2** (~10 ns) and exhibit second order decay kinetics, similar to 3^1-methoxy ZnChls studied in Chapter 3.

Table 4. The charge carrier mobilities of ZnChls **1-3** in the solid state obtained by PR-TRMC measurements. The values are obtained at room temperature and samples annealed at 100 ºC.

	ZnChl **1**	ZnChl **2**	ZnChl **3**
μ ($cm^2V^{-1}s^{-1}$) before annealing	0.004	0.009	0.148
μ ($cm^2V^{-1}s^{-1}$) after annealing	0.003	0.005	<0.001

Table 5. Temperature-dependent charge carrier mobility values for ZnChl **2** upon heating (left columns) and upon cooling (right columns).

Temperature (^oC)	Charge carrier mobility (cm^2/Vs)	Temperature (^oC)	Charge carrier mobility (cm^2/Vs)
30	0.0089	100	0.0032
40	0.0080	80	0.0023
50	0.0082	60	0.0045
60	0.0056	40	0.0062
70	0.0047	20	0.0050
80	0.0052	0	0.0054
90	0.0055	-20	0.0031

The differences in the 2D organization of ZnChls **1-3** on HOPG surfaces indicate presumably different morphologies for ZnChls **1-3** in the solid state as well. Interestingly, ZnChl **2** forms liquid crystalline mesophases that is attributed to the shape of the dendron wedge. For ZnChl **1**, the dendron wedge might be too small to form a column and for space filling in solid state. On the other hand, for ZnChl **3**, the bulky dendron wedges are likely to inhibit π-stacking and interfere with the formation of organized liquid crystalline states.

4.3. Discussion

Comprehensive studies on a variety of π-conjugated compounds bearing Percec-type dendrons have revealed guidelines towards different self-assembled architectures by making use of different branching patterns, generation numbers, apex functional groups and so on.[69] These studies have shown that dendron shapes and generation not only govern self-assembly on surface and in the bulk phase, but the sterics imposed by them have pronounced influence on π-π stacking of aromatic cores attached to their apex, as recently reported for dendron functionalized triphenylenes.[98] First generation dendrons with smaller wedges i.e., substitution patterns like (4)12G0, (3,4)12G1 or (4-3,4)12G1 promoted very strong π-π stacking of triphenylenes whereas wider wedges of second generation dendrons like (4-3,4-3,5)12G2 and (3,4-3,5)12G2 render these core π-π stacking interactions weak and even inhibit them respectively.[98] It is shown in Chapter 3 that 3^1-methoxy zinc chlorins functionalized with first generation Percec-type dendron (3,5)12G1-CH_2OH at the 17^2-position, form single and double row π stacks on HOPG surface,[72] and form closely spaced antiparallel π-stacks in solid-state, that extend into a three-dimensional periodic packing forming a microcrystalline

solid.[99] The self-assembly process was primarily driven by a combination of π-π stacking and coordination of central zinc ion with 3^1-methoxy functionality of a neighboring molecule, and the contributions of various bonding and non-bonding interactions involved were investigated in order to elucidate the precise solid-state pigment organization.[99]

On the other hand, ZnChl **2** molecules functionalized with wider and more bulky second generation dendron (3,4-3,4,5)12G2-CH_2OH, in the present case, self-assemble into columnar LC phases, that are self-organized into 2D oblique unit cell lattice. Obviously, here the dendron shape primarily controls the self-assembly of ZnChl **2** by nanophase segregation of chlorin cores and alkyl side chains, augmenting columnar arrangement. In order to gain further insight into the possible molecular arrangement within the column stratum, powder XRD data set was compared with STM results.

Comparison of X-ray diffraction with STM: Visualization of the physisorbed monolayers on surface by STM enables not only to shed light on the monolayer packing pattern but also provides useful indication on plausible solid-state packing modes.[100,101] Particularly, for liquid crystals, 2D ordering of molecules on surface (2D crystals) provides valuable information about the epitaxially induced 3D superstructure formation. In sufficiently thin films, homeotropic alignment from direct solution processing or from isotropic melt could be achieved on surfaces, from different columnar materials with a range of (supra)molecular designs.[85,86] X-ray and STM results have been compared for some LC compounds and similarities as well as differences for the lattice parameters and unit cells obtained from these two methods have been reported.[100-105]

The area of the 2D lattices of the columnar structures obtained from powder XRD and the cyclic structures observed by STM for ZnChl **2** are compared, in order to verify if similar molecular arrangement might prevail within the column stratum of the LC phases as on surface. Interestingly, the area of the 2D oblique unit cell ($A_{cell} = a \times b \times \sin \gamma$, A_{cell} = 4567.1 $Å^2$) calculated from the lattice parameters (a = 83.5 Å, b = 56.9 Å, γ = 106°) obtained from powder XRD at 115 °C upon cooling was found to be very similar to that obtained for the hexagonal unit cell in STM analysis (a = 73.7 Å, b = 73.7 Å, γ = 60°, A_{cell} = 4704.0 $Å^2$). Moreover, the calculated number of molecules in the column cross section upon cooling (n_{in} = 5 for ρ_{calc} = 1.11 g/cm^3 or n_{in}= 6 for ρ_{calc} = 1.33 g/cm^3, Table 3 for calculation details) was almost identical to that observed by STM.

Notably, the center-to-center distances of the hexameric cyclic structures obtained from STM (~ 7.37 nm) is also in good agreement to the maximum intercolumnar distances (~ 8.35 nm) obtained from powder XRD. The slightly smaller value obtained in STM could be attributed to the protrusion of the dendron alkyl chains in the supernatant solution instead of extending in full length flat on the HOPG surface.[106] Based on these comparisons of dimensions and considering the size of the aromatic and aliphatic segments of the molecule, it appears reasonable to propose a model for the molecular arrangement within the column stratum, similar to the nano-phase segregated cyclic arrangement revealed by STM, where the chlorin cores are arranged towards the column centre and dendron side chains radiate towards the column periphery (Figure 10a). The differences in the unit cells and lattice parameters by these two methods (i.e., XRD and STM) find its origin in the different interactions involved in the bulk solid-state and on surface. The constraints for a dense packing are less severe in the solid-state than for 2D coverage of a surface. The dense hexameric arrangement on HOPG is most probably favored due to very strong interaction of alkyl chains with graphite, whereas in the less dense LC phase, a pentameric arrangement prevails. In the solid-state, intermolecular interactions such as π-π stacking and nano-segregation drive the packing of pigments and the tilt of the aromatic cores along with higher conformational freedom of the alkyl chains leads to a structural organization with much lesser symmetry. However, on surface, the confinement of molecules to two dimensions eliminates several degrees of freedom leading to a structural organization with much higher symmetry. Finally, there might also be some epitactic effect related to the hexagonal symmetry of the underlying graphite lattice that influences the 2D packing of **2**. In order to compare the diameters for columns consisting of five or six molecules per column stratum, molecular models (Figures 10b and c, Hyperchem version 8.05) for column cross sections were constructed. The models were based on column cross sections with the cores oriented towards centre of the column and dendron side chains radiating towards the column periphery, similar to that observed by STM. Since the stacking distance of 3.5 Å is observed in powder XRD pattern, such cyclic assemblies might be stacked on top of each other to form nano-segregated columnar tubular superstructures. The column diameter for the first model with five molecules per column stratum (~ 9.2 nm, Figure 10b), estimated upto the outermost methyl hydrogens in the fully extended alkyl side chain conformation, was very similar to that with six molecules per column stratum (~ 9.5 nm, Figure 10c). Since powder XRD has been measured at a temperature of 115 ^{o}C, where the material is in liquid crystalline phase and the alkyl chains are partially coiled, the shrinkage in

the intercolumnar distances can be envisaged, leading to an experimental maximum intercolumnar distance of 83.5 Å (8.35 nm) obtained from XRD. Such conformational melting of dendron side chains leading to smaller experimental column diameters observed from XRD than those calculated from models have been reported previously.[107-110]

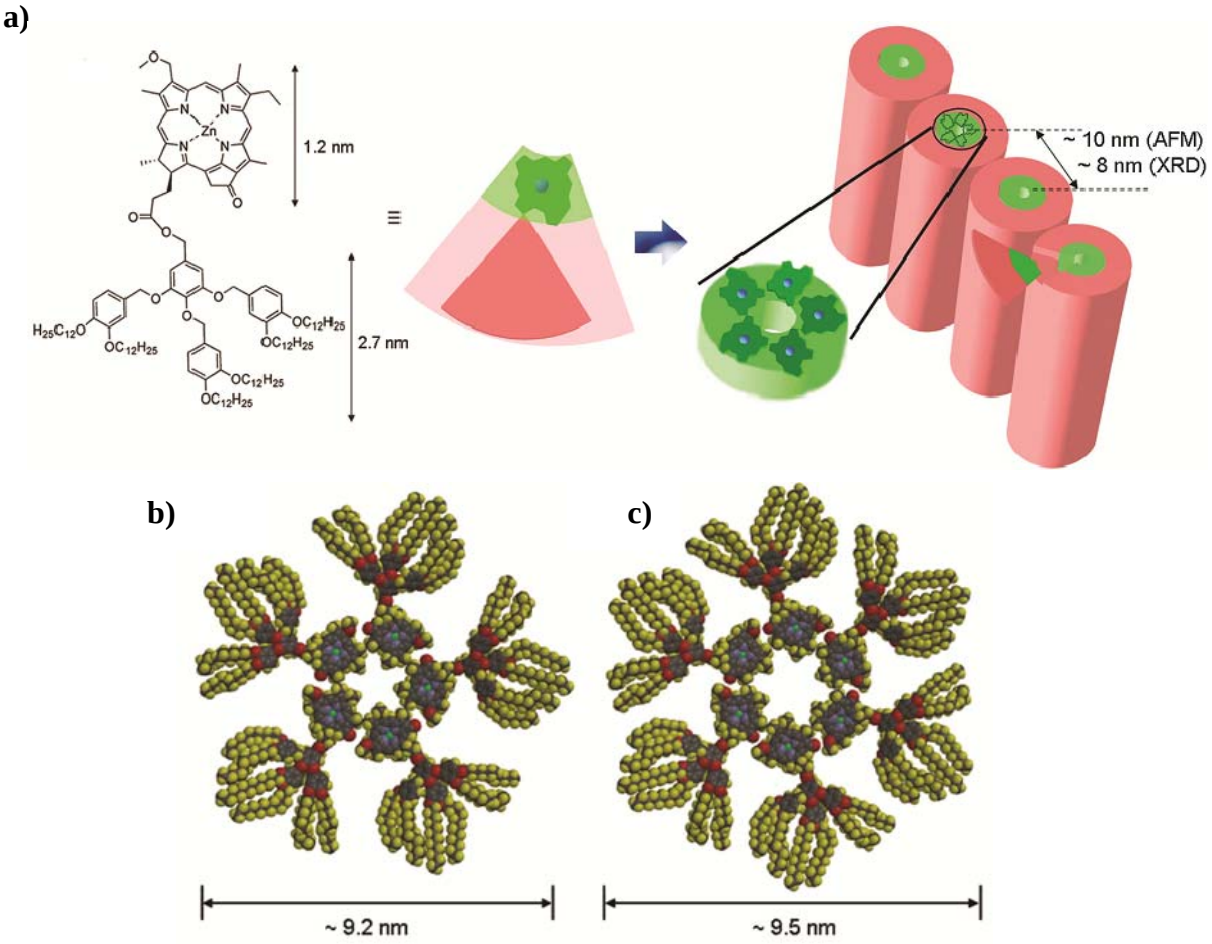

Figure 10. a) Proposed self-organization of ZnChl **2** molecules within the column stratum with indication of column diameter as obtained from AFM and XRD; Tentative models of b) pentameric and c) hexameric arrangements of ZnChl **2** molecules in the column stratum; numbers indicate calculated column diameters in the respective arrangements.

Based on the experimental results and their correlation, tilted columnar phases self-organized in a 2D oblique lattice, with column cross sections consisting of ~ five molecules is thus proposed for the LC phases of ZnChl **2**.

Charge carrier transport: The charge carrier mobility values of **2** are comparable to those found for simple columnar mesophases of discoid π-systems (~10^{-3}-1 cm^2/Vs)[18-22] and higher than those found for donor-acceptor substituted and fluorinated tapered dendrons (~ 10^{-4}-10^{-8} cm^2/Vs), evaluated by time of flight (TOF) method.[23,69,70] TOF charge carrier mobility of acene functionalized dendrons containing pyrene and naphthalene groups in their

cores exhibited similar hole mobilities in the range of 1-3.5 × 10^{-3} cm^2/Vs.[70,111] Previously, hole-mobilities of the order of 10^{-4}-10^{-5} cm^2/Vs were determined in microcrystalline chlorophyll *a* with TOF measurements.[112,113] In the framework of disorder formalism of Bässler and coworkers, maximum hole-mobility of 0.002 cm^2/Vs was predicted for microcrystalline Chl *a* in the absence of disorder.[112,113] The charge carrier mobility values observed in the present case for ZnChl **2** are thus, approximately of the same order of magnitude (~ 10^{-2}-10^{-3} cm^2/Vs).

4.4. Conclusion

To conclude, in this chapter we have demonstrated that the attachment of a second generation dendritic unit to zinc chlorin imparts mesomorphic behavior to the important class of chlorophyll pigments, particularly for ZnChl **2**. The LC behavior of **2** has been unequivocally confirmed and studied in detail by combination of experimental techniques i.e., POM, DSC, XRD and AFM in the mesophase temperature range, and the XRD results could be compared with STM studies, which suggested the plausible molecular arrangement within the column stratum. The dendron shape primarily governs the self-assembly of the taper-shaped molecular building blocks at the solid-liquid interface into cyclic rosette like structures composed of 5-6 units, that grow into columnar π-stacks in the bulk. These supramolecular columns self-organize further into a 2D oblique unit cell lattice. The fact that ZnChls **1** and **3** are not liquid crystalline might be attributed to the dendron wedge effect. Whereas in **1**, the side chains in the dendron are not enough to fill the space in solid state and form columnar structures, it can at best form lamellar structures whereas in **3**, the bulk of the dendron wedges probably interferes with the π-stacking of aromatic cores preventing the formation of organized assemblies. A strong effect of the appended dendron wedges in ZnChls **1**-**3** is observed on surface. Whereas ZnChl **1** forms layered antiparallel row structures on HOPG, cyclic structures observed for ZnChl **2** are reminiscent of the BChl organization in LH apparatus of purple bacteria. Charge carrier transport of ZnChls **1**-**3** in solid state have been investigated by PR-TRMC method that revealed appreciable charge carrier mobilities of the order of ~ 10^{-1}-10^{-2} cm^2/Vs, which is well in line to those of other dendron-mediated self-assembled nanostructures. The summarized self-assembly of **1** and **2** on surface and in solid state is schematically represented in Figure 11.

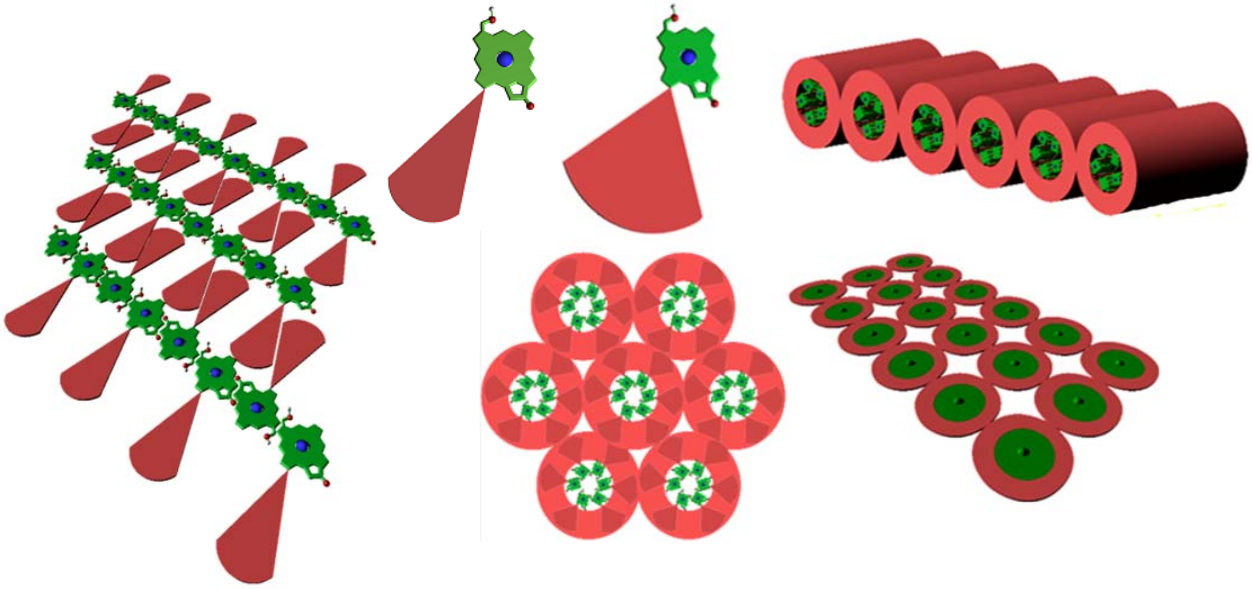

Figure 11. Schematic representation of surface and solid state packing of zinc chlorins **1** (left) and **2** (right) based on SPM and XRD studies.

The organized columnar superstructures constructed from semisynthetic ZnChl **2** are reminiscent of the tubular organization of the bacteriochlorophyll dyes in the light-harvesting chlorosomal antennae of green sulphur bacteria. In concert with their well-established exciton transport capabilities, ordered nanostructures composed of chlorophyll dyes accordingly hold promise for utilization in a variety of (opto)electronic and photovoltaic applications. The molecular design principle, based on taper-shaped dendrons for tailoring the LC phases, adopted in this work might prove beneficial for development of new soft materials based on chlorophylls or other building blocks of lower symmetry in the future.

4.5. Experimental Section

Reagents and solvents: All commercially available reagents and chemicals were obtained from common suppliers and used as such without further purification. Some of the solvents were dried according to literature known methods.[114]

High performance liquid chromatography (HPLC): Analytical HPLC was performed on a system (PU 2080 PLUS) with a photodiode array detector (MD 2015) from JASCO equipped with a ternary gradient unit (LG 2080–02) and line degasser (DG-2080-533). Semipreparative HPLC was performed on the same system (PU 2080 PLUS) with a photodiode array detector (UV 2077 PLUS). HPLC grade solvents (Rectapur®) purchased from VWR (Darmstadt, Germany) were used. Reverse phase columns obtained from Macherey-Nagel (Germany) (analytical: EC 250/4.6 NUCLEODUR 100-5 C18 ec, pre-

column: CC 8/4 NUCLEODUR 100-5 C18 ec; semipreparative: SP 250/21 NUCLEODUR 100-7 C18 ec, pre-column: SP 50/21 NUCLEODUR 100-7 C18 ec) were used.

^{1}H NMR spectroscopy: ^{1}H NMR spectra were recorded at 25 °C with a 400 MHz spectrometer from Bruker GmbH, Ettlingen (Bruker Avance 400). The chemical shifts (δ) are given in reference to TMS or the residual solvent signals in ppm values. The coupling constants *J* are expressed in Hertz (Hz) and values upto one decimal are given.

Mass spectrometry (MS): The high-resolution electron spray ionisation (ESI) and matrix assisted laser desorption ionisation (MALDI) mass spectra were measured with a Bruker Daltonics Micro TOF Focus instrument.

Polarization optical microscopy (POM): Recording of the melting points and observation of the optical textures were made on a optical polarization microscope Olympus BX41 equipped with a hot stage (Instec Inc., model HCS 402) and a 4 megapixel CCD camera.

Differential scanning calorimetry (DSC): Differential scanning calorimetry measurements were performed with a Q 1000 calorimeter from TA Instruments (Eschborn, Germany) under nitrogen gas atmosphere.

Scanning probe microscopy (SPM): All SPM investigations were carried out with Nanoscope IV (Veeco Instruments, Santa Barbara, CA). For the AFM investigations, commercial Si cantilevers with a resonance frequency ~330 KHz (Olympus) were used, and all samples were prepared by spincoating at 4000 rpm on HOPG (NT-MDT Co.) using THF solutions (ca. 5×10^{-5} M). All STM investigations were carried out at the solution–HOPG interface. Mechanical cut Pt/Ir (90/10) wires (0.25 mm) were used as STM tips. The solutions for STM investigation (1×10^{-5} to ~5×10^{-5} M) were prepared from the original THF solution in following manner: Proper volume of the original THF solution was dropped into a vial. After evaporation of THF, proper volume of solvents (1-phenyloctane for zinc chlorin **1** and a 1:1 mixture of 1-phenyloctane and octanoic acid for zinc chlorin **2** was dropped into the same vial. The scales of the images were calibrated after every investigation using the visualized lattice of the underlying HOPG.

X-ray diffraction: Powder X-ray investigations for ZnChl **2** was carried out with a Guinier film camera (Huber Diffraktionstechnik, Germany). Sample was kept in glass capillaries of 1 mm diameter in a temperature-controlled heating stage, quartz-monochromatized $Cu_{K\alpha}$ radiation was used and calibration was performed with the powder pattern of $Pb(NO_3)_2$.

Charge carrier mobility measurements: The conductive properties of ZnChls **1**-**3** was studied with the pulse-radiolysis time-resolved microwave conductivity (PR-TRMC) technique. Pressed pellet (30 mg) of the material to be investigated was irradiated with 10

nanosecond pulses of 3 MeV electrons from a Van-de-Graff accelerator, which results in the creation of a uniform micromolar concentration of electron-hole pairs. The resulting change in conductivity was monitored as the microwave power absorbed by the mobile charge carriers in the material at an electro-magnetic field frequency of 33 GHz. The mobility values are determined from the conductivity at the end of the electron pulse. This technique has been described in detail elsewhere.[21]

Synthesis: Chl *a* was extracted from algae *Spirulina Platensis* and was converted to pheophorbide *a* (pheo *a*) by literature procedure.[73] The latter compound was transformed into 3^1-methoxypheo *a* carboxylic acid in four steps according to published procedure.[72] The subsequent esterification at the 17^2-position with the second generation dendritic alcohols 3,4-(3,5)-12G_2-dodecylalkoxybenzyl alcohol, 3,4-(3,4,5)-12G_2-dodecylalkoxybenzyl alcohol, and 3,4,5-(3,4,5)-12G_2-dodecylalkoxybenzyl alcohol provided the precursors **1a-3a** respectively. Metalation of the free base compounds **1a-3a** with saturated solution of $Zn(OAc)_2$ in methanol and THF as solvent afforded the target zinc chlorins **1-3**. The dendritic alcohols 3,4-(3,5)-12G_2-CH_2OH, 3,4-(3,4,5)-12G_2-CH_2OH, and 3,4,5-(3,4,5)-12G_2-CH_2OH were synthesized according to convergent synthetic method developed by Percec and co-workers.[74]

3-devinyl-3-methoxymethyl-13^2-demethoxycarbonyl-pheophorbide *a* 3,4-(3,5)-dodecyl-oxybenzylester (1a)

The free base 3^1 methoxypheo *a* compound was obtained starting from according to literature known method.[72] Chlorin derivative (33 mg, 0.0597 mmol) was dissolved in dry CH_2Cl_2 (10 mL) followed by the addition of dendritic alcohol 3,4-(3,5)-12G_2-CH_2OH (63 mg, 0.0597 mmol), DCC (30.7 mg, 0.1492 mmol), DMAP (22.2 mg, 0.1791 mmol), and DPTS (52.7 mg, 0.1791 mmol). After stirring at RT for 5 min, Hünigs base (19.3 mg, 0.1492 mmol) was added. The reaction mixture was stirred for a further 3 h and then treated with CH_2Cl_2 (100 mL) and a saturated solution of NH_4Cl (20 mL), then it was washed with water (50 mL) several times. The combined organic phases were dried with Na_2SO_4, solvent was removed and the residue was purified by column chromatography with a mixture of CH_2Cl_2/methanol (95:5) as the eluent, and was further purified by semipreparative HPLC (55.2 mg, 0.0346 mmol, 58%). Analytical HPLC: **1a** was eluted after 5.9 min at a flow of 1 mL/min with methanol/CH_2Cl_2 (7:3) as the solvent. M.p. 120 ^oC; ^1H NMR (400 MHz, $CDCl_3$, TMS): 9.53 (s, 1H, 10-H), 9.30 (s, 1H, 5-H), 8.39 (s, 1H, 20-H), 6.98-6.57 (m, 9H, ArH-2, ArH-4, ArH-6, ArH-2', ArH-4', ArH-6'), 5.56 (s, 2H, 3^1-H), 5.34-4.86 (m, 8H, 13^2-CH_2, 1'-H, 1''-H), 4.46 (dq, ^3J (H, H)=7.3 Hz, ^3J (H, H) = 1.8 Hz, 1H, 18-H), 4.34 (td, ^3J(H, H) = 8.6 Hz, ^3J (H, H) = 2.7 Hz, 1H, 17-H),

3.99-3.58 (m, 16H, α-H, 8^1-H, 12^1-H, 3^1-OMe), 3.28 (s, 3H, 2^1-H), 3.26 (s, 3H, 7^1-H), 2.40-2.25 and 2.00-1.92 (m, 4H, 17^1-H, 17^2-H), 1.80-1.64 (m, 14H, β-H, 18^1-H, 8^2-H), 1.35-1.26 (m, 72H, $CH_3(CH_2)_9$), 0.87 (t, 12H, ^3J = 6.0 Hz, ω-H), 0.39 (s, 1H, NH), -1.72 (s, 1H, NH); HRMS (ESI): *m*/*z* calcd for $C_{102}H_{150}N_4O_{10}$ $[M+H]^+$: 1593.1451; found: 1593.1475.

3-devinyl-3-methoxymethyl-13^2-demethoxycarbonyl-pheophorbide *a* 3,4-(3,5)-dodecyl-oxybenzylester zinc complex (1)

Chlorin derivative **1a** (50 mg, 0.0314 mmol) was dissolved in THF (5 mL), followed by the addition of a saturated solution of zinc acetate in methanol (4 mL). The reaction was then terminated by the addition of CH_2Cl_2 (100 mL), water (100 mL), and a saturated aqueous solution of $NaHCO_3$ (20 mL). The resulting turquoise zinc chlorin **1** was then extracted several times with CH_2Cl_2 (200 mL), and the combined organic phases were dried over sodium sulphate, the desiccant was removed by filtration and the solvent was removed under vacuum. Zinc chlorin **1** was further purified by semipreparative HPLC (37.4 mg, 0.0226 mmol, 72%). Analytical HPLC: **1** was eluted after 4.88 min at a flow of 1 mL/min with methanol/CH_2Cl_2 (7:3) as the solvent. M.p.137-139 ^oC; ^{1}H-NMR (400 MHz, $CDCl_3$, TMS): 9.53 (s, 1H, 10-H), 9.30 (s, 1H, 5-H), 8.39 (s, 1H, 20-H), 6.98-6.57 (m, 9H, ArH-2, ArH-4, ArH-6, ArH-2', ArH-4', ArH-6'), 5.56 (s, 2H, 3^1-H), 5.34-4.86 (m, 8H, 13^2-CH_2, 1'-H, 1''-H), 4.46 (dq, ^3J (H, H)=7.3 Hz, ^3J (H, H) = 1.8 Hz, 1H, 18-H), 4.34 (td, ^3J(H, H) = 8.6 Hz, ^3J (H, H) = 2.7 Hz, 1H, 17-H), 3.99-3.59 (m, 16H, α-H, 8^1-H, 12^1-H, 3^1-OMe), 3.28 (s, 3H, 2^1-H), 3.26 (s, 3H, 7^1-H), 2.40-2.25 and 2.00-1.92 (m, 4H, 17^1-H, 17^2-H), 1.80-1.64 (m, 14H, β-H, 18^1-H, 8^2-H), 1.35-1.26 (m, 72H, $CH_3(CH_2)_9$), 0.87 (t, 12H, ^3J = 6.0 Hz, ω-H); MS (MALDI-TOF, matrix: DCTB) for $C_{102}H_{148}N_4O_{10}Zn$ Calculated value: 1654.05, found value: 1654.68 for $[M+H^+]$.

3-devinyl-3-methoxymethyl-13^2-demethoxycarbonyl-pheophorbide *a* 3,4-(3,4,5)-dodecyl-oxybenzylester (2a)

The precursor compound 3^1-methoxy-17^2-chlorin carboxylic acid was obtained starting from Chl *a* according to literature known methods.[72] This chlorin carboxylic acid derivative (30.0 mg, 0.0543 mmol) was dissolved in dry CH_2Cl_2 (10 mL), followed by the addition of the dendritic alcohol 3,4(3,4,5)12G_2-CH_2OH[74] (207.6 mg, 0.1357 mmol), DCC (56.06 mg, 0.2717 mmol), DMAP (20.2 mg, 0.1629 mmol), and DPTS (47.9 mg, 0.1629 mmol). After stirring the solution at RT for 5 min, Hünigs base (*N*,*N*-ethyldiisopropylamine) (17.5 mg, 0.023 mmol) was added. The reaction mixture was stirred for a further 3 h and then treated

with CH_2Cl_2 (100 mL) and a saturated solution of NH_4Cl (20 mL), then it was washed with water (50 mL) three times. The combined organic phases were dried with Na_2SO_4, solvent was removed and the residue was purified by column chromatography with a mixture of CH_2Cl_2/methanol (95:5) as the eluent, and was further purified by semipreparative HPLC to obtain compound **2a** (78.6 mg, 0.038 mmol, 63%). Analytical HPLC: **2a** was eluted after 5.9 min at a flow rate of 1 mL/min with methanol/CH_2Cl_2 (7:3) as the eluent. M.p. 127–130 ^oC; ^1H NMR (400 MHz, $CDCl_3$, 25 ^oC): δ = 9.48 (s, 1H, 10-H), 9.39 (s, 1H, 5-H), 8.49 (s, 1H, 20-H), 6.95-6.59 (m, 9H, 2''-H, 5''-H, 6''-H), 6.50 (s, 2H, 2'-H, 6'-H), 5.65-5.63 (m, 2H, 3^1-H), 5.25 (d, ^2J = 19.8 Hz, 1H, 13^2-H), 5.09 (d, ^2J = 19.8 Hz, 1H, 13^2-H), 4.94 (d, ^2J = 12.3 Hz, 1H, a-H), 4.92-4.79 (m, 6H, b-H), 4.55 (d, ^2J = 2.3 Hz, 1H, a-H), 4.34 (dq, ^3J = 7.3 Hz, ^3J = 1.8 Hz, 1H, 18-H), 4.29 (d, ^3J = 8.1 Hz, 1H, 17-H), 4.02-3.82 (m, 14H, α-H, 8^1-H), 3.67 (s, 3H, 12^1-H), 3.64 (s, 3H, 3^1-OCH_3), 3.40 (s, 3H, 2^1-H), 3.38 (s, 3H, 7^1-H), 2.71-2.48 and 2.30-2.10 (m, 4H, 17^1-H, 17^2-H), 1.86-1.71 (m, 18H, 18^1-H, β-H, 8^2-H), 1.31-1.18 (m, 108H, CH_2), 0.82-0.71 (m, 18H, ω-H), 0.34 (s, 1H, NH), -1.78 (s, 1H, NH); HRMS (ESI): *m*/*z* calcd for $C_{133}H_{204}N_4O_{13}$ $[M]^+$: 2067.5503; found: 2067.5564.

3-devinyl-3-methoxymethyl-13^2-demethoxycarbonyl-pheophorbide *a* 3,4-(3,4,5)-dodecyl-oxybenzylester zinc complex (2)

Free base chlorin derivative **2a** (60.0 mg, 0.029 mmol) was dissolved in THF (5 mL), followed by the addition of a saturated solution of zinc acetate in methanol (4 mL). The reaction was then terminated by the addition of CH_2Cl_2 (100 mL), water (100 mL), and a saturated aqueous solution of $NaHCO_3$ (20 mL). The resulting turquoise zinc chlorin compound **2** was then extracted four times with CH_2Cl_2 (150 mL), and the combined organic phases were dried over Na_2SO_4, the desiccant was removed by filtration and the solvent was evaporated under vacuum. Zinc chlorin **2** was further purified by semipreparative HPLC (38.9 mg, 0.0182 mmol, 70%). Analytical HPLC: **2** was eluted after 4.9 min at a flow rate of 1 mL/min with methanol/CH_2Cl_2 (7:3) as the eluent. M. p. 137–138 ^oC; ^1H-NMR (400 MHz, $CDCl_3$ with one drop of $[D_5]$pyridine, 25 ^oC): δ = 9.46 (s, 1H, 10-H), 9.25 (s, 1H, 5-H), 8.35 (s, 1H, 20-H), 6.98-6.46 (m, 11H, 2''-H, 5''-H, 6''-H, 2'-H, 6'-H), 5.50 (s, 2H, 3^1-H), 5.25 (d, ^2J = 19.5 Hz, 1H, 13^2-H), 5.00-4.78 (m, 9H, 13^2-CH_2, a-H, b-H), 4.50 (dq, ^3J = 7.3 Hz, ^3J = 2.0 Hz, 1H, 18-H), 4.34 (dt, ^3J = 8.3 Hz, ^3J = 2.3 Hz, 1H, 17-H), 3.90-3.67 (m, 12H, α-H), 3.65-3.51 (m, 8H, 8^1-H, 12^1-H, 3^1-OCH_3), 3.21 (s, 3H, 2^1-H), 3.20 (s, 3H, 7^1-H), 2.36-2.27 and 2.01-1.90 (m, 4H, 17^1-H, 17^2-H), 1.89-1.79 (m, 3H, 18^1-H) and 1.77-0.91 (overlapped peaks, 123H, 8^2-H, β-H, CH_2), 0.79 (t, 18H, ^3J = 6.3 Hz, ω-H); HRMS (ESI): *m*/*z* calcd for

$C_{133}H_{202}N_4O_{13}Zn$ $[M+H]^+$: 2130.4632; found: 2130.4615; UV/Vis (THF): λ_{max} (ε_{max}) = 648 nm (90,000 M^{-1} cm^{-1}).

3-devinyl-3-methoxymethyl-13^2-demethoxycarbonyl-pheophorbide *a* 3,4,5-(3,4,5)-dodecyloxybenzylester (**3a**)

The free base 3^1 methoxypheo *a* compound obtained according to literature known method.[72] (50 mg, 0.0833 mmol) was dissolved in dry CH_2Cl_2 (10 mL) followed by the addition of dendritic alcohol 3,4,5-(3,4,5)-12G2-CH_2OH (346 mg, 0.1666 mmol), DCC (182.2 mg, 0.8833 mmol), DMAP (51.7 mg, 0.4165 mmol), and DPTS (122.6 mg, 0.4165 mmol). After stirring at RT for 5 min, Hünigs base (21.4 mg, 0.1249 mmol) was added. The reaction mixture was stirred for a further 3 h and then treated with CH_2Cl_2 (100 mL) and a saturated solution of NH_4Cl (20 mL), then it was washed with water (50 mL) several times. The combined organic phases were dried with Na_2SO_4, solvent was removed and the residue was purified by column chromatography with a mixture of CH_2Cl_2/methanol (95:5) as the eluent, and was further purified by semipreparative HPLC (158 mg, 0.06 mmol, 66.4%). Analytical HPLC: **3a** was eluted after 5.9 min at a flow of 1 mL/min with methanol/CH_2Cl_2 (7:3) as the solvent. M.p. 135 ^oC; ^{1}H-NMR (400MHz, $CDCl_3$): Analytical HPLC: **3** was eluted after 4.8 min at a flow of 1 mL/min with methanol as the solvent. M.p.137-139 ^oC; ^{1}H-NMR (400MHz, $CDCl_3$ with one drop of [D_5]pyridne): 9.54 (s, 1H, 10-H), 9.46 (s, 1H, 5-H), 8.55 (s, 1H, 20-H), 6.98 (s, 2H, ArH-2, ArH-6), 6.66 (s, 2H, 3^1-H), 6.63-6.56 (m, 6H, 2''-H, 6''-H, 2'-H, 6'-H), 5.66-5.02 (m, 2H, 13^2-CH_2), 5.01 (s, 6H, b-H), 4.97 (s, 2H, a-H), 4.50-4.31 (m, 2H, 18-H, 17-H), 3.94-3.75 (m, 26H, 18^1-H, α-H at 3, 4, 5-(4′) position, α-H at 3, 5-(3′, 5′) position, α-H at 4-(3′, 5′) position, 8^1-H, 3-^{1}OMe), 3.67 (s, 3H, 12^1-H), 2.27 (s, 3H, 2^1-H), 2.21 (s, 3H, 7^1-H), 2.10-1.90 (m, 4H, 17^1-H, 17^2-H), 1.75-1.68 (m, 21H, β-H, 8^2-H), 1.43-1.25 (overlapped peaks, 162H, $CH_3(CH_2)_9$), 0.87 (t, ^3J = 6.4 Hz, 27H, ω-H), 0.38 (s, 1H; NH), -1.74 ppm (s, 1H; NH); MS (MALDI-TOF, matrix: DCTB) for $C_{169}H_{276}N_4O_{16}Zn$: calculated value : 2619.09, found value : 2619.04 for $[M]^+$.

3-devinyl-3-methoxymethyl-13^2-demethoxycarbonyl-pheophorbide *a* 3,4,5-(3,4,5)-dodecyloxybenzylester zinc complex (3)

Chlorin derivative **3a** (135 mg, 0.0513 mmol) was dissolved in THF (5 mL), followed by the addition of a saturated solution of zinc acetate in methanol (4 mL). The reaction was then terminated by the addition of CH_2Cl_2 (100 mL), water (100 mL), and a saturated aqueous

solution of $NaHCO_3$ (20 mL). The resulting turquoise blue zinc chlorin **3** was then extracted several times with CH_2Cl_2 (150 mL), and the combined organic phases were dried over sodium sulphate, the desiccant was removed by filtration and the solvent was removed under vacuum. Zinc chlorin **3** was further purified by semipreparative HPLC (87 mg, 0.0324 mmol, 63.5%). Analytical HPLC: **3** was eluted after 4.7 min at a flow of 1 mL/min with methanol/CH_2Cl_2 (7:3) as the solvent. M.p.140-142 ^oC; ^{1}H-NMR (400MHz, $CDCl_3$ with one drop of [D_5]pyridne): 9.54 (s, 1 H, 10-H), 9.46 (s, 1 H, 5-H), 8.55 (s, 1 H, 20-H), 6.98 (s, 2 H, ArH-2, ArH-6), 6.66 (s, 2 H, 3^1-H), 6.63-6.56 (m, 6 H, 2''-H, 6''-H, 2'-H, 6'-H), 5.66-5.02 (m, 2 H, 13^2-CH_2), 5.01 (s, 6H, b-H), 4.97 (s, 2H, a-H), 4.50-4.31 (m, 2H, 18-H, 17-H), 3.94-3.75 (m, 26H, 18^1-H, α-H at 3, 4, 5-(4´) position, α-H at 3, 5-(3´, 5´) position, α-H at 4-(3´, 5´) position, 8^1-H, 3-^{1}OMe), 3.67 (s, 3H, 12^1-H), 2.27 (s, 3H, 2^1-H), 2.21 (s, 3H, 7^1-H), 2.10-1.90 (m, 4H, 17^1-H, 17^2-H), 1.75-1.68 (m, 21H, β-H, 8^2-H), 1.43-1.25 (overlapped peaks, 162H, $CH_3(CH_2)_9$), 0.87 (t, ^3J = 6.4 Hz, 27H, ω-H); MS (MALDI-TOF, matrix: DCTB) for $C_{169}H_{274}N_4O_{16}$ calculated value: 2683.15, Obtained value: 2683.05 for $[M+H]^+$.

4.6. References and notes

(1) Forrest, S. R.; Thomson, M. E. *Chem. Rev.* **2007**, *107*, 923–925, and the articles published in this thematic issue of *Chem. Rev.* (**2007**, *107*, Issue 4).

(2) *Semiconducting Polymers: Chemistry, Physics and Engineering*; Hadziioannou, G., van Hutten P. F., Eds.; Wiley-VCH: Weinheim, 2000.

(3) *Electronic Materials: the Oligomer Approach*; Wegner, G., Müllen K., Eds.; Wiley-VCH: Weinheim, 1998.

(4) Hoeben, F. J. M.; Jonkeijm, P.; Meijer, E. W.; Schenning, A. P. H. J. *Chem. Rev.* **2005**, *105*, 1491–1546.

(5) Schenning, A. P. H. J.; Meijer, E. W. *Chem. Commun.* **2005**, 3245–3258.

(6) Hill, J. P.; Jin, W.; Kosaka, A.; Fukushima, T.; Ichihara, H.; Shimomura, T.; Ito, K.; Hashizume, T.; Ishii, N.; Aida, T. *Science* **2004**, *304*, 1481–1483.

(7) Yamamoto, Y.; Fukushima, T.; Suna, Y.; Ishii, N.; Saeki, A.; Seki, S.; Tagawa, S.; Taniguchi, M.; Kawai, T.; Aida, T. *Science* **2006**, *314*, 1761–1764.

(8) Yamamoto, Y.; Zhang, G.; Jin, W.; Fukushima, T.; Ishii, N.; Saeki, A.; Seki, S.; Tagawa, S.; Minari, T.; Tsukagoshi, K.; Aida, T. *Proc. Natl. Acad. Sci. U. S. A.* **2009**, *106*, 21051–21056.

(9) Grozema, F. C.; Siebbeles, L. D. A. *Int. Rev. Phys. Chem.* **2008**, *27*, 87–138.

(10) Kumar, S. *Chem. Soc. Rev.* **2006**, *35*, 83–109.

(11) Kumar, S. *Liq. Cryst.* **2009**, *36*, 607–638.

(12) Laschat, S.; Baro, A.; Steinke, N.; Giesselmann, F.; Hägele, C.; Scalia, G.; Judele, R.; Kapatsina, E.; Sauer, S.; Schreivogel, A.; Tosoni, M. *Angew. Chem., Int. Ed.* **2007**, *46*, 4832–4887.

(13) Cammidge, S. A. N.; Bushby R. J. B. *Handbook of Liquid Crystals, Vol. 2B: Low Molecular Weight Liquid Crystals II*, Wiley-VCH, Weinheim **1998**.

(14) Bushby, R. J.; Lozman, O. R. *Curr. Opin. Colloid Interface Sci.* **2002**, *7*, 343–354.

(15) Warman, J. M.; de Haas, M. P.; Dicker, G.; Grozema, F. C.; Piris, J.; Debije, M. G.; *Chem. Mater.* **2004**, *16*, 4600–4609.

(16) Chen, Z.; Stepanenko, V.; Dehm, V.; Prins, P.; Siebbeles, L. D. A.; Seibt, J.; Marquetand, P.; Engel, V.; Würthner, F. *Chem.–Eur. J.* **2007**, *13*, 436–449.

(17) Feng, X.; Marcon, V.; Pisula, W.; Hansen, M. R.; Kirkpatrick, J.; Grozema, F.; Andrienko, D.; Kremer, K.; Müllen, K. *Nat. Mat.* **2009**, *8*, 421–426.

(18) Sergeyev, S.; Pisula, W.; Geerts, Y. H. *Chem. Soc. Rev.* **2007**, *36*, 1902–1929.

(19) Simpson, C. D.; Wu, J.; Watson, M. D.; Müllen, K. *J. Mater. Chem.* **2004**, *14*, 494–504.

(20) Wu, J.; Pisula, W.; Müllen, K. *Chem. Rev.* **2007**, *107*, 718–747.

(21) Warman, J. M.; van de Craats, A. M. *Mol. Cryst. Liq. Cryst.* **2003**, *396*, 41–72.

(22) O'Neill, M.; Kelly, S. M. *Adv. Mater.* **2003**, *15*, 1135–1146.

(23) Eichhorn, H. *J. Porphyrins Phthalocyanines* **2000**, *4*, 88–102.

(24) Lemaur, V.; da Silva Filho, D. A.; Coropceanu, V.; Lehmann, M.; Geerts, Y. H.; Piris, J.; Debije, M. G.; van de Craats, A. M.; Senthilkumar, K.; Siebbeles, L. D. A.; Warman, J. M.; Brédas, J. -L.; Cornil, J. *J. Am. Chem. Soc.* **2004**, *126*, 3271–3279.

(25) Lehmann, M.; Kestemont, G.; Aspe, R. G.; Buess-Herman, C.; Koch, M. H. J.; Debije, M. G.; Piris, J.; de Haas, M. P.; Warman, J. M.; Watson, M. D.; Lemaur, V.; Cornil, J.; Geerts, Y. H.; Gearba, R.; Ivanov, D. A. *Chem.–Eur. J.* **2005**, *11*, 3349–3362.

(26) a) Schmidt-Mende, L.; Watson, M.; Müllen, K.; Friend, R. H. *Mol. Cryst. Liq. Cryst.* **2003**, *396*, 73–90; b) Schmidt-Mende, L.; Fechtenkötter, A.; Müllen, K.; Moons, E.; Friend, R. H.; MacKenzie, J. D. *Science* **2001**, *293*, 1119–1122; c) Chandrasekhar, S.; Sadashiva, B. K.; Suresh, K. A. *Pramana* **1977**, *9*, 471–480.

(27) Xiao, S.; Myers, M.; Miao, Q.; Sanaur, S.; Pang, K.; Steigerwald, M. L.; Nuckolls, C. *Angew. Chem., Int. Ed.* **2005**, *44*, 7390–7394.

(28) Guo, X.; Xiao, S.; Myers, M.; Miao, Q.; Steigerwald, M. L.; Nuckolls, C. *Proc. Natl. Acad. Sci. USA* **2009**, *106*, 691–696.

(29) Adam, D.; Schuhmacher, P.; Simmerer, J.; Häussling, L.; Siemensmeyer, K.; Etzbachi, K. -H.; Ringsdorf, H.; Haarer, D. *Nature* **1994**, *371*, 141–143.

(30) Kumar, S. *Liq. Cryst.* **2005**, *32*, 1089–1113.

(31) Van der Pol, J. F.; Neeleman, E.; Zwikker, J. W.; Nolte, R. J. M.; Drenth, W.; Aerts, J.; Visser, R.; Picken, S. J. *Liq. Cryst.* **2006**, *33*, 1378–1387.

(32) a) Hatsusaka, K.; Ohta, K.; Yamamoto, I.; Shirai, H. *J. Mater. Chem.* **2001**, *11*, 423–433; b) Tantrawong, S.; Sugino, T.; Shimizu, Y.; Takeuchi, A.; Kimura, S.; Mori, T.; Takezoe, H. *Liq. Cryst.* **1998**, *24*, 783–785; c) Cammidge, S. A. N.; Bushby R. J. *Discotic Liquid Crystals: Synthesis and Structural Features*. In *Handbook of Liquid Crystals; Vol. 2B: Low Molecular Weight Liquid Crystals II*; Demus, D., Goodby, J., Gray, G. W., Spiess, H.-W., Vill, V., Eds.; Wiley-VCH: Weinheim, 1998, pp. 730–739.

(33) Ohta, K.; Ando, N.; Yamamoto, I. *Liq. Cryst.* **1999**, *26*, 663–668.

(34) Kimura, M.; Saito, Y.; Ohta, K.; Hanabusa, K.; Shirai, H.; Kobayashi, N. *J. Am. Chem. Soc.* **2002**, *124*, 5274–5275.

(35) Cammidge, A. N.; Cook, M. J.; Harrison, K. J.; McKeown, N. B. *J. Chem. Soc.-Perkin Trans. 1* **1991**, 3053–3058.

(36) Martinez-Diaz, M. V.; de la Torrea, G.; Torres, T. *Chem. Commun.* **2010**, *46*, 7090−7108.

(37) Bartelmess, J.; Ballesteros, B.; de la Torre, G.; Kiessling, D.; Campidelli, S.; Prato, M.; Torres, T.; Guldi, D. M. *J. Am. Chem. Soc.* **2010**, *132*, 16202−16211.

(38) Nicolau, M.; Cabezon, B.; Torres, T. *Coord. Chem. Rev.* **1999**, *192*, 231–243.

(39) Garcia-Frutos, E. M.; Bottari, G.; Vazquez, P.; Barbera, J.; Torres, T. *Chem. Commun.* **2006**, 3107–3109.

(40) de la Escosura, A.; Martinez-Diaz, M. V.; Barbera, J.; Torres, T. *J. Org. Chem.* **2008**, *73*, 1475–1480.

(41) Li, J. Z.; Tang, T.; Li, F.; Li, M. *Dyes and Pigments* **2008**, *77*, 395–401.

(42) Dehm, V.; Chen, Z.; Baumeister, U.; Prins, P.; Siebbeles, L. D. A.; Würthner, F. *Org. Lett.* **2007**, *9*, 1085–1088.

(43) Debije, M. G.; Chen, Z.; Piris, J.; Neder, R. B.; Watson, M. M.; Müllen, K.; Würthner, F. *J. Mater. Chem.* **2005**, *15*, 1270–1276.

(44) Sautter, A.; Thalacker, C.; Würthner, F. *Angew. Chem., Int. Ed.* **2001**, *40*, 4425–4428.

(45) Wicklein, A.; Lang, A.; Muth, M.; Thelakkat, M. *J. Am. Chem. Soc.* **2009**, *131*, 14442–14453.

(46) a) Sautter, A.; Thalacker, C.; Würthner, F. *Angew. Chem., Int. Ed.* **2001**, *40*, 4425–4428; b) Würthner, F.; Thalacker, C.; Diele, S.; Tschierske, C. *Chem.–Eur. J.* **2001**, *7*, 2245–2253.

(47) Rohr, U.; Kohl, C.; Müllen, K.; van de Craats, A. M.; Warman, J. *J. Mater. Chem.* **2001**, *11*, 1789–1799.

(48) Sessler, J. L.; Callaway, W.; Dudek, S. P.; Date, R. W.; Lynch, V.; Bruce, D. W. *Chem. Commun.* **2003**, 2422–2423.

(49) Stępień, M.; Donnio, B.; Sessler, J. L. *Angew. Chem., Int. Ed.* **2007**, *46*, 1431–1435.

(50) Stępień, M.; Donnio, B.; Sessler, J. L. *Chem.–Eur. J.* **2007**, *13*, 6853–6863.

(51) Kim, J. Y.; Bard, A. J. *Chem. Phys. Lett.* **2004**, *383*, 11–15.

(52) Fox, M. A.; Grant, J. V.; Melamed, D.; Torimoto, T.; Liu, C.; Bard, A. J. *Chem. Mater.* **1998**, *10*, 1771–1776.

(53) Gregg, B. A.; Fox, M. A.; Bard A. J. *J. Phys. Chem.* **1990**, *94*, 1586–1598.

(54) Liu, C.; Pan, H.; Fox, M. A.; Bard, A. J. *Science* **1993**, *261*, 897–899.

(55) Giroud-Godquin, A. -M.; Maitlis, P. M. *Angew. Chem., Int. Ed.* **1991**, *30*, 375–402.

(56) Balaban, T. S.; Tamiaki, H.; Holzwarth, A. R. *Supramolecular Dye Chemistry* **2005**, *258*, 1–38.

(57) Tamiaki, H. *Coord. Chem. Rev.* **1996**, *148*, 183–197.

(58) Tamiaki, H. *Photochem. Photobiol. Sci.* **2005**, *4*, 675.

(59) Bryant, D. A.; Garcia Costas, A. M.; Maresca, J. A.; Gomez Maqueo Chew, A.; Klatt, C. G; Bateson, M. M.; Tallon, L. J.; Hostetler, J.; Nelson, W. C.; Heidelberg, J. F.; Ward, D. M. *Science* **2007**, *317*, 523–526.

(60) Prokhorenko, V. I.; Holzwarth, A. R.; Müller, M. G.; Schaffner, K.; Miyatake, T.; Tamiaki, H. *J. Phys. Chem. B* **2002**, *106*, 5761–5768.

(61) Brune, D. C.; King, G. H.; Infosino, A.; Steiner, T.; Thewalt, M. L. W.; Blankenship, R. E. *Biochemistry* **1987**, *26*, 8652–8658.

(62) Prokhorenko, V. I.; Steensgaard, D. B.; Holzwarth, A. R. *Biophys. J.* **2000**, *79*, 2105–2120.

(63) Scholes, G. D.; Rumbles, G. *Nat. Mater.* **2006**, *5*, 683–696.

(64) Jiang, D. L.; Aida, T. *Prog. Polym. Sci.* **2005**, *30*, 403–422.

(65) Li, W. -S.; Aida, T. *Chem. Rev.* **2009**, 109, 6047–6076.

(66) Handbook of Liquid Crystals, Vol. 2B: Low Molecular Weight Liquid Crystals II Wiley-VCH, Weinheim, **1998**.

(67) Cook, M. J. *J. Mater. Sci.* **1994**, *5*, 117–128.

(68) Chandrasekhar S. in Handbook of Liquid Crystals, Vol. 2B: Low Molecular Weight Liquid Crystals II, Wiley-VCH, Weinheim, **1998**.

(69) Rosen, B. M.; Wilson, C. J.; Wilson, D. A.; Peterca, M.; Imam, M. R.; Percec, V. *Chem. Rev.* **2009**, *109*, 6275–6540.

(70) Percec, V.; Glodde, M.; Bera, T. K.; Miura, Y.; Shiyanovskaya, I.; Singer, K. D.; Balagurusamy, V. S. K.; Heiney, P. A.; Schnell, I.; Rapp, A.; Spiess, H. W.; Hudson, S. D.; Duan, H. *Nature* **2002**, *419*, 384–387.

(71) Smith, K. M.; Goff, D. A.; Simpson, D. J. *J. Am. Chem. Soc*. **1985**, *107*, 4946–4954.

(72) Huber, V.; Lysetska, M.; Würthner, F. *Small* **2007**, *3*, 1007–1014.

(73) Huber, V.; Sengupta, S.; Würthner, F. *Chem.–Eur. J.* **2008**, *14*, 7791–7807.

(74) Balagurusamy, V. S. K.; Ungar, G.; Percec, V.; Johansson, G. *J. Am. Chem. Soc.* **1997**, *119*, 1539–1555.

(75) Beginn, U. *Prog. Polym. Sci.* **2003**, *28*, 1049–1105.

(76) Hudson, S. D.; Jung, H.-T.; Percec, V.; Cho, W.-D.; Johansson, G.; Ungar, G.; Balagurusamy, V. S. K. *Science* **1997**, *278*, 449–452.

(77) Percec, V.; Dulcey, A. E.; Balagurusamy, V. S. K.; Miura, Y.; Smidrkal, J.; Peterca, M.; Nummelin, S.; Edlund, U.; Hudson, S. D.; Heiney, P. A.; Duan, H.; Magonov, S. N.; Vinogradov, S. A. *Nature* **2004**, *430*, 764–768.

(78) Yoshio, M.; Kagata, T.; Hoshino, K.; Mukai, T.; Ohno, H.; Kato, T. *J. Am. Chem. Soc.* **2006**, *128*, 5570–5577.

(79) Prasad, S. K.; Rao, D. S. S.; Chandrasekhar, S.; Kumar, S. *Mol. Cryst. Liq. Cryst.* **2003**, *396*, 121–139.

(80) Balaban, T. S.; Linke-Schaetzel, M.; Bhise, A. D.; Vanthuyne, N.; Roussel, C.; Anson, C. E.; Buth, G.; Eichhöfer, A.; Foster, K.; Garab, G.; Gliemann, H.; Goddard, R.; Javorfi, T.; Powell, A. K.; Rösner, H.; Schimmel, T. *Chem.–Eur. J.* **2005**, *11*, 2268–2275.

(81) Hunter, C. A. *Chem. Soc. Rev.* **1994**, *23*, 101–109.

(82) Manickam, M.; Belloni, M.; Kumar, S.; Varshney, S. K.; Rao, D. S. S.; Ashton, P. R.; Preece, J. A.; Spencer, N. *J. Mater. Chem.* **2001**, *11*, 2790–2800.

(83) El-ghayoury, A.; Douce, L.; Skoulios, A.; Ziessel, R. *Angew. Chem., Int. Ed.* **1998**, *37*, 1255–1258.

(84) Immirzi, A.; Perini, B. *Acta Crystallographica Sec. A* **1977**, *33*, 216–218.

(85) Jung, H.-T.; Kim, S. O.; Ko, Y. K.; Yoon, D. K.; Hudson, S. D.; Percec, V.; Holerca, M. N.; Cho, W. -D.; Mosier, P. E. *Macromolecules*, **2002**, *35*, 3717–3721.

(86) Percec, V.; Rudick, J. G.; Wagner, M.; Obata, M.; Mitchell, C. M.; Cho, W.-D.; Magonov, S. N. *Macromolecules* **2006**, *39*, 7342–7351.

(87) Percec, V.; Rudick, J. G.; Peterca, M.; Staley, S. R. ; Wagner, M.; Obata, M.; Mitchell, C. M.; Cho, W. D.; Balagurusamy, V. S. K.; Lowe, J. N.; Glodde, M. ; Weichold, O.; Chung, K. J.; Ghionni, N.; Magonov, S. N.; Heiney, P. A. *Chem.–Eur. J.* **2006**, *12*, 5731–5746.

(88) Chen, Z.; Baumeister, U.; Tschierske, C.; Wurthner, F. *Chem.–Eur. J.* **2007**, *13*, 450–465.

(89) Elemans, J.; Lei, S. B.; De Feyter, S. *Angew. Chem., Int. Ed.* **2009**, *48*, 7298–7332.

(90) Kudernac, T.; Lei, S. B.; Elemans, J.; De Feyter, S. *Chem. Soc. Rev.* **2009**, *38*, 402–421.

(91) Moeltgen, H.; Kleinermanns, K.; Jesorka, A.; Schaffner, K.; Holzwarth, A. R. *Photochem. Photobiol.* **2002**, *75*, 619–626.

(92) Boussaad, S.; Tazi, A.; Leblanc, R. M. *Proc. Natl. Acad. Sci. U. S. A.* **1997**, *94*, 3504–3506.

(93) Xu, Q. M.; Wan, L. J.; Yin, S. X.; Wang, C.; Bai, C. L.; Ishii, T.; Uehara, K.; Wang, Z. Y.; Nozawa, T. *J. Phys. Chem. B* **2002**, *106*, 3037–3040.

(94) Iancu, V.; Hla, S. W. *Proc. Natl. Acad. Sci. U. S. A.* **2006**, *103*, 13718–13721.

(95) De Feyter, S.; De Schryver, F. *Supramolecular Dye Chemistry* **2005**, *258*, 205–255.

(96) Mamdouh, W.; Uji-i, H.; Ladislaw, J. S.; Dulcey, A. E.; Percec, V.; De Schryver, F. C.; De Feyter, S. *J. Am. Chem. Soc.* **2006**, *128*, 317–325.

(97) Ohta, K.; Hatsusaka, K.; Sugibayashi, M.; Ariyoshi, M.; Ban, K.; Maeda, F.; Naito, R.; Nishizawa, K.; van de Craats, A. M.; Warman, J. M. *Mol. Cryst. Liq. Cryst.* **2003**, *397*, 325–345.

(98) Percec, V.; Imam, M. R.; Peterca, M.; Wilson, D. A.; Graf, R.; Spiess, H. W.; Balagurusamy, V. S. K.; Heiney, P. A. *J. Am. Chem. Soc.* **2009**, *131*, 7662–7677.

(99) Ganapathy, S.; Sengupta, S.; Wawrzyniak, P. K.; Huber, V.; Buda, F.; Baumeister, U.; Würthner, F.; de Groot, H. J. M. *Proc. Natl. Acad. Sci. U. S. A.* **2009**, *106*, 11472–11477.

(100) Smith, D. P. E.; Hörber, H.; Gerber, C.; Binning, G. *Science* **1989**, *245*, 43–45.

(101) Foster, J. S.; Frommer, J. E. *Nature* **1988**, *333*, 542–545

(102) Azumi, R.; Götz, G.; Debaerdemaekar, T.; Bäuerle, P. *Chem.–Eur. J.* **2000**, *4*, 735–744.

(103) Tomović, Z.; van Dongen, J.; George, S. J.; Xu, H.; Pisula, W.; Leclère, P.; Smulders, M. M. J.; De Feyter, S.; Meijer, E. W.; Schenning, A. P. H. J. *J. Am. Chem. Soc.* **2007**, *129*, 16190–16196.

(104) Giorgi, T.; Lena, S.; Mariani, P.; Cremonini, M. A.; Masiero, S.; Pieraccini, S.; Rabe, J. P.; Samorì, P.; Spada, G. P.; Gottarelli, G. *J. Am. Chem. Soc.* **2003**, *125*, 14741–14749.

(105) Fischer, M.; Leiser, G.; Rapp, A.; Schnell, I.; Mamdouh, W.; De Feyter, S.; De Schryver, F. C.; Höger, S. *J. Am. Chem. Soc.* **2004**, *126*, 214–222.

(106) Kaneda, Y.; Stawasz, M. E.; Sampson, D. L.; Parkinson, B. A. *Langmuir* **2001**, *17*, 6185–6195.

(107) Percec, V.; Heck, J. A.; Tomazos, D.; Ungar, G. *J. Chem. Soc.-Perkin Trans. 2* **1993**, 2381–2388.

(108) Percec, V.; Heck, J.; Tomazos, D.; Falkenberg, F.; Blackwell, H.; Ungar, G. *J. Chem. Soc.-Perkin Trans. 1* **1993**, 2799–2811.

(109) Johansson, G.; Percec, V.; Ungar, G.; Abramic, D. *J. Chem. Soc.-Perkin Trans. 1* **1994**, 447–459.

(110) Percec, V.; Tomazos, D.; Heck, J.; Blackwell, H.; Ungar, G. *J. Chem. Soc.-Perkin Trans. 2* **1994**, 31–44.

(111) Shiyanovskaya, I.; Singer, K. D.; Percec, V.; Bera, T. K.; Miura, Y.; Glodde, M. *Phys. Rev. B.* **2003**, *67*, 035204(1)–035204(7).

(112) Kassi, H.; Hotchandani, S.; Leblanc, R. M. *App. Phys. Lett.* **1993**, *62*, 2283–2285.

(113) Kassi, H.; Leblanc, R. M.; Hotchandani, S. *Physica Status Solidi B-Basic Research* **2000**, *220*, 931–939.

(114) Perrin, D. D.; Amarego, W. L.; Perrin D. R. *Purification of Laboratory Chemicals*; Pergamon Press Ltd.: Oxford, 1980.

Chapter 5

Zinc Chlorins Functionalized with Peripheral Olefinic Groups for Covalent Stabilization of Nanorods

Abstract: Zinc chlorin **1** functionalized with undecyl chains bearing terminal olefinic groups at 17^2-position was synthesized. These molecular building blocks self-assemble into well-defined rod aggregates in non-polar solvents with functionalizable surface. The self-assembly has been studied by UV/Vis, circular dichroism (CD), dynamic light scattering (DLS), atomic force microscopy (AFM) studies. The aggregates of **1** possess appreciable charge carrier mobilities of ~ 0.03 cm^2/Vs in solid state according to pulse radiolysis-time resolved microwave conductivity (PR-TRMC) measurements. The electron-rich olefinic groups at the periphery of the self-assembled nanorods provided some contrast for electron microscopic studies. Consequently, transmission electron microscopy (TEM), scanning transmission electron microscopy (STEM) and scanning electron microscopy (SEM) enabled visualization of well-defined hollow, open-ended tube-like structures of these zinc chlorin aggregate suspensions. Furthermore, the chemically accessible peripheral olefinic groups of self-assembled nanorods of **1** provided the possibility to fix the morphology of these aggregates using in-situ metathesis polymerization. The intramolecularly cross-linked nanorods could be characterized by UV/Vis, fourier transform infrared (FTIR) spectroscopy and AFM studies. The present findings indicate the potential of these highly ordered robust materials in (bio)supramolecular electronics.

Charge carrier mobility measurements were performed by Dr. Sameer Patwardhan in the group of Prof. Dr. Laurens D. A. Siebbeles at the Technical University of Delft.

5.1. Introduction

The construction of functional molecular objects by directed non-covalent interactions with nanoscopic precision offers tremendous potential in materials science.[1,2] Extensive efforts have been devoted to develop synthetic capabilities to produce nanomaterials with desired electronic and photonic properties.[3,4,5,6] In this regard, considerable efforts have been directed to program π-conjugated molecules into self-assembled unidimensional objects such as nanorods and nanotubes that however still remain challenging and attractive targets in nanoscience.[2-7]

Tubular structures are one of the most versatile functional modules that offer precise control over inner and outer surface functionalities, can perform a variety of functions such as transport of charges, while at the same time providing the mechanical strength needed for efficient scaffolding.[1-3] Although self-assembly utilizing non-covalent interactions offers significant advantages such as minimization of synthetic efforts and emergent functions not intrinsic to the building blocks themselves,[1,2] the resulting supramolecular structures often exhibit low thermodynamic stability due to rapid assembly-disassembly processes in response to external factors. In order to utilize tubular structures in devices that have to operate under changing and demanding environmental conditions, it might be advantageous to covalently fix the morphology of such electronically active self-assembled material.[2] Post-polymerization of self-assembled molecular building blocks is often utilized for the enhancement [8] of their structural robustness and for their potential application in supramolecular electronics.[9,10,11]

Self-organization of molecules into tubular architectures provides one of the most significant structural features of peptides, proteins and nucleic acids. Tobacco mosaic virus, microtubulines, bacterial pili are few of the representative examples of natural tubular assemblies.[12,13] Inspired by such elegant organization in nature, construction of tubular assemblies from biomimetic and synthetic supramolecular systems received considerable attention. Artificial tubular structures have been realized from self-assembly of a wide variety of synthetic scaffolds including peptides,[14] rigid cycles,[15] dendrons and dendrimers,[16] aromatic oligomers through non-covalent interactions. In biological systems, tetrapyrroles such as porphyrins and chlorophylls are self-organized into nanoscale superstructures that perform the essential light-harvesting as well as energy- and electron-transfer functions. One

fascinating example is the chlorosomal light-harvesting antennae[17,18] of green-sulfur bacteria (phylum *Chlorobi*), some filamentous anoxygenic phototrophs of the phylum *Chloroflexi* and in the recently discovered aerobic phototroph, *Candidatus* chloracidobacterium thermophilum[19] of phylum *Acidobacteria.* Chlorosomes are large protein-free enclosures of bacteriochlorophyll (BChl) *c*, *d*, or *e* pigments, where vital non-covalent interactions hold the pigments in proper geometrical arrangement for optimal and rapid excitation energy transfer.[20,21] The chlorosomal superstructure is established by self-assembly driven by non-covalent interactions, namely (i) coordination of the 3^1-hydroxy to the magnesium ion, (ii) hydrogen bonding between 3^1-OH and 13^1-C=O group that connects the chlorins into tube-like superstructures, (iii) π-π stacking of chlorin macrocycles. Furthermore, owing to their high exciton mobilities,[20,21] chlorosomal BChl assemblies provide a basis for the rational design of biomimetic, self-assembling, functional materials such as nanorods/tubes for (opto)electronic applications.

Self-assembled nanotubular assemblies that are covalently stabilized are potentially useful for electronic applications since polymerization does not alter the morphology but enhances the rigidity of these nanostructures.[2,8] In pioneering work, Aida and co-workers reported that Gemini-shaped amphiphilic HBCs bearing polymerizable double bonds and two triethylene glycol (TEG) chains can be subjected to acyclic diene metathesis (ADMET) leading to spontaneous formation of graphitic nanotubes with a cross-linked surface.[2] The cross-linked graphitic nanotubes were characterized by fourier transform infrared (FTIR) spectroscopy and microscopic techniques such as transmission electron microscopy (TEM) and scanning electron microscopy (SEM) of air-dried suspensions.[2] They also reported on site-selective post-modification of radially diblock graphitic nanotubes by [3+2] cycloaddition of azides and alkynes.[2b] Mataka and co-workers reported polymerization of self-assembled triazine triamide fibers by ring closing metathesis reaction using Grubbs first generation catalyst in *n*-hexane and monitored the polymerization by IR and CD spectroscopy.[9a] In recent years, Würthner and co-workers have reported covalent stabilization of amphiphilic perylene bisimide (PBI) vesicles by in-situ photopolymerization reaction and the insoluble polymerized product was characterized by FTIR and TEM studies.[8a]

As discussed in Chapters 2 and 3, the self-assembly of BChl *c*, *d*, and *e* into rod like architectures can be mimicked by using semisynthetic zinc chlorin (ZnChl) molecules (**1a-1c**, Figure 1) that are pre-programmed for tubular mode of self-assembly.[22,23] Spectroscopic,

crystallographic [24] and scanning-probe techniques [25] have provided wealth of information regarding the self-assembly of semisynthetic zinc chlorins in solution, solid state and on surface. In Chapter 3, detailed electron microscopic (EM) studies of 3^1-hydroxy zinc chlorins **1c** esterified with oligoethylene glycol (OEG) chains at 17^2-position provided unequivocal evidence for hollow tubular aggregates in aqueous media. These studies provided indication that the chains are presumably oriented to the outside of the tubular assemblies. This is an important conclusion considering the possibility of functionalizing/modifying the surface of these nanotubes. Towards the aim of designing self-assembled zinc chlorin system that can be studied in non-polar solvent by EM as well as self-assemblies of which can be covalently stabilized, ZnChl **1** was developed. In this chapter, we report on synthesis and detailed characterization of ZnChl **1** (Figure 1) bearing electron-rich terminal olefinic groups, usable for providing contrast in EM studies and for surface functionalization of nanotubes by metathesis reaction in order to enhance the robustness of such assemblies. These building blocks self-assemble into rod-like aggregates (analogous to all 3^1-hydroxy ZnChls **1a-1c** discussed in Chapters 2 and 3, Figure 1) in non-polar solvents. The self-assembly properties have been studied in detail by temperature-dependent UV/Vis, CD, dynamic light scattering (DLS) and AFM studies that revealed formation of well-defined nanorods in solution and on highly oriented pyrolytic graphite (HOPG) surface. Charge transport properties of the aggregates of **1** in solid state have been investigated by pulse radiolysis-time resolved microwave conductivity (PR-TRMC) experiments.

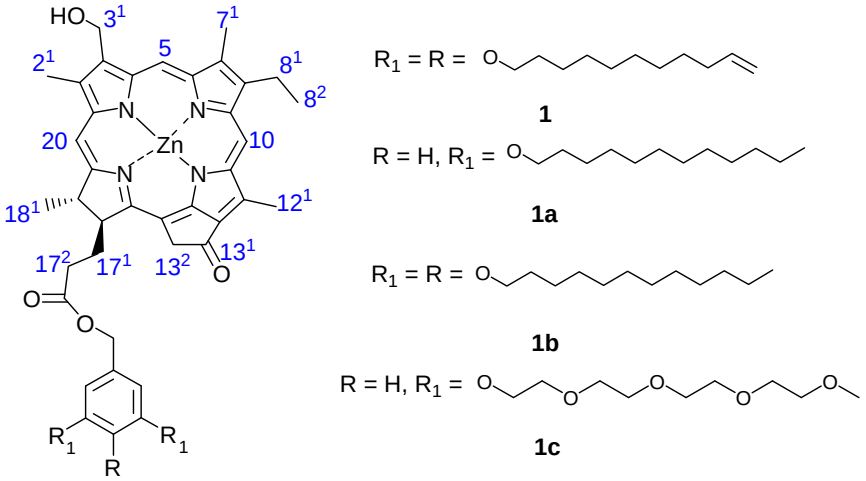

Figure 1. Chemical structures of ZnChl **1** functionalized with peripheral olefinic groups and model ZnChl compounds **1a**, **1b** and **1c**.[22a]

Importantly, the electron-rich olefinic groups in the periphery provided sufficient contrast even in non-polar media for electron microscopic studies such as transmission electron microscopy (TEM), scanning transmission electron microscopy (STEM) and scanning electron microscopy (SEM), allowing visualization of fibrous tube-like aggregates in fresh aggregate solutions and large tubular aggregates in suspensions of ZnChl **1** aggregates. Furthermore, in order to enhance the chemical stability of these nanorod assemblies for their utilization in electronic applications, the chemically accessible olefinic functionalities on the periphery were subjected to in-situ metathesis polymerization reaction by Grubbs first generation catalyst. The polymerized nanorods could be characterized by UV/Vis and CD spectroscopy, AFM and FTIR spectroscopy. Covalent stabilization allowed the dimensions and shapes of these nanorods/tubes to be captured, and endowed the nanotubes with increased stability rendering them suitable for supramolecular electronic applications.

5.2. Results

5.2.1. Synthesis

The synthetic route to ZnChl **1** is outlined in Scheme 1. Chl *a* was extracted from cyanobacterium *Spirulina Platensis* and was converted to pheophorbide *a* (pheo *a*) according to literature procedures. [26] Subsequently, the 3^1-vinyl group was transformed into corresponding diol with osmium tetroxide, followed by oxidative cleavage of the diol by sodium periodate to afford the respective formyl derivative. The resulting 3^1-aldehyde was hydrolyzed with conc. hydrochloric acid that afforded the chlorin 17^2-carboxylic acid **2**, followed by its esterification with 3, 4, 5-triundecyloxybenzylalcohol in the presence of coupling reagents dicyclohexylcarbodiimide (DCC), 4-dimethylaminopyridine (DMAP), 4-(dimethylamino)pyridinium-*p*-toluenesulfonate (DPTS) and *N*-ethyldiisopropylamine in dry dichloromethane (DCM) as solvent in 56% yield. The 3^1-aldehyde functionality in ester **3** was subsequently reduced to corresponding 3^1-alcohol **4** by 10 equivalents of borane-*t*-butylamine complex (BH_3(*t*-Bu)NH_2) in DCM in 82% yield. The final step involved the metalation of the free base compound **4** with saturated solution of $Zn(OAc)_2$ in methanol and in tetrahydrofuran (THF) as solvent, that afforded the target building block **1** in 61% yield. The intermediates and final products were purified by silica gel column chromatography, followed by HPLC purifications and characterized by ^{1}H NMR spectroscopy and high-resolution mass

spectrometry (HRMS). The alcohol 3, 4, 5-trisundecyloxybenzylalcohol (ROH in Scheme 1) was synthesized starting from 3, 4, 5-trihydroxyethylbenzoate. The hydroxy groups of 3, 4, 5-trihydroxyethylbenzoate were subjected to alkylation with 11-bromo-1-undecene in presence of K_2CO_3 and dry dimethylformamide (DMF) as solvent to yield the corresponding ester that was subsequently reduced in the presence of $LiAlH_4$ in dry THF to afford the corresponding alcohol 3, 4, 5-trisundecyloxybenzylalcohol (ROH, Scheme 1).

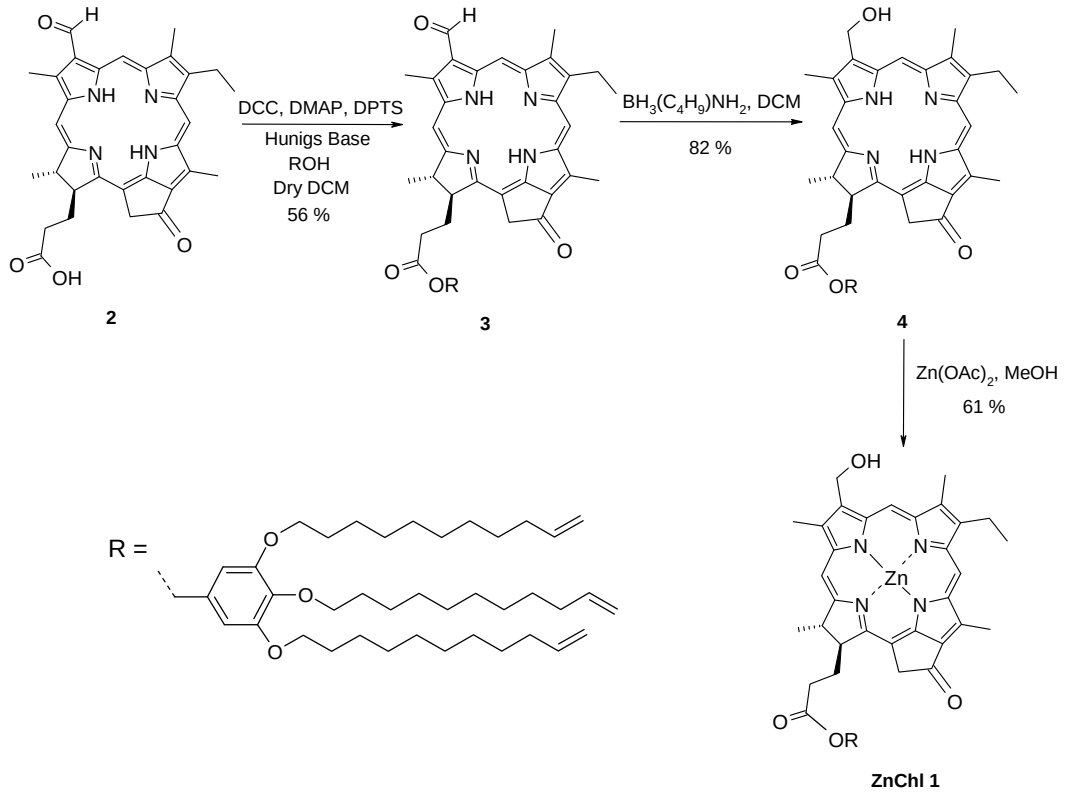

Scheme 1. Synthesis of zinc chlorin (ZnChl) compound **1**.

5.2.2. Optical and microscopic properties

5.2.2.1. UV/Vis and CD spectroscopy: The optical properties of monomers and aggregates of ZnChl **1** have been characterized by UV/Vis spectroscopy. For this purpose, monomer stock solutions of ZnChl **1** was prepared in THF and subsequently added to non-polar solvents like *n*-hexane or *n*-heptane to prepare aggregate solutions containing 0.5-1 vol % THF. The formation of aggregates could visually be observed by the instantaneous color change of turquoise blue monomer solutions to pale green aggregate solutions. Characteristic for dye aggregates in chlorosomes of *Chloroflexus aurantiacus* and for the in-vitro aggregates of BChl *c* is a bathochromic shift of the Q_y band (about 80–110 nm) with respect to the

corresponding Q_y absorption in the monomer at about 650 nm. Compared with the absorption bands of the monomeric zinc chlorins, aggregates of these dyes show red-shifted absorption maxima due to J-type excitonic coupling between the S_0-S_1 transition dipole moments of the chlorin Q_y bands. This is ascribed to the interaction between the metallochlorins comparable to Scheibe- or other J-aggregates.[27] The aggregation properties of ZnChl **1** can be assessed conveniently by UV/Vis spectroscopy as the aggregate Q_y band shows a large bathochromic shift (of about 100 nm) compared to that of the corresponding monomers. The maxima of the Q_y absorption bands of the monomers of ZnChl **1** in THF appear at 648 nm, whereas for the corresponding aggregates in *n*-hexane/THF (100:0.5) (dotted line) the Q_y band maxima occur at 740-741 nm (bold line) (Figure 2).

For characterization of the self-assembly of ZnChl **1**, the aggregation process was investigated by temperature-dependent UV/Vis spectroscopy in the temperature range between 288 K and 368 K in a solvent mixture di-*n*-butylether/*n*-heptane (1:4) ($c = 3 \times 10^{-6}$ M). For this purpose, ZnChl **1** was dissolved in di-*n*-butylether followed by the addition of non-polar solvent *n*-heptane (in the ratio of di-*n*-butylether/*n*-heptane 1:4) to initiate the self-assembly process. With increasing temperature, the Q_y band of the aggregates at 740 nm decreases and the monomer band at 648 nm increases (Figure 3a).

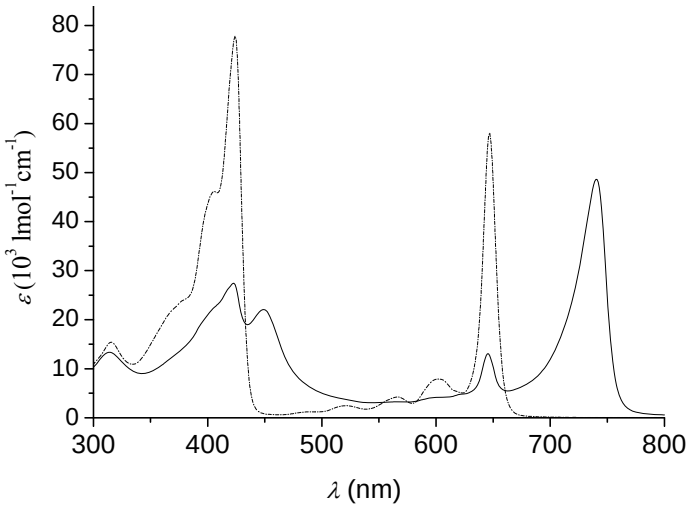

Figure 2. UV/Vis absorption spectra of monomers of ZnChl **1** in THF (dotted line) and aggregate in *n*-hexane/THF (100:0.5) (solid line) at concentration of 3×10^{-6} M.

These spectral changes reveal that the aggregates dissociate at higher temperature. Upon cooling to initial temperature of 288 K, the Q_y band was completely recovered, which is indicative of the reversibility of the aggregation of ZnChl **1**. Another remarkable feature of ZnChl **1** is that no precipitation was observed upon heating and cooling processes, proving the

thermodynamic stability of these aggregates in the given solvent system. Temperature-dependent UV/Vis measurement was performed by allowing the sample to equilibrate at each temperature for 1 hour prior to measurement.

For the rational design of supramolecular assemblies, insights into the mechanism of aggregate formation and the thermodynamic stability of the self-assembled supramolecular structures are of crucial importance. The model that is often used to describe the self-assembly of quasi-one-dimensional polymer-like chains is based on the isodesmic self-assembly in which every monomer addition to the growing chain is governed by a single equilibrium constant, K_e (equal-K model).[28] On the other hand, cooperative processes in self-assembly involve an unfavourable activation step, governed by equilibrium constant K_a that precedes chain elongation or growth with equilibrium constant K_e.[28]

In isodesmic assembly, there is a gradual increase in the number and length of the aggregated species and it is only for high binding constants that long nanometre-sized structures are formed.[28] From the temperature-dependent (T-dependent) measurements, the complete transition from the monomeric (at high T) to the polymeric state (at lowest T) can be probed. From the temperature-dependent measurements, all the relevant thermodynamic parameters can be deduced. As discussed in Chapter 3, based on thermodynamical considerations, 3^1-hydroxy zinc chlorins self-assemble into nanotubes following the isodesmic pathway. Following similar evaluation, the T-dependent absorption data were normalized to obtain the degree of aggregation, α, and fitted to the isodesmic model, in which α is approximated by Equation (1), with $\alpha_{agg}(T)$ being the mole fraction of aggregate at each temperature, and $\varepsilon(T)$, ε_{agg}, and ε_{mon} being the apparent absorption coefficients of the aggregate at temperature T, the absorption coefficient of the aggregate, and the monomer, respectively. The UV/Vis absorption coefficients of aggregate bands of 448.6 nm and 741 nm are plotted as a function of temperature show a clear sigmoidal shape (Figure 3b), indicative of an isodesmic self-assembly mechanism. The absorption coefficients of pure monomer ε_{mon} and aggregate ε_{agg} were determined by extrapolation of the measured apparent absorption coefficients to their asymptotic values at high and low temperatures. In Equation (1a), T_m is the melting temperature defined as the temperature for which $\alpha = 0.5$, ΔH is the molar enthalpy release related to the formation of non-covalent intermolecular interactions and R is the gas constant.

$$\alpha(T) = \frac{\varepsilon(T) - \varepsilon_{\max}}{\varepsilon_{agg} - \varepsilon_{\max}} \tag{1}$$

$$\alpha(T) \cong \frac{1}{1 + \exp\left[-0.098\Delta H \frac{T - T_m}{RT_m^2} \right]} \tag{1a}$$

Inserting the degree of aggregation α into Equation (2) yields the degree of polymerization, DP_N, as well as the equilibrium constant, $K(T)$ at temperature T according to the following equation.

$$DP_N = \frac{1}{\sqrt{1-\alpha(T)}} = \frac{1}{2} + \frac{1}{2}\sqrt{4K(T)c_T + 1} \tag{2}$$

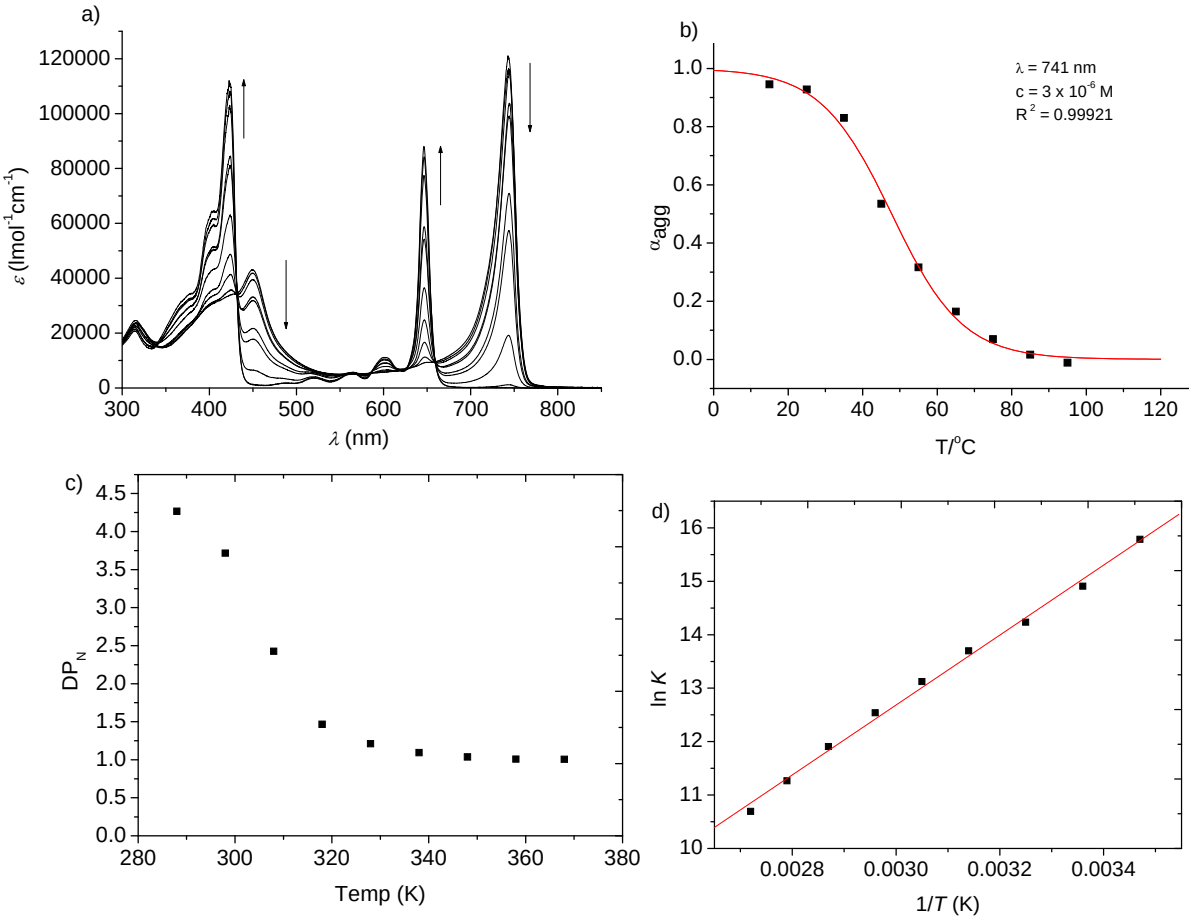

Figure 3. a) Temperature-dependent UV/Vis spectra of ZnChl **1** in *n*-heptane/di-*n*-butyl ether (4:1) at a conc. of 3.1×10^{-6} M. The initial temperature of 288 K was increased successively in intervals of 10 degrees upto 368 K and at each temperature the solution was allowed to equilibrate prior to measurement; arrows indicate changes upon increasing temperature; b) Plot of degree of aggregation, α, calculated from the UV/Vis absorption at 741 nm vs temperature (T) fitted to isodesmic model; c) Number-averaged degree of polymerisation, DP_N, as a function of temperature; d) Van't Hoff plot (ln K vs $1/T$) for ZnChl **1**.

The average *K* value at 288 K at two different wavelengths of the aggregate bands (741 nm, 448.6 nm) was 4.49×10^6 M^{-1}, as determined by *T*-dependent spectroscopy. Also, by plotting the logarithm of *K* versus the reciprocal temperature (Van't Hoff plot, Figure 3d), a ΔH value of 54.4 kJ/mol and ΔS value of -57.8 J/K/mol were obtained from a linear relationship, which imply that aggregation is an enthalpy driven process and entropically disfavoured. Gibbs free energy, ΔG was calculated to be -37.7 kJ/mol at 288 K using the ΔH and ΔS values obtained from the Van't Hoff plot. Comparison of the enthalpy and entropy contributions to the Gibbs free-energy changes for aggregation leads to the conclusion that the self-assembly process of ZnChl **1** is enthalpically driven, whereas it is entropically disfavored. The values at 741 nm and 448.6 nm are very similar thus only the latter ones were used for further analysis of temperature-dependence. The temperature dependence of equilibrium constant *K* at 448.6 nm is shown in Table 1.

Table 1. Thermodynamic parameters *K* (M^{-1}), DP_N obtained from monitoring the aggregate band at 448.6 nm from temperature-dependent self-assembly of ZnChl **1** ($c = 3.1 \times 10^{-6}$ M, di-*n*-butylether/heptane = 1:4 vol %) based on the isodesmic model.

T (K)	1/*T* (1/K)	*K* ($Lmol^{-1}$)	ln *K*	DP_N
288	0.00347	4.5×10^6	15.3	4.3
298	0.00336	3.3×10^6	15.0	3.7
308	0.00325	1.1×10^6	13.9	2.4
318	0.00314	2.2×10^5	12.3	1.5
328	0.00305	8.2×10^4	11.3	1.2
338	0.00296	3.3×10^4	10.4	1.1
348	0.00287	1.2×10^4	9.4	1.0
358	0.00279	2.6×10^3	7.8	1.0
368	0.00272	2.0×10^3	7.6	1.0

Further insight into the aggregation process for ZnChl **1** was obtained by temperature-dependent CD spectroscopy in *n*-heptane/di-*n*-butyl ether (4:1) in the temperature range between 288 K and 368 K at 10 degree steps. The shape of the CD spectrum and the position of the Q_y absorption band are dependent on orientations of the monomeric transition moments of the aggregate. The *T*-dependent CD spectra (Figure 4) show the distinct feature of these rod aggregates,[29] an induced CD effect which occurs on chiral excitonic coupling of transition dipole moments and consist of two bands with opposite signs (+/-) in the region of Q_y aggregate band. This excitonic coupling reversibly arises and disappears on temperature change and does not undergo any time-dependent changes at a particular temperature.

Theoretical studies have shown that for chlorosomal aggregates longer than 60 nm the shape of the CD spectrum remains unchanged.[29] This is in line with the experimental observation that the CD spectra of previously studied zinc chlorin rod aggregates of **1a**, **1b**[22] in Chapters 2 and 3 and ZnChl **1** do not change in shape if smallest aggregates in the experiment were long enough. From Figure 4 it is clear that even at the highest temperature of measurement, the molecules are aggregated to some extent.

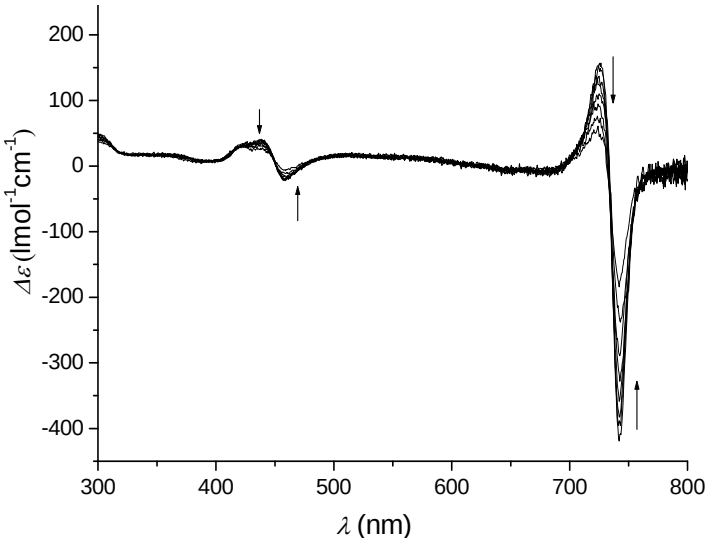

Figure 4. Temperature-dependent CD spectra of aggregates of ZnChl **1** in *n*-heptane/di-*n*-butylether (4:1) at a concentration of 3.1×10^{-6} M. The initial temperature of 15 °C was increased successively in 10 °C steps upto 85 °C and at each temperature the solution was allowed to equilibrate prior to measurement; arrows indicate spectral changes upon increasing temperature.

5.2.2.2. Atomic Force Microscopy (AFM): Followed by optical spectroscopic investigation, structural properties of ZnChl **1** aggregates were elucidated by AFM. Not only the spectroscopic properties but also the structural features of ZnChl **1** assemblies are quite similar to those of the model system ZnChl **1a** discussed in Chapter 2.[22,23] Tapping-mode AFM of aggregate solutions of ZnChl **1** at different concentrations ranging from 1.24×10^{-5} M to 3×10^{-6} M in *n*-hexane/ THF (100:0.5) were measured onto HOPG shown in Figure 5 and rod-like aggregate structures could be observed with diameters of ~ 6-8 nm and lengths varying from 300 nm upto few micrometers. The diameters of the rods are comparable to the electron microscopic data for the chlorosomal (*Chloroflexus aurantiacus*) BChl *c* rod aggregates and the tubular model of Holzwarth. The longest observed aggregates show contour lengths in the range of 3-5 micrometers (Figure 5).

In the cross section analysis, (Figure 5b,c), the vertical distance between the red triangles shows that the height of the rod aggregates is ~ 2.57 ± 0.2 nm, which is significantly less than

that observed previously for ZnChl **1a** rod aggregates with 17^2-dodecyl side chains (5.8 ± 0.4 nm)[22] and ZnChl rods with additional NBI dyes (7.3 ± 0.2 nm).[23]

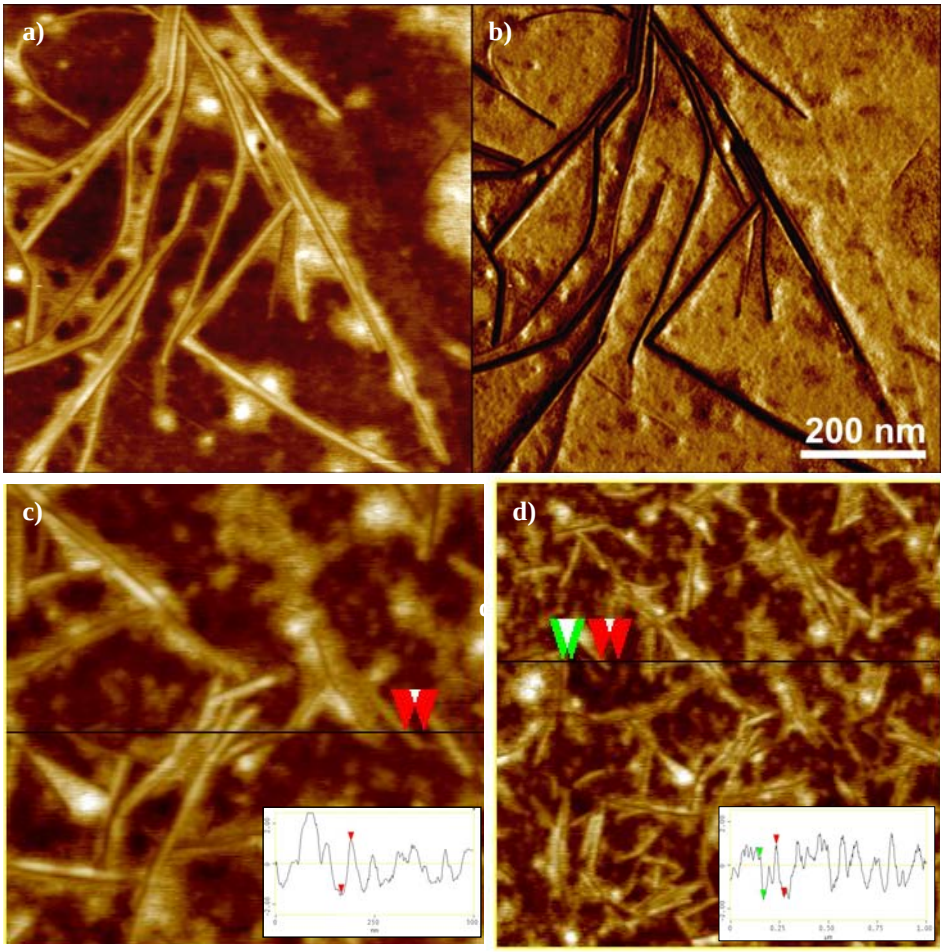

Figure 5. a, b) Tapping-mode™ AFM images of aggregates of ZnChl **1** on HOPG. a) AFM height image and b) phase image of ZnChl **1** nanorods at a concentration of 3×10^{-6} M in *n*-hexane/THF (100:0.5) onto HOPG with spin coating at 4000 rpm; c, d) AFM images of aggregates of ZnChl **1** at a concentration of 3×10^{-5} M showing nanorods with a height of ~ 2.5 nm. The sample was prepared by spin-coating a solution of **1** in *n*-hexane/THF (100:0.5) on HOPG and measured in air. Insets in c) and d) show the height profile of the nanorods along the red and green arrows. Scalebars in both figures c) and d) is 1 µm.

Histogram analysis in Figure 6 show statistical distribution of the number of nanorods based on their persistence lengths and heights. The length of the nanorods vary from 250 nm upto 3 µm, whereas the diameters vary from ~ 6-8 nm. It is to be noted that the zero level in the cross section analysis is arbitrary and thus the analysis of the heights of the nanorods are subject to small errors.

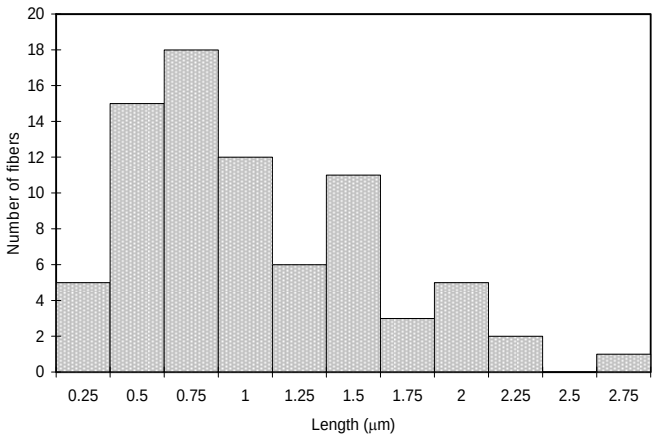

Figure 6. Histogram analysis showing a statistical distribution of the nanorods of ZnChl **1** based on their lengths as obtained by AFM investigations.

5.2.3. Dynamic Light Scattering (DLS)

Dynamic light scattering (DLS) technique is commonly used to determine the sizes of sub micrometric dispersed particles by measuring their diffusion coefficients. In this technique, the rate of diffusion of particles (supramolecular aggregates in the present case) depends on temperature and viscosity of the fluid and the particle size.[30] The particles undergoing Brownian motion are detected and analyzed by illuminating with laser and measuring the scattered light. The time dependent fluctuations in the scattering intensity is used to determine the translational diffusion coefficient (D), and subsequently the hydrodynamic radius of the (supramolecular) polymers. The fluctuations in intensity contain information about the rate of diffusion of the particles. Large particles change positions relatively slowly and cause slow intensity fluctuations at the detector and conversely, small particles move faster and cause rapid intensity fluctuations. In order to estimate the diffusion coefficient and therefore the particle size from the changing light intensity signal, the signal is mathematically transformed into the autocorrelation function (ACF). If the ACF at time τ has a high value, there is a strong correlation between the intensity at any instant compared to that at a later time τ. The intensity is related to the pattern of the particle positions and a higher correlation between the intensity at two different times means that particles have diffused slowly and indicative of large particle sizes.

DLS measurements were performed for 1.24×10^{-5} M solution of aggregates of ZnChl **1** in *n*-hexane/THF (100:0.5). The light scattering data were collected for at least two different aggregate solutions and at six scattering angles twice to check for reproducibility, and the results were consistent within the experimental error. The autocorrelation functions at two

different angles ($63.8^o, 90^o$) are shown (Figure 7) obtained from three sets of measurements and a sigmoidal behavior is observable in all the cases. Furthermore, an ACF that remains at high magnitudes for long time intervals (Figure 7) indicates large slowly moving particles. An aggregate solution of ZnChl **1** in *n*-hexane/THF (100:0.5) (3×10^{-5} M) revealed very broad distribution of average particle sizes from 100 nm to 2000 nm (intensity, weight and number distribution, Figure 8). DLS measurement data are analyzed by two methods i.e., unimodal distribution and size distribution processor (SDP) analysis. The unimodal analysis provides the particle mean size and the polydispersity index (PI) of the particle size distribution. The mean is based on cumulants fittings and polydispersity index of the size distribution. For PI values less than 0.1, the sample is considered monomodal (narrow particle size distribution), whereas for values above 0.3, the sample is considered polydisperse.[30] The unimodal distribution results (at six scattering angles with three repetitions at each angle) obtained for ZnChl **1** yields an average PI value of 1.19 which indicates significantly high polydispersity or broadness in aggregate size distribution in solution.

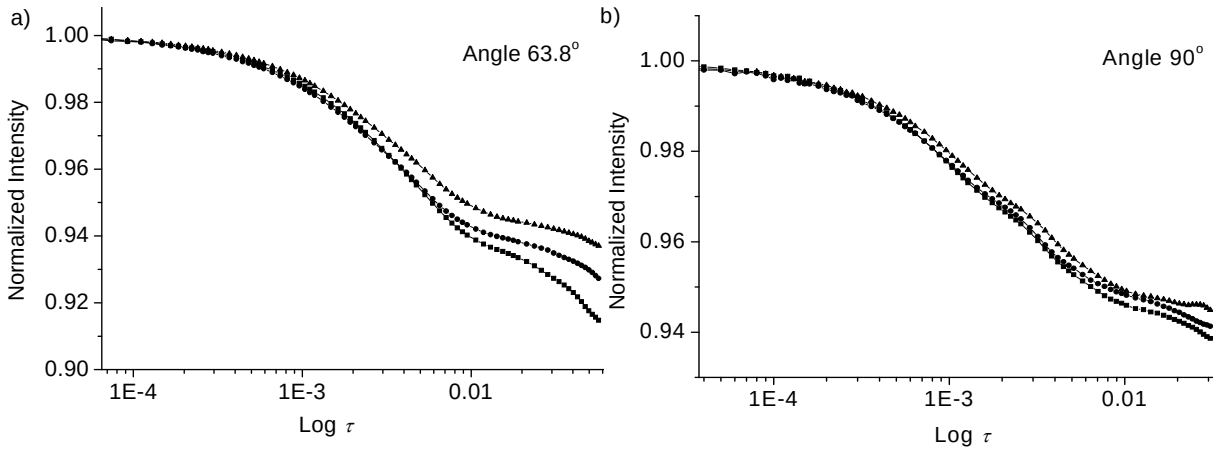

Figure 7. Logarithmic autocorrelation functions with normalized intensities at scattering angles of a) 63.8^o and b) 90^o for the aggregates of ZnChl **1** in *n*-hexane/THF (100:0.5) ($c = 1.24 \times 10^{-5}$ M) obtained by DLS measurements.

Such broad distribution of sizes and a comparatively high degree of polydispersity is expected for supramolecular polymers of ZnChl **1** in solution where rapid dynamic equilibrium between free and self-assembled species takes place. The limitation of unimodal analysis is that it is less accurate for complex distributions. Thus, for highly polydisperse systems such as supramolecular polymers of ZnChl **1**, the SDP analysis is more accurate as it provides particle size distribution in terms of intensity, weight and number distributions (Figure 8). In the intensity distribution histogram (Figure 8a), the magnitude of each peak is

proportional to the percent of total scattered intensity due to the particles (aggregates) in solution.

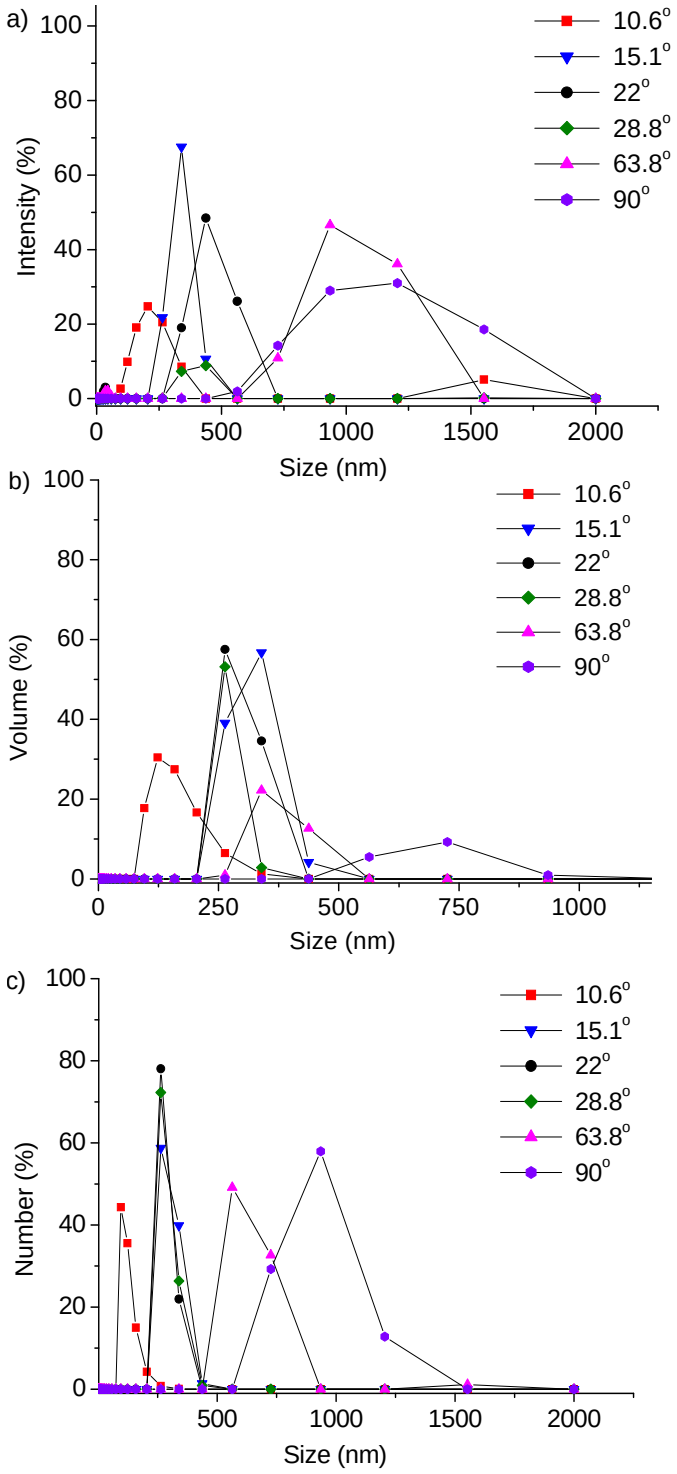

Figure 8. a) Intensity distribution of aggregates of ZnChl **1** in *n*-hexane/THF (100:0.5) (c = 1.24 × 10^{-5} M) obtained at scattering angles of 10.6°, 15.1°, 22°, 28.8°, 63.8° and 90° from DLS measurements; b) Volume distribution of aggregates of ZnChl **1** in *n*-hexane/THF (100:0.5) (c = 1.24 × 10^{-5} M) obtained from DLS measurements; c) Number distribution of aggregates of ZnChl **1** in *n*-hexane/THF (100:0.5) obtained from DLS measurements.

Angle-dependent DLS results show different size distributions at different angles thereby providing evidence for the anisotropy of the aggregates of ZnChl **1** and their one dimensional (rod/tube-like) shape rather than spherical nature. Volume distribution (Figure 8b) gives the relative volume of particles of each size in the sample. Intensity results are dependent on scattering angles whereas volume results are not. On the other hand, number percentage distributions (Figure 8c) are determined by dividing the volume percentage results by cubed diameter of the particles in the distribution.

The unimodal results provided the mean diffusion coefficient (D) as 1.77×10^{-12} m^2/s. Using Stokes Einstein equation, $r = k_B T/6\pi\eta D$, where r is the hydrodynamic radius, k_B is the Boltzmann constant, T is the temperature of measurement, η is the viscosity of the solvent at the temperature of measurement, particle sizes in solution were roughly estimated. Taking into account the viscosity of the solvent (*n*-hexane) as 0.0042 poise, k_B as 1.38×10^{-23} J/K, and D as 1.77×10^{-12} m^2/s determined from DLS measurement, the hydrodynamic radius r was roughly estimated to be ~ 396 nm. It is to be noted that the size obtained from unimodal result is not very accurate for polydisperse species like for ZnChl **1** aggregates. Nevertheless, these results are indicative of presence of very large aggregates of ZnChl **1** in solution.

In order to obtain insights about the aggregate size and local packing of the dyes, ^{1}H NMR measurements (600 MHz) were performed with aggregates of ZnChl **1** in *n*-hexane/THF (100:0.5). However, the NMR signals were extremely broad throughout therefore useful structural insights could not be obtained from NMR experiments.

5.2.4. Electron microscopy

Electron microscopic techniques and in particular transmission electron microscopy (TEM) is one of the powerful techniques used to investigate core/shell or hollow nanostructures.[31] In this technique, electron beams scatter when they pass through thin sections of a specimen and transmitted electrons that do not scatter are used to produce images.[31] Two contrast mechanisms namely, amplitude and phase contrast, contribute to image formation. Whereas phase contrast arises from coherent interference of the scattered and transmitted beams,[31] amplitude contrast arises due to the fact that some regions in the specimen scatter electrons more efficiently (related to density and atomic number), therefore fewer electrons are detected in the corresponding region of the image. TEM image contrast

depends further on thickness and composition of the material. Samples are generally stained with electron dense material or with heavy metal, which artificially enhance contrast for visualization of the structure and shape of the material under investigation.[31] Negative staining has, however, one drawback that it enhances only the contrast of the water-accessible surfaces; the small negative stain clusters do not penetrate the hydrophobic interior. Indeed, the breakthrough in the understanding of the structure and morphology of tubular assemblies of 3^1-hydroxy ZnChls was achieved for ZnChl **1c** by TEM that self-assemble in aqueous media described in Chapter 3. Nevertheless, TEM measurements of ZnChl **1** aggregates were performed with and without staining. TEM studies with aggregates of ZnChl **1** in *n*-hexane/THF (100:1, $c = 10^{-5}$-10^{-6} M) and in isooctane/THF (100:1) were not as clear as those of ZnChl **1c** studied in Chapter 3, apparently because of the fact the aqueous staining agent being less effective in organic solvent mixture, sufficient contrast could not be achieved. Such problem was encountered for TEM measurements of aggregates of ZnChl **1a** and **1b** discussed in Chapter 3 previously. In some cases, scanning TEM (STEM) which operates at comparatively lower accelerating voltages, provides higher signal levels and better spatial resolution of images. Hence STEM studies were performed with the aggregate solutions in *n*-hexane/THF (100:1) without staining. STEM studies of these aggregates enabled visualization of fibrous aggregates of **1** (Figure 9) and the diameters (~ 6-8 nm) were in good agreement to those observed by AFM studies.

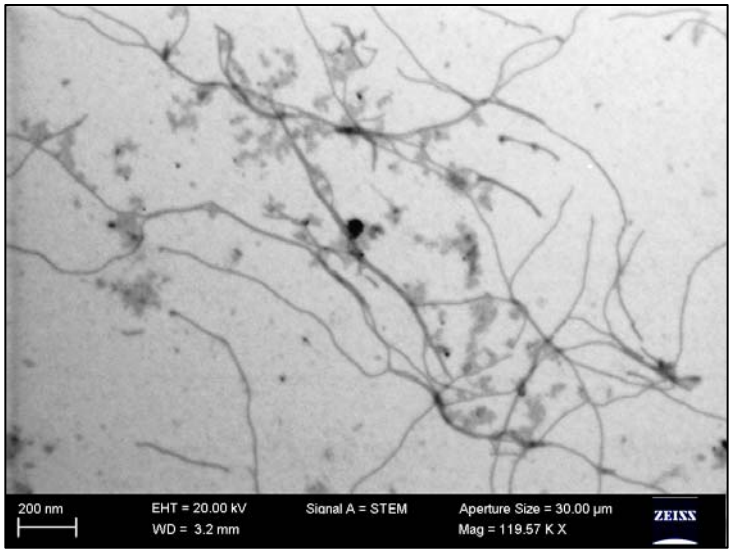

Figure 9. STEM micrograph of ZnChl **1** aggregates in *n*-hexane/THF (100:1) ($c = 3 \times 10^{-5}$ M) at accelerating voltage of 20 kV.

The long rod assemblies have a wide polydispersity in their lengths varying from 200-300 nm upto as long as 1 μm. In some STEM micrographs, nanorod bundles could also be observed. Although fibrous assemblies observed by STEM have diameters similar to those in AFM, it was not possible to conclude from these micrographs whether these aggregates are hollow.

5.2.4.1. Transmission electron microscopy (TEM): Extensive TEM measurements were performed with varying sample preparation methods employing different solvent combinations and ageing times. TEM measurements were performed with samples stained with 0.5 % uranyl acetate (negative staining), and 1 % osmium tetroxide staining (prepared from 10 % stock aqueous solution). Whereas aggregate solutions at dilute concentrations, like those used for AFM investigations (1-4 × 10^{-6} M) revealed occasionally fibrous aggregates in STEM, measurements with suspensions of more concentrated aggregated solutions (1.5 × 10^{-4} M, 2.5 × 10^{-4} M) that were allowed to age for four to six weeks prior to measurement revealed large well-defined hollow tubular structures in TEM. The formation of such tubular structures was very efficient in the sample suspensions, and almost no amorphous (or irregular) aggregates could be observed. The tubular aggregates from suspensions were almost monodisperse in size and shape under the TEM measurement conditions. In contrast, no regular tubular aggregates from freshly prepared samples at more dilute concentrations of ~ 10^{-5}-10^{-6} M could be observed in TEM and films prepared from sample concentrations of 5 × 10^{-3} M were too thick for electron beams to pass through. The isolated robust tubes had average widths of ~ 150 nm with lengths of ~ 600-800 nm (Figure 10). Accordingly, their dimensions are almost as large as whole intact chlorosomes and not related at all to individual small-sized tubular rod aggregates (diameters ~ 5 nm) discussed in Chapters 2 and 3.

The diameters of these large-sized tubes were extremely homogeneous and were apparently individual entities with regular tube wall thicknesses of ~ 15 nm (Figure 10). Furthermore, a clear contrast difference between the inner part and the periphery i.e., the light centre and darker shell is also indicative of the tubular nature of the nanostructures (Figure 10). When one tube overlaps with other tubes they result in relatively darker areas, further indicating their tubular nature. Moreover, closer assessment of some TEM micrographs indicated that the nanotubes are presumably open-ended and hollow (Figure 10b, c). TEM measurements without staining and with 1 % osmium tetroxide staining indicated similar tubular structures with dark peripheries of aggregates of ZnChl **1**. However, no further details

or differences in TEM images could be observed in stained (0.5% uranyl acetate staining) and unstained samples. High resolution TEM (HR-TEM) imaging that operates at very high accelerating voltage of 300 kV also revealed similar morphologies of these large nanotubes (data not shown).

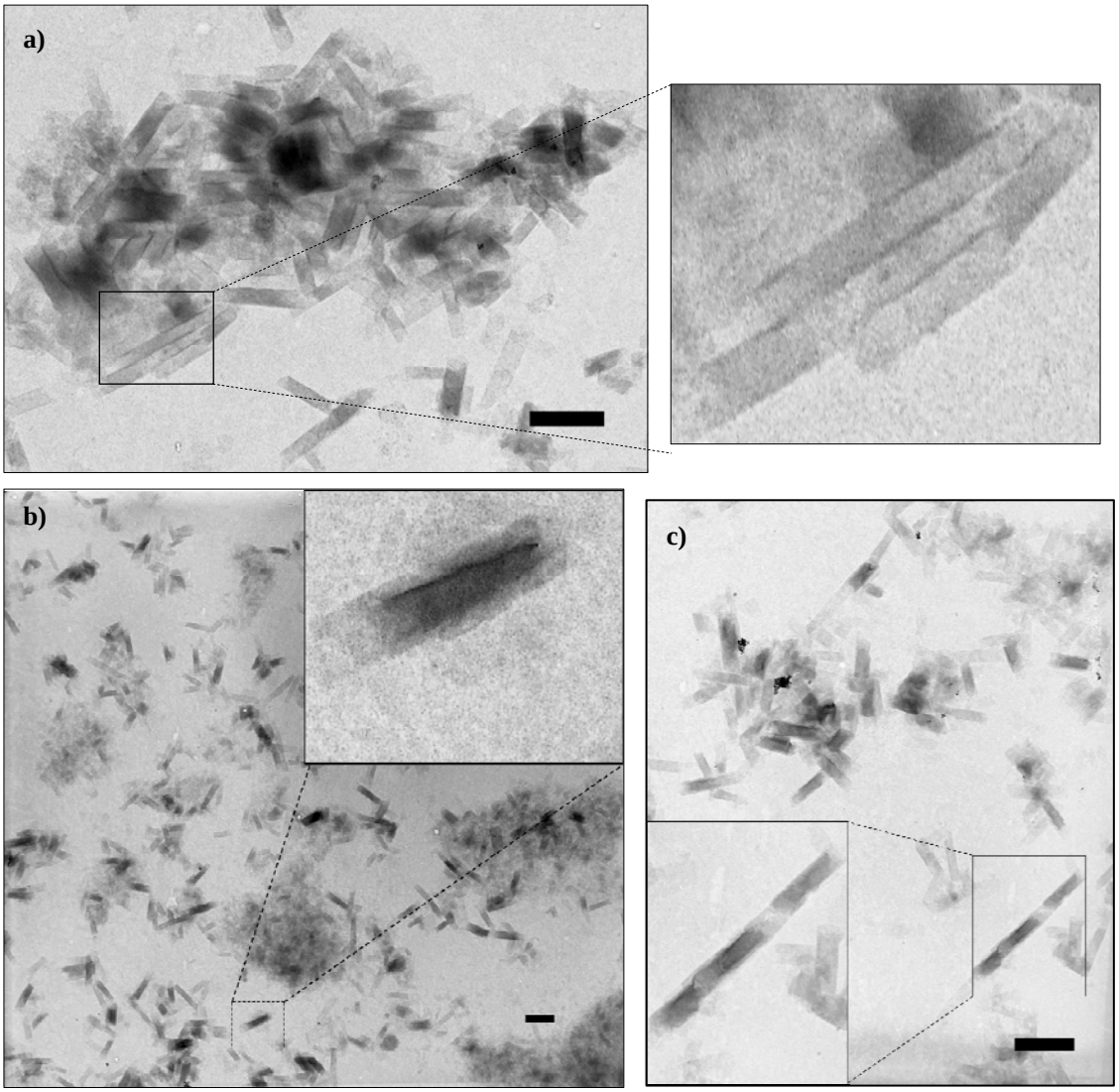

Figure 10. a) TEM micrographs of ZnChl **1** drop-cast from aggregate suspension in *n*-hexane/THF (100:0.5) ($c = 1.2 \times 10^{-4}$ M) and stained with 0.5 % aqueous uranyl acetate, showing peripheral dark shell and light centre indicating hollow tubular structures. Scalebar is 600 nm; b, c) TEM micrographs of ZnChl **1** drop-cast from aggregate suspension in *n*-hexane/THF (100:0.5) ($c = 4.2 \times 10^{-4}$ M) and stained with 0.5 % uranyl acetate showing hollow tubular structures. Scalebar is 800 nm in b and 600 nm in c); inset shows magnification of tubes that are presumably open ended and hollow.

It is to be noted that our aggregates visualized in suspensions (Figure 10) apparently differ from the nanorod aggregates shown in Figure 5 by AFM and Figure 9 by STEM. The origin of difference in rod/tube diameter observed from AFM and STEM in freshly prepared

aggregates and those prepared from aged aggregate suspensions is not very clear. However, this might be attributed to the concentration, sample preparation and ageing time of the aggregate solutions.

To further investigate the morphology of these large tubular aggregates of ZnChl **1** under similar sample preparation used for TEM measurements, tapping-mode AFM measurements of the same suspension of the aggregates of ZnChl **1** were performed on HOPG and silicon wafer (Figure 11). Similar short tubular assemblies as in TEM could be observed on silicon wafer (SiO_x) surface along with some bundles of nanotubes (Figure 11). These assemblies were extremely uniform with widths of 140 ± 10 nm and heights of ~ 7.0 ± 0.4 nm (Figure 11b, inset). Similar morpholgies were observed also by other electronic microscopic techniques such as STEM and SEM (see Appendix section).

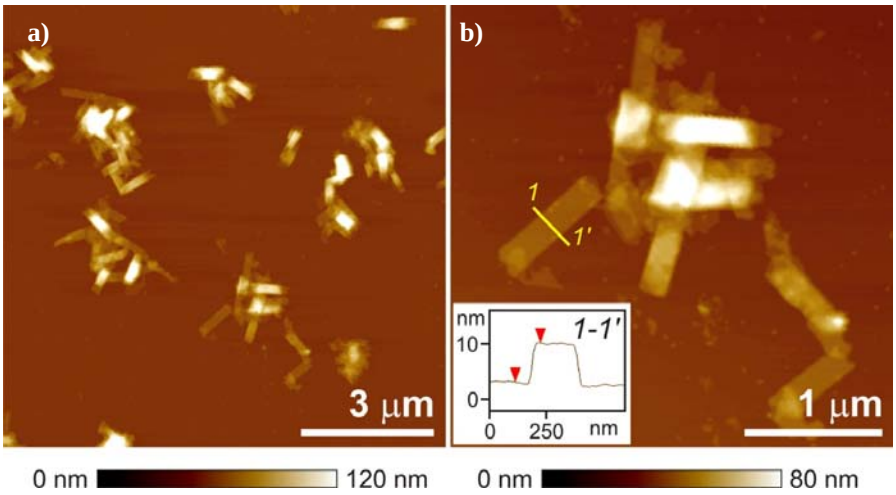

Figure 11. AFM images of aggregates of ZnChl **1** in *n*-hexane/THF (100:0.5) solution prepared from a suspension from a concentration of 4.0×10^{-4} M by drop-casting onto SiO_x wafer for 20 sec followed by removal of the residual solution and drying in vacuum.

5.3. Covalent stabilization of zinc chlorin nanorods

To stabilize the nanorods of ZnChl **1**, in-situ polymerization reaction was attempted with ZnChl **1** aggregates by metathesis polymerization reaction by Grubbs first generation catalyst, i.e., benzylidene-bis(tricyclohexylphosphine) dichlororuthenium complex as illustrated schematically in Figure 12.

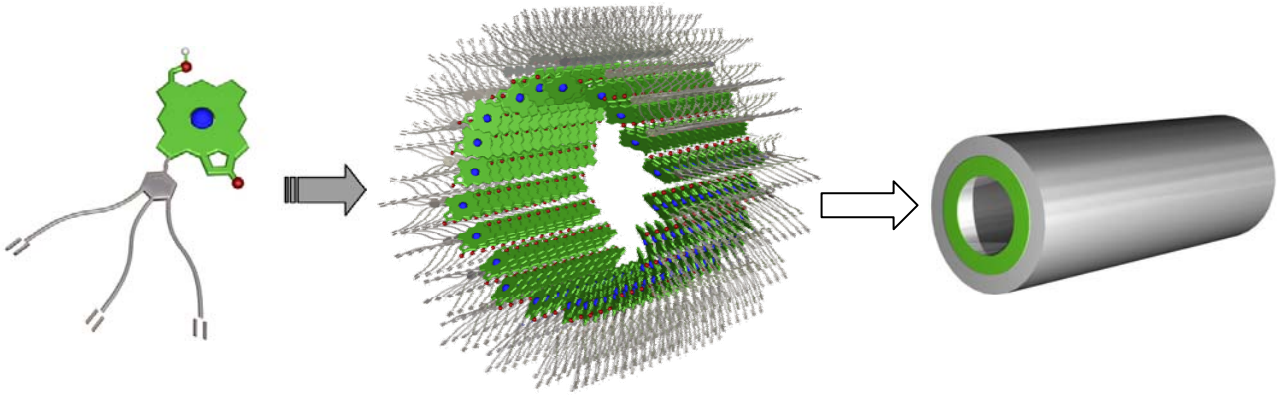

Figure 12. Schematic representation of covalent stabilization of ZnChl **1** nanorods/tubes via in-situ metathesis polymerization reaction.

In contrast to other olefin metathesis catalysts, Grubbs catalysts are versatile, have a broad range of functional group tolerance and are compatible with a wide range of solvents with varying polarity.[32] In-situ metathesis polymerization reactions of pre-formed aggregates have been reported in a variety of non-polar solvents such as *n*-hexane, octane and benzene.[9a,32]

Since ZnChl **1** forms well-defined tube-like/rod aggregates in non-polar solvents such as *n*-hexane or *n*-heptane/THF (100:0.5) at lower concentrations in freshly prepared solutions, in situ metathesis polymerization of aggregates was performed in similar solvent combinations. At first, the reaction was attempted at a moderate concentration of 1 mM of the aggregate solution. Several attempts of in-situ metathesis polymerization reaction were made with aggregate solutions of ZnChl **1** at ~ 0.1 mM, ~ 0.01-0.05 mM, 0.001 mM in order to optimize the conditions for metathesis polymerization reaction. After addition of the Grubbs catalyst (0.5-1 mol %), the reaction mixture was stirred in dark under argon for 2 hours and subsequently quenched by few drops of ethyl vinyl ether. However, after evaporation of the solvents, the resulting polymeric material showed extremely poor solubility in common organic solvents that prevented its further characterization by spectroscopy or microscopy. The poor solubility might be attributed to the moderate reaction concentration where presumably intercolumnar polymerization dominates over the desired intracolumnar polymerization to produce a three-dimensional network structure. The most important parameter that should be controlled is the concentration of aggregate solution in order to ensure that desired intracolumnar and not intercolumnar polymerization takes place.[9a] Based on the studies in section 5.2.4, it was indeed important to attempt the polymerization reactions at dilute concentrations. To overcome the probable intercolumnar polymerization, the reaction was attempted at several dilutions (10^{-5}-10^{-6} M) after confirming the existence of rod like

structures at those concentrations by AFM and UV/Vis studies. The dilute conditions are suitable for facilitating intracolumnar polymerization and preventing intercolumnar polymerization. At higher dilutions, metathesis polymerization reaction of the olefinic groups led to extensively crosslinked periphery with negligible interoligomer crosslinking as evident from microscopic and spectroscopic investigations. To a higher diluted aggregate solution of ZnChl **1** (1.1×10^{-6} M), catalytic amount of Grubbs first generation catalyst (~ 1-0.5 mol %) was added at room temperature. The reaction mixture was stirred in dark for 3-4 hours and subsequently quenched with few drops of ethyl vinyl ether. The reaction mixture was then subjected to Fourier transform infra red (FTIR) spectroscopy, UV/Vis, CD and AFM measurements without further purifications.

UV/Vis measurement of the reaction mixture showed the retention of the aggregate spectra (Figure 13). Upon heating up the aggregate reaction mixture solution after polymerization to 50 ^{o}C, no significant changes in the bathochromically shifted Q_y and Soret bands of the aggregates were observed, which indicate that the nanorod aggregate structure was retained after the polymerization reaction (Figure 13c). After polymerization of the terminal olefinic funtionalities, the nanorod architecture is almost preserved as evident from the retention of the CD excitonic couplet (Figure 13d, thick curve) as well as upon heating the aggregate reaction mixture to 50 ^{o}C (Figure 13d, dotted curve).

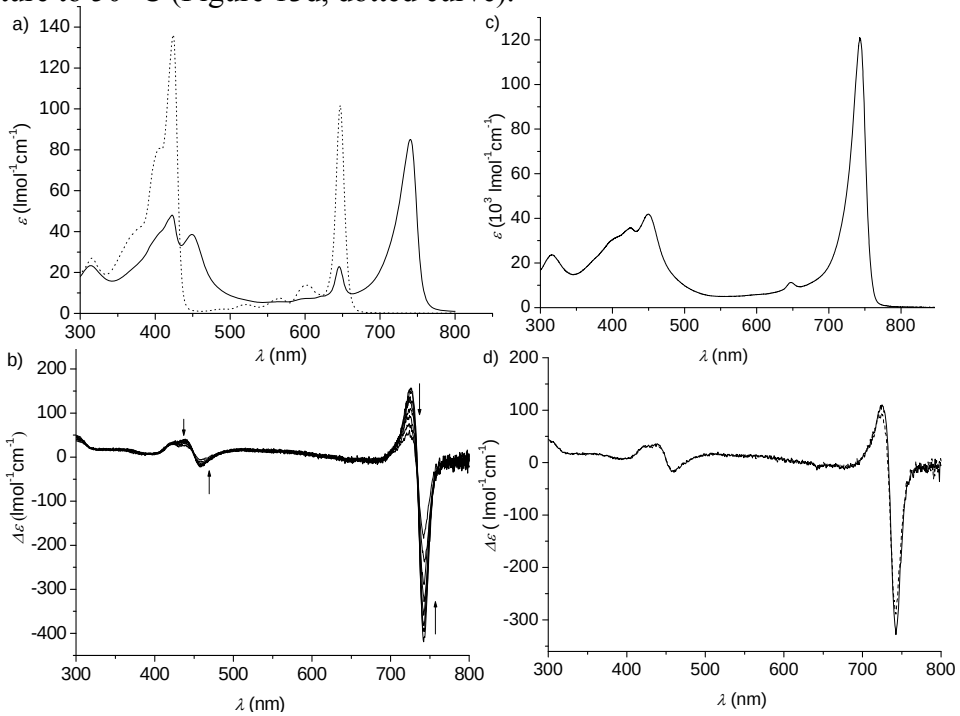

Figure 13. a, b) UV/Vis and CD spectra for unpolymerized aggregates of ZnChl **1** with variation in temperature (15 ^{o}C to 85 ^{o}C); c) UV/Vis spectra of polymerized aggregates at 50 ^{o}C and d) CD spectra of polymerized aggregates of ZnChl **1** after in-situ metathesis reaction at room temperature (thick line) and at 50 ^{o}C (dotted line).

FTIR spectroscopy provided important indication about the extent of polymerization reaction. In order to verify whether the terminal olefinic groups were converted into internal ones after the metathesis polymerization reaction, FTIR measurements were performed by preparing KBr pellets of ZnChl **1** before and after the metathesis reaction. The vibration band at 1646 cm^{-1} (characteristic of terminal olefin H_2C=C group) decreases in relative intensity after the polymerization reaction. Compared to those of the intact nanorods before metathesis polymerization reaction, the isolated product in the IR displayed a large drop in intensity of a vibrational band at 1646 cm^{-1}, characteristic of C=C stretch (Figure 14).

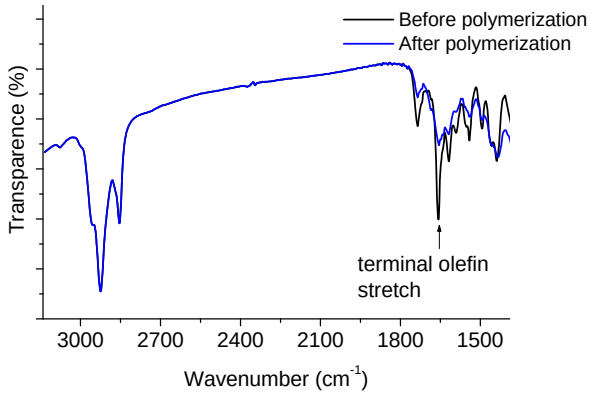

Figure 14. FTIR spectra (KBr) of ZnChl **1** (black curve) and the polymerized product isolated from the aggregate solution after in-situ metathesis reaction (blue curve).

The decrease in the intensity of the vibrational bands due to IR active C=C at 1646 cm^{-1} is indicative of the conversion of the terminal olefinic groups into internal olefins. However, owing to the large number of olefinic units present in the rod aggregates of ZnChl **1**, some of these terminal groups might remain unreacted hence a complete disappearance of the IR band at 1646 cm^{-1} was not observable. Similar results have been reported by Aida and co-workers for the crosslinking of graphitic nanotubes, where a decrease in the intensity of the terminal C=C stretch was attributed to near quantitative conversion of terminal olefins into internal ones.[2h]

Solvent denaturation experiment: The dissociation of ZnChl **1** aggregates takes place not only at increasing temperature but also in the presence of coordinating or polar solvents. Thus, addition of upto 10 % THF to the uncross-linked aggregate solution of ZnChl **1** in *n*-hexane/ THF (100:0.5) leads to a pronounced decrease of the aggregate band at 741 nm and a concomitant increase in the monomer band at 650 nm and thus complete disruption of the nanorod aggregate structures. The cross-linked nanorods of **1** however, exhibited an enhanced

resistivity to aggregate disrupting solvents such THF or methanol and no significant spectral changes were observed with addition of upto 6-8% of THF denaturant, thus demonstrating presumably the presence of the covalently locked nanorod aggregates (Figure 15).

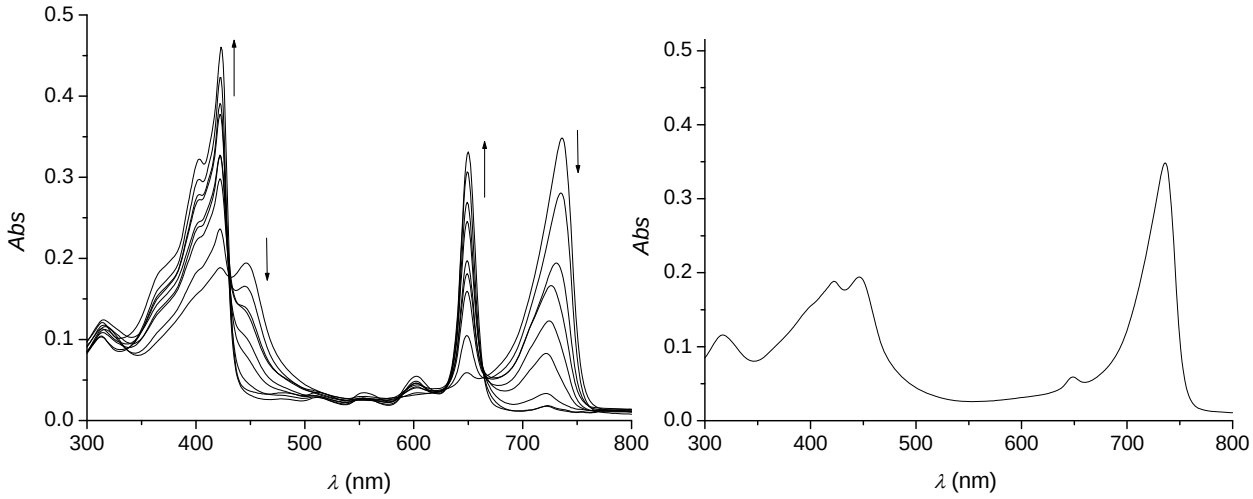

Figure 15. a) UV/Vis spectra of ZnChl **1** in *n*-hexane/THF (c = 1.1 × 10^{-6} M) with variation of THF content from 1-10 %; b) after polymerization in *n*-hexane/THF (c = 1.1 × 10^{-6} M) after addition of THF (8 %).

AFM measurement before and after polymerization reaction: AFM measurements were performed with aggregate solutions (c = 1.1 × 10^{-6} M) before and after the polymerization reaction. Figures 16a-d show well-defined nanorods deposited onto HOPG with large contour lengths and significantly lesser stiffness prior to the metathesis polymerization reaction. AFM measurements with the reaction mixture directly after in-situ metathesis polymerization reaction showed that the structural integrity of the nanorods were mostly preserved. Furthermore, AFM results showed that the polymerization was predominantly intratubular as isolated nanorods could be observed onto HOPG (Figure 16e, f) and no bundles or network like structures were visible. Moreover, the diameters and heights of the nanorods changed a little after in-situ polymerization reaction. The diameters of the nanorods were slightly decreased (~ 10 nm) and the heights of the nanorods were slightly increased (~ 3 nm) compared to those before the polymerization reaction. The slight increase in height is indicative of the increased rigidity of the nanorods. The aggregates appeared highly ordered and stiffer compared to those prior to the polymerization reaction. Sections g, h, i, j in Figure 16e show individual nanorod/tubes which appear more rigid than the nanorods before polymerization in Figures 16a-d.

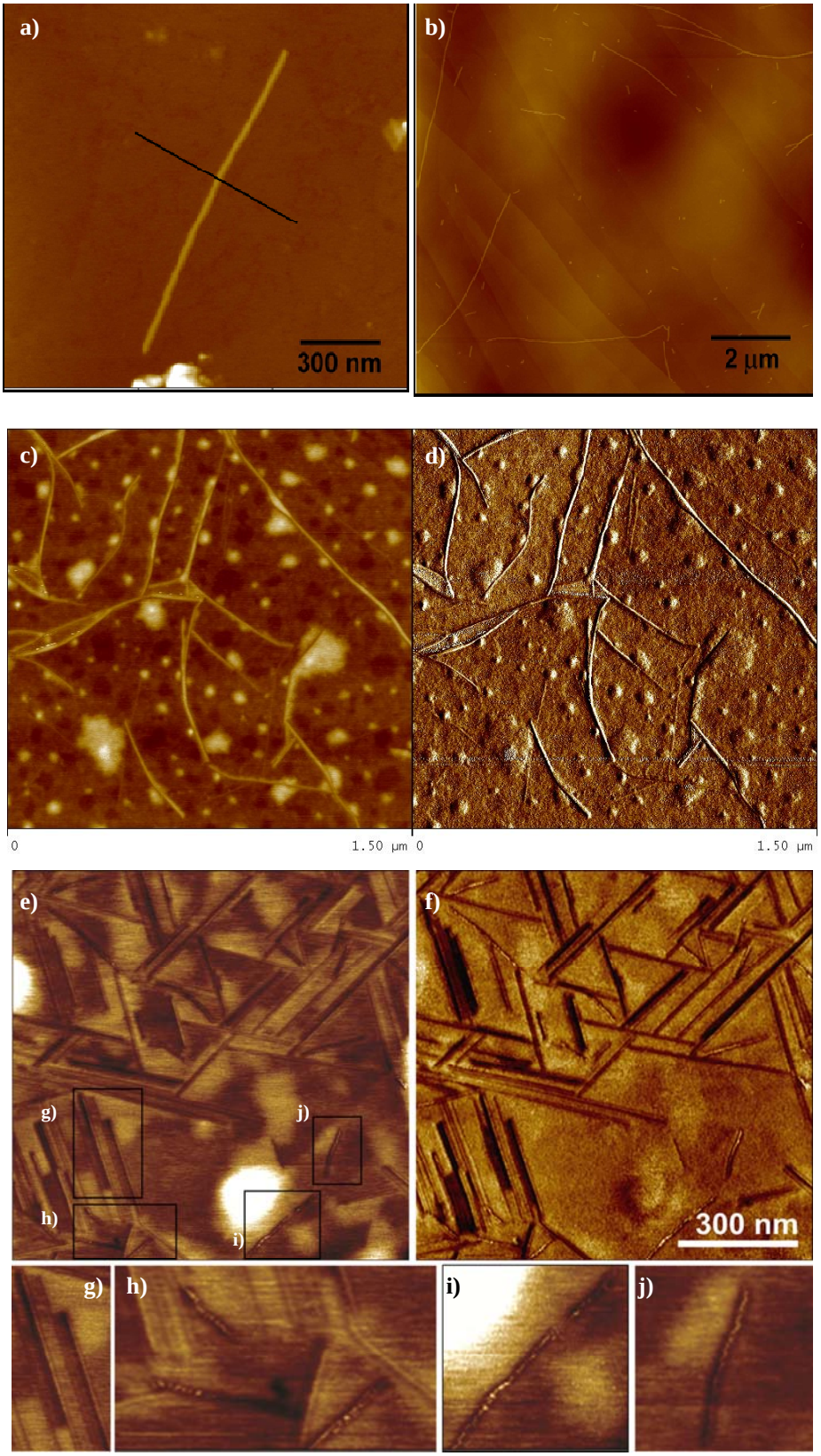

Figure 16. a, b, c) AFM phase image profiles for the aggregate solutions of ZnChl **1** before metathesis reaction (c =1.1 × 10^{-6} M); d) height image of c; e, f) AFM phase and height images for the aggregate solution of ZnChl **1** after in-situ metathesis reaction at concentrations of 1.1 × 10^{-6} M. Regions in figure e) are magnified and shown in figures g), h), i) and j) and indicate presence of rigid nanorod aggregate structures.

If the samples were treated with strongly coordinating solvent such as THF or methanol at room temperature, the unpolymerized rods were dissolved and no regular aggregates could be observed by AFM, whereas the polymerized nanorods/tube[a] mostly maintained their structural integrity even after addition of 5-6 % THF as confirmed by AFM studies.

5.4. Charge carrier mobility

The intrinsic charge transport properties of ZnChl **1** aggregates in solid state have been investigated by pulse radiolysis-time resolved microwave conductivity (PR-TRMC) technique, which has been used to determine charge carrier mobilities in a large number of organic materials.[33] As discussed in Chapters 3 and 4, the charges are generated directly in the bulk solid state with this technique, their transport properties are probed on a very local spatial scale and the charges trapped by impurities or structural defects are not responsive. The temporal decay of the conductivity signal (i.e. microwave absorbance) reflects the lifetime of the electro-generated carriers. The charge carrier mobilities depend rather on supramolecular organization and long-range order inside the material.[33a,b] Appreciably long lifetimes (~ 1 μs) and slow charge recombination is observed for the aggregates of **1** as shown in Figure 17. These studies indicate that the zinc chlorin cores and the hydrophobic chains are phase separated from one another at a molecular level to enhance the ordering of aromatic units responsible for charge-carrier transport. The charges recombine by tunneling through the insulating hydrocarbon side chains surrounding and separating the tubular aggregates. Charge carrier mobilities of ~ 0.02-0.03 cm^2/Vs were obtained for ZnChl **1** by temperature-dependent PR-TRMC measurements (Table 2). The charge carrier mobilities increased with increase in temperature indicating a thermally activated charge carrier transport along the rod aggregates. The charge carrier mobilities have been shown to be directly related to the size and planarity of aromatic cores.[33c] Previously, hole mobilities of the order of ~ 0.002 cm^2/Vs have been observed for microcrystalline chlorophyll *a* evaluated by time of flight method (TOF) method. Considering

[a] Electron microscopic studies were also attempted with these aggregate solutions and TEM studies were unfortunely not successful with these aggregates as sufficient contrast was not achievable. However, STEM investigation of the nanorods post cross-linking revealed similar fibrous morphology as observed for the aggregates prior to cross-linking indicating that the tubular structures are preserved indeed. However, in absence of higher resolution TEM images, it was not possible to assess further detail of the stabilized nanotubular assemblies by electron microscopy.

that zinc chlorin units are moderately sized non-planar aromatic cores, the charge carrier mobilities obtained are thus appreciably high.

Table 2. Temperature-dependent charge carrier mobilities of ZnChl **1** obtained by PR-TRMC measurements.

Temperature (^{o}C)	Charge carrier mobility (cm^2/Vs)	Temperature (^{o}C)	Charge carrier mobility (cm^2/Vs)
25	0.0146	25	0.0169
50	0.0225	0	0.0169
75	0.0225	-25	0.0158
100	0.0270	-50	0.0113
75	0.0225	-25	0.0128
50	0.0225	0	0.0133
		25	0.0133

The charge transport properties i.e., charge carrier mobility, recombination kinetics, lifetime and temperature-dependence are similar to those of 3[1]-hydroxy zinc chlorins **1a-1c** studied in Chapter 3, and thus are indicative of similar tubular nanostuctures for ZnChl **1** aggregates in the solid state.

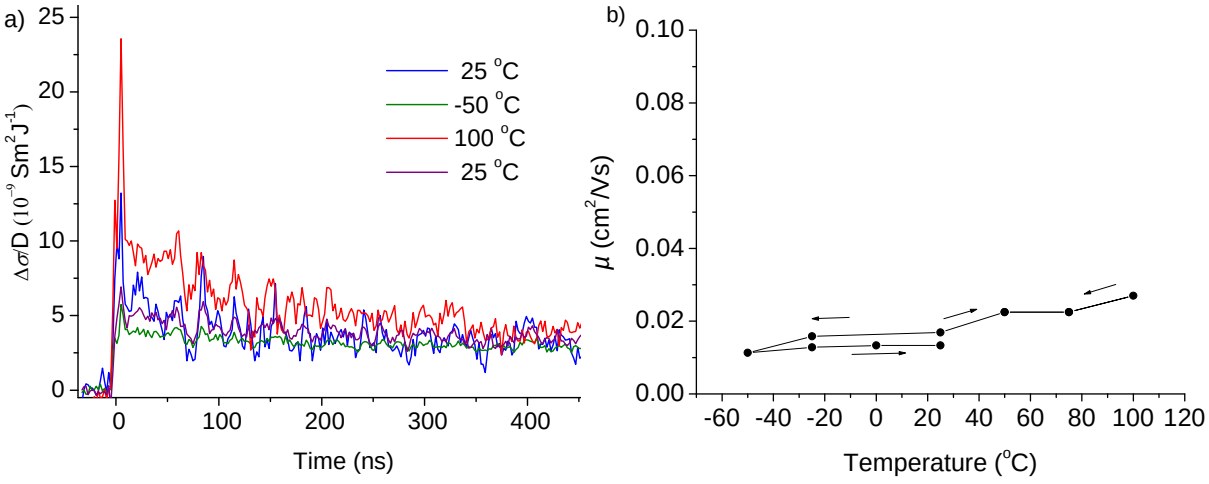

Figure 17. a) PR-TRMC transients at temperatures of 25 ^{o}C, -50 ^{o}C, 100 ^{o}C and 25 ^{o}C for ZnChl **1** aggregates showing a first order decay kinetics and slow recombination time of the charge carriers; b) temperature-dependent charge carrier mobilities of ZnChl **1**, arrows indicate the temperature sequence in which mobility measurements were performed.

5.5. Discussion of Concentration-dependent Aggregate Structures of ZnChl 1

Variable morphology of chlorosomes have recently been discussed in detail in the literature and the chlorosomes from different species can differ by at least a factor of 5 in their volume

and in shape.[34] Some are ellipsoid shaped, whereas other are conically shaped or irregularly shaped. Electron microscopic studies of chlorosomes have revealed strongly divergent structures with variable diameters among different species, which are believed to be either results of functional morphology or a result of different stages in the biogenesis of chlorosomes, different fixation protocols[34,35] or originate from different sample preparation. Early EM studies by Cohen-Bazire and co-workers on thin sections have suggested the presence of 1.2 to 2 nm wide fibrils inside chlorosomes of *Chlorobaculum parvum*.[36] Staehelin et al. concluded from freeze-fracture EM that BChls are organized into rod-shaped structures, with a diameter of approx. 5 and 10 nm in *Chloroflexus aurantiacus* and *Chlorobium tepidium*, respectively.[37] High resolution EM images revealed fine interval structures with spacing of 2 nm which could be explained by a simple lamellar organization of pigment molecules.[38] Tamiaki and co-workers reported rod-shaped nanostructures in chlorosomes of green photosynthetic bacteria *Chl. vibrioforme* C-substrain, D-substrain, *Chl. tepidum*, and *Cfl. aurantiacus* by cryo-EM studies. The diameters of these nanostructures in three types of green sulfur bacteria were approximately 10 nm, whereas those of the green filamentous bacterium were approximately 5 nm.

To account for the formation of large tubular nanostructures formed by ZnChl **1** in aggregate suspensions, it might be possible to envisage that in concentrated suspensions of aggregate solutions, van der Waals interaction of hydrophobic side chains leads to face-to-face ordering of individual nanorods/tubes (of diameters ~ 5 nm) presumably into sheet-like structure which rolls up subsequently to form large nanotubes with diameters of ~ 150 nm. When such a sheet/tape rolls up, a smaller curvature and hence a larger tube diameter might be preferred. Such a reasonable suggestion is shown schematically in Figure 18.

Similar phenomena have been observed for J-aggregates of cyanine dyes.[39] Von Berlepsch et al. have reported tubular J-aggregates of sulfonate-substituted amphiphilic cyanine dyes[39] in aqueous solution which transformed with time into ribbon aggregates and later into giant tubes. Cryo-TEM investigations of these aggregates revealed that the uniform tubular assemblies with diameters of ~ 17 nm in fresh solution have strong tendency to assemble into rope-like bundles after several weeks and months of storage. In a second type of tubular cyanine aggregate with diameter ~ 13 nm, dramatic structural transformation into ribbon-like structures and finally into very large nanotubes with diameters of upto ~ 500 nm was observed in presence of small amount of methanol. The formation of these giant tubes

was qualitatively explained by the fact that the driving force for such structural transformation is the competition between the free energy gain from face-to-face attraction between tubular aggregates and the penalty due to the edge energy. When stacking of ribbons is favorable, as evident for some of the cyanine aggregates, large edge energy can be tolerated. For some other cyanine aggregates, such stacking was unfavorable and the edge energy promoted growth of ribbons mostly in length. Yet closure into tubular structures could further minimize the total free energy and relatively large tubes (with diameters of upto 500 nm) were formed as a result. However, intermediate states, which could help to clarify the process of such structural transformation could not be detected by optical spectroscopy or electron microscopy in this study.[39]

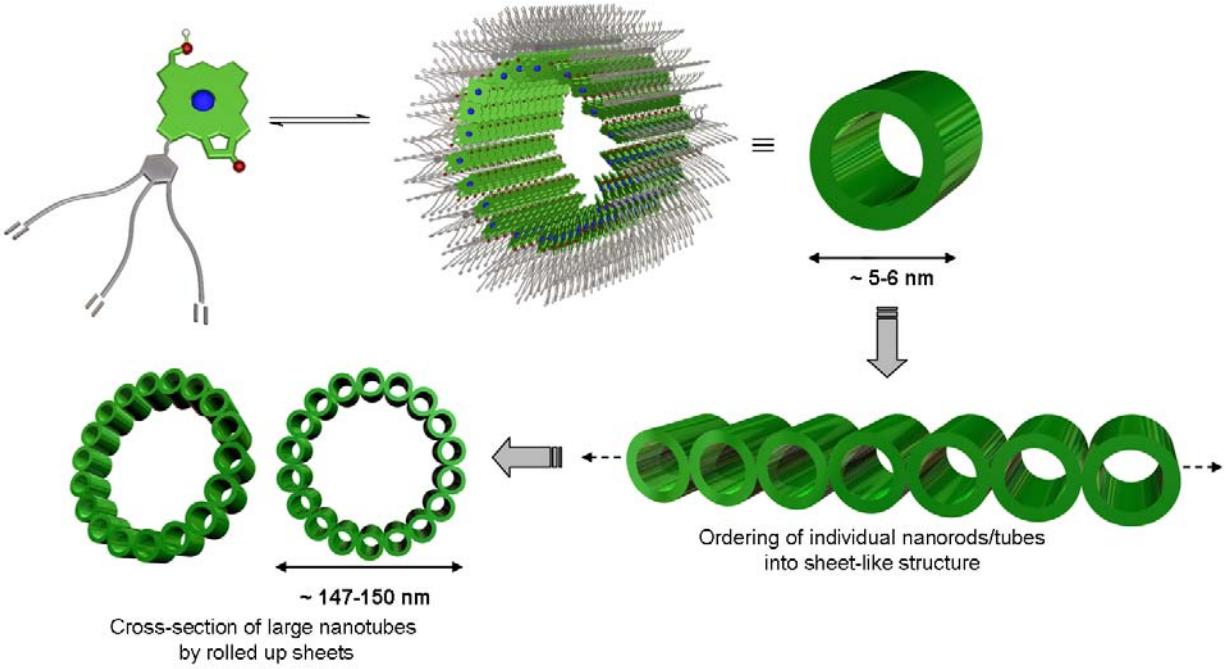

Figure 18. Suggestive schematic representation of formation of larger nanotubes of **1** at concentrated aged aggregate suspensions from nanorod/tubular aggregates (of diameter ~ 5 nm) at higher dilutions.

Nanotubes with large diameters have been obtained for other tetrapyrroles such as porphyrins and phthalocyanines as well. Porphyrin based nanotubes have been reviewed recently by Shelnutt and co-workers.[3b] They reported robust nanotubes prepared by ionic self-assembly of two oppositely charged porphyrins in aqueous solution.[3b,40] TEM images of the assemblies confirmed hollow tubular structures of porphyrin nanotubes with diameters in the range of ~ 70 nm with approximately 20 nm thick tube walls and lengths of upto few micrometers. These nanotubes were composed entirely of porphyrins driven by electrostatic forces between the porphyrin tectons and van der Waals interactions. In addition, hydrogen-

bonding, axial coordination, and other weak intermolecular interactions contributed to the formation of these aggregates. Absorption spectroscopy showed J-type aggregation behavior as indicated by bathochromically shifted Q_y and Soret bands, however, no aggregation model for these large nanotubes was proposed.[40] Dosch and coworkers reported nanotubes based on copper phthalocyanines studied by TEM, with wall thickness of the nanotubes ranging from 10 to 37 concentric layers and tube diameters of ~ 80 nm.[5]

5.6. Conclusion

In conclusion, ZnChl **1** functionalized with peripheral olefinic groups was synthesized and its self-assembly behavior in solution was studied by temperature-dependent UV/Vis, CD spectroscopy, DLS and AFM studies. The electron-rich olefinic functionalities are important for providing some contrast for electron microscopic studies such as TEM, STEM and SEM measurements and fibrous aggregates of **1** were visualized. Interestingly, structural transformation of these aggregates in concentrated suspension was observed upon ageing into large nanotubes-like assemblies. These structures are presumably formed by ordering of individual nanorods into sheets that might roll up forming large hollow open-ended tubular structures. They were characterized in detail by TEM, STEM and SEM studies. The aggregate nanorod/tube structure in freshly prepared solution had functionalizable olefinic groups on the outer side and hence they could be subjected to in-situ metathesis polymerization reaction mediated by Grubbs first generation catalyst. The polymeric cross-linked product was characterized by UV/Vis, CD, AFM and FTIR spectroscopy. UV/Vis studies showed retention of the aggregate spectra and AFM enabled visualization of stiffer nanorods with slightly lesser diameter. Such chemical stitching of the non-covalently assembled zinc chlorins endows the nanotubes with enhanced stability against solvents. Efficient charge transport properties were observed for aggregates of **1** with charge carrier mobilities of ~ 0.03 cm^2/Vs, evaluated by PR-TRMC experiments. In concord with their well-established exciton transport properties and promising charge transport properties, their micrometer-scale one dimensionality and robust nature, such self-assembled zinc chlorin nanotubes thus seem highly promising for supramolecular electronic applications in future.

5.7. Experimental section

Reagents and Solvents: All the reagents and chemicals commercially obtained from Merck, Acros, Aldrich, or Fluka, were used as such without further purification. Some of the solvents were dried according to literature known methods.[41]

High Performance Liquid Chromatography (HPLC): Analytical HPLC was performed on a system (PU 2080 PLUS) with a photodiode array detector (MD 2015) from JASCO equipped with a ternary gradient unit (LG 2080–02) and line degasser (DG-2080-533). Semipreparative HPLC was performed on a system (PU 2080 PLUS) with a photodiode array detector (UV 2077 PLUS) from JASCO. HPLC grade solvents (Rectapur) from VWR (Darmstadt, Germany) were used. Reverse phase columns obtained from Macherey-Nagel (Germany) (analytical: EC 250/4.6 NUCLEODUR 100-5 C18 ec, pre-column: CC 8/4 NUCLEODUR 100-5 C18 ec; semipreparative: SP 250/21 NUCLEODUR 100-7 C18 ec, pre-column semipreparative: SP 50/21 NUCLEODUR 100-7 C18 ec).

^{1}H NMR Spectroscopy: ^{1}H NMR spectra were recorded at 25 °C with a 400 MHz spectrometer from Bruker GmbH, Ettlingen (Bruker Avance 400). The chemical shifts (δ) are given in reference to TMS or the residual solvent signals in ppm values. The coupling constants J are expressed in Hertz (Hz) and values upto one decimal are given.

Mass Spectrometry (MS): The high resolution electron spray ionisation (ESI) mass spectra were measured with a Bruker Daltonics Micro TOF Focus instrument.

UV/Vis Spectroscopy: All spectroscopic measurements were performed in pure spectroscopic grade solvents (Merck UVASOL) in 0.5 cm or 1 cm quartz glass cuvettes. Studies for the monomers and aggregates of zinc chlorins were performed in water free solvents *n*-hexane, di-*n*-butyl ether and THF (dried and distilled over sodium). The UV/Vis spectra were measured with a PE Lambda 40 P instrument from Perkin Elmer GmbH (Rodgau, Germany) under ambient conditions. Molar extinction coefficients ε were calculated according to Lambert-Beer's law and are referred to respective monomers.

Circular Dichroism (CD): CD spectra were measured with a spectrometer from JASCO (J-810), provided with a Peltier element and measurements were carried out in spectroscopic grade pure solvents under ambient conditions using 0.5 cm or 1 cm quartz glass cuvettes.

Atomic force microscopy (AFM): The AFM measurements were performed with a Multimode Nanoscope IV system (Veeco Instruments Inc., Santa Barbara) in Tapping Mode in air. Silicon cantilever (Olympus, OMCL-AC160TS) with a resonance frequency of ~ 300

kHz was used. The aggregate samples of ZnChl **1** were spin-coated (5000 rpm) and drop casted onto highly oriented pyrolytic graphite (HOPG) and silicon wafer (SiO_x) surfaces and measured under ambient conditions.

Transmission electron microscopy (TEM): TEM measurements were performed on a Siemens Elmiskop 101 Electron Microscope at the Biocentre of University of Würzburg, operating at an acceleration voltage of 80 kV. For the observation of aggregates, a drop of sample suspension was placed on 300-mesh formvar copper grids coated with carbon. About 2 min after the deposition, the grid was tapped with filter paper to remove solvent to yield a thin film with a thickness of typically about 100 nm. Staining was performed by addition of a drop of aqueous solutions of uranyl acetate (0.5 %) onto the copper grid. After 1 min, the surface liquid on the grid was removed by tapping with filter paper.

Scanning electron microscopy (SEM): SEM images of the sample were recorded using a ZEISS Ultra Plus scanning electron microscope. The sample was prepared by drop-cast of sample solution onto SiO_x wafer. The sample was imaged with an accelerating voltage of 1-3kV as indicated in the respective SEM micrographs.

Scanning transmission electron microscopy (STEM): STEM images of the sample were recorded using a ZEISS Ultra Plus scanning transmission electron microscope. The samples (on carbon coated copper grids stained with uranyl acetate as used in TEM) were imaged with accelerating voltages (EHT) of 18-19 kV indicated in the respective STEM images.

Dynamic light scattering (DLS): DLS measurements were performed at 25 °C on a N5 Submicron Particle Size Analyzer, Beckman Coulter, using a 25 mW helium-neon laser (632.8 nm). Sample solutions were filtered into a dust-free vial through a 0.45 mm hydrophobic polytetrafluoroethylene (PTFE) filter. Data were collected at scattering angles of 10.6^o, 15.1^o, 22^o, 28.8^o, 63.8^o, 90^o and analyzed with a PCS control software.

Fourier transform infrared (FTIR) spectroscopy: FTIR spectra were measured on a Jasco FTIR-410 spectrometer with solid samples prepared as KBr pellets.

Pulse radiolysis time resolved microwave conductivity (PR-TRMC): The conductive properties of ZnChl **1** was studied with the pulse-radiolysis time-resolved microwave conductivity (PR-TRMC) technique. Pressed pellet (20-30 mg) of the material to be investigated was irradiated with 10 nanosecond pulses of 3 MeV electrons from a Van-de-Graff accelerator, which results in the creation of uniform micromolar concentration of electron-hole pairs. The resulting change in conductivity was monitored as the microwave

power absorbed by the mobile charge carriers in the material at an electro-magnetic field frequency of 33 GHz. The mobility values are determined from the conductivity at the end of the electron pulse. This technique has been described in detail elsewhere.[33a]

Synthetic details and characterization:

Synthesis of 3, 4, 5-tris-undecyloxybenzylester

3,4,5-trihydroxyethylbenzoate (300 mg, 1.51 mmol) and 11-bromo-1-undecene (1.7 ml, 7.66 mmol) were added in a suspension of K_2CO_3 (209 mg, 1.51 mmol) in dry DMF and the reaction mixture was stirred for about 48 hours. It was then poured into water and extracted with diethylether (30 × 30 ml). The aqueous layers were neutralized using saturated NH_4Cl solution and the combined organic layers were dried over Na_2SO_4 and the solvent was subsequently evaporated to obtain an yellow oil. The crude product so obtained was purified to isolate only the first fraction using *n*-pentane/diethylether (4:1) as the eluent to obtain the desired product (165 mg, 50% yield); ^{1}H NMR (400 MHz, $CDCl_3$, 25 ^{o}C): δ = 7.22 (s, 2H, ArH-2, ArH-6), 5.81-5.71 (m, 3H, H-2), 4.97-4.87 (m, 6H, H-1), 4.31 (q, J = 7.2 Hz, 2H, OCH_2CH$_3$), 3.43 (t, J = 7.08 Hz, 6H, H-11), 2.00 (q, J = 7.32 Hz, 6H, H-3), 1.81-1.73 (m, 6H, H-4), 1.71-1.26 (m, 36H, H-5 to H-10). 1.16 (t, J = 6.96 Hz, 3H, OCH$_2$CH_3). MS (MALDI-TOF, matrix: DCTB) for $C_{42}H_{70}O_5$: 654.523 for $[M]^+$.

Synthesis of 3, 4, 5-tris-undecyloxybenzylalcohol

To a stirred suspension of $LiAlH_4$ (15.3 mg, 0.37 mmol), a solution of the 3, 4, 5-triundecyloxybenzylester (160 mg, 0.24 mmol) was added and the reaction mixture was stirred at 0 ^{o}C in an ice bath. The stirring was continued for 3 h and when the reaction was completed as indicated by the TLC, it was quenched with few drops of water and extracted with diethyl ether. The aqueous layer was neutralized with dilute H_2SO_4, combined organic layers were dried over Na_2SO_4 and solvent was evaporated to obtain the alcohol as a colorless oil (137 mg, 92% yield); ^{1}H NMR (400 MHz, $CDCl_3$, 25 ^{o}C): δ = 6.56 (s, 2H, ArH-2, ArH-6), 5.81-5.71 (m, 3H, H-2), 5.02-4.91 (m, 6H, H-1), 4.59 (d, J = 4.8 Hz, 2H, CH_2OH), 3.98-3.91 (m, 6H, H-11), 2.05 (q, J = 7.32 Hz, 6H, H-3), 1.81-1.73 (m, 6H, H-4), 1.46 (s, 1H, OH) 1.71-1.26 (m, 36H, H-5 to H-10). MS (MALDI-TOF, matrix: DCTB): calculated for $C_{40}H_{68}O_4$: 612.23, observed value: 612.516 for $[M]^+$.

3-devinyl-3-formyl-13^2-demethoxycarbonyl-pheophorbide *a* 3,4,5-tris-undecyloxy-benzylester (3)

Chlorin 17^2-carboxylic acid, **2** was obtained from pheophorbide a by literature methods.[22,26] To a solution of the 17^2-carboxylic acid derivative (120 mg, 0.2238 mmol) in dry dichloromethane (CH_2Cl_2), 3, 4, 5-trisundecyloxybenzylalcohol (205.5 mg, 0.3358 mmol) was added and stirred under argon atmosphere at room temperature. Subsequently the coupling reagents DCC (461.7 mg, 2.238 mmol), DMAP (138.9 mg, 1.119 mmol), DPTS (329.5 mg, 1.119 mmol) were added to the reaction mixture. After 20 minutes, 57 µL of diisopropylethylamine was added and stirred under room temperature for several hours and then the reaction mixture was stirred overnight. The reaction mixture was extracted using CH_2Cl_2 and the aqueous layers were neutralized using saturated NH_4Cl. The combined organic extracts were washed with brine, dried over anhydrous Na_2SO_4 and solvent was removed under vacuum. The crude product was purified using silica gel column chromatography with diethylether/*n*-pentane (60:40) as the eluent to isolate the aldehyde compound **3** (140.8 mg, 56% yield).

Analytical HPLC: The solvent combination used was methanol/CH_2Cl_2 (75:25), compound was eluted at 8.92 mins. M.p. 130–135 ^oC; ^1H NMR (400 MHz, $CDCl_3$, 25 ^oC): δ = 11.52 (s, 1H, CHO), 10.34 (s, 1H, 10-H), 9.64 (s, 1H, 5-H), 8.82 (s, 1H, 20-H), 6.56 (s, 1H, ArH-6), 6.45 (s, 1H, ArH-2), 5.88-5.74 (m, 3H, H-2), 5.10-4.88 (m, 10H, 13^2-CH_2, 13^2-CH_2, 1´H, 1´´H, H-1, H-1´), 4.50 (dq, J = 4.52 Hz, *J* = 2 Hz, 1H, 18-H), 4.30 (td, *J* = 8.52 Hz, *J* = 2.68 Hz, 1H, 17-H), 3.96-3.76 (m, 8H, 8^1-H, H-3), 3.75-3.41 (m, 15H, 12^1-H, 2^1-H, 7^1-H, H-11), 2.66-2.54 and 2.56-2.26 (m, 4H, 17^1-H, 17^2-H), 2.03-2.00 (m, 6H, H-4), 1.77-1.70 (m, 6H, 18^1-H, 8^2-H), 1.39-1.20 (m, 36H, H-5 to H-10), 0.36 (s, 1H, NH), -1.75 (s, 1H, NH); HRMS (ESI): m/z calcd for $C_{72}H_{98}N_4O_7$ $[M+H]^+$: 1131.7517; found: 1131.7513.

3-hydroxymethyl-13^2-demethoxycarbonyl-pheophorbide *a* 3,4,5-tris-undecyloxy-benzylester (4)

The 3^1-aldehyde derivative **3** (140 mg, 0.1238 mmol) was dissolved in CH_2Cl_2 and boron-hydride (tert-butyl) amine reagent (107 mg, 1.2389 mmol) was added to it. The reaction mixture was then allowed to stir under argon at room temperature for two hours and the organic layer was subsequently extracted using diethylether as the solvent. The aqueous layer was neutralized using saturated NH_4Cl solution and the combined organic extracts were

washed with brine, dried over anhydrous Na_2SO_4 and solvent was removed under vacuum. The crude product was purified using silica gel column chromatography using diethylether/*n*-pentane (70:30) as the eluent to isolate the corresponding alcohol, compound **4** as an olive green product (115 mg, 82% yield).

Analytical HPLC: The solvent combination used was methanol/dichloromethane (70:30), compound peak was obtained at 6.72 mins. M.p. 98–105 ^oC; ^1H NMR (400 MHz, $CDCl_3$, 25 ^oC): δ = 9.52 (s, 1H, 10-H), 9.49 (s, 1H, 5-H), 8.56 (s, 1H, 20-H), 6.56 (s, 1H, ArH-2), 6.26 (s, 1H, ArH-6), 5.83-5.74 (m, 5H, 3^1-H, H-2), 5.07-4.88 (m, 10H, 13^2-CH_2, 13^2-CH_2, 1´H, 1´´H, H-1, H-1´), 4.48 (dq, J = 4.52 Hz, J = 2 Hz, 1H, 18-H), 4.36-4.30 (m, 2H, 17-H, 3^1-OH), 3.93-3.81 (m, 8H, 8^1-H, H-3), 3.67 (s, 3H, 12^1-H), 3.42-3.37 (m, 6H, H-11), 3.29 (s, 3H, 2^1-H), 3.26 (s, 3H, 7^1-H), 2.75-2.28 (m, 4H, 17^1-H, 17^2-H), 2.03-2.00 (m, 6H, H-4), 1.84-1.70 (m, 6H, 18^1-H, 8^2-H), 1.39-1.27 (m, 36H, H-5 to H-10), 0.36 (s, 1H, NH), -1.79 (s, 1H, NH); HRMS (ESI): m/z calcd for $C_{72}H_{100}N_4O_7$ $[M]^+$: 1132.7654; found: 1132.7636.

3-hydroxymethyl-13^2-demethoxycarbonyl-pheophorbide *a* 3,4,5-tris-undecyloxy-benzylester zinc complex (**1**).

To the alcohol derivative **4** (70 mg, 0.0617 mmol) dissolved in THF (15 mL), of a saturated solution of $Zn(OAc)_2$ in MeOH was added (10 mL) and the reaction mixture was stirred under argon at room temperature for two hours. Subsequently, it was extracted with dichloromethane and the aqueous layer was neutralized with saturated $NaHCO_3$ solution. The organic extracts were washed with brine, dried over anhydrous Na_2SO_4 and the solvent was removed under vacuum. The crude product was then rapidly purified using silica gel column chromatography with THF/MeOH (1:1) as eluent to isolate the zinc chlorin compound **1** which is a turquoise green solid, which was purified subsequently at the HPLC with a solvent combination of methanol/dichloromethane (4:1) to obtain the zinc chlorin compound **1** (45.2 mg, 61% yield).

Analytical HPLC: The solvent combination used was methanol/dichloromethane (7:3), compound was eluted at 5.82 mins. M.p. 190–196 ^oC; ^1H NMR (400 MHz, $CDCl_3$, 25 ^oC): δ = 9.61 (s, 1H, 10-H), 9.49 (s, 1H, 5-H), 8.48 (s, 1H, 20-H), 6.56 (s, 1H, ArH-6), 6.53 (s, 1H, ArH-2), 5.88-5.72 (m, 5H, 3^1-H, H-2), 5.07-4.87 (m, 10H, 13^2-CH_2, 13^2-CH_2,1´H, 1´´H, H-1, H-1´), 4.52 (dq, J = 4.52 Hz, J = 2 Hz, 1H, 18-H), 4.44-4.29 (m, 2H, 17-H, 3^1-OH), 3.98-3.81 (m, 8H, 8^1-H, H-3), 3.67 (s, 3H, 12^1-H), 3.42-3.37 (m, 6H, H-11), 3.29 (s, 3H, 2^1-H), 3.26 (s,

3H, 7^1-H), 2.75-2.58 and 2.33-2.24 (m, 4H, 17^1-H, 17^2-H), 2.05-2.00 (m, 6H, H-4), 1.77-1.69 (m, 6H, 18^1-H, 8^2-H), 1.39-1.27 (m, 36H, H-5 to H-10); HRMS (ESI): m/z calcd for $C_{72}H_{98}N_4O_7Zn$ $[M]^+$: 1195.6724; found: 1195.6799.

5.8. References and notes

(1) a) Schenning, A.; Meijer, E. W. *Chem. Commun.* **2005**, 3245–3258; b) Hoeben, F. J. M.; Jonkheijm, P.; Meijer, E. W.; Schenning, A. P. H. J. *Chem. Rev.* **2005**, *105*, 1491–1546; c) Meijer, E. W.; Schenning, A. P. H. J. *Nature* **2002**, *419*, 353–354.

(2) a) Yamamoto, Y.; Zhang, G. X.; Jin, W. S.; Fukushima, T.; Ishii, N.; Saeki, A.; Seki, S.; Tagawa, S.; Minari, T.; Tsukagoshi, K.; Aida, T. *Proc. Natl. Acad. Sci. U. S. A.* **2009**, *106*, 21051–21056; b) Mynar, J. L.; Yamamoto, T.; Kosaka, A.; Fukushima, T.; Ishii, N.; Aida, T. *J. Am. Chem. Soc.* **2008**, *130*, 1530–1531; c) Zhang, G.; Jin, W.; Fukushima, T.; Kosaka, A.; Ishii, N.; Aida, T. *J. Am. Chem. Soc.* **2007**, *129*, 719–722; d) Aida, T.; Fukushima T. *Phil. Trans. R. Soc. A*, **2007**, *365*, 1539–1552; e) Yamamoto, Y.; Fukushima, T.; Saeki, A.; Seki, S.; Tagawa, S.; Ishii, N.; Aida, T. *J. Am. Chem. Soc.* **2007**, *129*, 9276–9277; f) Yamamoto, Y.; Fukushima, T.; Suna, Y.; Ishii, N.; Saeki, A.; Seki, S.; Tagawa, S.; Taniguchi, M.; Kawai, T.; Aida, T. *Science* **2006**, *314*, 1761–1764; g) Yamamoto, T.; Fukushima, T.; Yamamoto, Y.; Kosaka, A.; Jin, W.; Ishii, N.; Aida, T. *J. Am. Chem. Soc.* **2006**, *128*, 14337–14340; h) Motoyanagi, J.; Fukushima, T.; Ishii, N.; Aida, T. *J. Am. Chem. Soc.* **2006**, *128*, 4220–4221; i) Motoyanagi, J.; Fukushima, T.; Kosaka, A.; Ishii, N.; Aida, T. *J. Polym. Sci. Part a-Polymer Chemistry* **2006**, *44*, 5120–5127; j) Yamamoto, Y.; Fukushima, T.; Jin, W.; Kosaka, A.; Hara, T.; Nakamura, T.; Saeki, A.; Seki, S.; Tagawa, S.; Aida, T. *Adv. Mater.* **2006**, *18*, 1297–1300; k) Fukushima, T. *Polym. J.* **2006**, *38*, 743–756; l) Jin, W.; Fukushima, T.; Kosaka, A.; Niki, M.; Ishii, N.; Aida, T. *J. Am. Chem. Soc.* **2005**, *127*, 8284–8285; m) Jin, W.; Fukushima, T.; Niki, M.; Kosaka, A.; Ishii, N.;, Aida, T. *Proc. Natl. Acad. Sci. U. S. A.* **2005**, *102*, 10801–10806; n) Hill, J. P.; Jin, W. S.; Kosaka, A.; Fukushima, T.; Ichihara, H.; Shimomura, T.; Ito, K.; Hashizume, T.; Ishii, N.; Aida, T. *Science* **2004**, *304*, 1481–1483.

(3) a) Shao, H.; Seifert, J.; Romano, N. C.; Gao, M.; Helmus, J. J.; Jaroniec, C. P.; Modarelli, D. A.; Parquette J. R. *Angew. Chem., Int. Ed.* **2010**, *49*, 7688–7691; b) Medforth, C. J.; Wang, Z. C.; Martin, K. E.; Song, Y. J.; Jacobsen, J. L.; Shelnutt, J. A. *Chem. Commun.* **2009**, 7261–7277; c) Yao, P. P.; Wang, H. F.; Chen, P. L.; Zhan, X. W.; Kuang, X.; Zhu,

D. B.; Liu, M. H. *Langmuir* **2009**, *25*, 6633–6636; d) Elemans, J. A. A. W.; Van Hameren, R.; Nolte, R. J. M.; Rowan, A. E. *Adv. Mater.* **2006**, *18*, 1251–1266; e) Ajayaghosh, A.; Varghese, R.; Mahesh, S.; Praveen, V. K. *Angew. Chem., Int. Ed.* **2006**, *45*, 7729–7732; f) Yang, W. Y.; Lee, E.; Lee, M. *J. Am. Chem. Soc.* **2006**, *128*, 3484–3485; g) Balbo Block, M. A.; Kaiser, C.; Khan A.; Hecht S. *Top. Curr. Chem.*; Springer-Verlag Berlin Heidelberg, **2005**; Vol. 245, 89–150; h) Horne, W. S.; Ashkenasy, N.; Ghadiri, M. R. *Chem.–Eur. J.* **2005**, *11*, 1137–1144; i) Bong, D. T.; Clark, T. D.; Granja, J. R.; Ghadiri, M. R. *Angew. Chem., Int. Ed.* **2001**, *40*, 988–1011.

(4) Zhang, X. J.; Zhang, X. H.; Zou, K.; Lee, C. S.; Lee, S. T. *J. Am. Chem. Soc.* **2007**, *129*, 3527–3532.

(5) Barrena, E.; Zhang, X. N.; Mbenkum, B. N.; Lohmueller, T.; Krauss, T. N.; Kelsch, M.; van Aken, P. A.; Spatz, J. P.; Dosch, H. *Chemphyschem* **2008**, *9*, 1114–1116.

(6) Steinhart, M.; Wehrspohn, R. B.; Gosele, U.; Wendorff, J. H. *Angew. Chem., Int. Ed.* **2004**, *43*, 1334–1344.

(7) Patzke, G. R.; Krumeich, F.; Nesper, R. *Angew. Chem.*, *Int. Ed.* **2002**, *41*, 2446–2461.

(8) a) Zhang, X.; Chen, Z.; Würthner, F. *J. Am. Chem. Soc.* **2007**, *129*, 4886–4887; b) Zhang, X.; Li, Z. C.; Li, K. B.; Lin, S.; Du, F. S.; Li, F. M. *Prog. Polym. Sci.* **2006**, *31*, 893–948; c) Mueller, A.; O'Brien, D. F. *Chem. Rev.* **2002**, *102*, 727–758.

(9) a) Ishi-i, T.; Kuwahara, R.; Takata, A.; Jeong, Y.; Sakurai, K.; Mataka, S. *Chem.–Eur. J.* **2006**, *12*, 763–776; b) Kim, Y.; Mayer, M. F.; Zimmerman, S. C. *Angew. Chem.*, *Int. Ed.* **2003**, *42*, 1121–1126; c) Ikeda, C.; Satake, A.; Kobuke, Y. *Org. Lett.* **2003**, *5*, 4935–4938; d) Hartgerink, J. D.; Beniash, E.; Stupp, S. I. *Science* **2001**, *294*, 1684–1688; e) Won, Y.-Y.; Davis, H. T.; Bates, F. S. *Science* **1999**, *283*, 960–963; f) Zubarev, E. R.; Pralle, M. U.; Li, L.; Stupp, S. I. *Science* **1999**, *283*, 523–526; g) Clark, T. D.; Kobayashi, K.; Ghadiri, M. R. *Chem.–Eur. J.* **1999**, *5*, 782–792.

(10) Hecht, S.; Khan, A. *Angew. Chem.*, *Int. Ed.* **2003**, *42*, 6021–6024.

(11) Klug A. *Angew. Chem.*, *Int. Ed.* **1983**, *22*, 565–582.

(12) a) Shimizu, T.; Masuda, M.; Minamikawa, H. *Chem. Rev.* **2005**, *105*, 1401–1444; b) Bong, D. T.; Clark, T. D.; Granja, J. R.; Ghadiri, M. R. *Angew. Chem.*, *Int. Ed.* **2001**, *40,* 988–1011; c) Hill, D. J.; Mio, M. J.; Prince, R. B.; Hughes, T. S.; Moore, J. S. *Chem. Rev.* **2001**, *101*, 3893–401.

(13) Gellman, S. H. *Acc. Chem. Res.* **1998**, *31*, 173–180.

(14) a) Ryu, J.-H.; Oh, N.-K.; Lee, M. *Chem. Commun.* **2005**, 1770–1772; b) Höger, S. *Chem. –Eur. J.* **2004**, *10*, 1320–1329; c) Zhao, D.; Moore, J. S. *Chem. Commun.* **2003**, 807–818.

(15) a) Rosen, B. M.; Wilson, C. J.; Wilson, D. A.; Peterca, M.; Imam, M. R.; Percec, V. *Chem. Rev.* **2009**, *109*, 6275–6540; b) Percec, V.; Dulcey, A. E.; Balagurusamy, V. S. K.; Miura, Y.; Smidrkal, J.; Peterca, M.; Nummelin, S.; Edlund, U.; Hudson, S. D.; Heiney, P. A.; Duan, H.; Magonov, S. N.; Vinogradov, S. A. *Nature* **2004**, *430*, 764–768; c) Percec, V.; Glodde, M.; Bera, T. K.; Miura, Y.; Shiyanovskaya, I.; Singer, K. D.; Balagurusamy, V. S. K.; Heiney, P. A.; Schnell, I.; Rapp, A.; Spiess, H. W.; Hudson, S. D.; Duan, H. *Nature* **2002**, *419*, 384–387.

(16) a) Nelson, J. C.; Saven, J. G.; Moore, J. S.; Wolynes, P. G. *Science* **1997**, *277*, 1793–1796; b) Petitjean, A.; Nierengarten, H.; van Dorsselaer, A.; Lehn, J.-M. *Angew. Chem., Int. Ed.* **2004**, *43*, 3695–3699; c) Kim, H.- J.; Zin, W.-C.; Lee, M. *J. Am. Chem. Soc.* **2004**, *126*, 7009–7014; d) Ryu, J.-H.; Bae, J.; Lee, M. *Macromolecules* **2005**, *38*, 2050–2052.

(17) a) Blankenship, R. E., Matsuura, K. Antenna Complexes from Green Photosynthetic Bacteria, in Light-Harvesting Antennas in Photosynthesis (Green, B. R., and Parson, W. W., Eds.) **2003**, *217*, pp 195, Kluwer Academic Publishers, Dordrecht, The Netherlands; b) Olson, J. M. *Photochem. Photobiol.* **1998**, *67*, 61–75; c) Blankenship, R. E.; Olson, J. M.; Miller, M. Antenna Complexes from Green Photosynthetic Bacteria, in Anoxygenic Photosynthetic Bacteria (Blankenship, R. E., Madigan, M. T., Bauer, C. E., Eds.) **1995**, pp 399–435, Kluwer Academic Publishers, Dordrecht, The Netherlands; d) Oelze, J.; Golecki, J. R. Membranes and Chlorosomes of Green Bacteria: Structure, Composition and Development, in Anoxygenic Photosynthetic Bacteria (Blankenship, R. E., Madigan, M. T., and Bauer, C. E., Eds.) **1995**, pp 259–278, Kluwer Academic Publishers, Dordrecht, The Netherlands.

(18) a) Balaban, T. S.; Tamiaki, H.; Holzwarth, A. R. *Supramolecular Dye Chemistry* **2005**, *258*, 1–38; b) Tamiaki, H. *Coord. Chem. Rev.* **1996**, *148*, 183–197; c) Tamiaki, H. *Photochem. Photobiol. Sci.* **2005**, *4*, 675–680.

(19) Bryant, D. A.; Costas, A. M. G.; Maresca, J. A.; Chew, A. G. M.; Klatt, C. G.; Bateson, M. M.; Tallon, L. J.; Hostetler, J.; Nelson, W. C.; Heidelberg, J. F.; Ward, D. M. *Science* **2007**, *317*, 523–526.

(20) a) Prokhorenko, V. I.; Holzwarth, A. R.; Müller, M. G.; Schaffner, K.; Miyatake, T.; Tamiaki, H. *J. Phys. Chem. B* **2002**, *106*, 5761–5768; b) Brune, D. C.; King, G. H.;

Infosino, A.; Steiner, T.; Thewalt, M. L. W.; Blankenship, R. E. *Biochemistry* **1987**, *26*, 8652–8658; c) Prokhorenko, V. I.; Steensgaard, D. B.; Holzwarth, A. F. *Biophys. J.* **2000**, *79*, 2105–2120.

(21) Scholes, G. D.; Rumbles, G. *Nat. Mater.* **2006**, *5*, 683–696.

(22) a) Huber, V.; Sengupta, S.; Würthner, F. *Chem.–Eur. J.* **2008**, *14*, 7791–7807; b) Huber, V.; Katterle, M.; Lysetska, M.; Würthner, F. *Angew. Chem., Int. Ed.* **2005**, *44*, 3147–3151.

(23) a) Röger, C.; Miloslavina, Y.; Brunner, D.; Holzwarth, A. R.; Würthner, F. *J. Am. Chem. Soc.* **2008**, *130*, 5929–5939; b) Röger, C.; Müller, M. G.; Lysetska, M.; Miloslavina, Y.; Holzwarth, A. R.; Würthner, F. *J. Am. Chem. Soc.* **2006**, *128*, 6542–6543.

(24) a) Ganapathy, S.; Sengupta, S.; Wawrzyniak, P. K.; Huber, V.; Buda, F.; Baumeister, U.; Würthner, F.; de Groot, H. J. M. *Proc. Natl. Acad. Sci. U. S. A.* **2009**, *106*, 11472–11477; b) Huber, V.; Lysetska, M.; Würthner, F. *Small* **2007**, *3*, 1007–1014.

(25) a) Sengupta, S.; Uemura, S.; Patwardhan, S.; Huber, V.; Grozema, F. C.; Siebbeles, L. D. A.; Baumeister, U.; Würthner F. *Chem.–Eur. J.* **2011**, *17*, 5300–5310; b) Uemura, S.; Sengupta, S.; Würthner, F. *Angew. Chem., Int. Ed.* **2009**, *48*, 7825–7828.

(26) Smith, K. M.; Goff, D. A.; Simpson, D. J. *J. Am. Chem. Soc.* **1985**, *107*, 4946–4954.

(27) Würthner, F.; Kaiser, T. E.; Saha-Möller C. R. *Angew. Chem., Int. Ed.* **2011**, *50*, 3376–3410.

(28) a) De Greef, T. F. A.; Smulders, M. M. J.; Wolffs, M.; Schenning, A. P. H. J.; Sijbesma, R. P.; Meijer, E. W. *Chem. Rev.* **2009**, *109*, 5687–5754. b) Smulders, M. M. J.; Nieuwenhuizen, M. M. L.; de Greef, T. F. A.; van der Schoot, P.; Schenning, A. P. H. J.; Meijer, E. W. *Chem.–Eur. J.* **2010**, *16*, 362–367; c) Chen, Z.; Lohr, A.; Saha-Möller, C. R.; Würthner, F. *Chem. Soc. Rev.* **2009**, *38*, 564–584; d) van der Schoot, P. Supramolecular Polymers, 2nd ed. (Eds: A. Ciferri), CRC Press, Taylor & Francis Group, New York, **2005**, pp. 77–106.

(29) a) Linnanto, J. M.; Korppi-Tommola, J. E. I. *Photosynth. Res.* **2008**, *96*, 227–245; b) Prokhorenko, V. I.; Steensgaard, D. B.; Holzwarth, A. R. *Biophys. J.* **2003**, *85*, 3173–3186; c) Didraga, C.; Klugkist, J. A.; Knoester, J. *J. Phys. Chem. B* **2002**, *106*, 11474–11486; d) Griebenow, K.; Holzwarth, A. R.; van Mourik, F.; van Grondelle, R. *Biochim. Biophys. Acta* **1991**, *1058*, 194–202.

(30) a) Berne, B. J.; Pecora, R. *Dynamic Light Scattering*; Wiley: NewYork, 1976; b) Kroeger, A.; Belack, J.; Larsen, A.; Fytas, G.; Wegner, G. *Macromolecules* **2006**, *39*, 7098–7106.

(31) Friedrich, H.; Frederik, P. M.; With, G. de; Sommerdijk N. A. J. M. *Angew. Chem.*, *Int. Ed.* **2010**, *49*, 7850–7858.

(32) For reviews, see: a) Grubbs, R. H. *Angew. Chem.*, *Int. Ed.* **2006**, *45*, 3760–3765; b) Trnka, T. M.; Grubbs, R. H. *Acc. Chem. Res.* **2001**, *34*, 18–29; c) Buchmeiser, M. R. *Chem. Rev.* **2000**, *100,* 1565–1604.

(33) a) Warman, J. M.; van de Craats, A. M. *Mol. Cryst. Liq. Cryst.* **2003**, *396*, 41–72; b) Warman, J. M.; de Haas, M. P.; Dicker, G.; Grozema, F. C.; Piris, J.; Debije, M. G.; *Chem. Mater.* **2004**, *16*, 4600–4609; c) van de Craats, A. M.; Warman, J. M. *Adv. Mater.* **2001**, *13*, 130–133.

(34) a) Oostergetel, G. T.; van Amerongen, H.; Boekema E. J. *Photosynth. Res.* **2010**, *104*, 245–255; b) Staehelin, L. A.; Golecki, J. R.; Drews, G. *Biochim. Biophys. Acta* **1980**, *589*, 30–45.

(35) a) Saga, Y.; Tamiaki, H. *J. Biosci. Bioeng.* **2006**, *102*, 118–123; b) Hohmann-Marriott, M. F. ; Blankenship R. E.; Roberson, R. W. *Photosyn. Res.* **2005**, *86*, 145–154.

(36) Cohen-Bazire, G.; Pfennig, N.; Kunisawa, R. *J. Cell Biol.* **1964**, *22*, 207–225.

(37) Staehelin, L. A.; Golecki, J. R.; Fuller, R. C.; Drews, G. *Arch. Microbiol.* **1978**, *119*, 269–277.

(38) a) Ikonen, T. P.; Li, H.; Pšenčík, J.; Laurinmäki, P.; Butcher, S. J.; Frigaard, N. -U.; Serimaa, R. E.; Bryant, D. A.; Tuma, R. *Biophys. J.* **2007**, *93*, 620–628; b) Pšenčík, J.; Arellano, J. B.; Ikonen, T.P.; Borrego, C. M.; Laurinmäki, P.; Butcher, S. J.; Serimaa, R. E.; Tuma, R. *Biophys. J.* **2006**, *91*, 1433–1440; c) Pšenčík, J.; Ikonen, T. P.; Laurinmäki, P.; Merckel, M. C.; Butcher, S. J.; Serimaa, R. E; Tuma, R. *Biophys. J.* **2004**, *87*, 1165–1172.

(39) von Berlepsch, H.; Kirstein, S.; Hania, R.; Pugžlys, A.; Böttcher C. *J. Phys. Chem. B* **2007**, *111*, 1701–1711.

(40) Wang, Z.; Medforth C. J.; Shelnutt J. A. *J. Am. Chem. Soc.* **2004**, *126*, 15954–15955.

(41) Perrin, D. D.; Amarego, W. L.; Perrin D. R. *Purification of Laboratory Chemicals*; Pergamon Press Ltd.: Oxford, 1980.

Appendix

Additional electron microscopic studies

Scanning electron microscopy (**SEM**): Scanning electron microscopy (SEM) technique images a sample by scanning it with a high-energy beam of backscattered electrons in raster pattern. The signals result from interactions of the electron beam with constituent atoms at or near the surface of the sample. The electrons interact with the atoms constituting the sample producing signals containing information about the sample's topography, composition, and electrical conductivity. Due to the very narrow electron beam, SEM micrographs have a large depth of field yielding a characteristic three-dimensional appearance to the aggregates. Interestingly, SEM measurements of the suspensions of aggregates of ZnChl **1** (discussed in section 5.2.4.) revealed similar morphologies (Figure 1) i.e., short tube-like aggregates with diameters of ~ 147.4 nm as observed in TEM and AFM studies (on silicon wafer).

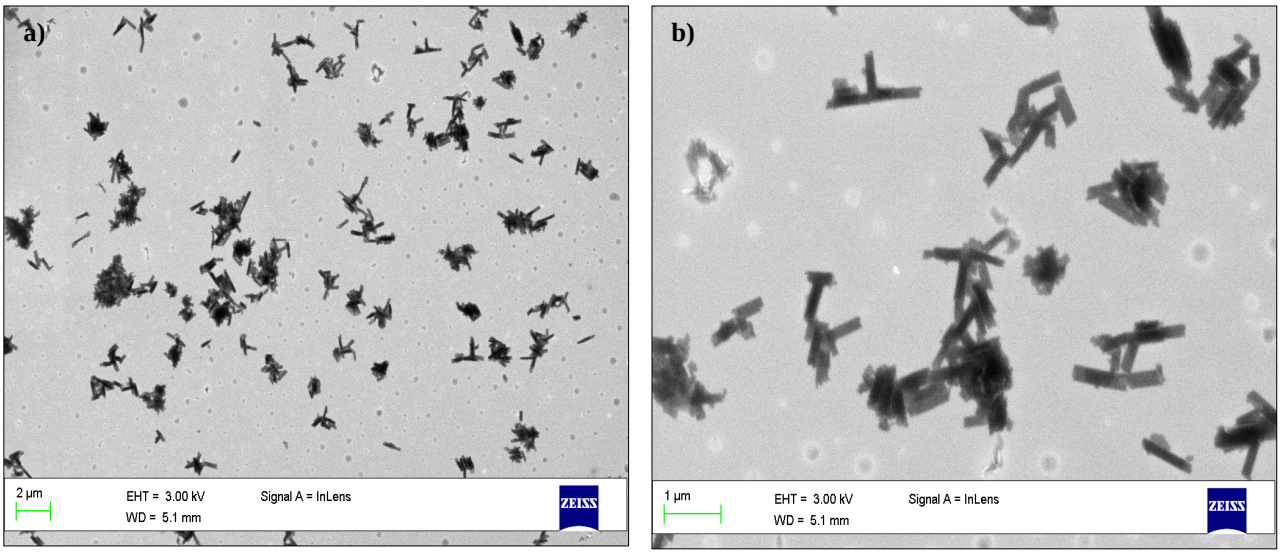

Figure 1. SEM images of aggregates of ZnChl **1** in *n*-hexane/THF (100:0.5) solution with an accelerating voltage of 3 kV, a) $c = 4.0 \times 10^{-4}$ M and b) $c = 1.2 \times 10^{-4}$ M drop-casted onto silicon wafer with average widths of ~ 147.4 nm. Scalebars in the figures (a) and (b) are 2 µm and 1 µm respectively.

Scanning transmission electron microscopy (STEM): Scanning transmission electron microscopy (STEM) is a technique closely related to SEM but uses transmitted electron beams to image a sample. It works on the same principle as the normal SEM, by forming a focused beam of electrons that is scanned over the sample while the desired signal is collected to form an image. As in the SEM, secondary or backscattered electrons can be used for imaging in STEM; but higher signal levels and better spatial resolution in STEM are obtainable by detecting the transmitted electrons. STEM analysis of aggregates of ZnChl **1** in THF/*n*-hexane (0.5 % v/v) (c = 1.2 × 10^{-4} M and c = 4.2 × 10^{-4} M) revealed similar hollow tube-like structures with clear contrast difference between the periphery and centre and average widths of ~ 145 nm of the nanotubes (Figure 2). Based on these detailed EM studies, it can be concluded that in aged aggregate suspensions, large robust nanotubes (~ 150 nm) of ZnChl **1** are observed which are higher order species and presumably result from ordering of the individual nanotubes (of ~ diameters 5-6 nm) into sheets that roll up subsequently, as suggested section 5.5.

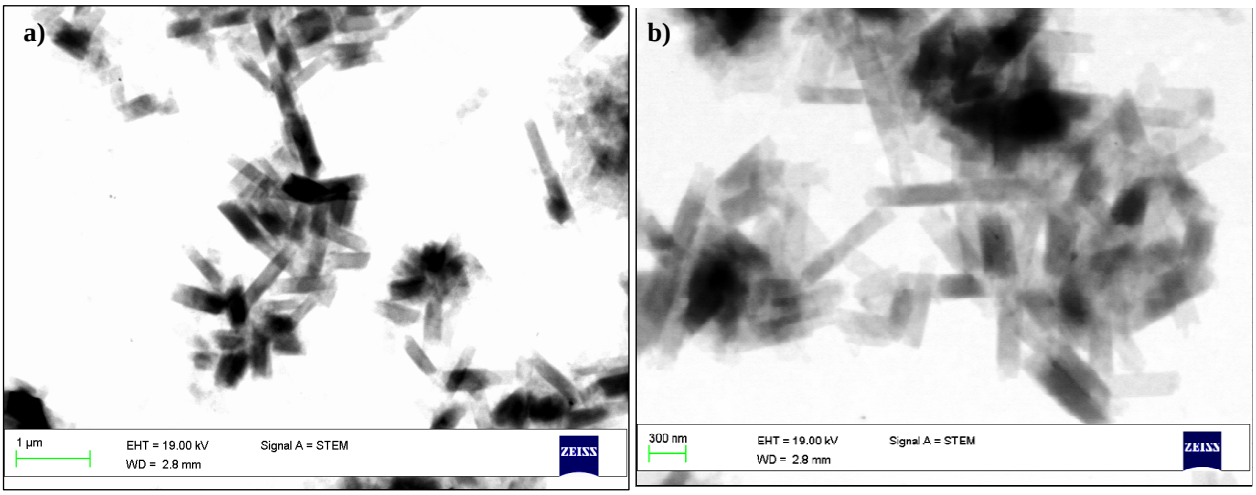

Figure 2. STEM images of aggregates of ZnChl **1** in *n*-hexane/THF (0.5 % v/v) solution, prepared from aged suspensions (a: c = 1.2 × 10^{-4} M and b: c = 4.2 × 10^{-4} M) onto carbon coated copper grid (stained with 0.5 % aqueous uranyl acetate) at accelerating voltage of 19 kV and scalebars in figures (a) and (b) are 1 µm and 300 nm respectively.

Chapter 6

Summary

Chlorophylls are the most important pigments owing to their involvement in photosynthesis. They perform multiple functions that arise due to their optical and redox as well as packing properties. Semisynthetic zinc chlorins investigated in this thesis are the counterparts for the natural protein-free bacteriochlorophyll (BChl) *c* assemblies in light-harvesting (LH) systems in bacterial chlorosomes. The major advantage of the zinc chlorin model compounds over the native BChls lies in their facile semisynthetic accessibility from chlorophyll *a* (Chl *a*), their higher chemical stability and the possibility to influence their packing by suitable chemical modifications of peripheral side chains. Whilst the favorable excitonic properties and the suitability of ZnChl and natural BChl *c* dye aggregates for long distance exciton transport are well documented, charge transport properties of aggregates of semisynthetic ZnChls are hitherto unexplored.

The present study involves structural elucidations of aggregates of a variety of semisynthetic zinc chlorin derivatives in solution, in solid state and on surfaces by combination of spectroscopic, crystallographic and microscopic techniques, followed by investigation of charge transport properties and conductivities of these aggregates. Chart 1 shows the different ZnChls synthesized in this work that are functionalized with hydroxy or methoxy substituents at 3^1-position and contain different substituents at the 17^2-position benzyl ester functional group.

The self-assembly of these dyes is strongly dependent upon their chemical structures. While ZnChls **1a**, **2a**, **3**, which are functionalized with 3^1-hydroxy group bearing dodecyl and oligoethylene glycol side chains form well-soluble rod aggregates, the corresponding 3^1-methoxy functionalized counterparts **1b**, **2b** form stacks in solution and on surfaces. These supramolecular polymers have been studied in detail in **Chapter 3** by UV/Vis and circular dichroism (CD)

spectroscopy and dynamic light scattering (DLS). These studies provided useful insights into the aggregation process of these two types of aggregates. Whereas 3^1-hydroxy functionalized ZnChl **1a** self-assemble into rod aggregates via an isodesmic mechanism, corresponding stack aggregates of ZnChl **1b** are formed by a cooperative nucleation-elongation pathway. Detailed electron microscopic studies such as transmission electron microscopy (TEM) and scanning transmission electron microscopy (STEM) provided unequivocal evidence for hollow tubular nanostructures of water-soluble 3^1-hydroxy zinc chlorin **3** aggregates for the first time. The measured tube diameter of ~ 5-6 nm of these aggregates is in excellent agreement with electron microscopy data of BChl *c* rod aggregates in chlorosomes (*Chloroflexus aurantiacus*, diameter ~ 5-6 nm) and thus complied with the tubular model postulated by Holzwarth and Schaffner.

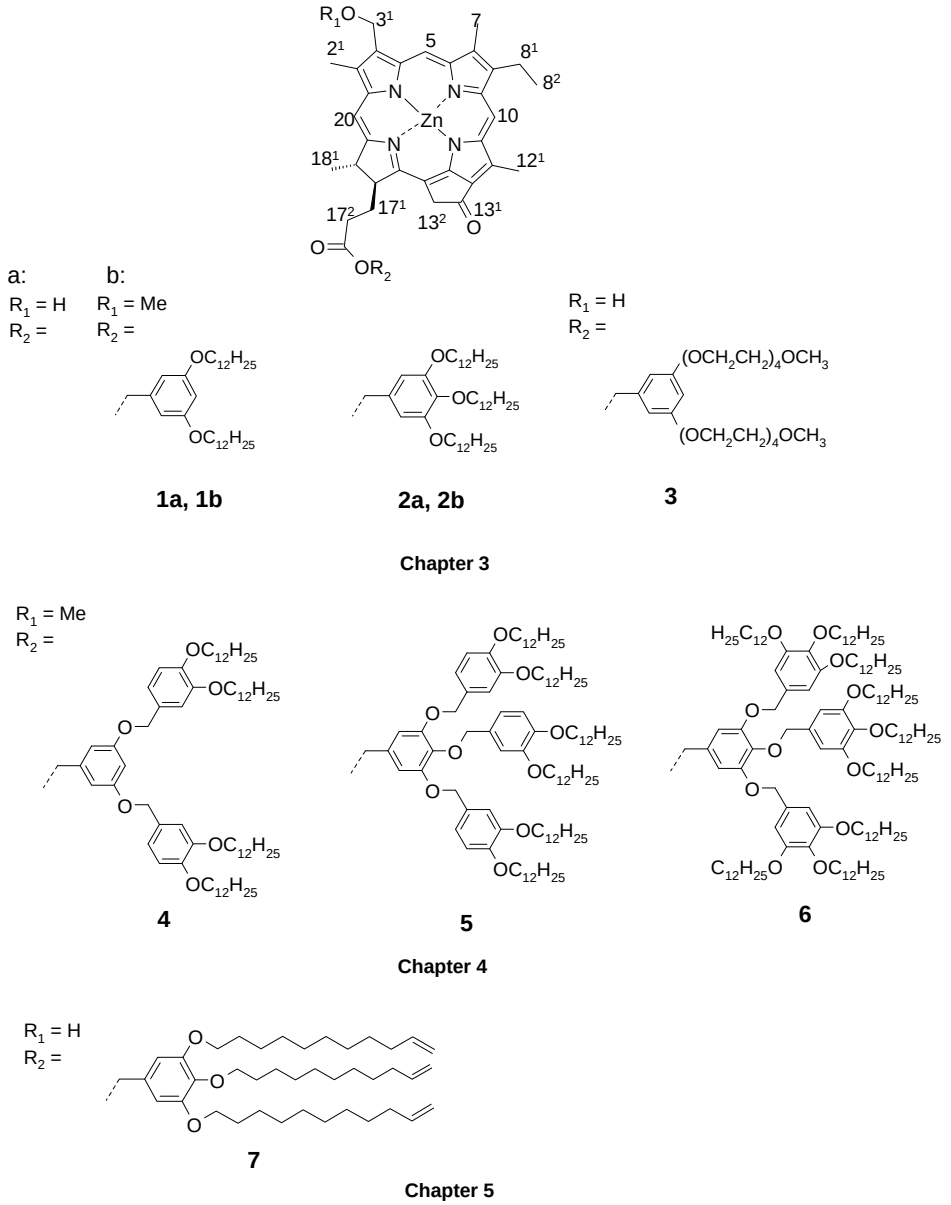

Chart 1. Chemical structures of ZnChls **1**-**7** synthesized and studied within this work.

The tubular and stack aggregated structures formed in solution could be successfully transferred to the solid state by lyophilization. Subsequently, the microstructures of these two types of aggregated π-stacks of chlorophylls in the solid-state, i.e. rod and stack aggregates, have been solved by a combination of solid-state magic angle spinning (MAS) NMR, molecular modelling and powder X-ray diffraction (XRD) and DFT calculations. The combination of these techniques provided a unique three-dimensional packing of these π-stacks in solid state. Both compounds formed excitonically coupled microcrystalline material with local antiparallel packing (Figure 1) and seemed conducive to directional and efficient charge transport.

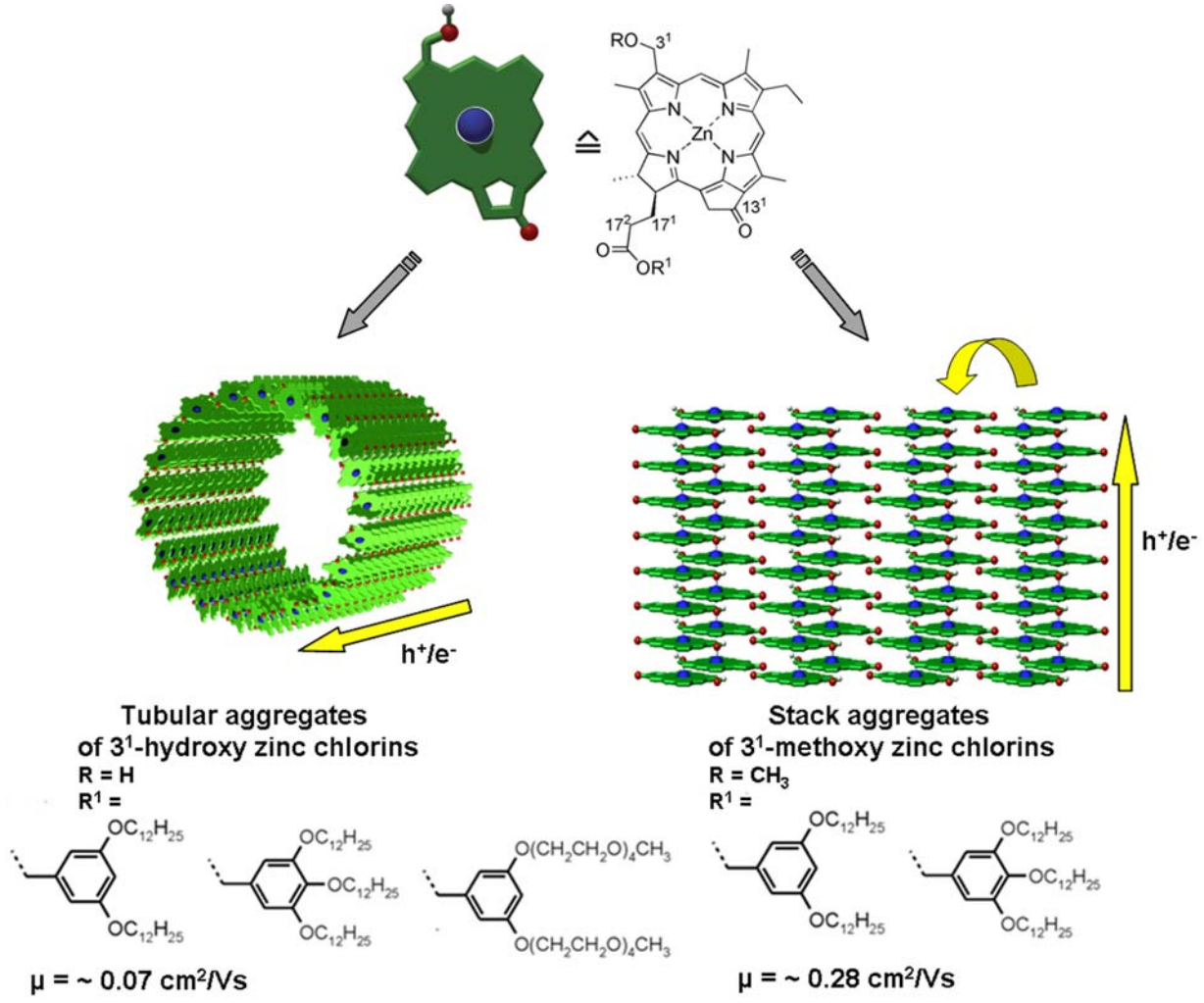

Figure 1. Schematic representation of structural models of zinc chlorin tubular and stack aggregates based on electron microscopy, solid-state NMR and powder XRD and their respective charge transport properties.

In the next part of this work, the charge transport properties of the aggregates of a series of synthesized 3^1-hydroxy and 3^1-methoxy zinc chlorins in the solid state were investigated by an electrodeless technique i.e., pulse radiolysis-time resolved microwave conductivity (PR-TRMC). The charge transport properties (i.e., charge carrier mobilities and charge recombination kinetics) were distinct for rod and stack aggregates with the highest mobilities being 0.07 cm^2/Vs and 0.28

cm^2/Vs for ZnChls **1a** and **1b** respectively (Figure 1). Furthermore, electrical charaterization was performed on isolated nanotubes of ZnChl **3** on non-conductive substrate with conductive-AFM technique. These chlorin nanowires exhibited high electrical conductivity (~ 0.3 S/m) over micrometer length scale, with conductance that varies linearly with the length of the wire. The corresponding PR-TRMC mobility values obtained for ZnChl **3** were ~ 0.03-0.04 cm^2/Vs. Figure 1 thus summarises our findings on the structural and charge transport properties of zinc chlorin tubular and stack assemblies.

In **Chapter 4**, a series of ZnChls **4-6** bearing peripheral second-generation dendron wedge units were synthesized and their surface and solid-state properties were investigated in detail. ZnChl **4** has the smallest wedge in this series that self-assembles into linearly ordered adlayers on highly oriented pyrolytic graphite (HOPG) surface. In ZnChl **5**, the dendron group acts as an effective wedge for the formation of cyclic self-assembled nanostructures on HOPG. Both wedges in ZnChls **4** and **5** can adopt planar orientations that lead to better interaction of the aromatic chlorin cores with the HOPG surface, rendering their visualization as ordered layers by atomic force microscopy (AFM). Furthermore, scanning tunneling microscopy (STM) study revealed the precise hexameric molecular ordering within the cyclic nanostructures of ZnChl **5** (Figure 2). This is the first example of cyclic nanostructures that was achieved based on chlorin derivatives and are truly reminiscent of the BChl organization in the LH apparatus of purple bacteria. In contrast, a conic shape was suggested for ZnChl **6** owing to the large number of alkyl chains on the dendron wedge. The spatial demand and steric effect imposed by this dendron is apparently disadvantageous for planarization of the dyes on graphite surface leading to disordered and featureless topography. Interestingly, ZnChl **5** formed a thermotropic liquid crystalline (LC) phase whereas ZnChls **4** and **6** did not exhibit such LC behavior. The mesomorphic behavior of ZnChl **5** was studied by differential scanning calorimetry (DSC), polarized optical microscopy (POM), AFM, powder XRD studies that indicated formation of columnar 2D oblique lattice for the LC phases of **5** with ~five molecules per column cross section. The intrinsic charge carrier mobilities of ZnChls **4-6** were investigated by PR-TRMC method and ZnChl **5** was found to possess charge carrier mobilities of ~ 0.01 cm^2/Vs, which are lower than those of discotic liquid crystalline material based on other p-type semiconductors such as phthalocyanines, porphyrins and hexabenzocoronenes. The mobilities are however, comparable to those of dendron mediated self-assembled nanostructures (10^{-3}-10^{-4} cm^2/Vs) reported by Percec and co-workers. This is the first example of a LC zinc chlorin derivative and the columnar tubular organization of ZnChl **5** in solid state is reminiscent to the BChl organization in LH chlorosomal antennae of green sulphur bacteria.

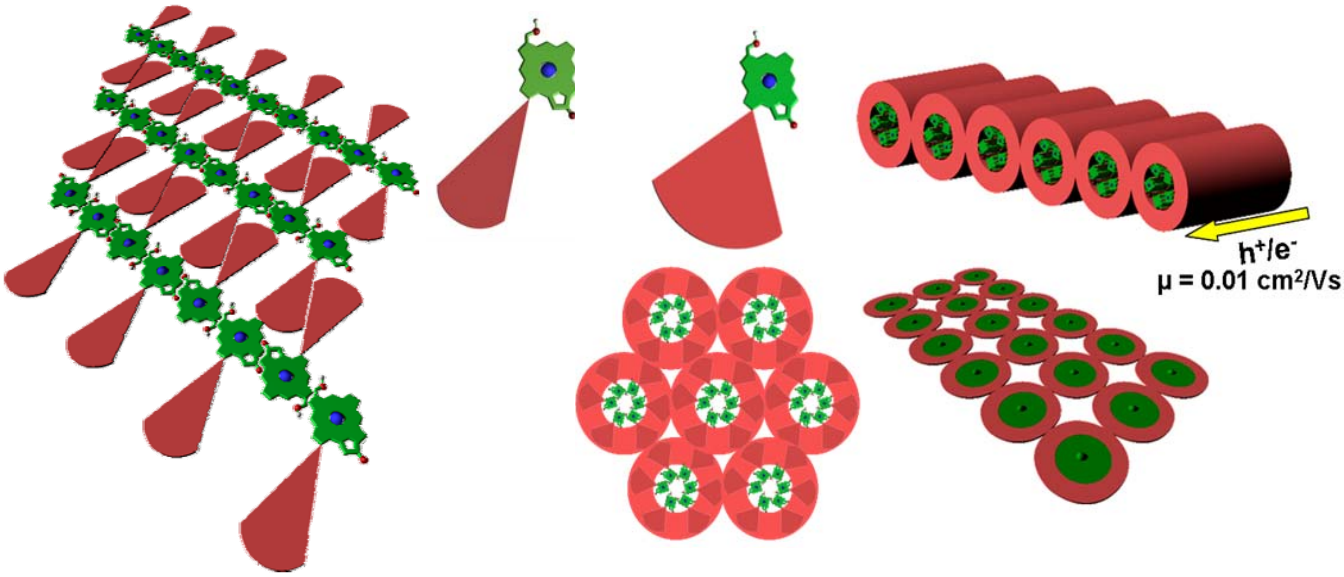

Figure 2. Schematic representation of the surface packing and solid state packing of dendron functionalized ZnChls **4** and **5** based on SPM and XRD results.

In **Chapter 5**, ZnChl **7** functionalized with undecyl chains bearing terminal olefinic groups was synthesized and characterized in detail by spectroscopic and microscopic techniques. These molecular building blocks form well-defined nanorod aggregates in non-polar solvents and their self-assembly has been studied by UV/Vis absorption, CD spectroscopy and DLS as well as AFM studies. Importantly, the electron rich olefinic groups at the periphery of nanorods provided good contrast in electron microscopic studies. As a result, TEM, STEM and scanning electron microscopy (SEM) studies enabled visualization of fibrous aggregates at lower concentrations and hollow, open ended tube-like structures in aggregate suspensions. Furthermore, the chemically accessible peripheral double bonds of the aggregated nanorods at lower concentrations were subjected to in-situ metathesis polymerization reaction mediated by Grubbs first generation catalyst (Figure 3). The intramolecularly cross-linked nanorods could be characterized by UV/Vis, CD spectroscopy, AFM and fourier-transform infrared (FT-IR) studies. Appreciable charge carrier mobilities of ~ 0.02-0.03 cm^2/Vs were obtained for aggregates of **7** in solid state by PR-TRMC technique which indicate suitability of these assemblies for supramolecular electronic applications.

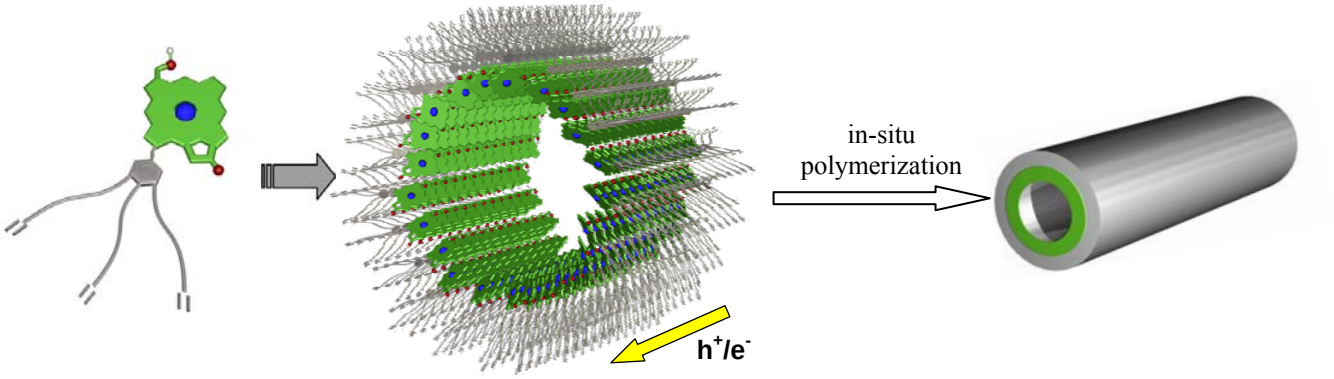

Figure 3. Schematic representation of covalently stabilized zinc chlorin **7** nanotubes by post-polymerization (in-situ metathesis polymerization) of the aggregates **7**.

In concord with their highly organized structures, micrometer-scale one dimensionality, robust nature and efficient charge transport capabilities, these self-assembled ZnChl nanotubular, stack and liquid crystalline assemblies are highly promising for supramolecular electronic applications. Research efforts in utilizing these assemblies for (opto)electronic device fabrication, for instance, in organic field effect transistors, should thus be rewarding in the future.

Zusammenfassung

Die Chlorophylle stellen in der Natur die wichtigsten Pigmente dar, weil sie verantwortlich für die Photosynthese sind und hierbei vielfältige Funktionen wahrnehmen, die sich aus ihrer Selbstassemblierung sowie den vorteilhaften optischen und Redox-Eigenschaften ergeben. Die in dieser Arbeit untersuchten semisynthetischen Zinkchlorine stellen Modellverbindungen des natürlichen Bacteriochlorophylls *c* (BChl *c*) der Lichtsammelsysteme (*light-harvesting*: LH) in Chlorosomen von Bakterien, jedoch ohne Proteingerüst, dar. Die entscheidenden Vorteile dieser Zinkchlorine (ZnChl) gegenüber den natürlichen BChls bestehen im einfachen semisynthetischen Zugang ausgehend von Chlorophyll *a* (Chl *a*), ihrer gesteigerten chemischen Stabilität sowie der Möglichkeit ihre Selbstassemblierung durch gezielte chemische Modifizierung der Seitenketten in der Peripherie zu steuern. Während bereits mehrfach über die vielversprechenden Redox- und excitonischen Eigenschaften von Aggregaten von ZnChl und natürlichem BChl *c* und den damit verbundene Voraussetzungen für Excitontransport über große Distanzen berichtet wurde, sind die Ladungstransporteigenschaften von Aggregaten der biomimetischen ZnChl bis heute unerforscht.

Die vorliegende Arbeit beschäftigt sich mit der Aufklärung der Struktur von Aggregaten einer Vielzahl von semisynthetischen Zinkchlorophyllderivaten im Feststoff, in Lösung und auf Oberflächen durch die Kombination verschiedenster spektroskopischer, kristallographischer und mikroskopischer Techniken an die sich Untersuchungen zum Ladungstransport in den Aggregaten anschließen. Schema 1 zeigt die verschiedenen, in dieser Arbeit synthetisierten ZnChls, die entweder mit einer Hydroxy- oder Methoxygruppe in der 3^1-Position funktionalisiert sind sowie Substituenten unterschiedlicher Art, Länge und Verzweigung an der Benzylestergruppe in 17^2-Position tragen.

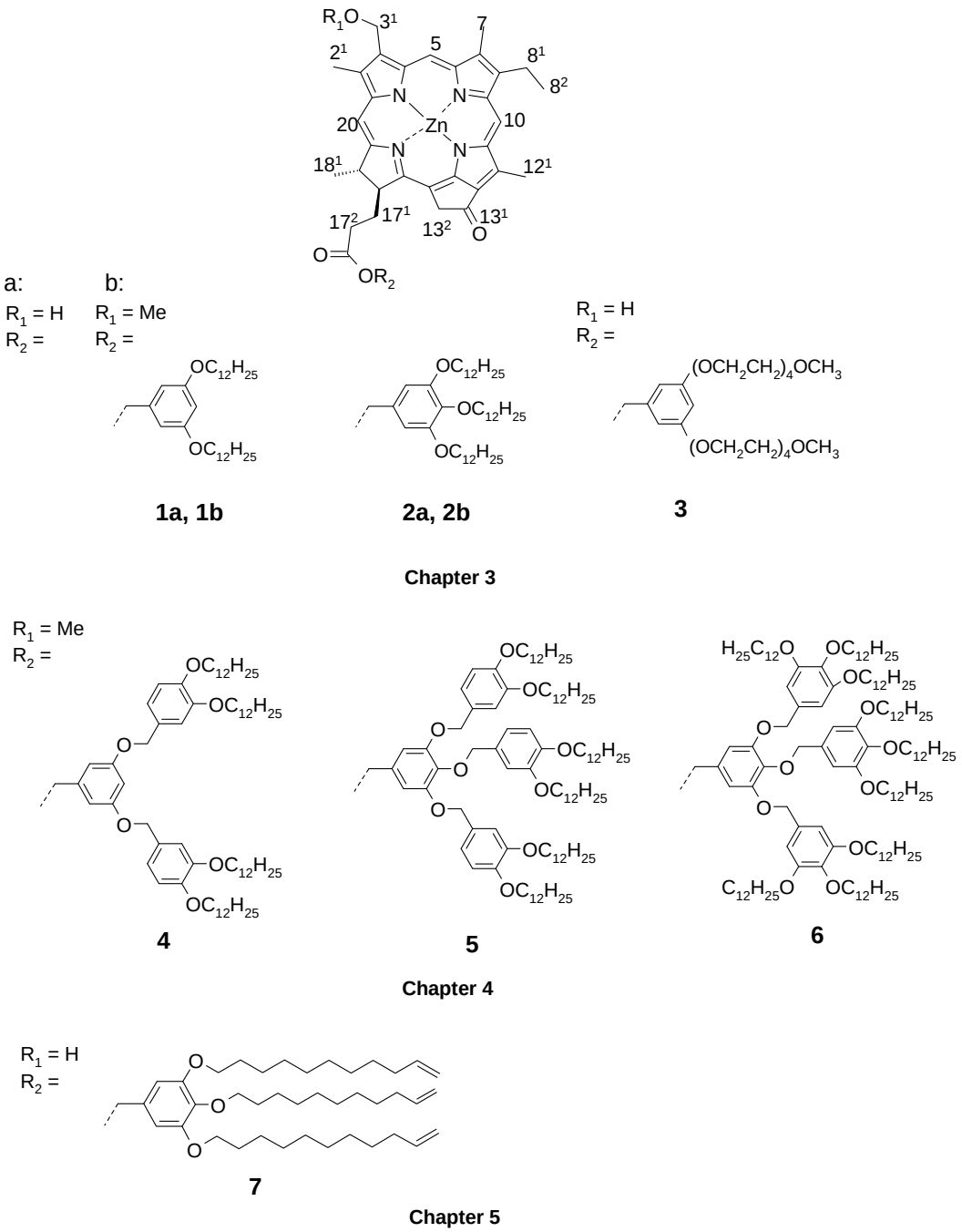

Schema 1. Chemische Strukturen der Zinkchlorine (ZnChl) **1**-**7**, die im Rahmen dieser Arbeit synthetisiert und charakterisiert wurden.

Die Packung dieser Farbstoffe hängt entscheidend von ihrer chemischen Struktur ab. Während die ZnChls **1a**, **2a**, **3** mit 3^1-Hydroxygruppe und Alkylseitenketten (Dodecyl bzw. Oligoethylenglykol) gut lösliche stabförmige Aggregate bilden, lagern sich die analogen Verbindungen mit 3^1-Methoxygruppe (**1b**, **2b**) zu Stapeln in Lösung und auf Oberflächen zusammen. Diese supramolekularen Polymere wurden im Detail in **Kapitel 3** mit Hilfe von UV/Vis- und CD-Spektroskopie (*circular dichroism*: CD) sowie dynamische Lichtstreuung (*dynamic light scattering*: DLS) untersucht. Darüber hinaus lieferten temperaturabhängige UV/Vis- in Kombination mit DLS-Messungen wertvolle Informationen über die Aggregationsprozess dieser beiden Sorten von Aggregaten. Während sich die ZnChl **1a** mit

3^1-Hydroxygruppe entsprechend dem isodesmischen Modell zu röhrenförmigen Aggregaten zusammenlagern, bilden sich die stapelförmigen Aggregate von **1b** nach einem kooperativen Keimbildungs-Wachstums-Mechanismus (*nucleation-elongation mechanism*). Detaillierte elektronenmikroskopische Studien lieferten erstmals überzeugende Beweise für röhrenförmige Nanostrukturen der Aggregate des wasserlöslichen 3^1-Hydroxy Zinkchlorin **3**. Die gemessenen Durchmesser der Röhren von ~ 5-6 nm dieser Aggregate liegen in hervorragender Übereinstimmung mit den Elektronenmikroskopie-Daten von BChl *c* Stabaggregaten in Chlorosomen (*Chloroflexus aurantiacus*, Durchmesser ~ 5-6 nm) und entsprechen damit dem von Holzwarth und Schaffner postulierten röhrenförmigen Modell.

Die in Lösung gebildeten Aggregatstrukturen konnten erfolgreich durch Lyophilisierung in den Festkörper überführt werden. Die Mikrostrukturen dieser zwei Arten von π-gestapelten Chlorophyllen im Festkörper, d. h. röhrenförmige und stapelförmige Aggregate, konnte mit Hilfe einer Kombination aus MAS-NMR-Spektroskopie (*magic angle spinning NMR spectroscopy*) im Feststoff in Verbindung mit Molecular Modeling, Röntgenpulverdiffraktometrie sowie DFT-Rechnungen erfolgreich aufgeklärt werden. Die Kombination dieser Methoden ermöglichte erstmals die eindeutige Bestimmung der dreidimensionalen Packung dieser π-Stapel im Feststoff. Beide Verbindungsklassen **1a** and **1b** bilden excitonisch gekoppelte mikrokristalline Materialien aus, in denen die ZnChl eine antiparallele Anordnung einnehmen (Abbildung 1), die vorteilhaft für einen gerichteten und effizienten Ladungstransport erscheinen.

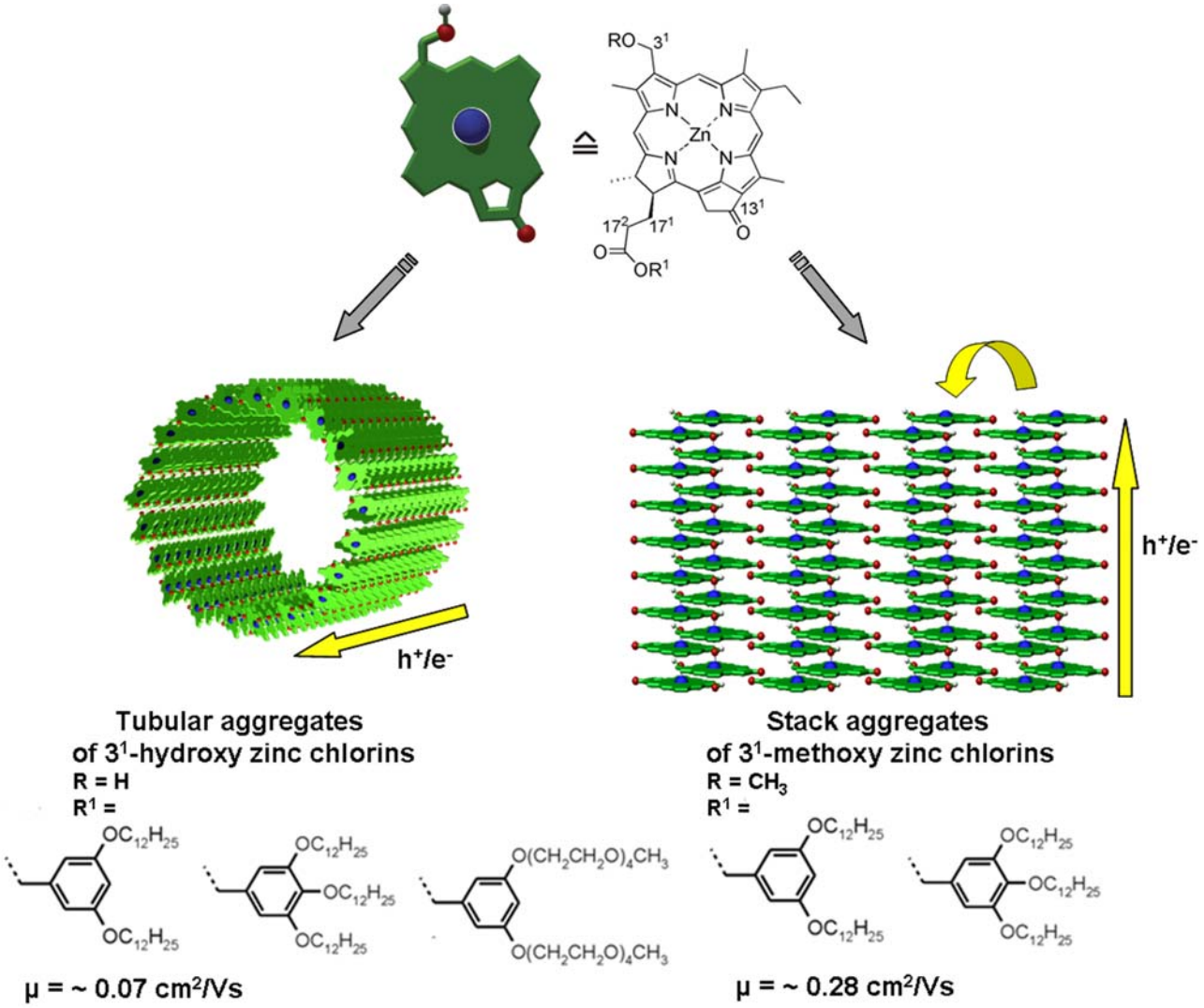

Abbildung 1. Schematische Darstellung der strukturellen Anordnung der Zinkchlorinröhre und gestapelter Aggregate auf Basis von Elektronenmikroskopie, Festkörper-NMR und Pulver-XRD und ihre Ladungstransporteigenschaften.

Daraufhin wurde eine Serie von in 3^1-Position mit Hydroxy- bzw. Methoxygruppen funktionalisierten Zinkchlorinen in Hinblick auf ihre Fähigkeiten zum Ladungsträgertransport im Festkörper mit Hilfe einer Messtechnik ohne Elektroden untersucht (*pulse radiolysis-time resolved microwave conductivity*: PR-TRMC). Es konnten ausgeprägte Unterschiede bei der Fähigkeit zum Ladungstransport (d. h. Ladungsträgerbeweglichkeit, Kinetik der Rekombination von Ladungen) zwischen röhren- und stapelförmigen Aggregaten beobachtet werden, wobei die höchsten Ladungsträgerbeweglichkeiten bei 0.07 cm^2/Vs bzw. 0.28 cm^2/Vs für die ZnChls **1a** und **1b** lagen. Darüberhinaus wurden die elektronischen Eigenschaften einzelner, isolierter Nanoröhren von ZnChl **3** auf nicht leitenden Substraten mit Hilfe spezieller Rasterkraftmikroskopiemethoden bestimmt (*conductive-atomic force microscopy:* conductive-AFM). Die Chlorinnanodrähte sind in der Lage über einige Mikrometer effizient zu leiten (mit hohe Leitfähigkeit von ~ 0.3 S/m), wobei die Leitfähigkeit linear mit der Länge der Drähte

korreliert. Die entsprechenden Untersuchungen der Ladungsträgerbeweglichkeit mit Hilfe von PR-TRMC von **3** ergab Werte von ~ 0.03-0.04 cm^2/Vs. Abbildung 1 fasst die Ergebnisse der bestimmten Struktureigenschaften und gemessenen Ladungsträgerbeweglichkeiten der Röhren- oder Stapel-Aggregate der Zinkchlorine zusammen.

Im **Kapitel 4** wurde die Synthese einer neuen Serie von ZnChls **4**-**6**, die in der Peripherie mit Dendron-Keile der zweiten Generation bestückt sind, vorgestellt und ihre Eigenschaften im Festkörper und auf Oberflächen eingehend untersucht. Verbindung **4** besitzt den kleinsten Keil der gesamten Serie und selbstassembliert zu linearen, hoch geordneten Strukturen auf HOPG (*highly oriented pyrolytic graphite*). Im Fall von Zinkchlorin **5** bewirkt die Dendrongruppe als effektiver Keil die Bildung von cyclischen selbstassemblierten Strukturen auf HOPG. Beide Keile von **4** und **5** nehmen planare Anordnungen ein, sodass sich eine vorteilhafte Wechselwirkung zwischen dem aromatischen Kern der Chlorine und der Graphitoberfläche bilden kann, worauf hin einzelne Schichten durch AFM visualisiert werden können. Darüber hinaus konnte mit Hilfe von Rastertunnelmikroskopie (*scanning tunneling microscopy*: STM) die exakte Anordung der Moleküle in den cyclischen Nanostrukturen von Verbindung **5** aufgeklärt werden (Abbildung 2). Diese cyclischen Nanostrukturen stellen das erst bekannte Beispiel von Derivaten des Chlorophylls dar, die tatsächlich an die Organisation der BChls im LH-Komplex von Purpurbakterien erinnern. Im Unterschied dazu besitzt Zinkchlorin **6** auf Grund der größeren Zahl an Alkylketten in der Peripherie eine eher konische Form, sodass deren sterischer Anspruch sich anscheinend nachteilig auf die Planarisierung auf der Graphitoberfläche auswirkt, was eine ungeordnete Topographie zur Folge hat.

Interessanterweise konnten für Verbindung **5** thermotrope flüssigkristalline Eigenschaften (*liquid crystalline*: LC) nachgewiesen werden, wohingegen die Derivate **4** und **6** keine Anzeichen dafür zeigten. Die Eigenschaften der Mesophase von ZnChl **5** wurde mit Hilfe von dynamischer Differenzkalorimetrie (*differential scanning calorimetry*: DSC), polarisierter Lichtmikroskopie (*polarization optical microscopy*: POM), AFM und Röntgenpulverdiffraktometrie untersucht und deuten auf die Ausbildung säulenförmiger, schräger zweidimensionaler Gitteranordnungen in der LC Phase von **5** hin, mit ca. fünf Molekülen im Säulenquerschnitt. Die intrinsischen Ladungsträgerbeweglichkeiten der Verbindungen **4**-**6** wurden mit Hilfe der PR-TRMC Methode bestimmt. Für das Derivat **5** wurde hierdurch eine temperaturabhängige Ladungsträgerbeweglichkeit von ~ 0.01 cm^2/Vs nachgewiesen, die niedriger als bei anderen discotischen flüssigkristallinen Merialen von p-Halbleitern wie z. B. Phthalocyaninen, Porphyrinen und Hexabenzocoronenen ist. Die Ladungsträgerbeweglichkeit ist jedoch vergleichbar mit denen anderer durch Dendronen

vermittelter, selbstassemblierter Nanostrukturen (10^{-3}-10^{-4} cm^2/Vs), über die Percec und Mitarbeiter berichteten. Dies stellt das erste bekannte Beispiel eines Flüssigkristalls eines Zinkchlorins dar und die säulenförmige Organisation des ZnChl **5** im Feststoff erinnert stark an die Organisation des BChls in LH-Systemen der chlorosomalen Antennen von grünen Schwefelbakterien.

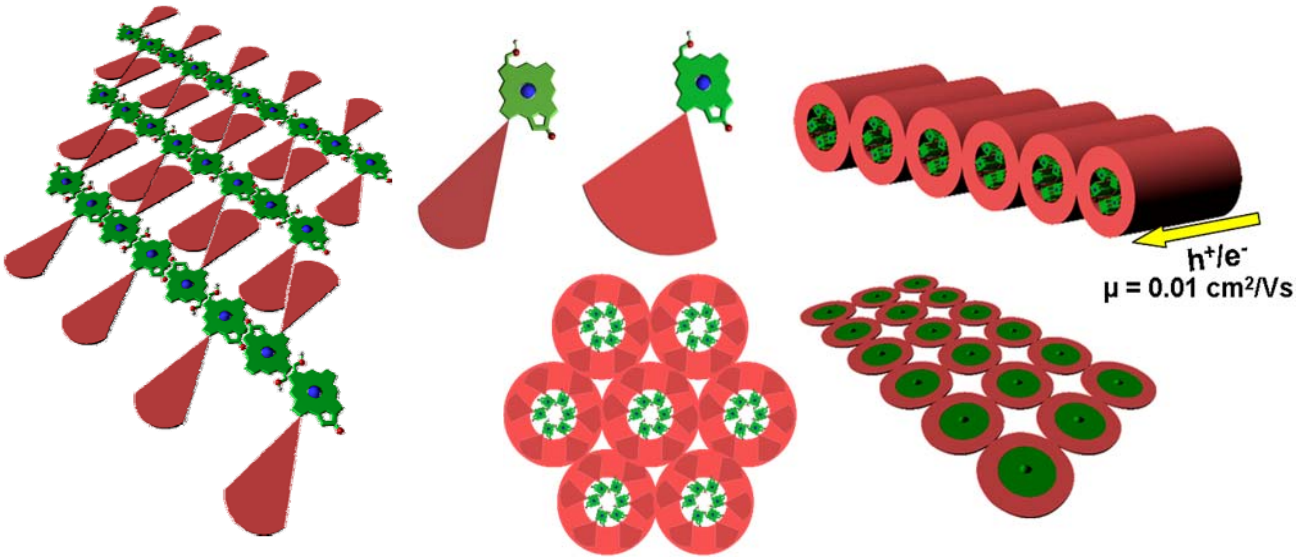

Abbildung 2. Schematische Darstellung der Packung von mit Dendronen bestückten Zinkchlorinen **4** und **5** auf Oberflächen und im Feststoff nach den Ergebnissen von SPM und XRD Messungen.

In **Kapitel 5** wird die Synthese des ZnChl **7** beschrieben sowie seine Charakterisierung mit Hilfe spektroskopischer und mikroskopischer Methoden. ZnChl **7** ist mit Undecylketten mit terminalen Doppelbindungen substituiert. Diese molekularen Bausteine bilden wohldefinierte, röhrenförmige Nanoaggregate in unpolaren Lösungsmitteln und ihre Selbstassemblierung wurde mit Hilfe von UV/Vis- und CD-Spektroskopie, DLS und AFM untersucht. Die elektronenreichen Alkenylgruppen in der Peripherie der Nanoröhren führten zu einem gesteigerten Kontrast bei Aufnahmen mit Hilfe eines Elektronenmikroskops. Hierdurch konnten erstmals hohle, am Ende offene, röhrenförmige Strukturen von Aggregaten der ZnChls mit Hilfe von Transmissionselektronenmikroskopie (*transmission electron microscopy*: TEM), Rastertransmissionselektronenmikroskopie (*scanning transmission electron microscopy*: STEM) und Rasterelektronenmikroskopie (*scanning electron microscopy*: SEM) visualisiert werden. Darüber hinaus wurden die chemisch zugänglichen peripheren Doppelbindungen der aggregierten Nanoröhren einer in-situ metathetischen Polymerisation mit Hilfe von Grubbs-Katalysatoren der ersten Generation unterworfen (Abbildung 3). Die hierdurch intramolekular verknüpften Nanoröhren wurden daraufhin mit Hilfe von UV/Vis-, CD-, FT-IR-Spektroskopie

und AFM untersucht. Ansprechende Ladungsträgerbeweglichkeiten von ~ 0.02-0.03 cm^2/Vs konnten für die Aggregate von **7** im Feststoff durch die PR-TRMC Technik bestimmt werden und lassen auf eine mögliche Eignung in supramolekularen elektronischen Anwendungen schließen.

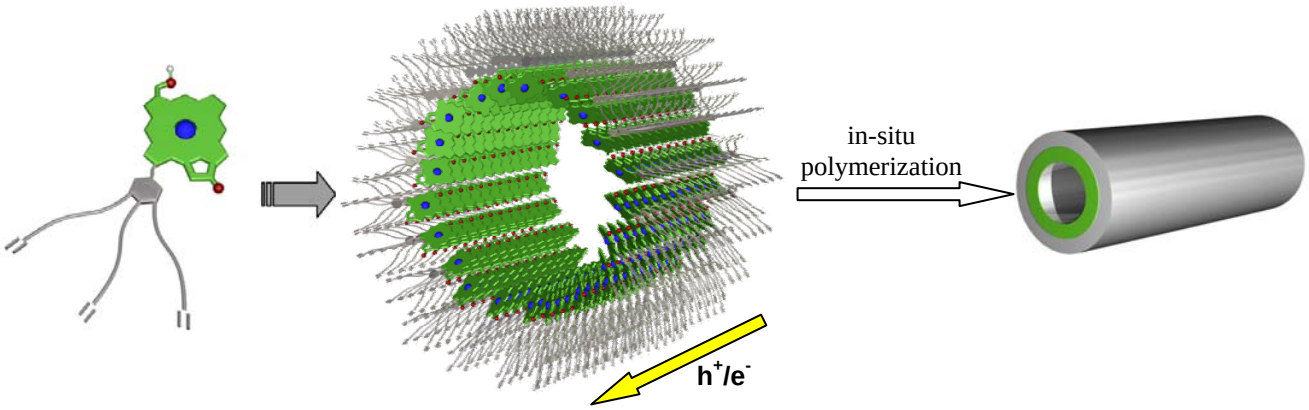

Abbildung 3. Schematische Darstellung der Bildung von Nanoröhren von kovalent-verbrückten Zinkchlorinen, die durch Post-Polymerisation (*ring closing metathesis polymerization*) der Aggregate von ZnChl **7** gebildet werden.

Im Einklang mit ihren hoch geordneten, robusten Strukturen, die sich eindimensional in einer Größenordnung von Mikrometeren erstrecken, sowie ihrer Fähigkeit zum effizienten Ladungsträgertransport stellen diese selbstassemblierten Nanoröhren von ZnChls vielversprechende Ausgangsmaterialien für die Fertigung supramolekularer elektronischer Bauteile dar. Wissenschaftliche Bemühungen einige dieser Moleküle und ihre entsprechenden supramolekularen Polymere für die Fertigung von (opto-)elektronischen Bauteilen wie organischen Feldeffekttransistoren zu benutzten, stellen lohnende Aufgaben für die Zukunft dar.

Publication List

1.“Columnar Mesophases Based On Zinc Chlorin Derivatives Bearing Peripheral Dendron Wedges.”
S. Sengupta, S. Uemura, S. Patwardhan, V. Huber, F. C. Grozema, L. D. A. Siebbeles, U. Baumeister, F. Würthner *Chem. Eur. J* **2011**, *17*, 5300–5310.

2.“Theoretical study of the Optical Properties of artificial self-organizing zinc chlorins.” S. Patwardhan, **S. Sengupta**, F. Würthner, L. D. A. Siebbeles, F. C. Grozema *J. Phys. Chem. C* **2010**, *114* (48), pp 20834–20842.

3.“Cyclic Self-Assembled Structures of Chlorophyll Dyes on HOPG by the Dendron Wedge Effect.”
S. Uemura, **S. Sengupta**, F. Würthner, *Angew. Chem.* **2009**, *121*, 7965–7968; *Angew. Chem. Int. Ed.* **2009**, *48*, 7825–7828.

4.“Zinc chlorins for artificial light-harvesting self-assemble into antiparallel stacks forming a microcrystalline solid-state material.”
S. Ganapathy, **S. Sengupta**, P. Wawzryniak, V. Huber, F. Buda, U. Baumeister, F. Würthner, H. J. M. de Groot *Proc. Natl. Acad. Sci. U. S. A.* **2009**, *106*, 11472–11477.

5. “Structure-Property Relationships for Self-assembled Zinc Chlorin Light Harvesting Dye Aggregates.”
V. Huber, **S. Sengupta**, F. Würthner, *Chem. Eur. J.* **2008**, *14*, 7791–7807.